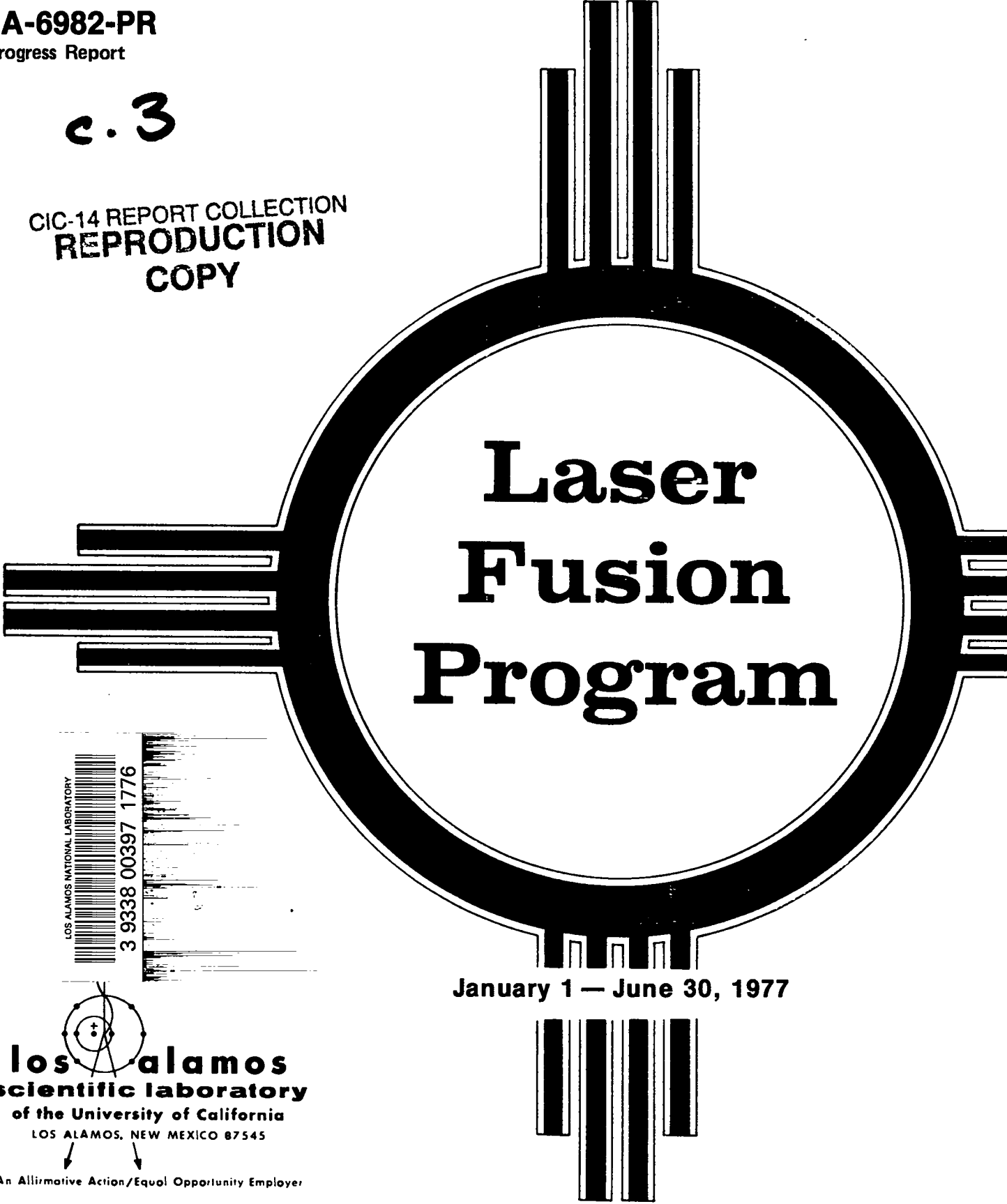


LA-6982-PR
Progress Report

c. 3

CIC-14 REPORT COLLECTION
**REPRODUCTION
COPY**

A large, stylized graphic of a laser beam. It consists of a central circle with a thick black border. Inside the circle, the words "Laser Fusion Program" are written in a bold, sans-serif font. The circle is surrounded by several vertical bars of varying heights, resembling a laser beam's structure. The bars are arranged in a way that they appear to be entering and exiting the circle.

Laser Fusion Program



January 1 — June 30, 1977

The logo for Los Alamos Scientific Laboratory, featuring a stylized atomic symbol with a central nucleus and three orbiting electrons.

los alamos
scientific laboratory
of the University of California
LOS ALAMOS, NEW MEXICO 87545

An Affirmative Action/Equal Opportunity Employer

UNITED STATES
DEPARTMENT OF ENERGY
CONTRACT W-7405-ENG. 36

The four most recent reports in this series, unclassified, are LA-6245-PR, LA-6510-PR, LA-6616-PR, and LA-6834-PR.

This work was supported by the US Energy Research and Development Administration,* Division of Laser Fusion.

* As of October 1, 1977, all funds originally under the Energy Research and Development Administration were transferred to the newly established Department of Energy.

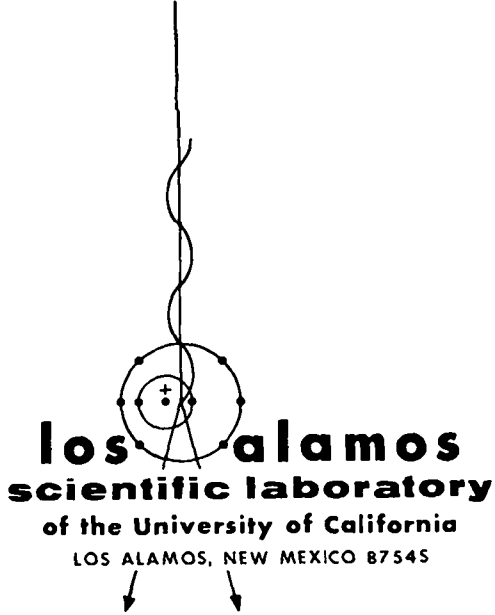
Printed in the United States of America. Available from
National Technical Information Service
U.S. Department of Commerce
5285 Port Royal Road
Springfield, VA 22161

		Microfilm		\$ 3.00					
901-025	4.00	126-150	7.25	251-275	10.75	376-400	13.00	501-525	13.25
026-050	4.50	151-175	8.00	276-300	11.00	401-425	13.25	526-550	13.50
051-075	5.25	176-200	9.00	301-325	11.75	426-450	14.00	551-575	14.25
076-100	6.00	201-225	9.25	326-350	12.00	451-475	14.50	576-600	14.50
101-125	6.50	226-250	9.50	351-375	12.50	476-500	15.00	601-up	--1

1. Add \$2.50 for each additional 100-page increment from 601 pages up.

This report was prepared as an account of work sponsored by the United States Government. Neither the United States nor the United States Department of Energy, nor any of their employees, nor any of their contractors, subcontractors, or their employees, makes any warranty, express or implied, or assumes any legal liability or responsibility for the accuracy, completeness, or usefulness of any information, apparatus, product, or process disclosed, or represents that its use would not infringe privately owned rights.

LA-6982-PR
Progress Report
UC-21
Issued: April 1978



Laser Fusion Program at LASL

January 1 — June 30, 1977

Compiled and edited by

Frederick Skoberne
Eugene Stark



CONTENTS

ABSTRACT	1
SUMMARY AND PROGRAM OVERVIEW	2
Introduction	2
CO ₂ Laser Development	2
Antares	4
Laser Fusion—Theory, Experiments, and Target Design	5
Laser Fusion Target Fabrication	6
Target Diagnostics	7
Applications of Laser Fusion—Systems Studies	7
I. CO ₂ LASER PROGRAM	8
Single-Beam System	8
Two-Beam System	9
Eight-Beam System	9
Optical Systems	17
CO ₂ Laser Technology	20
References	41
II. ANTARES—HIGH-ENERGY GAS LASER FACILITY	42
Introduction	42
Prototype Power Amplifier	42
Antares Design	46
III. LASER FUSION THEORY, EXPERIMENTS, AND TARGET DESIGN	73
Laser Fusion Experiments	73
Military Applications Experiments and Studies	83
Theoretical Support and Direction	87
References	99
IV. LASER FUSION TARGET FABRICATION	100
Introduction	100
Microballoon Separation, Measurement, Characterization, and Fabrication	100
Pusher Shell Deposition and Characterization	109
Metal Films	110
Plastic Shell Deposition	111
Plastic Films	113
Nondestructive Fuel-Gas Assay	114
Cryogenic Targets	115
References	123

V.	TARGET DIAGNOSTICS124
	Introduction124
	Diagnostics124
	References131
VI.	APPLICATIONS OF LASER FUSION—FEASIBILITY AND SYSTEMS STUDIES132
	Systems Analysis Computer Programs132
	Reactor Concept Studies135
	Laser Studies139
	Preliminary Assessment of Environmental Effects of Laser Fusion Electric Generating Stations142
	References147
VII.	RESOURCES, FACILITIES, AND OPERATIONAL SAFETY148
	Manpower Distribution148
	Facilities148
	Operational Safety149
	Miscellaneous149
VIII.	PATENTS, PRESENTATIONS, AND PUBLICATIONS150
	Patents Issued150
	Presentations150
	Publications153

**LASER FUSION PROGRAM AT LASL
JANUARY 1—JUNE 30, 1977**

Compiled and Edited by

Frederick Skoberne and Eugene Stark

ABSTRACT

Progress in the development of high-energy short-pulse CO₂ laser systems for fusion research is reported. Experiments, which led to the generation of $\sim 5 \times 10^6$ fusion neutrons on our Two-Beam System in early 1977, with laser output powers of 0.16 to 0.4 TW, are described. These significant results and recent theoretical advancements indicate that the CO₂ laser is the driver of greatest promise for commercial laser fusion application. Initial test runs on the Eight-Beam System achieved an output energy of ~ 850 J with one beam of less than 1-ns duration, which makes us certain that the design goal of the system will be met on time. Antares, our 100- to 200-TW target irradiation system, is progressing on schedule. Very promising test results obtained on the prototype, as well as encouraging progress in optics development, are summarized.

Modifications to the LASNEX code are described, which demonstrated that strong ponderomotive force effects can explain various, seemingly anomalous experimental laser-target interaction results. The studies indicate that laser-plasma interaction is less dependent on wavelength than hitherto believed, and that breakeven target designs are attainable even in the presence of a hot-electron spectrum. Layered-target experiments corroborate our theories on wavelength scaling. These results give us confidence that our comparably inexpensive CO₂ laser systems will achieve significant yield leading to breakeven conditions with Antares.

Further progress in various target fabrication and nondestructive fuel-assay techniques is reported, and the development of new diagnostic tools is described. Among new tools are single-channel and four-channel x-ray diode assemblies, both using aluminum cathodes, to study the time history of soft x-ray emission; and a 10- μ m microscope, developed in-house, which aids us in verifying optimum target alignment and laser focusing.

A design modification of the magnetically protected reactor cavity concept is being investigated.

SUMMARY AND PROGRAM OVERVIEW

(R. B. Perkins, Laser Fusion Program Manager)

INTRODUCTION

The Laser Fusion Program at the Los Alamos Scientific Laboratory is part of a vital national research program aimed at harnessing the virtually limitless fusion energy resource. The inertial-confinement approach to fusion, including laser and electron- and ion-beam driver options, is the only one known to work on Earth, as evidenced by the successful operation of thermonuclear weapons. In fact, it was only after the success of these weapons that the scientific community seriously considered that Earth-bound control of thermonuclear reactions for peaceful energy uses was feasible. The theoretical possibility of fusing hydrogen atoms with the help of powerful laser beams and thus obtaining a virtually inexhaustible energy source was first recognized in the early 1960s. However, it was not until the late 1960s that advances in laser technology and the recognized need for alternatives to magnetic-confinement fusion led to the initiation of a national research effort by the former Atomic Energy Commission. A formal laser fusion program began at the Los Alamos Scientific Laboratory in 1969 with the investigations of high-pressure CO₂ laser systems. Within the next few years, we developed the electron-beam-controlled CO₂ laser amplifier and expanded our efforts into a complete, balanced research program of laser fusion for commercial and military applications.

The major goal of our program is the demonstration that laser fusion is scientifically feasible, that is, to obtain an output energy from our fusion targets that is at least equal to the input laser energy using a laser with the potential efficiency and repetition-rate capability needed for a reactor system. We at LASL are using CO₂ as the lasing medium, the only known laser with an efficiency and scalability required for commercial applications of laser fusion. We are addressing our objectives in a prudent program of constructing ever larger CO₂ laser systems for target experimentation. Supportive goals are the development of diagnostic instrumentation for the program as well as the refinement of targets and their fabrication in support of

the experimental program. In the short term, military applications are expected to constitute an important effort in our laser fusion program, because we can make use of our current intense, short-pulse lasers to study material properties at very high excitations. Systems studies support both the near-term military application and the long-range goal of commercial energy generation by laser fusion.

Early concerns that the long-wavelength CO₂ laser at 10.6 μm was unsuitable for laser fusion have given way to well-based optimism that there is little wavelength dependence in laser-target interactions. We now believe that the CO₂ laser is the driver of greatest promise for commercial laser fusion applications. Particularly significant was the first observation of fusion neutrons produced by a CO₂ laser in early 1977. Its potential for efficiency, high repetition rate, and relatively low capital cost has been demonstrated, and our experimental program will prove within the next six years that laser fusion with CO₂ lasers is scientifically feasible.

CO₂ LASER DEVELOPMENT

General

Our optimism that CO₂ lasers will drive inertial-confinement fusion is evidenced by our shift in laser development from substantial efforts in HF and other advanced lasers as recently as early 1976, to complete concentration on CO₂. Our rate of progress toward scientific breakeven and the attainment of intermediate milestones are determined by the availability of larger laser systems.

Single-Beam System (SBS)

Our first CO₂ system was the Single-Beam System (SBS). It includes an oscillator and four electron-beam-controlled amplifiers, three of which were used in our first 10.6- μm laser target experiments early in 1973, delivering 10 J in a 1-ns pulse.

Since then, the SBS has been upgraded to generate a maximum of 520 J in a 1-ns pulse and to deliver 180 J to a target with a peak intensity of 7×10^{14} W/cm². The SBS also serves as a developmental test bed for new laser system components, for example, oscillators, isolation schemes, and optical systems.

The optical train and the target alignment system were improved, but major emphasis was placed on experimental investigation of basic target interaction physics.

Two-Beam System (TBS)

The heart of this system is a dual-beam amplifier module, in which two gain chambers share one cold-cathode electron-beam ionization gun. The oscillator pulse is split into two beams, each of which is amplified in three passes through a single gain chamber. The TBS was originally intended only as a prototype for a subsequent Eight-Beam System. However, when the need for target experiments at higher intensities became apparent, the TBS program was enlarged to include a target irradiation capability. The first CO₂ laser-produced fusion neutrons were observed on this system in early 1977.

Eight-Beam System (EBS)

The EBS will be our first integrally designed CO₂ target irradiation facility when completed in April 1978. Building upon experience gained with the dual-beam modules (DBMs), the EBS incorporates four DBMs of similar design, which will deliver 10 to 20 TW (10 kJ in 1 ns or 5 kJ in 0.25 ns) to laser fusion targets.

We have made significant progress in the development of each subsystem: The EBS front end was reconfigured to improve its stability and to meet system requirements. Checkout of the DBMs continued successfully; studies of short-pulse energy extraction and of means to suppress parasitic oscillations, performed on one of the eight beams, led to an energy of ~850 J at acceptable gain; control-system code development proceeded on schedule; and conceptual designs were developed and models fabricated for one of the most demanding subsystems, the target insertion mechanism.

These three laser systems are leading up to our most ambitious CO₂ laser system, Antares, expected to demonstrate the feasibility of laser fusion in 1983. Antares progress is summarized separately below.

Optical Systems

Significant advances in the precision and range of diagnostics for laser-target interactions have placed increasingly stringent requirements on the accuracy and repeatability of beam and target alignment. Early visual techniques with an alignment accuracy of ~1 mm in the SBS have given way to sophisticated Hartmann-mask and infrared-microscope methods: alignment can now be based on the true (approximately flat) transverse beam profile rather than on an idealized Gaussian one. A base-line beam-alignment system has been designed for the EBS, and target-alignment methods developed on other systems will be incorporated. New optical diagnostics will permit us to determine beam energy and beam quality with improved accuracy.

CO₂ Laser Technology

This effort provides the basic technology for the design, construction, and upgrade of our CO₂ laser systems. In front-end development, pulse contrast ratios were improved markedly, due to advances in ultrafast electro-optic switches. A conceptual front-end design was proposed allowing significant flexibility in pulse shaping and wavelength content, the latter as a function of time during the pulse. Theoretical and experimental studies of parasitic oscillations in our high-gain laser amplifier reached quantitative agreement, which greatly increases our confidence in future system performance. Related encouraging results were obtained in the development of broadband saturable absorbers for the suppression of amplifier parasitic oscillations. The behavior of p-doped germanium as a saturable absorber was well characterized for possible use in the EBS. Work on promising Faraday rotator material for future parasitic suppression systems continued. Additional progress was made in the development of both sequence-band CO₂ laser oscillators and calorimetry for measuring energetic laser pulses.

ANTARES

General

The most important milestone in our program is the demonstration of scientific feasibility of laser fusion with a scalable, efficient CO₂ laser system. This milestone will be reached with Antares, a 100- to 200-TW CO₂ target-irradiation system scheduled for completion in October 1982. Because of the cost and importance of this effort, we are conducting a prototype development program that is giving us great confidence that the Antares system will achieve its design objectives.

Optics

Two-dimensional calculations in support of prototype efforts to predict the spatial gain distribution for large-aperture amplifiers show that the elimination of discharge fringing would substantially improve gain uniformity and overall performance.

Significant progress has been made in both optical-component manufacture and system design. Harshaw Chemical Company has successfully produced NaCl boules of adequate size by using the Kyropoulis/Czochralski process, which represents a major breakthrough for Antares because both time and cost are greatly reduced over the usual Stockbarger process.

Off-axis paraboloids of high optical quality have been produced for the EBS at Union Carbide Corporation's Y-12 plant, which also represents an important technological contribution to Antares.

As a significant step toward the final design of the optical system, we established a point design for the entire Antares optical train, from the oscillator to the target chamber.

An apparatus for measuring absolute surface reflectance has been assembled. Bidirectional reflectance has been measured quantitatively on a variety of materials that hold promise to eliminate reflections that might produce parasitic oscillations.

Calculations have been performed to predict the net optical performance of the entire optical train. Effects of manufacturing error in the form of an error budget were included in these calculations.

The results show that each of the 72 Antares beams can be nearly diffraction-limited. A parallel experimental effort has been performed that verifies some of these calculations.

Power Amplifier Module

The power amplifier design has not changed significantly from that described in the last progress report (LA-6834-PR). New features and refinements have been incorporated for such tasks as retropulse protection and path-length equalization, but the design remains essentially a 72-beam system, divided into 6 annular arrays.

Energy extraction efforts have concentrated on monitoring the experimental results obtained on the EBS and assessing their impact on Antares. Most significant is the reduction of the maximum gain-length product to 6.0, which changes Antares back to a single-band system (10.6 μm) and greatly increases the required output from the preamplifier. Work also continued on techniques to improve the Antares efficiency through better energy extraction conditions.

High-Voltage System

In the gridded cold-cathode electron-gun design effort, the self-generated magnetic fields remain a major concern because they deflect the electron beams and adversely affect gun-emission uniformity. To reduce these effects, we will change the cathode from a sectioned design to a continuous cylinder. A calculated twofold reduction in magnetic effects is being verified experimentally. In addition, we are considering the use of multiple gun feeds. A single-section center-feed arrangement has been chosen, which should result in an additional twofold reduction.

It now appears that high-impedance cables can be used between the pumping pulsers and the power amplifiers. These cables will be less expensive and much easier to handle than the larger core low-impedance ones.

The gun bushing design for the power amplifier is taking full advantage of the experience gained on the power amplifier prototype. An attempt is being

made to develop a straight vacuum bushing to reduce cost. Experiments on preliminary designs are promising.

Mechanical Design

The conceptual design for an amplifier with four longitudinal sections has been developed, which provides the necessary anode spacing and support of internal components, and makes allowance for assembly requirements. Preliminary design studies have been completed for two power amplifier optical support arrangements. Both concepts are being subjected to further design and analysis.

Controls

The use of fiber-optics communication links to avoid electromagnetic interference problems appears extremely promising; a low-attenuation, pure silica cable has been tested for 10^{10} bits over 86 m at 38 kbps with no error.

The control computer, an HP 3000, was acquired and is operational. Software for the HP 3000 is being developed and software requirements for microcomputers are being studied.

Construction

The Title II design has been completed for Package I, consisting of the laser building, mechanical building, office building, and warehouse. The bid packages have been sent to interested contractors, and bid opening is scheduled for July 1977. The Title II design for Package II, the target building plus remaining site and utilities work, has been received and is being reviewed internally.

Title II review for the Optics Evaluation Laboratory and for the High-Voltage Development Laboratory is complete. The construction contract is scheduled for award in October 1977.

LASER FUSION—THEORY, EXPERIMENTS, AND TARGET DESIGN

General

The laser fusion program is a coordinated effort in theory, experiments, and target design. Because the interaction of high-intensity laser pulses with target plasmas represents a new regime of physics not previously studied in detail, there have been many uncertainties in modeling the relevant processes. Experimentally, we require precise spatial and temporal resolutions, the spectra of emitted particles and radiation, as well as a complete characterization of the incident laser pulse. These experiments are conducted to test theoretical models and often lead to major revisions of theory. Theoretical efforts examine, for example, the various light-absorption mechanisms, hydrodynamic motion and instabilities, energy-transport mechanisms, and the deposition of nuclear reaction products. In turn, target design efforts must take account of our present theoretical understanding and of problems that may have arisen with previous designs.

Laser Fusion Experiments

On the SBS, we collected data in studies involving vacuum insulation concepts to shield the targets against fast electrons and absorption measurements. The vacuum insulation study was preceded by conductivity measurements of target-mounting stalks and by comparison of the hot-electron temperatures as determined by x-ray and ion measurements. We then carried out vacuum insulation experiments with a double foil, with and without a short circuit. The absorption measurements used a novel light collector to study flat-target absorption by collecting all the scattered and reflected $10.6\text{-}\mu\text{m}$ light.

Several support experiments were also performed. Layered-target experiments produced evidence for laser intensity-dependent electron spectra, whereas

the thin-foil (100 to 1000 Å) absorption measurements corroborated recent theories on wavelength scaling. Visible-probe measurements on the thin-foil experiment demonstrated the usefulness of this new method for measuring plasma expansion and profile modification.

We also made several measurements related to CO₂ laser technology and laser-beam diagnostics. The vacuum-aperture retro-pulse isolator, using a plasma shutter based on ablation of an aperture's edge, was tested at higher energies than previously and displayed useful characteristics. Infrared calorimeters, including prototypes for the EBS, were studied carefully. Several calorimeters were cross-calibrated and tested for damage threshold and linearity. Another test involved comparing a microscope and an autocollimating mask for purposes of aligning and focusing the 10.6- μ m beam on target. Both systems utilize pyroelectric vidicon detection of the ir beam. These tests depended on the beam's spatial profile. Both the calorimetry and target-alignment tests had an immediate impact on EBS development. Another test measured the damage threshold of a metallized plastic-foil beam splitter-attenuator. We also explored the possibility of using a multiple-pulse technique to monitor the efficacy of attenuators and isolators.

The TBS was used successfully for imploding spherical glass microballoons (GMBs) filled with 1 to 10 atm of DT fuel. With total laser output powers of 0.16 to 0.4 TW, we obtained neutron yields as high as 5×10^6 , similar to the yields obtained with Nd:glass lasers operating at the same peak power levels.

A variety of x-ray spectral and imaging diagnostics, charged-particle diagnostics, and scattered-light diagnostics were used to compare target performance to predictions of LASNEX and PIC (particle-in-cell) simulation codes.

Theoretical Support and Direction

Our studies continued in areas of hot-electron generation, hot-electron transport, and critical-surface stability. Careful LASNEX modeling has demonstrated that strong ponderomotive force effects can explain experimental results which, originally, had been thought to be evidence for anomalously inhibited electron thermal conduction.

Calculations on vacuum insulation have been extended to spherical geometry with a self-consistent treatment allowing for return-current electron flow across the vacuum. Simulation studies of hot-electron generation by resonant absorption have been refined; and simulation studies and fluid modeling of critical-surface rippling phenomena have continued.

LASER FUSION TARGET FABRICATION

Fabrication and characterization of target pellets are important areas of supporting technology in our laser fusion program. Small, often complex, target pellets must be fabricated to strict specifications, e.g., filling a sphere to several hundred atmospheres with DT and depositing a uniform DT-ice layer on the inside of a microballoon. The characterization of completed pellets is also an important and challenging task.

The use of surface acoustic waves as a sorting mechanism for microballoon size and uniformity was investigated and found to be promising. This method will be used with a one-at-a-time microballoon feeder as a production-line microballoon separator. The shearing-plate interferometer was developed for contractors trying to improve GMB uniformity and surface finish. Further developments in x-ray microradiography and image analysis have led to an ability to characterize and measure opaque microballoons with a sensitivity approaching that of GMB measurements with the optical interferometer. Measurements of gas permeation through microballoon walls and studies of fuel-gas-loss mechanisms continued. We began to study the possibility of improving the wall-thickness uniformity by spinning microballoons in a high-temperature environment. We continued to refine our capabilities in chemical vapor deposition, sputtering, glow-discharge polymerization, and film molding to produce target shells and films. Our nondestructive fuel-gas assay methods were further refined. Cryogenic targets with uniform solid DT layers produced by the fast isothermal freezing technique were characterized.

We obtained positive results on a variation of the temperature-gradient technique for maintaining cryogenic targets in a target-chamber environment. Instead of using a cold jet of helium gas to stabilize

the target, a high-conductivity support stalk provides the required heat removal. A cryogenic-target insertion mechanism for a beam system was further developed, and property measurements of cryogenic DT continued.

TARGET DIAGNOSTICS

Measurements of laser-plasma interactions, which may last from 50 ps to 1 ns, impose severe constraints on the diagnostics, requiring much equipment to be designed in-house and pacing the state of the art in many areas.

In further development of diagnostics for plasma density profiles we turned our attention to diagnostics based on probe-beam absorptance. A ray-tracing code was used to generate simulated data which were used to test data-unfolding techniques. The unfolding is quite accurate for special cases, but a more general method has not yet been developed.

To study the time history of soft x rays, we designed, built, and calibrated a single-channel and a four-channel x-ray diode, both using aluminum cathodes. A 10- μ m microscope was installed in the SBS as an alignment aid and focal-spot diagnostic. This assembly was used to test the effectiveness of the autocollimating mask test for system alignment.

APPLICATIONS OF LASER FUSION—SYSTEMS STUDIES

Our feasibility and systems studies are performed to analyze the various commercial and military applications of laser fusion, and to identify technological problems requiring long-term development. Analysis, optimization, and trade-off studies are performed on conceptual power plant

designs, and alternative applications of laser fusion are investigated.

The program for improving our capability to estimate capital and operating costs of experimental and commercial laser fusion facilities and installations was continued on schedule. A new computer code, VENTURE, has been completed to perform venture-worth analyses and to compute lifetime-discounted average or leveled costs of production for a projected enterprise.

A new approach to conceptual laser fusion reactor design—a modification of the magnetically protected reactor cavity concept—has been investigated. An MHD duct is included in each end of the cylindrical cavity to decelerate the pellet debris and thus to prevent excessive damage to the reactor components that collect the debris energy.

Initial results have been obtained from a study of scaling relationships for cavity wall loads and stresses due to energy deposition by fusion pellet microexplosion emissions. These relationships will be embodied in the computer program TROFAN for use in parametric analyses of laser fusion power plants.

We have developed a model for calculating the compressor power required to circulate a lasing gas for cooling during pulsed laser operation. Computational results indicate a reduction of $\sim 30\%$ in overall laser efficiency due to these power requirements.

Preliminary assessment of the environmental effects of conceptual laser fusion generating stations indicates that the dominant hazard stems from a large-scale lithium fire, and not from an accidental release of radioactivity. The probability of such fires is, however, exceedingly small. Our analyses included comparisons between the environmental effects of laser fusion power plants and those of other potential energy sources, where appropriate.

I. CO₂ LASER PROGRAM

The research and development programs on high-energy short-pulse CO₂ lasers were begun at LASL in 1969. Three large systems are now either operating or being installed. The SBS, a four-stage prototype, was designed in 1971 and has been in operation since 1973 with an output energy of 250 J in a 1-ns pulse with an on-target intensity of 7.0×10^{14} W/cm². Target experimentation continued on the TBS, which will ultimately generate pulses of 2 to 4 TW for target-irradiation experiments, and construction is under way on the EBS, which is scheduled for completion in April 1978 and will begin target experiments at 10 to 20 TW in 1978.

SINGLE-BEAM SYSTEM (G. T. Schappert)

Introduction

The SBS is operated both as a service facility for single-beam laser target interaction experiments at $10.6 \mu\text{m}$ with a 1.0-ns pulse as well as a developmental system for many aspects of operating and controlling high-energy CO₂ laser systems for target experiments. The SBS consists of a gated oscillator and four electron-beam-sustained amplifiers. The system delivers on target a maximum intensity of 7×10^{14} W/cm² and yields new information for fusion target development.

In addition to using the SBS as a target-irradiation facility, we are continuing to upgrade the SBS to produce higher target irradiances. This upgrading involves reducing the problems of laser-pulse feedthrough, self-lasing, and retroreflected pulses; and improving the beam quality.

During this reporting period, the SBS was operated mainly for laser-target interaction experiments. A few experiments relating to component testing and/or to alignment schemes and calorimetry were also performed. With all systems operating well electrically, the system delivered ~115 J in 1-ns pulses on target.

Experiments

Experiments included essential target studies of vacuum insulation and absorption measurements as

well as several support experiments on layered targets to study electron and x-ray energy spectra. Performance and damage studies of components developed for the EBS alignment scheme were also conducted; the nonlinearity of a large-aperture (35.5-cm) calorimeter was measured and several prototypes were tested. The accuracies of the Hartmann mask and of the ir vidicon telescope target-alignment schemes were compared. Detailed discussions of these experiments may be found elsewhere in this report.

System Upgrade

Optics. The upgrade of the optical train was completed. All the mirrors and salt windows up to Amplifier IV have been renewed. The new, stable optical stands and mounts discussed in the previous report (LA-6834-PR) have definitely improved beam stability and alignment. The optics on the oscillator table were simplified by installing a new beam expander and spatial filter.

Target Alignment. A Hartmann mask and ir telescope alignment system were installed in the target-chamber screen room. Both systems are still in the developmental stages and we are still perfecting our skill in their use. Depending on the target, either one or both systems can be used for alignment. Considerable effort was expended in comparing the two schemes. An initial discrepancy between the two methods has meanwhile been

resolved conceptually, and a simple modification of the hardware is under way.

Oscillator. Minor modifications on the oscillator and switch-out system improved their overall stability and reliability.

Amplifiers. All four amplifiers failed occasionally and caused some system downtime. The typical failure mode is arcing in the pumping chamber, which ruptures the electron-beam foil and may damage the gun filament structure. The triggering mechanism has yet to be identified, but, unless the failure mode is clearly electrical, we suspect that a higher electron-beam voltage, and hence range, may reduce the possibility of such arcs. Minor modifications to the electron-beam pulsers are under way to increase their operating voltages where possible.

TWO-BEAM SYSTEM (J. V. Parker)

Introduction

The two major functions of the TBS are to serve as a developmental prototype for the dual-beam modules of the EBS, and to provide a facility for target-irradiation experiments for military and laser fusion applications.

Tests and Modifications

During this reporting period, the TBS became a major facility for laser-induced fusion research. More than a hundred target-irradiation shots were performed, 69 on DT-filled glass microspheres. Compression and measurable neutron production were attained on several occasions. Hundreds of additional shots have been fired for calibration purposes or electrical-noise reduction.

The TBS has been quite reliable since mid-January 1977 when a triggering malfunction was diagnosed and repaired.

The maximum energy that can be delivered to a spherical target remains at ~ 250 J per beam due to system oscillation problems. Measurements of output pulse risetime range from 150 to 300 ps depending upon the DBM gain and the risetime of the input pulse. Peak power at 250 J per beam was

0.3 ± 0.1 TW, based upon the measured pulse shape.

The alignment problem was resolved by choosing the Hartmann alignment system over the He:Ne laser alignment scheme. Hartmann alignment can be carried out in less than 10 min per target, which is compatible with the present 20- to 30-min interval between shots.

We have developed and installed a diagnostic instrument for detecting target damage due to pre-lasing. The instrument has proved to be valuable in detecting DBM and system oscillations, which may occur from 5 to 150 ns before the main pulse.

On-line pulse-shape measurements have been implemented on one beam, utilizing a 70-ps risetime pyroelectric detector and a 5-GHz oscilloscope.

The oscillator was replaced with a low-inductance device, which produces multiline output when operated with a 1:1::CO₂:N₂ mix. Evaluation of this system showed that at gains compatible with successful target shots, only the P(18) and P(20) transitions are present and that the intensity of P(18) is only 10 to 20% that of P(20). At higher gains, P(18) typically is roughly 30 to 50% of P(20), and all other transitions are less than 10% of P(20). The multiline content at higher DBM gains shows promise of improved peak power performances when the DBM oscillation issue is resolved.

We are considering a more comprehensive revision of the TBS, which will include (1) a saturable absorber (either gaseous or p-doped germanium) in the DBM to increase gain and energy input, (2) a new oscillator switch-out unit, which will provide 1-ns multiline output without the need for modelocking, and (3) a revised preamplifier arrangement with improved contrast.

EIGHT-BEAM SYSTEM

Introduction (S. Singer)

The EBS represents the next generation of high-power short-pulse CO₂ laser systems we will use to study the interaction of intense light beams with matter, with emphasis on investigating problems relating to laser fusion. This system is designed to deliver 10 to 20 TW to a target—10 kJ in a 1-ns pulse or 5 kJ in a 0.25-ns pulse. The EBS will consist of an oscillator-preamplifier system which generates a

0.25-ns multiline optical pulse at the several-hundred-megawatt level, and which will drive four DBMs clustered around a target chamber. Each of the eight 35-cm-diam beams will deliver ~650 to 1250 J (depending on pulse length) to the target chamber, which will contain an optical system to focus these beams onto a target.

The front end of this system is operational and is being used to support multiline energy-extraction and pulse-shape measurements on one side of the first DBM. Construction of the other DBMs is on schedule.

Front End (R. L. Carlson, D. Casperson, J. S. Ladish, M. D. Montgomery)

General. The front end has been predominantly used to support the triple-pass amplifier (TPA) energy-extraction measurements. These measurements employed the large 40.5- by 35.5-cm (16- by 14-in.) slab of polycrystalline p-doped germanium in front of the 40.5-cm-diam collimating mirror of the TPA. The front end was used additionally to study the saturation characteristics and damage levels of test pieces of polycrystalline germanium from the large slab. Multiline saturation of SF₆ was also investigated.

The front end has been reconfigured to improve the mechanical stability, to reduce the number of optical elements, to improve the reliability, as well as to meet drive energy, pulse width, multiline content, and contrast-ratio requirements.

A double Pockels-cell switchout has been installed and characterized along with measurements of the prepulse energy content of the gain-switched TEA oscillator. A triple Pockels cell is being installed and tested. A method of enclosing the switch-out system containing crystals, mirrors, and polarizer stacks in a clean, permanently aligned environment is being developed. The first of four Lumonics driver preamplifiers has been installed and evaluated. Controls are continually being upgraded, and significant operating parameters of the subsystem components are being fed to the main computer system in the control room.

Developments. Figure I-1 is the schematic of a base-line, front-end design to meet the requirements of driving the TPA to saturation with correct pulse

width, multiline content, and contrast ratio. The energies indicated after Preamplifier 1 are the results of computer modeling although many of these energies are also in excellent agreement with measured values. The average prepulse energy of the gain-switched TEA oscillator has been measured to be 1/10th the total pulse energy of 500 mJ. Each switch-out section has an average energy extinction ratio of 500:1, giving a total of 1.25×10^6 ; saturated absorbers (SATABS) 1, 2, 3 are hence operated at their indicated small-signal loss for prepulse energy.

The total small-signal gain of the front end is $\exp [3(4.7) - 2.4 - 5 - 6] \approx 2$. Much higher gains have been shown to be stable in tandem operation with the TPA. The prepulse energy of the front end is thus calculated to be $\sim 8 \times 10^{-7}$ mJ. For a contrast ratio of 4.7×10^6 , a fourth switch-out crystal and/or an increase in saturable absorber loss might additionally be employed. Note that no saturable absorber has been placed after Preamplifiers 3, 4, 5, and 6, as previously anticipated. This omission will permit us to inject a 50-W cw probe laser at the first beam splitter for initial EBS alignment.

TEA Oscillator and Plasma Tube. The TEA oscillator was operated at 45 kV with a 1:1:1::He:N₂:CO₂ mix producing a 500-mJ, 100-ns FWHM output pulse. The energy in the 40-ns interval to peak intensity was 50 mJ, implying that prepulse energy prior to the 1-ns pulse switchout is 1/10th the total feedthrough energy. The oscillator has also been operated at 50 kV with a 1:1:1::He:N₂:CO₂ mix producing less energy in a higher peak power pulse.

Recent measurements indicate that the CdTe switchout crystal coatings are apparently damaged by total energy density (≈ 20 MW/cm²) of the gain-switched pulse. Hence, an oscillator with a higher peak power but lower total energy could be attenuated to produce a beam of the same intensity on the coating surface with substantially lower energy density.

Switchout System. A double Pockels-cell switchout has been installed, characterized, and operated without failure for several hundred shots. The extinction ratio between a pair of crossed polarizers ranged from 500 to 1000 for the first crystal and from 250 to 500 for the second. The lower extinction ratio

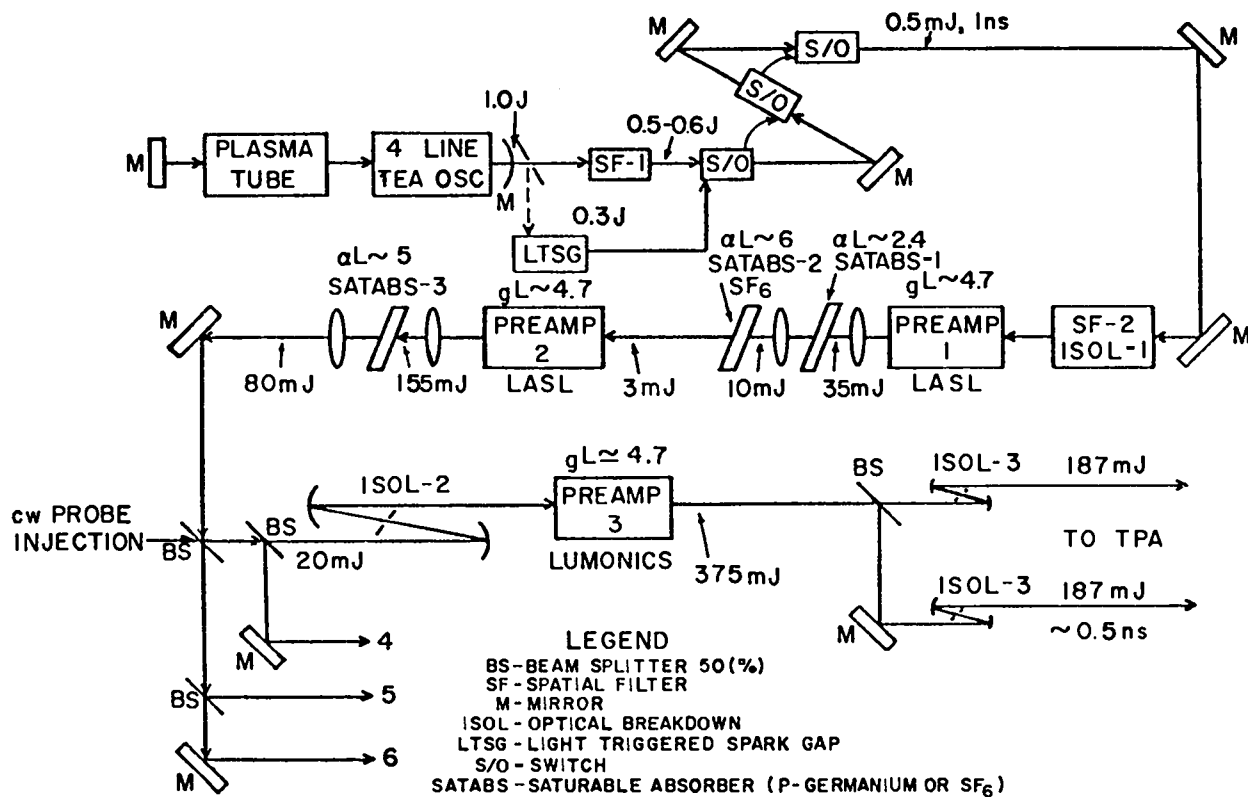


Fig. I-1.
 Schematic of EBS 1-ns front end.

of the second crystal was probably due to random polarization introduced by the birefringency of the first crystal. The energy contrast ratio varied from 250 to 400. Voltage transfer between crystals was ~90%. As a result, the second crystal switches to less than half-wave voltage and the optical pulse energy is consequently reduced. The peak intensity was reduced by 10 to 15% at the exit of the second crystal. Pulses as short as 500 ps were produced, and the charge line of the laser-triggered spark gap was adjusted to produce the desired 1-ns FWHM pulse after the second crystal.

Saturable Absorbers 1 and 2 (SATABS 1 and 2). SATABS 1 is now a compensated Brewster pair of p-doped germanium having an absorption coefficient (αL) of 2.4. The intensity of the beam impinging on the germanium is ~60 MW/cm², which is easily an order of magnitude below the damage threshold.

Preamplifiers 1 and 2 are operated in tandem with SATABS 1 between them without any problems of

self-oscillation. A new net gain of $\exp [2(4.7) - 2.4]$ or $\exp [7]$ has been shown to be stable in the current experimental arrangement.

SATABS 2 is an SF₆ cell which has been positioned in the system such that the long-pulse (~100-ns) feedthrough is subjected to nearly the small-signal loss of $\alpha L \approx 8$. Measurements using the multiline front end indicate that the energy density of the feedthrough must be kept below 0.1 mJ/cm² to take advantage of small-signal loss attainable with a given amount of SF₆. In fact, a background energy density equal to or less than 0.01 mJ/cm² is desirable. The 400-ps double switchout should satisfy this requirement.

Experiments were conducted to measure the multiline transmission of p-doped germanium and SF₆, while simultaneously recording the input and output spectra for each 1-ns pulse. The results of these measurements were recently reported at the 1977 CLEA Conference. In summary, the transmission of these saturable absorbers was dependent upon only

the total energy of all the p-branch transitions (14, 16, 18, 22) and not upon the individual line strengths.

Preamplifiers 3, 4, 5, and 6. The first of the four driver-amplifiers from Lumonics has been installed and tested. Using a gas mix of 63.5:10.8:25.7::He:N₂:CO₂, we measured a small-signal P-20 gain of 4.3%/cm. The device has been fired several hundred times without failure.

DBM Acceptance Testing (R. F. Haglund, Jr., M. D. Montgomery, J. S. Ladish)

The small-signal gain (SSG) on Modules 2A, 2B, 3A, and 3B of the EBS has been measured to determine whether these amplifiers had acceptable gains; the modules were roughly comparable in gain homogeneity and self-lase threshold. The SSG was measured for two beam paths in each module: near the anode and near the cathode.

For Modules 2A, 2B, and 3B at self-lase threshold, the anode path showed an average SSG of 6.0 and the cathode path an average of ~4.8. In Module 3A, the high gain (anode) and the low gain (cathode) averaged 6.8 and 3.9, respectively. This anomalous gain inhomogeneity may arise from electron-range effects, an assumption that will be investigated in further tests.

The average stable gain for the tested modules was ~2.5 to 3.0%/cm, and the pumping-voltage threshold for all modules tested ranged from 4 x 40 to 4 x 42 kV. The low self-lase threshold is most probably due to a two-pass oscillation between the recollimating mirror and the throat or end plate of the module.

Pinhole Isolator Evaluation

A major concern in the triple-pass amplifier (TPA) is how to dissipate the energy in the amplified target reflection pulse (retropulse). The present scheme places a pinhole at the focal point of the triple-pass optical train and anticipates only a small transmission of the retropulse through the breakdown plasma and pinhole. To avoid breakdown at the pinhole with the incident pulse, the gas pressure inside this section is reduced to an

experimentally determined value of ~10 torr. Figure I-2 shows the optical path of the TPA and the experimental setup. The pinhole was placed after the first beam passed through the TPA. In normal operation, the reflecting side of the pinhole faces toward the target. However, for our measurements we used pulses from the front end, and the reflecting surface was turned to this direction. A 100-ns gain-switched pulse of ~1.0 J was used for the measurements. The energy incident on the pinhole was determined by placing a small calorimeter in the TPA arm and comparing its energy reading with that from a NaCl beamsplitter in the front-end room.

In all, 60 shots were made at various pressures, with and without the pinhole in place. The results are shown in Fig. I-3. The following conclusions are drawn: (1) the interesting region of pressure is ~10 torr for a 0.5-mm pinhole, (2) the marked difference in structure between Curves A and B is due to diffraction by the plasma formed in front of the pinhole, (3) investigations should continue with larger pinholes, and (4) the curve-C vacuum value of ~32% implies rather severe filtering of the beam (that is, relatively poor beam quality) and/or some misalignment through the pinhole.

P-Doped Germanium Measurements

The measured saturation characteristics of polycrystalline and single-crystal p-doped germanium have been compared for the first time. Two polycrystalline samples from the large TPA germanium slab were subjected to the multiline, 1-ns, Gaussian front-end pulse after Preamplifier 1. The transmission through the samples was measured as a function of incident intensity, ranging from 20 to 225 MW/cm². The ar coatings sustained no damage

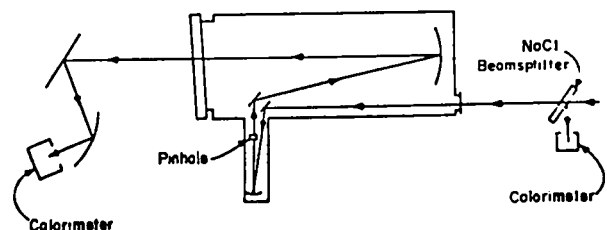


Fig. I-2.
Optical path in TPA.

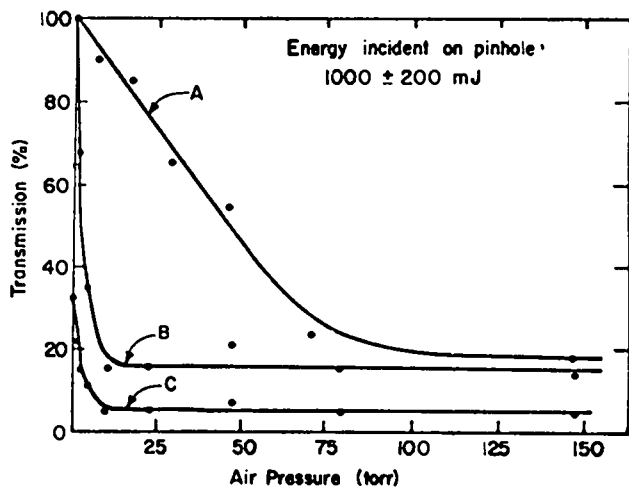


Fig. I-3.

Pinhole isolator evaluation. A, transmission as a function of air pressure in the TPA arm normalized to vacuum, no pinhole; B, same as A, except with 0.5-mm pinhole in place; C, same as B, except absolute transmission related to case of 0 torr, no pinhole.

in 20 shots at the high intensity. These measurements were compared to the transmission of the single-crystal Brewster pair of SATABS 1, which has a similar small-signal loss. A computer model was also run for comparison purposes. The results are summarized in Table I-I.

The data indicate that the saturation characteristics of polycrystalline p-doped germanium are similar to those of single crystals at low incident intensities.

One-Beam Experiment—Energy Extraction with Large Germanium Slab (M. D. Montgomery, R. L. Carlson, D. Casperson, R. Haglund, J. S. Ladish)

The first energy-extraction measurements were made in which a large p-doped germanium slab was used to inhibit parasitic oscillations in the triple-pass amplifier (TPA). The highest amount of energy (~900 J) so far extracted from an EBS power amplifier was obtained due to the increased isolation provided by the germanium slab.

The measurements are put into perspective in Fig. I-4. Only two shots were made because of sur-

face damage suffered by the slab on the first try (Data Point 2).

The output energy was measured by collecting the entire beam in a large thermocouple calorimeter, and applying various corrections to arrive at the true value. The following corrections have been made to the originally indicated energy of 870 J at the calorimeter:

- Subtraction of feedthrough (long-pulse) component (150 to 200 J) yields 670 to 720 J;
- Correction for 10% calorimeter nonlinearity at 700 J gives ~770 J;
- Finally, correction for 8% NaCl reflection and 5% calorimeter shadowing yields ~850 J inside the output salt which we compare with the calculations.

As can be seen, agreement with predictions is good. We briefly summarize our results as follows:

- The saturation of p-doped germanium can be described by an inhomogeneously broadened model with a saturation intensity of 3.5 MW/cm².
- The energy thereby extracted was in good agreement with model predictions.
- Peak intensities incident on the germanium were near or above the known damage threshold of germanium.

TPA Stability Studies (M. D. Montgomery)

Evaluation of ABS Plastic Shield and Mylar Linear Absorber in the TPA. As part of our efforts to prevent TPA self-lasing, we installed an ABS plastic shield in Module 1B because we expected that the plastic would reduce the feedback due to the diffuse reflectivity of its Nextel paint. Preliminary measurements indicate some modest improvement.

Comparison of TPA Multiline and Single-Line Pulse Shapes (J. S. Ladish). Temporal pulse-shape measurements were performed on the output pulse of Module 1A, which is used for the single-beam experiments in the EBS.

In all, ~30 shots were made; ten in the control portion of the output beam and 20 in the midplane on the anode side of the output pulse, because the highest gain in the TPA exists near the anode.

Deconvolution of the data has not yet been completed, but some noteworthy facts have emerged as summarized in Table I-II.

TABLE I-I

SATURATION CHARACTERISTICS OF P-DOPED GERMANIUM

Pulse Intensity (MW/cm ²)	Transmission (%)	
	Measured	Computed
•Single Crystal, $\alpha L = 2.3$ to 2.4		
40	43	---
18	21	---
13	19	---
6	19	---
4	11	---
small signal	9.5	---
•Polycrystalline Sample, $\alpha L = 1.65$		
200	47	---
93	47	---
63	45	---
29	42	---
20	28	---
small signal	19	---
•Polycrystalline Sample, $\alpha L = 2.78$		
225	28	43
72	33	28
34	20	18
23	14	15
small signal	6	6

In summary, a comparison of pulse-shape measurements clearly demonstrates that the multiline pulses are temporally shorter than the single-line pulses.

Controls and High-Voltage Technology (E. L. Jolly)

DBM Electron Guns. A modified foil window installed and tested on Module 4B performed in vacuum comparably to the standard window. However, the modified window will be further improved to eliminate the present blockage of 18% of the electrons by redesign of the grillwork.

DBM Tests. DBMs 2, 3, and 4 have been tested successfully at 90% of design voltage. Tests for small-signal gain and threshold of oscillation have been completed on Modules 2 and 3.

Control Program. A program code to operate the DBMs has been written and tested. This program, which analyzes small-signal gain measurements, has been used to operate all DBMs simultaneously.

Other programs are being written for the laser gas system.

Control systems have also been written for the following:

- Target chamber vacuum systems,
- Target insertion device,

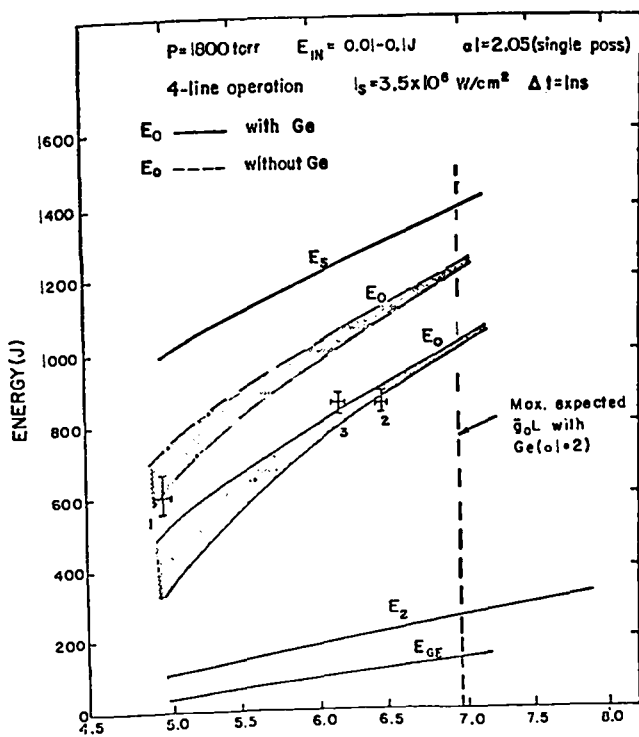


Fig. I-4.

TPA performance with large saturable absorber.

- Controls—front end (redesigned due to amplifier changes),
- Spatial-filter pressure monitoring,
- Amplifier gas cooling, and
- Delta mirror mounts.

The controls for facility monitoring have been designed, purchased, and partially installed. The control cables and electronic hardware for the triple-pass mirror mount have been installed.

Controls for the laser gas system have been designed, installed, and tested. All hardware for the system has been installed.

Target Chamber Elevator (R. D. Day)

Installation of the hydraulic elevator that will raise people and equipment into the target chamber is nearly complete. A hole 66 cm (18 in.) in diameter by 550 cm (18 ft) deep has been bored beneath the target chamber to accommodate the hydraulic cylinder. A trench 66 cm deep by 66 cm wide was

dug to contain the hydraulic line and electrical control lines for the elevator. The trench will also accommodate liquid-helium and nitrogen lines, electrical service lines, and vacuum lines. The hydraulic cylinder and the pump are on site. Installation and acceptance testing should be complete by mid-July 1977.

Insertion Mechanism for Cryogenic Targets (R. D. Day)

A target-positioning system for the EBS will (1) move a target through an airlock into the proper locations; (2) cool the targets to 4 K; (3) maintain an absolute target-positioning accuracy of $\pm 5 \mu\text{m}$ (0.0002 in.) in the x, y, and z directions for a cold target; (4) contain an optically finished alignment sphere which will serve as the alignment reference for the laser beams and prevent target heating by ambient thermal radiation; (5) maintain the relative positional accuracy of the alignment sphere and target centers to within $5 \mu\text{m}$ (0.0002 in.) in the x, y, and z directions for a cold target; (6) move the reference sphere out of the beam paths before each shot in 0.001 s. Figure I-5 shows the disassembled and assembled views of a conceptual design in the region of the target.

Insertion Mechanism for Room-Temperature Targets (R. D. Day)

Due to the expediency of having a target-insertion mechanism ready for installation in the target chamber by September 1977, we delayed the design of a cryogenic-target insertion mechanism and concentrated on a device that would operate exclusively at room temperature.

A track-and-cart arrangement for carrying the target through the airlock to the final target position has been designed and is shown in Fig. I-6. A model has been fabricated and is being tested. Two ways of locating the targets in the chamber were evaluated: the hard stop and the kinematic-mount method. The latter was selected because it places the target well within the $\pm 2.5\text{-}\mu\text{m}$ ($\pm 0.0001\text{-in.}$) tolerance and does not depend upon a precision cart, but only upon a stationary receptacle for target placement.

TABLE I-II

COMPARISON OF MULTILINE AND SINGLE-LINE PULSE WIDTHS

	Multiline τ_p FWHM (ns)	Single Line τ_p FWHM (ns)
Central position	1.53 ± 0.15	1.77 ± 0.06
Anode position	1.39 ± 0.11	1.61 ± 0.15

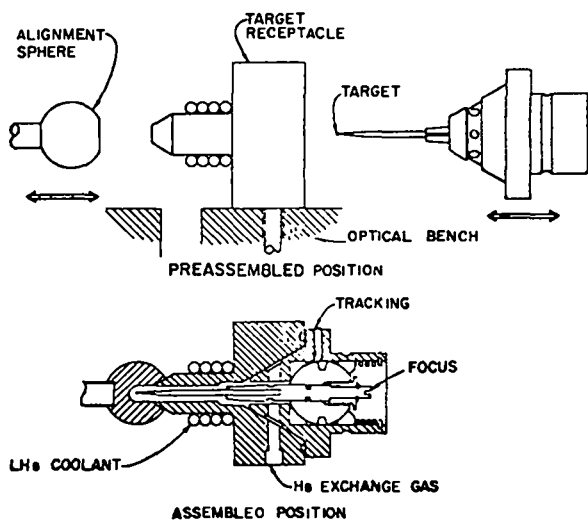


Fig. I-5.

Cryogenic target insertion mechanism for EBS.

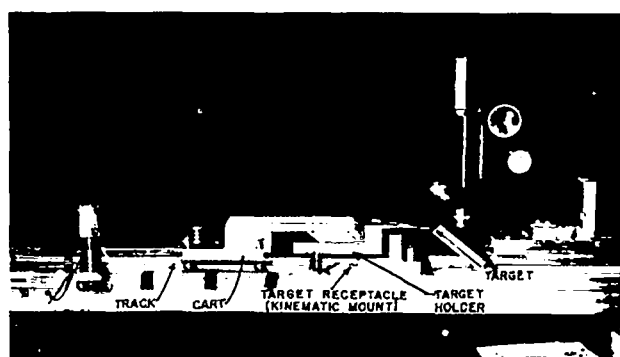


Fig. I-6.

Room-temperature target insertion mechanism.

Analysis of Target-Chamber Turning Mirrors (R. D. Day)

A stress analysis was performed on the EBS target-chamber turning mirrors to determine the deflections in the mirrors when mounted and loaded by their own weight. A finite-element stress-analysis code was used. Mirror orientation with respect to the horizontal and vertical planes is shown in Fig. I-7, which also defines the x, y, and z directions.

Results indicate that the six-point mount will cause the lowest deflections of the schemes analyzed.

EBS Assembly (E. L. Zimmermann, D. Ingwerson)

DBMs 1, 2, and 3 have been assembled completely, including the triple-pass optics. Chamber 2A has been fitted with a gas cell and salt-flat holder between the large end mirror and the pumping-chamber flange to check out the viability of using gaseous absorbers in suppressing self-oscillations.

Module 4 is in its final stages of assembly. Chamber 4A has been fitted with the new high-voltage oil pots and terminations. A high-voltage failure in a chamber feedthrough caused a testing delay, but

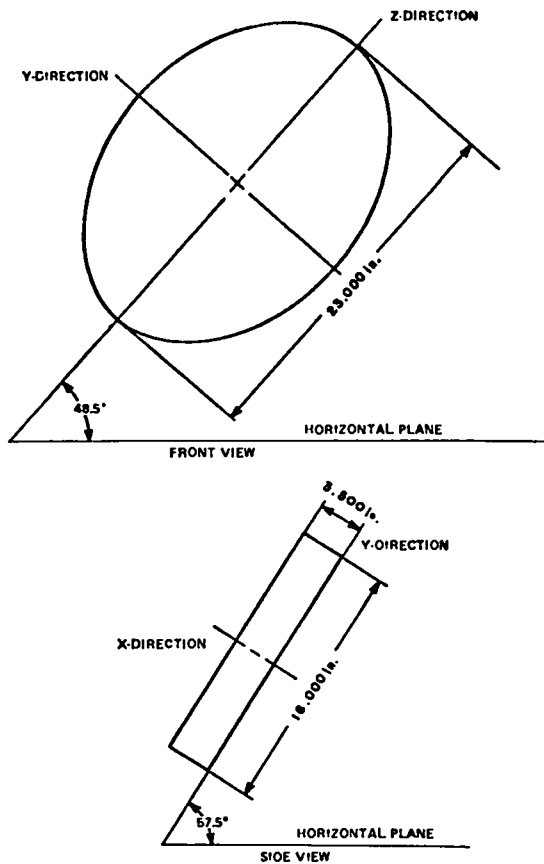


Fig. 1-7.

EBS target chamber turning-mirror orientation.

further firings seemed to substantiate the viability of the new high-voltage retrofit. We intend to change all other oil-chamber configurations to this design.

Considerable labor has been spent repairing high-voltage failures in the feedthrough region of the epoxy-fiber glass pumping chamber. About eight damaging arcs have occurred, mostly due to entrapment of air pockets in the high-stress feedthrough regions. Repairs, consisting of stripping away fiber glass layers and of filling voids, have been fairly successful. At present, only Chamber 4A has been tested at maximum operating voltage.

Because of various leaks and voltage failures in modules, the date for complete assembly of the EBS has been delayed to about July 15, 1977.

OPTICAL SYSTEMS (I. Liberman)

SBS

Two target-alignment techniques have been compared: the Hartmann-mask spherical retroreflector and the ir microscope methods. Both are deficient, mainly because the alignment beam has a Gaussian profile, whereas the actual beam has a uniform distribution. Thus, the microscope method emphasizes the central portion of the aperture, which receives a relatively small fraction of the total beam energy. If beam aberrations are negligible, this poses no problem, but with aberrations of typical optical systems, the region for alignment lies along an annulus at $\sim 70\%$ from the center of the aperture. The Hartmann-mask holes are located at 0.7 of the aperture. However, due to the 4:1 energy density gradient across the 5-cm- (2-in.-) diam hole with the alignment beam, the asymmetry of the return diffraction pattern leads to an apparent focal shift. By placing a simple apodizer onto the camera tube face, asymmetry of the alignment beam can be corrected. When this is done the agreement between the microscope alignment and the Hartmann alignment is better than the resolution of either technique, each of which, in turn, is limited by the Rayleigh criterion. The effect of tilting and defocusing the paraboloids on focal range was analyzed with ray tracings and spot diagrams. Qualitatively, good agreement was observed with the ir microscope.

TBS

A unit magnification system consisting of off-the-shelf germanium singlets for checking the resolution of pyroelectric vidicons was found to be inadequate. The 9.2 X microscope germanium objective was optimized for diffraction-limited performance by using measured radii and thicknesses of the actual manufactured lenses.

EBS

Beam Alignment. A base-line path for the automatic EBS alignment system from the oscillator to the target chamber has been defined and

will be applied to one leg of the EBS by the end of September 1977.

The path is shown schematically in Fig. I-8. Motor-driven mirrors that will steer the beams are labeled M_n , where n indicates the sequential position of the mirror in the beam path; M'_n designates a mirror with a function identical to that of M_n , but which can only be moved after M_n movement has been completed; detector positions are indicated by D_n , where n again specifies the position of the detector in the beam path and corresponds to the subscript of the mirror used in conjunction with that particular detector.

Silicon wafer thermopower detectors will be used as large-area detectors to position the beams on mirrors at Points D_1 , D_3 , and D_6 . These detectors will swing out of the beam path after alignment, although we still consider the possibility of keeping them permanently mounted in the beam path.

Two thermal pinhole detectors (developed by EG&G) and a thick-film thermocouple quadrant detector will check spatial filter alignment. Thermal pinholes will be mounted permanently at Points D_4 and D_6 , whereas, due to lack of energy, a thick-film thermocouple quadrant detector will be used at position D_2 . This detector will swing out of the pathway after its alignment function is completed.

Appropriate electronic components are being manufactured in-house for the large-area detectors. Digital data readout from each detector will be displayed for manual alignment, and appropriate signals will be produced for interfacing with the electronics that will drive the mirror motors. Thus, the system will be compatible with both manual and automatic beam alignment.

Target Alignment. The severity of the target-alignment problem depends on the types of saturable absorbers used to suppress laser oscillations. On the assumption that sufficient energy for a Hartmann test-vidicon detector alignment scheme will be available, we have designed and ordered the vidicon system we need. Sufficient energy can be obtained by either (a) removing the saturable absorber during alignment (with possible beam-steering problems), (b) firing the final amplifier during alignment (reducing the time between failure of the amplifiers), or (c) frequency-doubling the alignment signal to $5 \mu\text{m}$, at which value the saturable absor-

ber is relatively transparent (efficiency of conversion and beam-steering problems need to be studied). Alternative systems that require less energy and are more adaptable to automatic alignment are being studied.

Optical Diagnostics. We wish to measure the beam quality and focal energy distribution of the full beam. To do this, we must attenuate the beam by a factor of $\sim 10^6$. Calculations show that this can be achieved with a hole grating without introducing further aberrations in the zero order. The effects of aberrations in using a hole grating in converging geometry are being computed.

Optical quality will be measured with a Smartt interferometer. The optical parameters for the Smartt interferometer plate, for example, optical quality of the plate, hole size, transmission, thickness, and index-of-refraction variations, have been determined and a silicon wafer plate is being studied in detail. A high-quality pyroelectric vidicon and a digital frame grabber capable of a dynamic range of 250 have been ordered and will be used to record the interference pattern and, in conjunction with an ir microscope, to measure the focal energy distribution.

Code Development. A fairly successful scheme for using FRINGE in reducing interferograms to optical-path-difference maps has been evolved, and attempts to make the scheme efficient are continuing. LOTS is being modified for end-to-end modeling of the EBS, accepting the output from FRINGE for manufactured components and handling, for example, near-field and far-field diffraction effects, saturable absorbers, saturating gain, and tolerances. The code should be easily usable by the end of the summer in its final form.

Miscellaneous. Ray-trace analysis shows that the 3.0-m (120-in.) EG&G spherical $f/1$ mirror used as a collimator produces a rms wave-front error of $\lambda/100$ at most and hence is usable as a collimator to test large optics up to a diameter of 40 cm (16 in.). We intend to use this mirror to test the target-chamber paraboloids for encircled-energy distribution at $10.6 \mu\text{m}$ and to test various target-alignment schemes.

Studies of longitudinal and transverse focal sensitivity at the focus of the final parabola have shown

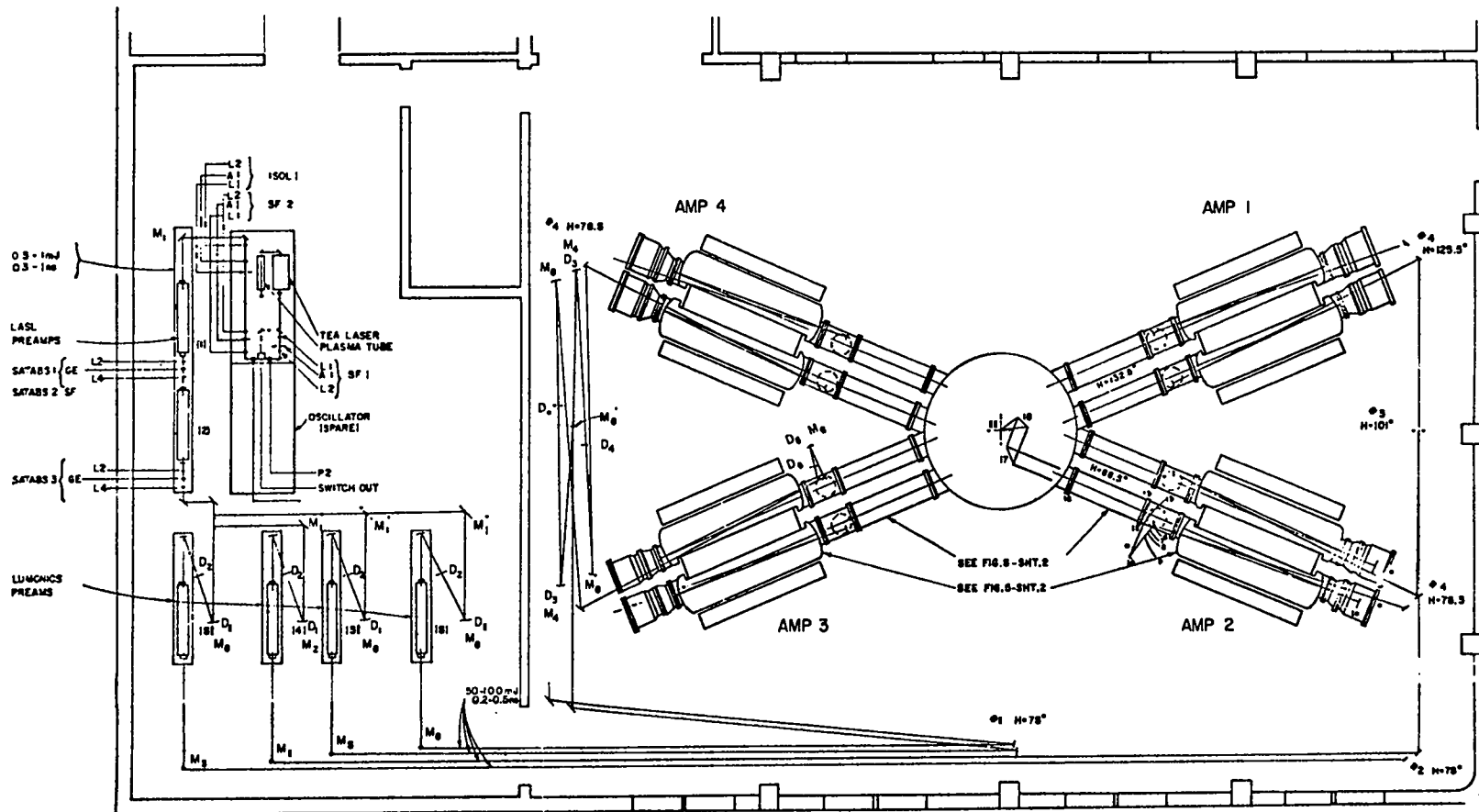


Fig. I-8.

Schematic of EBS beam path and mirror locations.

that in the transverse direction misalignment is far more sensitive than longitudinal misalignment to directing energy through an aperture (energy-in-the-bucket measurements).

The use of baffles in eliminating parasitic oscillations of the final amplifier may be an attractive alternative to saturable absorbers. Several schemes are being investigated in detail.

CO₂ LASER TECHNOLOGY

Introduction

Each of our CO₂ laser systems described earlier represents a significant advance in the state of the art of reliable CO₂ laser subsystems, components, and diagnostics. The design, construction, and improvement of the systems require, therefore, basic support of CO₂ technology. Some important areas are: the development of short-pulse multifrequency oscillators, amplifier optimization, development of subsystems for the prevention of system self-oscillation and removal of prepulse energy, improvement of the transverse profile of the amplified laser pulses, and measurements of optical damage thresholds in system components.

Front-End Development

General. A two-pass amplifier system, which may be considered for inclusion in the front end of our high-power CO₂ gas lasers, has been operated successfully at full power. These lasers also require front-end drive pulses of subnanosecond duration and high contrast, which led to advances in fast-pulse high-voltage technology, involving the development and testing of a wide-bandwidth, high-speed electro-optical switch capable of scalable prepulse extinction ratios.

In a manner analogous to the generation of ultrashort optical pulses via free-induction decay (FID), we succeeded in generating ultrashort CO₂ laser pulses in reflection from a Fabry-Perot interferometer and a new pulse-generation scheme is being investigated, which should remove one of the principal difficulties in large laser systems—the lack of reproducibility in pulse production.

Multipass Amplification Studies (S. J. Thomas, C. R. Phipps, D. E. Watkins, R. F. Harrison). Recent interest in using multiline pulses for large CO₂ amplifiers to improve energy extraction led us to study the multiline output of a recently developed high-power CO₂:N₂ oscillator. The oscillator consisted of a uv-preionized 90-cm-long transverse-discharge laser with an optical aperture of 1.5-cm diam. A 1:1::CO₂:N₂ mixture at 600 torr gave a gain risetime of 490 ns, with a risetime to peak pulse in the modelocked train of 30 ns. The highest single-mode energy was 750 mJ.

A new method was used to observe multiline output simultaneously for a single pulse: a Moletron eight-channel pyroelectric array was attached to an Optical Engineering Co. spectrometer so that the eight elements were aligned with eight rotational lines at the focal plane of the spectrometer. A 17%-reflection output mirror provided the highest energy, but the 50% reflection gave the best multiline output (see Fig. I-9). By using this oscillator as the input driver, a two-pass amplifier was constructed capable of gigawatt output powers. The two-pass amplification scheme is shown in Fig. I-10. The amplifier contains a photopreionized TEA medium, and has a cross-sectional aperture of 3.5 cm and a gain length of 130 cm. The measured gain on discharge center in one pass was 225.

A modelocked pulse from the high-power oscillator was attenuated and passed through an electro-optic switch, yielding a single 1.6-ns, 10-mJ pulse. This pulse was introduced into the amplifier through a 3-mm-diam hole positioned below the perimeter of the output beam. The beam expanded from the hole through the gain medium to a collimating mirror with a focal length of 2.5 m. After a second saturated pass through the gain medium, the beam was ejected at 90° to the amplifier axis.

The output energy in multiline operation was 2.5 J; the average output spectrum is shown in Fig. I-11. In single-line amplification, the output energy was 2.9 J. Standard deviation of laser output energy was less than 15% in single-line operation. This energy corresponds to ~70% extraction of the stored energy in the amplifier. Interstage isolation was unnecessary.

A measured input/output energy curve for the two-pass amplifier is shown in Fig. I-12. The input in this case was a 1.6-ns pulse tuned to the P(20) transition of the 10.6- μ m band.

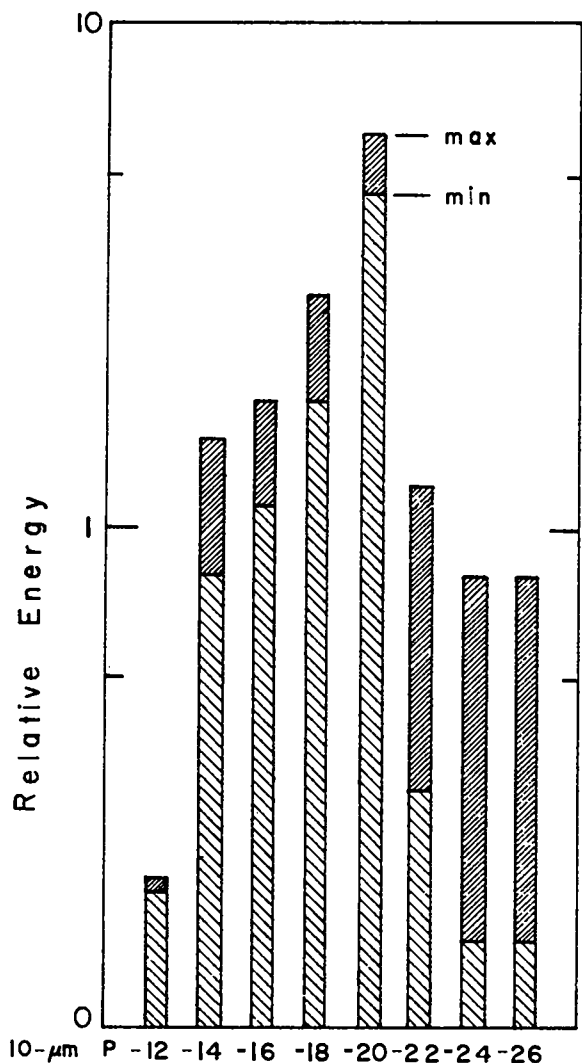


Fig. I-9.

Multiline output spectra obtained with high-power $\text{CO}_2\text{-N}_2$ oscillator.

Development of High-Speed Electro-Optical Switch (E. McClellan) The high-gain CO_2 oscillator/amplifier systems either operating or in design at LASL require front-end drive pulses of subnanosecond duration and high contrast (high main pulse intensity to background intensity ratio). These requirements have led to advances in the state of the art in high-speed Pockels cells and fast-pulse high-voltage technology.

A 50- Ω impedance-matched Pockels cell with a 15-mm aperture has been developed, which can be series-stacked to generate high-extinction-ratio, subnanosecond pulses from a CO_2 laser. To drive

three or more cells, each cell must be designed for maximum frequency response. The frequency response was measured by sending a 35-ps risetime voltage step through the cell and measuring the resulting degraded risetime. Figure I-13 shows that the pulse risetime (10 to 90%) is 270 ps, which corresponds to a transmission bandwidth for the cell of 1.3 GHz.

To drive this 15-mm-aperture Pockels cell, improvements in the current state of the art in high-voltage, short-pulse production were necessary. We have therefore modified a standard laser-triggered spark gap (LTSG) to operate with dc charge voltages of 50 kV and to produce pulse widths variable from 600 ps to tens of nanoseconds. Extensive tests have been conducted on the LTSG configured for producing 1-ns pulses. Figure I-14 shows a 1.2-ns high-voltage pulse with the LTSG configured for long-pulse operation.

By combining the high-speed Pockels cell and the fast LTSG we can produce an electro-optical switch system capable of subnanosecond performance: with the LTSG run in the low-speed mode, optical pulses of 10.6- μm radiation 1.25 ns wide are produced (Fig. I-15), whereas in the high-speed mode, optical pulse widths of 600 ps with risetimes (10 to 90%) of 220 ps are obtained (Fig. I-16). Because of the wide bandwidth of the Pockels cells and the nonlinear behavior of a Pockels cell's transmission function with voltage, several cells can be stacked in series to obtain high contrast ratios and shorter pulse widths. Figure I-17 shows the predicted performance of a 1.2-ns three-stage electro-optical switch based on the measured performance of a one-stage unit. Contrast ratios of 10^8 and pulse risetimes of 200 ps can be produced in this configuration. Full-scale tests of the three-stage system are in progress.

FID Pulse Generation with Fabry-Perot Interferometer (R. Fisher). With temporally smooth but abruptly terminated CO_2 laser input pulses, we have generated ultrashort pulses in reflection from a Fabry-Perot interferometer. This effect is analogous to the generation of ultrashort optical pulses via FID. FID was first demonstrated to be practical by Yablonovitch and Goldhar¹ who passed a temporally smooth abruptly terminated CO_2 laser pulse through a narrow-band absorbing cell of hot CO_2 .

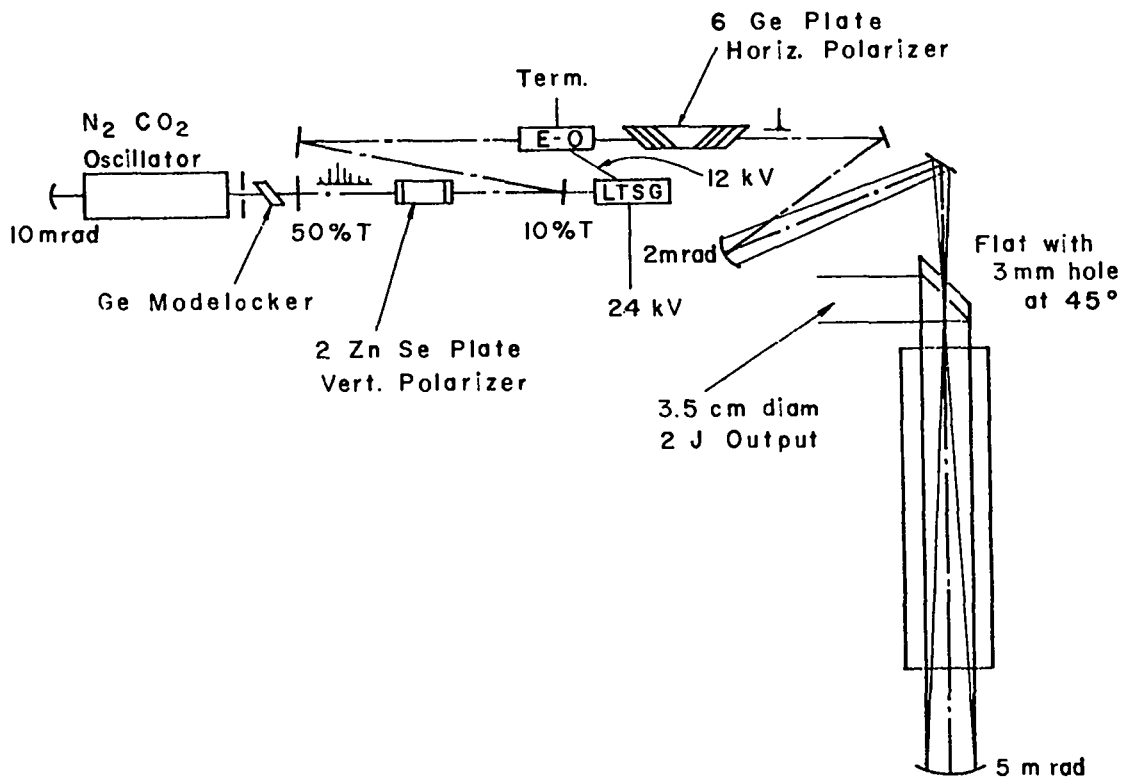


Fig. I-10.
 Experimental arrangement for two-pass amplification of single- and multiline signals.

The application of parallel-plate interferometers for temporal pulse reshaping has been discussed previously.² For suitably high reflectivity of each individual plate, the overall reflectivity of a Fabry-Perot interferometer is quite high except in the narrow wavelength region about each transmission resonance. Thus the device behaves in reflection similarly to a simple narrow-band absorber. The application to short-pulse generation follows from this property. The properly tuned interferometer transmits the temporally smooth long pulse while reflecting an ultrashort pulse at the time the input pulse is abruptly terminated. In the "spectral" interpretation, the narrow-band spectrum associated with the temporally smooth portion of the input pulse is within the transmission resonance of the instrument and is therefore transmitted. The broadband spectrum associated with the abrupt pulse termination lies outside the transmission resonance of the instrument and is therefore reflected.

For understanding this interferometer transient more precisely, the "temporal" interpretation (as

outlined in Fig. I-18) is especially appealing. Note that the initial reflection (often labeled "rEo" in optics texts) corresponds to the "passed" pulse in the case of the resonant absorber, whereas the set of slightly tardy partial waves (marked "canceling field" in Fig. I-18) corresponds to the reradiated out-of-phase pulse in the resonant absorber case. The fact that no light is reflected on resonance results from the destructive interference between the initial reflection and the canceling field. In this temporal description, one can readily envision the evolution of the reflected interferometer transient; as the transmission-resonant input pulse slowly rises, there is time for the canceling field to follow, but as the pulse is abruptly shut off, the initial reflection disappears first. At this time only the canceling field remains (with nothing left to cancel). Thus an instantaneous rise in reflected signal is generated. Every interferometer round-trip transit time t_0 , a corresponding transit of the canceling field is terminated and the backward reradiated pulse drops one abrupt step.

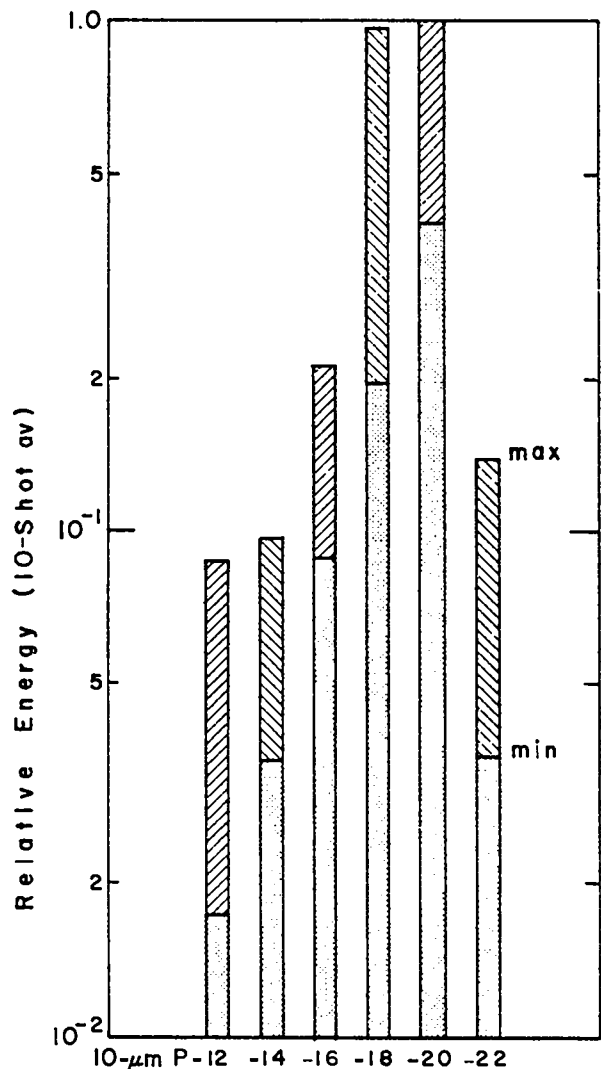


Fig. I-11.
Output spectra obtained after two-pass amplification of Fig. I-9 spectrum.

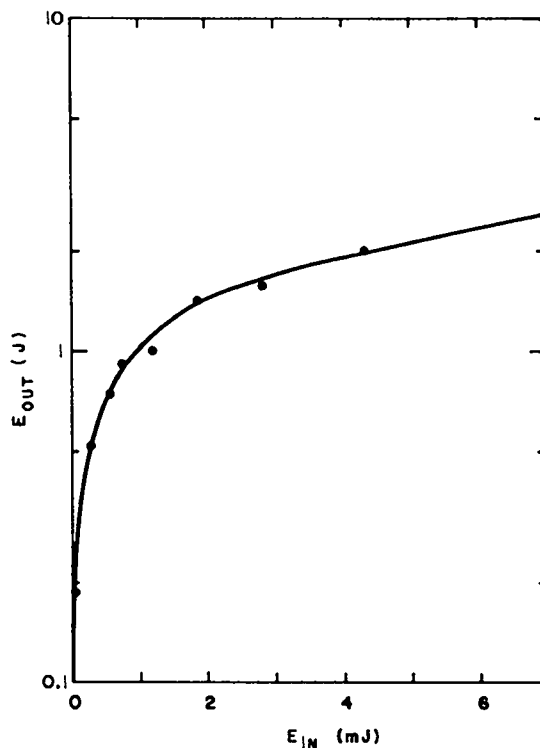


Fig. I-12.
Energy extraction obtained with single-line input.

In ultrashort pulse generation both by FID and by Fabry-Perot reflection the pulse duration is tunable. In the first case the tuning can be carried out by modifying either the absorption length or the pressure of the narrow-band absorber, and in the latter case by modifying either the reflectivity or the spacing of the Fabry-Perot. The ultrashort pulse duration in both cases is limited only by the duration of the breakdown termination. In the FID process the intensity of the ultrashort pulse is limited by the saturation properties of the narrow-band absorber, whereas with the interferometer the

intensity is limited only by the optical damage susceptibility of the Fabry-Perot mirrors. In contrast to multiline narrow-band absorbers, a simple Fabry-Perot cannot be used for multiline laser pulses.

Our experimental setup is shown in Fig. I-19. A 70-ns temporally smooth 10.6- μm P(20) pulse from a cw smoothing-tube stabilized hybrid⁸ CO₂ TEA laser oscillator was focused into an atmospheric-pressure flowing mix of N₂ and traces of air. The mix ratio was adjusted to obtain self-induced optical breakdown and termination at the peak of the pulse. The abruptly terminated pulse was then spatially filtered and carefully recollimated before reflection by a Burleigh Fabry-Perot interferometer set to 5-mm spacing. The Fabry-Perot ZnSe flats ($\lambda/30$ at 10.6 μm) had an 80% reflecting front surface and an antireflection-coated secondary wedged surface. The reflected signal was then delayed ~150 ns before being focused onto a Molectron P5-00 pyroelectric detector directly connected (no cable)

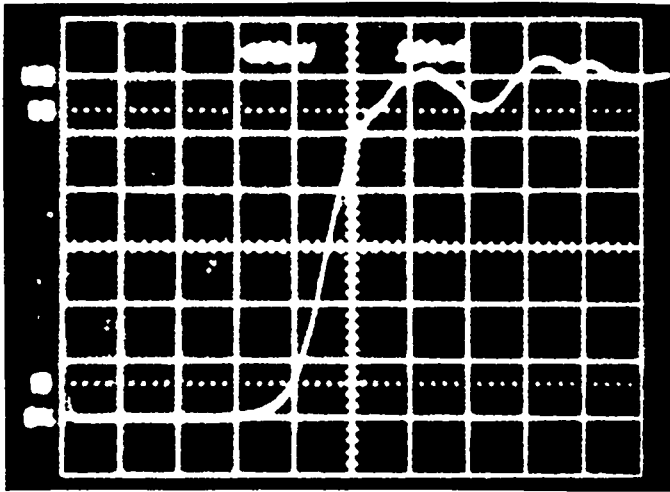


Fig. I-13.

TDR measurement of voltage reflection characteristics of 15-mm by 15-mm-aperture 50- Ω Pockels cell (500 ps/div).

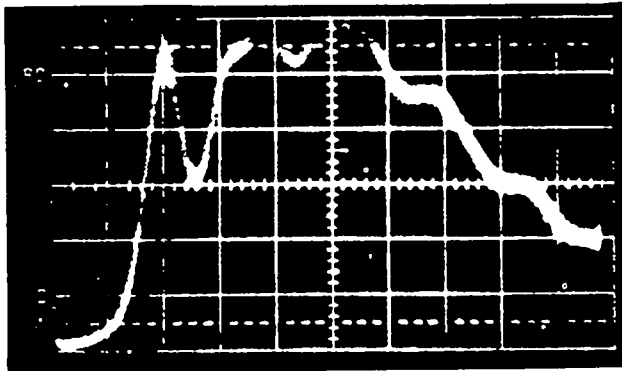


Fig. I-15.

CO₂ laser pulse chopped out by 15-mm-aperture Pockels cell with 1.2-ns LTSG voltage pulse (500 ps/div).

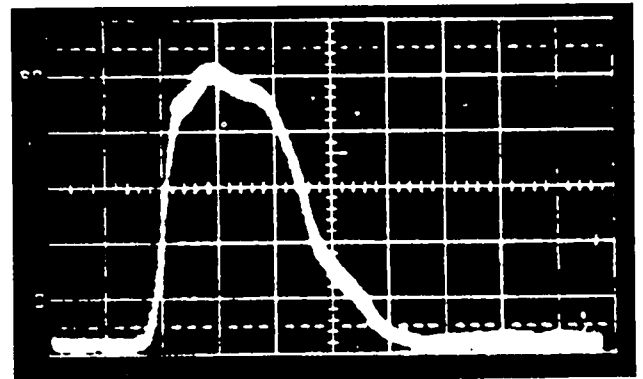


Fig. I-14.

High-voltage pulse from the LTSG configured for 1.2-ns pulses (200 ps/div horizontal; 4.1 kV/div vertical).

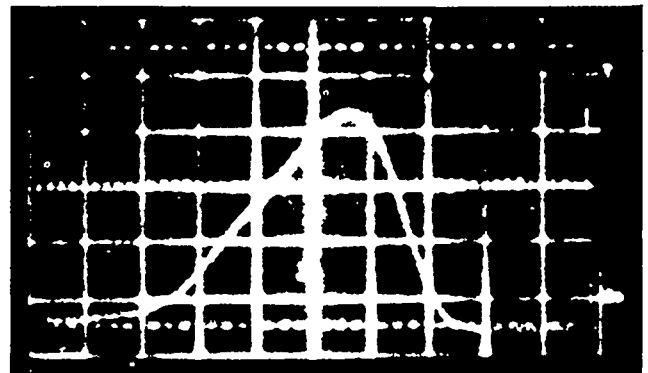


Fig. I-16.

CO₂ laser pulse chopped out by 15-mm-aperture Pockels cell with 600-ps LTSG voltage pulse (200 ps/div).

to the input channel of an improved 5-GHz single-sweep oscilloscope.⁴ An S-20 IT&T vacuum photodiode was exposed to the visible breakdown flash, providing a reliably synchronized pulse (risetime ~ 1 V/ns) for externally triggering the oscilloscope. As a check of the interference condition, a card was temporarily inserted *between* the plates of the interferometer. With the card in place, the reflectivity of the instrument to the cw beam increased tenfold.

Figure I-20 shows typical oscilloscope traces at 200 ps/division. In Fig. I-20a the card was inserted into the interferometer and an attenuator was put in the beam to compensate for the increased reflectivity. This trace shows the waveform of the abruptly terminated pulse. In Fig. I-20b the card and attenuator were both removed; the formation of the ultrashort pulse (limited by the response of the oscilloscope-detector combination) is clearly evident. The observed 120-ps FWHM trace is consistent with a 66-ps ($2t_0$) FWHM pulse convolved with

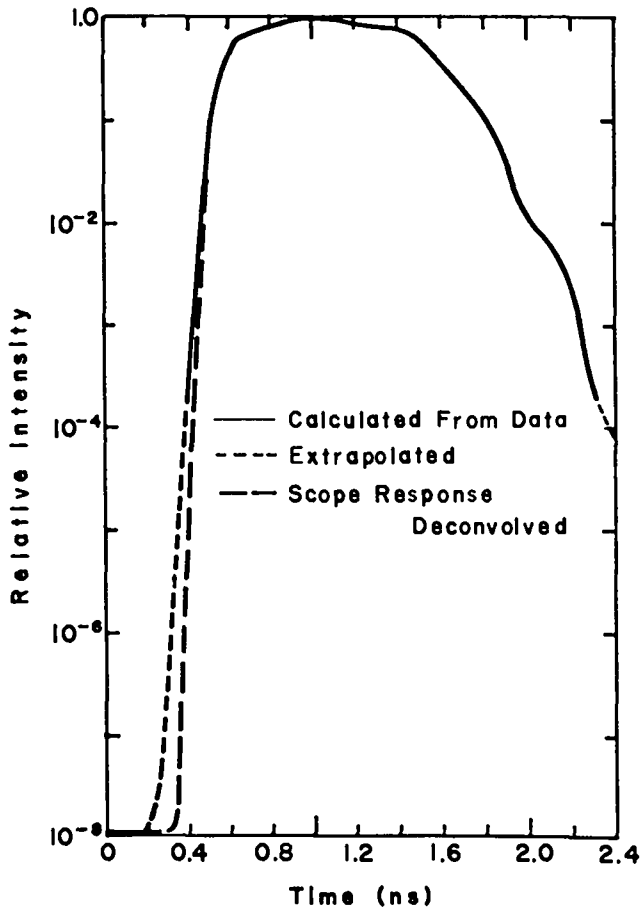


Fig. I-17.

Predicted pulse shape from a three-stage 15-mm by 15-mm-aperture electro-optical switch.

the combined oscilloscope detector point-spread function (FWHM) of ~100 ps.

Performance of the LDC Multiline-Multiband CO₂ Laser (B. Feldman). A modified operating version of the Laser Development Corp. (LDC) laser has been installed. The laser is a CO₂ oscillator designed to operate simultaneously (and independently) on several transitions in the 9- and 10- μ m bands. A schematic of the system is shown in Fig. I-21. The basic resonator structure contains two flat mirrors, three gratings, and a curved 80%-reflecting output mirror. The TEA medium is in the portion of the optical cavity for which all laser lines are spatially overlapped (called the "common arm").

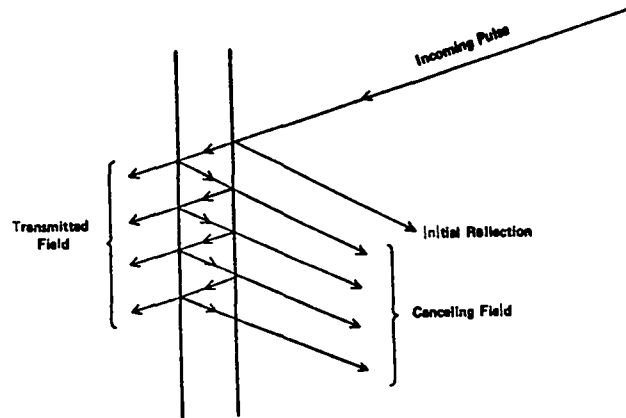


Fig. I-18.

Schematic temporal description of ultrashort pulse generation in reflection from a Fabry-Perot interferometer adjusted for maximum transmission.

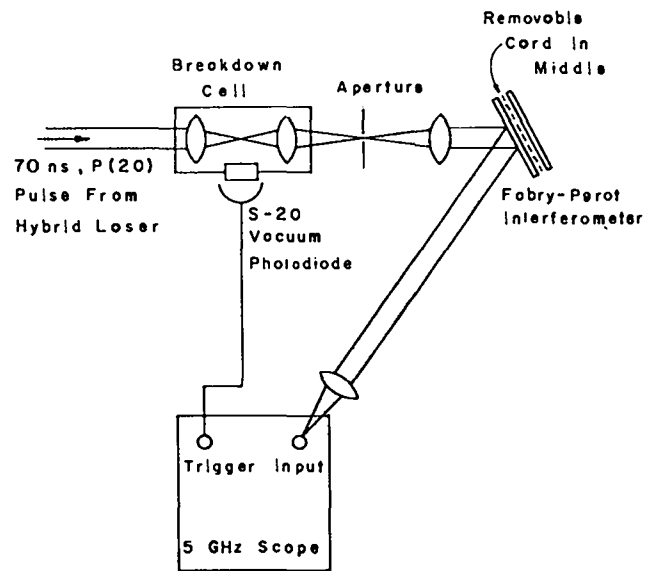


Fig. I-19.

Experimental setup. Initial alignment and analysis of the input pulse are both performed with a card between the plates of the interferometer. In observing ultrashort pulses, the card and the filter are removed. The detector is directly mounted on the oscilloscope. The interferometer incidence angle is exaggerated.

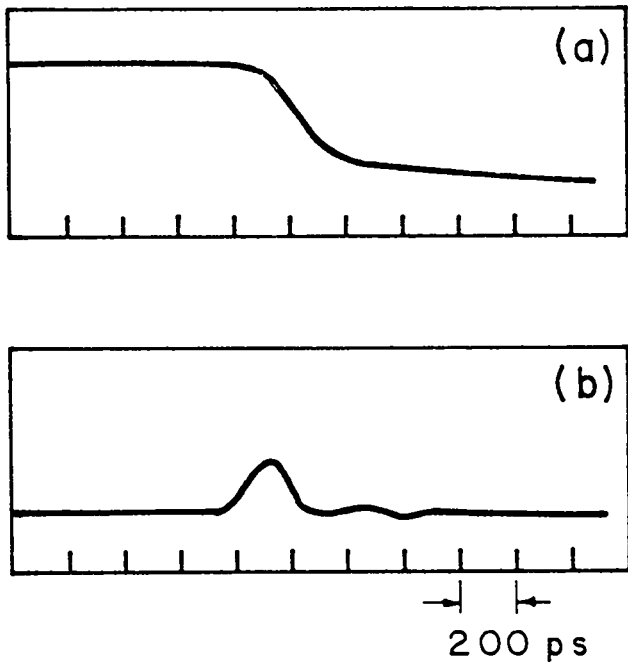


Fig. I-20.

Experimental results: (a) The abruptly terminated pulse as seen on the oscilloscope; the card is in the interferometer. (b) Ultrashort pulse generation with the card removed from the interferometer.

The bending grating deflects the different lines in slightly different directions, and the recollimating gratings bend the beams a second time so that they are all parallel to the beam line in the common arm. In this system the $9\text{-}\mu\text{m}$ light strikes one recollimating grating and the $10\text{-}\mu\text{m}$ light strikes the other. The different lines travel different paths in the "dispersed arms." Each dispersed arm contains a rectangular aperture for low-pressure discharge, and stops can be placed in various regions of the dispersed arms to eliminate all but particularly selected lines.

With the exception of the dispersed geometry of the LDC laser system, the operation is similar to that of pulsed smoothing-tube controlled oscillators used at LASL. The low-pressure gain cells are fired a few microseconds prior to the firing of the main TEA discharge and temporally smooth pulses are emitted. Low-intensity radiation builds up because of the pulsed gain in the low-pressure tubes, and this forces the TEA oscillator to lase on the injected lines.

As delivered, maximum output power of the device was $\sim 30\text{ kW}$. To achieve megawatt operation, we substituted a LASL-designed amplifier (active length, 90 cm ; active area, 2 cm^2), for the LDC TEA laser head (gain length, 40 cm ; active area, 2

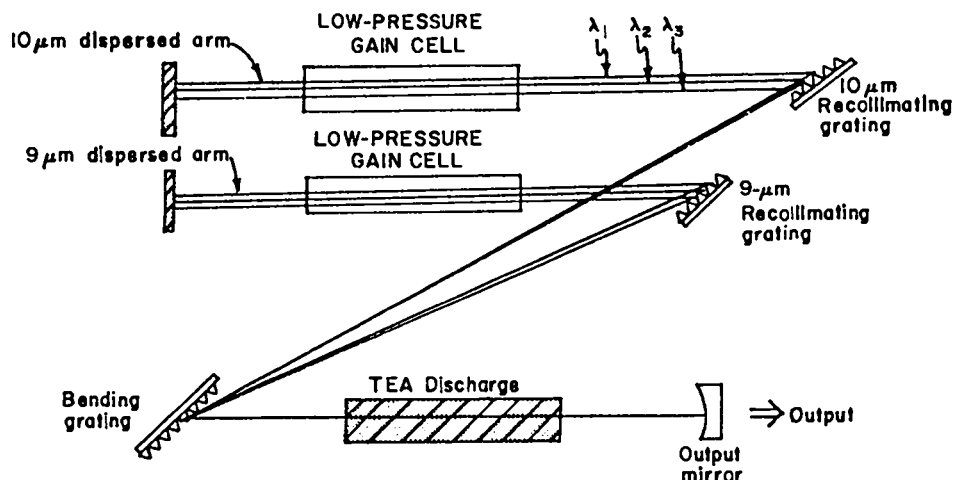


Fig. I-21.

Schematic of the Laser Development Corporation multiline/multiband laser.

cm²). The operating parameters of the LDC-LASL hybrid system are listed in Table I-III.

Laser Pulse-Shaping (R. L. Carman, L. J. Garwin, N. Clabo, H. Lane). Laser pulse-shaping for fusion is important at higher output energies where ablatively driven implosions replace the exploding pushers. Pulse-stacking and other simple pulse-shaping schemes employed on Nd:glass lasers are less applicable to CO₂ systems because the normal intensity range over which time-programming is required is expanded by the ratio of saturated to unsaturated amplifier gain. We have started work on a pulse-shaping scheme, which should eliminate the need for expanding the dynamic range of programming for CO₂ lasers. At the same time, for laser pulse risetimes of the order of, or less than, 1 ns, we are attempting to meet the requirement that more than one rotational transition is required in the output to maintain efficient energy extraction from the power amplifier. As a final requirement, the pulse-generation scheme must be a stable source of reproducible laser pulses. We are taking advantage of stabilization schemes employed in CO₂ cw lasers, where Invar structures of good thermal and mechanical properties are combined with piezoelectrically driven translators to provide feedback in adjusting the cavity length for optimum output.

Figure I-22 shows details of the new pulse-generation scheme. First, six independent and active feedback-stabilized, low-pressure CO₂ lasers are run in a pulsed high-repetition-rate mode. Each laser has a grating to allow selection of any rotational transition in the P- or R-branches of either the 9- or 10- μ m transitions. Two apertures within the cavity ensure that directionality is constant at optimum output, whereas the mode-limiting aperture allows the far-field diffraction angles to be independently adjusted.

The six beams are combined in a low-loss manner using a high-dispersion diffraction grating. A triple-stage Pockels-cell pulse clipper shortens the pulse with high extinction from $\sim 1\text{-}\mu\text{s}$ to 1-ns width. The various rotational lines are delayed by varying amounts by use of a grating-adjustable mirror system as illustrated. The pulse shape is further refined by using saturable absorbers in the delay-time system. Finally, the proper line-intensity ratios

TABLE I-III

OPERATING PARAMETERS OF LASL-LDC HYBRID MULTILINE, MULTIBAND CO₂ LASER

Pulse duration (FWHM), ns	140
Pulse energy, Total mJ	150
Power, MW	1
Energy, mJ (10- μ m operation only)	150
Energy, mJ (9- μ m operation only)	100
Smoothing—less than 10% ripple?	yes
Number of simultaneous lines	four 9 μ m and four 10 μ m
Simultaneity of all lines, ns	± 15
Energy stored in main-bank capacitor, J	91
Length of active TEA gain medium, cm	90

are obtained by using fixed attenuators in the delay-line system. The pulse-shaped output is obtained as the beam rejected for Polarizer 3 of the pulse clipper.

Much more precise pulse-shaping can be obtained by using an optional, independent pulse-clipping system, instead of, or in addition to, the pulse clipper described above. The main disadvantage of the optional system is the very large cost for obtaining proper pulse contrast.

Such a pulse-generation system allows the required dynamic range of time-programming to be compressed back to that of an unsaturated gain

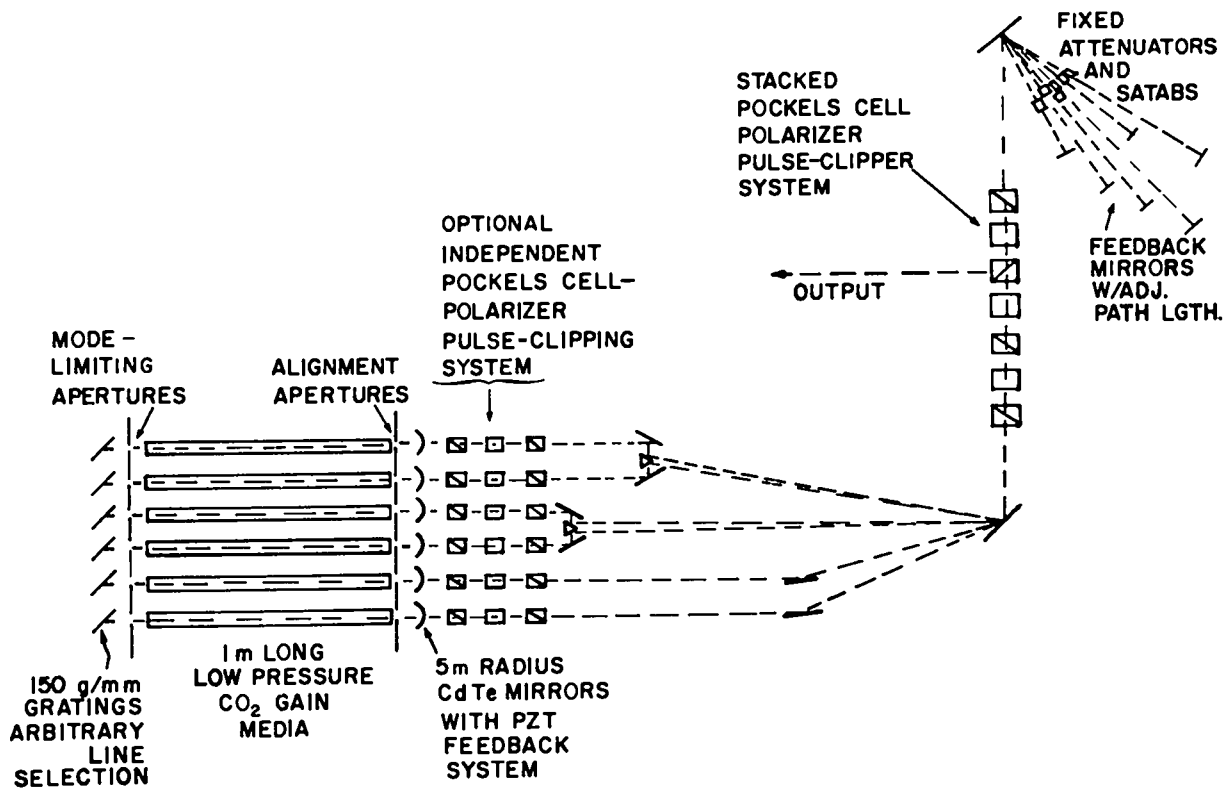


Fig. I-22.
Schematic of new pulse-generation scheme.

system. By supplying the main part of the pulse with P(20) 10- μ m radiation, the highest stored energy is accessible to the pulse, but, because this line has the largest emission cross section, it also has the largest unsaturated gain coefficient and the lowest saturation energy density. The P(20) 10- μ m line thus has the largest ratio of saturated to unsaturated gain. By providing the prepulse tailoring with either very much lower or (preferably) very much higher P-branch rotational transitions, the peak emission cross section for this energy can be lowered three- or fourfold: that is, the unsaturated gain coefficient can be reduced and the saturated energy density increased by this factor. This is just the effect that is required to compress the dynamic range of the time-programming at the front end of a large system to obtain reliable time-programmed outputs from the final amplifier stages.

In Antares, further time-programming can be obtained by inserting relative-path delays for the driving energy between the segments of the 12-segment annulus. In this manner, the temporal history of the

energy deposition at the target will be further modified.

As an additional advantage of this multiline pulse-generation scheme, the high-repetition-rate pulsed output can be combined with time-gated detection methods, sampling oscilloscopes, and other very sensitive diagnostics to accomplish the alignment and desired output. Routine monitoring and the use of feedback servos will allow these settings to be maintained. This removes one of the principal difficulties in large laser systems, namely, uncertainties and lack of reproducibility in pulse production.

Calculations of Parasitic Oscillations (C. J. Elliott)

When stray light in a laser amplifier acquires more gain because of the laser medium than is lost due to reflections, a parasitic oscillation can occur. We have developed the tools which describe this

problem in the ray-tracing limit for any geometry and we are systematically applying these techniques to the TBS, the EBS, and Antares. Quantitative agreement has been obtained with experiments on the TBS and qualitative agreement has been reached on the EBS.

The mathematical description of the problem proceeds in two steps: (1) determination at the static gain threshold of the oscillation and (2) determination of the dynamic effects which allow us to exceed the static threshold. The dynamic effects take advantage of the fast pumping at the laser medium and of the separation of the target from the amplifier module. The static threshold can be simply expressed in an approximate way and can be refined by calculation.

The general types of parasitic oscillations are classified as internal and noninternal modes. When a laser system is first being tested, the internal modes are examined experimentally. This process guarantees that all unblackened surfaces are blackened and also serves to establish the internal threshold as an experimental fact. When a target is in position a new type of mode could appear. An oscillation may occur between the target and some internal surface of the laser amplifier or the front-end optics. These modes are considered noninternal and are the most critical. Target reflection may be specular or diffuse.

The target modes, in addition to being diffuse or specular, are classified according to the number of passes through the laser medium for a complete return of the light. Asymptotic analysis shows that only paths along the optical axis are important to the problem. For the EBS, only six-pass, four-pass, and two-pass target oscillations are important, whereas for Antares, only the two-pass and four-pass modes are. The six-pass mode involves a reflection from the target—three passes of gain and a very small reflection $\sim 10^{-3}$ /sr from the exit salt window, followed by three more passes of gain and refocusing upon the target. Threshold calculations for this EBS mode give a static gain-length product of 6.3, which can be increased by ~ 0.5 with dynamic effects.

The four-pass mode involves light that is reflected off the target, makes two passes through the gain medium of the EBS or Antares, and then reflects near an optical element such as a turning mirror. Analyses of this mode and of the two-pass mode are not yet complete.

In dealing with parasitic oscillations, approximate formulas are invaluable in developing a feel for the problem. For most nonspecular surfaces in large lasers, the condition can be written:

$$R_1 R_2 \exp(2g_0 L) = 1 \quad , \quad (1)$$

where R_1 is the return fraction from the first of the two surfaces involved in the oscillation, R_2 is the return fraction from the second surface, and $g_0 L$ is the gain-path length product for a transit from Surface 1 to Surface 2. The return fraction R can be written as the product of a reflection coefficient per unit solid angle ρ , of the solid angle $\Delta\Omega$ of the mode, and of a factor on the order of unity T :

$$R = \rho \Delta\Omega T \quad , \quad (2)$$

where T depends on the mode pattern. For a Lambertian diffuse surface the reflection coefficient per unit solid angle ρ is the total reflection coefficient of that surface divided by π . Most surfaces are sufficiently different from being Lambertian that measured values of the reflection coefficient should be used.

When T is to be determined more precisely, or when the mode pattern of the oscillation is required, the integral equation for the mode can be solved directly. An example of such a calculation shows the mode pattern for the four-pass oscillation (see Fig. I-23) in the TBS. This oscillation occurred between a flat target and itself via multiple bounces through the optical system. Shown to scale is a 200- μ m target and an oversized stalk. When the ball target is used, the four-pass oscillation does not occur from either the ball or the stalk, but rather from the wall of the target chamber.

Isolator Development

Gas Isolator Development (S. J. Czuchlewski, A. V. Nowak, E. Foley).

Introduction. An intensive effort was made to develop a broadband gas isolator capable of suppressing parasitic self-lasing in the TPA of the EBS and TBS. A cell containing such a gas will be installed within the TPA directly in front of the large mirror, so that the laser pulse traverses the cell

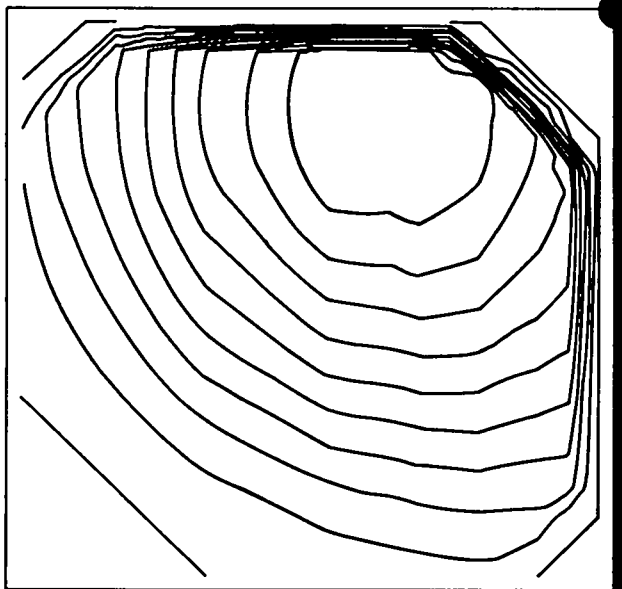


Fig. I-23.

Contour plot showing intensity distribution in the TBS four-pass mode on a flat target. The solid ball is to scale with a diameter of $200\ \mu\text{m}$, and the entire square region measures $3\ \text{mm}$ by $3\ \text{mm}$. The contours are graded by 10% of peak intensity, the outermost contour being zero intensity, and the innermost, 90% of peak.

twice between its second and third passes through the gain medium. Development of the gas isolator consists of three phases: first, of developing a gas mix that completely suppresses all lasing in the cavity of a small, conventional double-discharge CO_2 oscillator; second, of determining the saturation characteristics of the mix by measuring its high-intensity transmission; and finally, of a performance evaluation of the gas in the TPA. Results of the first two phases are encouraging and are reported below.

Mockup Amplifier. To suppress self-lasing in the TPA, the following relationship must be satisfied on each line of the CO_2 spectrum:

$$g_o L - \alpha L P \geq (g_o L)_{\text{thresh}} \quad (3)$$

where $g_o L$ is the single-pass small-signal gain, $\alpha L P$ is the small-signal absorption of the gas isolator, and $(g_o L)_{\text{thresh}}$ is the small-signal gain below which

the TPA is stable against self-lasing. If one uses a small laser whose gain (for example, $g_o L \approx 3$) is smaller than that of the TPA ($g_o L \approx 8$), the self-lasing problem can still be investigated by scaling the other two terms in the above equation.

We have assembled a pulsed CO_2 TEA laser to simulate the self-lasing characteristics of the triple-pass amplifier. With this mocked-up amplifier we determine a saturable gas mix which, when introduced into the optical cavity, will suppress all lasing. From this result we are able to estimate the pressure and composition of a gas mix needed to suppress self-lasing in the TPA.

By using the analog amplifier system, we have found three mixes (630B, 615, and 628B) that show promise of being an effective broadband isolator for the TPA. The components of these mixes are listed in Table I-IV, and a typical absorption spectrum for 630B is shown in Fig. I-24. Also illustrated are the locations of the branches of the CO_2 laser spectrum

TABLE I-IV

GAS MIXES THAT ARE EFFECTIVE BROADBAND ISOLATORS

Mix-630B (P, 8.82 torr) ^a	Composition (%)
	SF_6 0.84
	C_4F_8 4.02
	FC-115 9.97
	FC-1113 18.10
	FC-12 67.07
Mix 615 (P, 13.3 torr)	
	SF_6 0.54
	C_4F_8 5.44
	FC-1112a 9.64
	FC-115 11.30
	FC-1113 17.80
	FC-12 55.28
Mix 628B, (P, 8.44 torr)	
	FC-152a 66.2
	FC-1113 22.2
	FC-115 11.6

^aThe pressure P will provide an $\alpha L P = 3.0$ on the $10\text{-}\mu\text{m}$ P(20) line when used in a 75-cm cell within the TPAs.

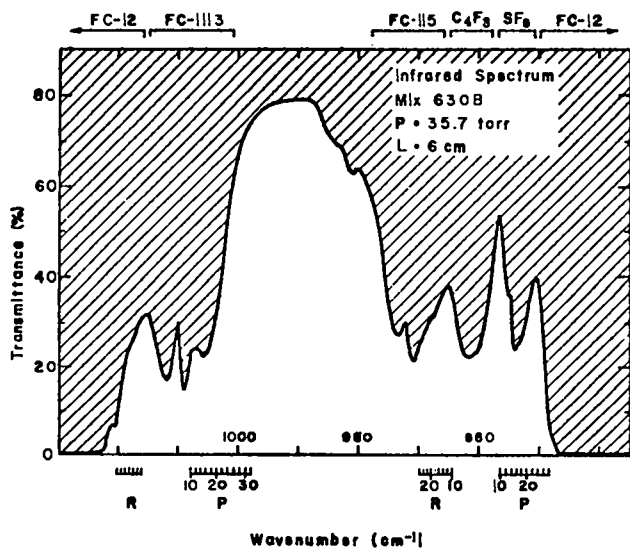


Fig. 1-24.

Infrared absorption spectrum of gas-isolator mix 630B. Absorption region of each gas is indicated at the top; location of CO₂ laser lines is shown at the bottom.

and the region in which each gas is an effective absorber. Two of the mixes (630B and 615) rely on SF₆ as the P-branch saturable absorber, whereas mix 628B uses fluorocarbon-152a. Because the absorption spectrum of FC-152a is much broader than that of SF₆, it also allows us to eliminate two other components (C₄F₈ and FC-12) which had to be added to the SF₆ mixes to suppress lasing on the low and high 10- μ m P-branch lines. The performance of these mixes will be discussed below.

Note that the spectral gain profile of the mockup amplifier is not identical to that of the TPA. Because the TPA is operated at 1800 torr, while the mockup amplifier is at 600 torr, the bandwidth of each laser line in the TPA is wider than that in our amplifier. Thus, our present mixes may not yet be perfectly tuned to the TPA spectrum; it is, therefore, essential that the precise composition of the mixes be determined and evaluated in the TPA.

Single-Frequency Saturation Measurements.

The saturated transmission of our gas isolators has been studied for irradiation by intense [10 to 200 MW/cm², 10- μ m P(20)] CO₂ laser pulses. Data were obtained for multicomponent mixes as well as for

single-component gases. Because the laser pulse will traverse the saturable-absorber gas mix twice in our TPAs, we have made these transmission measurements for both single- and double-pass geometries. (All the double-pass experiments on the three mixes indicate that the net double-pass transmission is simply equal to the square of the single-pass value.) These measurements were conducted in the Gigawatt Test Facility by using a spatially filtered laser pulse whose duration (FWHM) was 1.2 ns. The length of the test cell was 48.0 cm.

Three gases have been evaluated⁶ as P-branch saturable absorbers: SF₆, Fluorocarbon-152a (CF₃HCH₃; 1,1-difluorethane), and dimethyl ether (CH₃OCH₃). The saturation properties of SF₆ have already been studied extensively; it has been shown⁶ that for single-line irradiation SF₆ exhibits very efficient bleaching on each CO₂ line from P(12) to P(24). Table I-V lists the residual, saturated absorption coefficients for SF₆ at various CO₂ laser lines. For use in a broadband gas isolator, SF₆ suffers from the disadvantage of not being an effective absorber at either the high or low ends of the P-branch spectrum. Thus, other gases must be used to absorb in these regions, and, unfortunately, these also have a small, but unbleachable, absorption on the P(14) to P(22) lines, and, hence, they reduce the overall efficiency of SF₆. We have therefore investigated other, more broadbanded saturable absorbers.

TABLE I-V

RESIDUAL, SATURATED ABSORPTION COEFFICIENT FOR SF₆

CO ₂ Laser Line	Pressure (torr)	Residual Saturated Absorption Coefficient (10 ⁻³ cm ⁻¹ · torr ⁻¹)
P(12)	15.0	5.9
P(14)	9.0	9.4
P(16)	3.7	10.2
P(18)	5.8	24.7
P(20)	6.4	20.7
P(22)	10.9	36.3
P(24)	20.0	39.4

⁶Input intensity of the 1.2-ns CO₂ laser pulses was ~100 MW/cm². The SF₆ pressure P was chosen so that the small-signal transmission was ~5 × 10⁻⁵ at each laser wavelength.

Both dimethyl ether and FC-152a appear to absorb effectively over the entire P-branch. However, at P(20) neither bleaches as efficiently as SF₆. The relatively poor bleaching of dimethyl ether would seem to exclude it from further consideration as a practical isolator. Fluorocarbon-152a, on the other hand, holds promise.

As seen in Table I-IV, Mixes 615 and 630B employ SF₆ as the saturable absorber, whereas Mix 628B uses FC-152a. Figure I-25 shows the net double-pass (that is, round-trip) transmission of the three mixes under operating conditions that pertain to the TPAs. A cell length of 75 cm is assumed and the pressures are adjusted to suppress a gain-length product of 3 on the 10- μ m P(20) line. Mix 615 is considered the worst, providing an excessive amount of absorption on several CO₂ lines at the cost of reduced high-intensity transmission at P(20). Mix 630B is expected to provide a much better match to the spectrum that must be suppressed to prevent self-lasing in the TPAs, and it exhibits significantly larger high-intensity transmission. The transmission of Mix 628B containing 66.2% FC-152a has a stronger energy-dependence than either of the SF₆-based mixes and saturates less efficiently.

In conclusion, Mix 630B provides the design-point transmission of ~50%. Fine-tuning of the mixes to match the characteristics of the amplifiers could

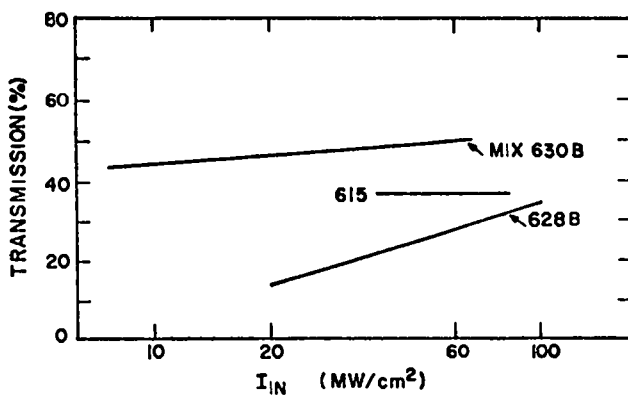


Fig. I-25.

The high-intensity saturated transmission of three gas-isolator mixes is plotted as a function of input pulse intensity. This is the net double-pass (i.e., round-trip) transmission of the gases as they would be used in the TPA.

change these transmissions slightly. A hybrid mix of SF₆ and FC-152a might provide even better performance.

Pulse-Shaping Effects. The focusing effects of any absorbing medium are an important consideration in selecting a practical isolator. Figure I-26 shows the input and output transverse spatial profiles of a laser pulse that was passed through a cell containing pure SF₆. (Spatial profiles were obtained with a linear pyroelectric array whose interelement spacing is 1 mm.) Because low-intensity signals are absorbed more strongly than those of high intensity, one would expect the wings of the pulse to be much more severely absorbed than the peak, but just the opposite is observed. This may be attributed to a defocusing that occurs when the pulse traverses the SF₆. Javan and Kelly⁷ have predicted that such a defocusing effect should occur in an absorbing medium when it transmits a laser pulse whose frequency lies on the low side of the absorption profile. The CO₂ 10- μ m P(20) frequency fulfills this condition in SF₆; but some of the other lines might be expected to experience a focusing effect. Investigation of this question will continue.

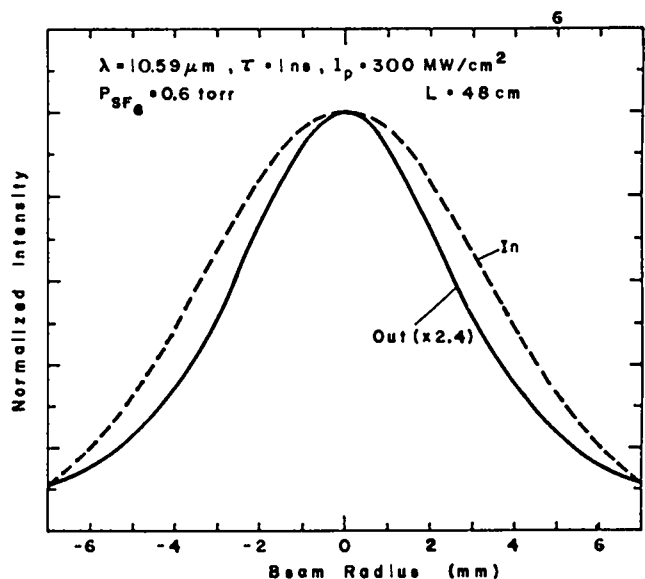


Fig. I-26.

Input and output transverse spatial profile of a CO₂ laser pulse that passes through an SF₆ absorber. Self-defocusing of the pulse is indicated.

Solid State Isolators.

Single-Band, Multiline Saturation Behavior of Single-Crystal Germanium (C. Phipps, S. Thomas). Understanding the dynamics of optical saturation of p-type germanium by a 10- μm multiline, single-band spectrum is crucial to the successful application of this material to interstage isolation of CO₂ laser systems. Theoretical considerations⁹ involving the breadth of the inhomogeneous line width in p-type germanium predict that energy distributed in a multiline single-band spectrum should saturate the responsible transition collectively. That is, the degree of bleaching achieved should be the same for the same total input flux whether the input spectrum is single-band multiline or single-line.

To verify these theoretical predictions, single-line and multiline saturation measurements were made on p-type germanium samples, by using the experimental setup shown in Fig. I-27.

To determine multiline transmission characteristics, the CO₂ laser source was modified to produce a spectrum of 4 to 5 adjacent lines at 10.5 to 10.6 μm , as shown earlier in Fig. I-11. Pulse width was 1.75 ns with a standard deviation of 15% and energy was in excess of 2.0 J.

The sample tested was p-type, gallium-doped, single-crystal germanium, with a high-power an-

tireflection coating. Small-signal transmission corresponded to an absorption coefficient (αL) of 5.0 at 10.59 μm . Optical path length was 3.5 cm. Illumination was at normal incidence, with the electric field \vec{E} parallel to the (111) orientation of the crystal. Electric-field orientation was irrelevant to bleaching behavior.

Figures I-28 and -29 display measured peak intensity transmission and the time-averaged transmission, respectively. Here, a residual (unbleachable) absorption of 0.02 cm^{-1} was assumed in generating the computer fit to the data (solid line).

Saturation intensity (I_s) determined from the time-averaged data and from the peak intensity data agree well, giving an average multiline value of $I_s = 3.75 \text{ MW/cm}^2$.

To provide a direct comparison, single-line transmission was also measured on the same test sample in the same orientation. These results are shown in Figs. I-30 and -31. The average single-line saturation intensity of $I_s = 3.11 \text{ MW/cm}^2$ is in excellent agreement with other single-line saturation measurements.

Isotropy of the Single-Line Saturation Parameter in Germanium. Further tests were conducted with the same germanium crystal to determine whether the single-line saturation parameter could be characterized as isotropic.

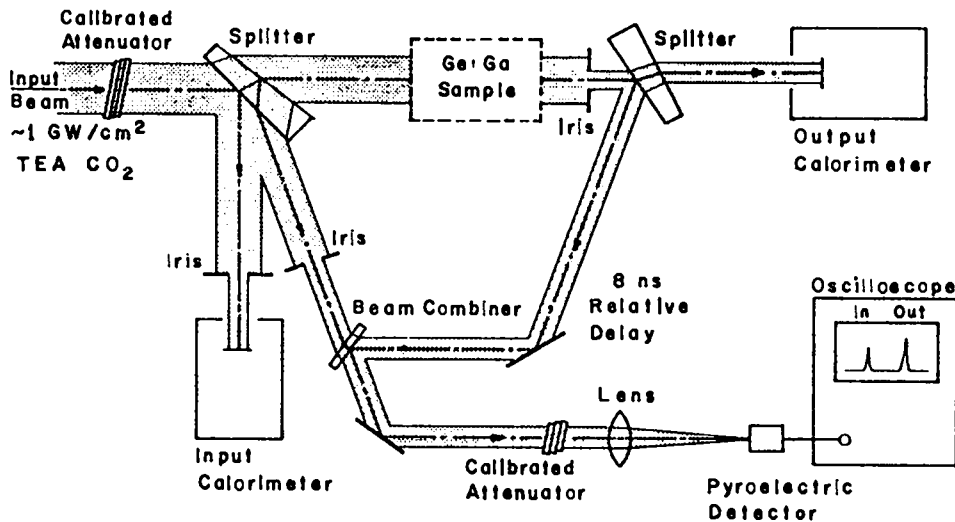


Fig. I-27.

Experimental arrangement for measuring germanium saturation properties.

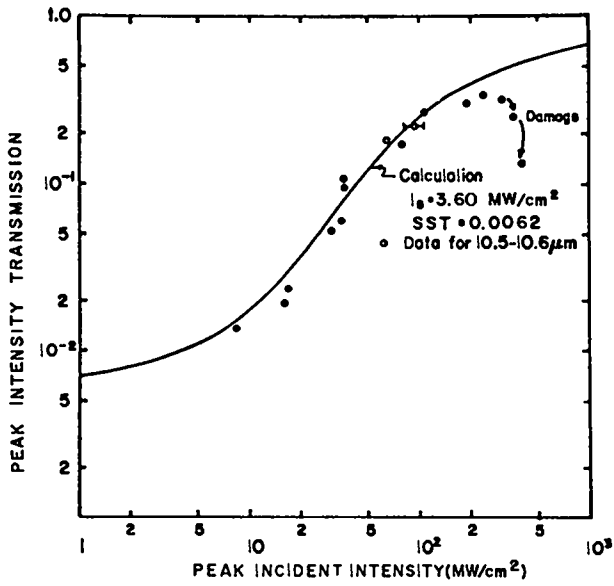


Fig. I-28.

Peak transmission of multiline spectrum by single-crystal p-type germanium.

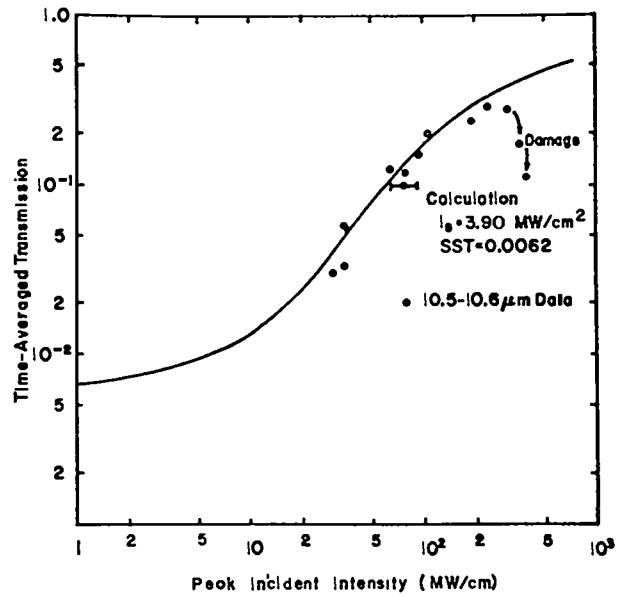


Fig. I-29.

Time-averaged transmission of multiline spectrum by single-crystal p-type germanium.

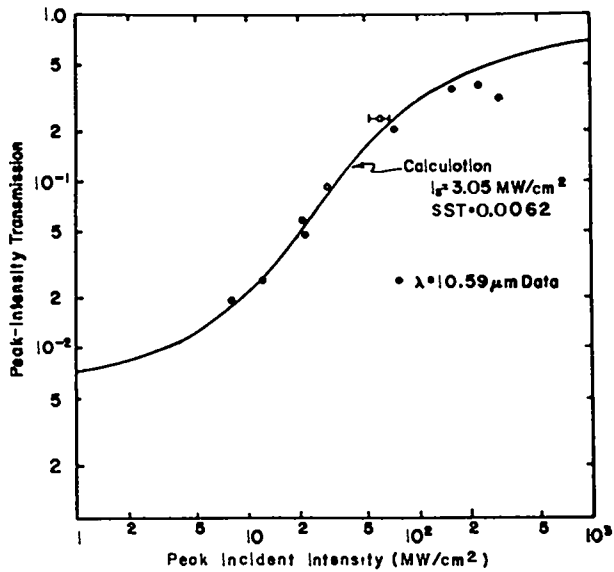


Fig. I-30.

Peak transmission of single-line spectrum by single-crystal p-type germanium.

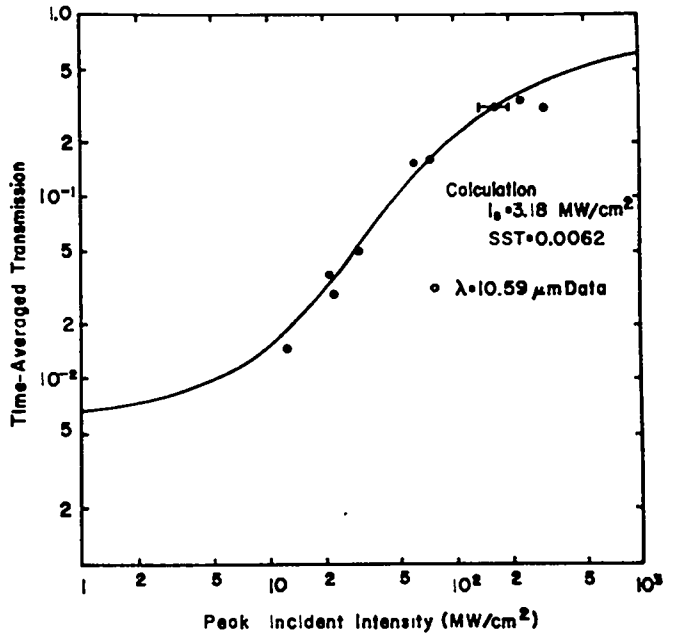


Fig. I-31.

Time-averaged transmission of single-line spectrum by single-crystal p-type germanium.

This germanium crystal had been manufactured so that two ar-coated faces had $[\bar{1}00]$ planes. Then, for normally incident illumination, the incident electric vector could be swept through the principal crystal axes, including the $[100]$, $[110]$, and $[111]$ families, by simply rotating the crystal about the axis defined by the incident beam (see Fig. I-32). Sample transmission was measured at $10.59 \mu\text{m}$ for 80 MW/cm^2 intensities as a function of crystal rotation. Starting with \vec{E} parallel to the $[111]$ -axis family, transmission measurements were made at 5-deg increments over a total 120-deg rotation. Then the measured transmission and input intensity were used to deduce a saturation-intensity value with the aid of computer-generated universal transmission curves for this absorber.

Results of this experiment are plotted in Fig. I-33. The mean I_s value of 3.3 MW/cm^2 is independent of optical electric-field orientation in the crystallographic frame. For comparison, note that saturation measurements in polycrystalline germanium-gallium agreed with our mean I_s within the experimental error of $\pm 15\%$.

Pulse Compression in Germanium. Pulse compression can occur in any saturable absorber. The exact characterization of this effect is necessary for a complete understanding of laser pulse propagation in a CO_2 amplifier system using saturable-absorber isolation. We have now characterized the compression process in germanium-gallium so that we can predict pulse reshaping in germanium with good ac-

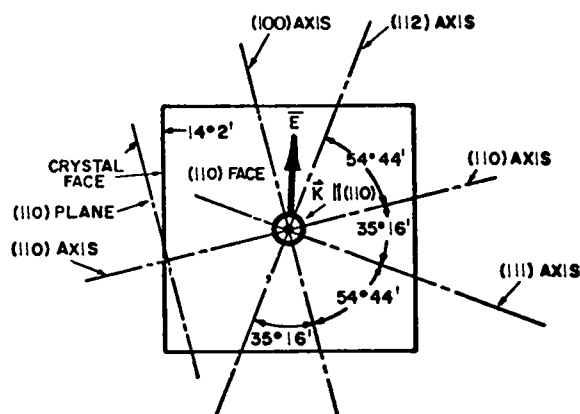


Fig. I-32.

Crystallographic geometry for test of orientation effects on germanium saturation.

curacy, and have shown that the degree of reshaping is the same for the multiline spectra as it is for single-frequency illumination.

The test setup employed was essentially as shown in Fig. I-27. Measurements were made with a single-line ($10.59\text{-}\mu\text{m}$) signal and with a 1% bandwidth multiline spectrum consisting predominantly of the P(18) and P(20) lines of the $10\text{-}\mu\text{m}$ CO_2 band, with 5 to 10% contributions from P(14), P(16), and P(22), as shown in Fig. I-11.

Figure I-34 shows the forward intensity-transfer function for the p-type germanium sample employed. This function was generated numerically as a best fit to the measured transmission-vs-intensity data for the crystal. A saturation intensity of 3.2 MW/cm^2 was employed for the calculation.

Figure I-35 shows the pulse compression calculated for the transfer characteristic of Fig. I-34 for an input pulse with a Gaussian time dependence (solid line), and the experimental data obtained for multiline (open circles) and single-line (closed circles) illumination.

These results demonstrate that pulse compression obtained in this way can, on the average, be predicted quite well. The vertical scatter in the data arises because of individual departures from Gaussian temporal behavior in the pulses. Peak intensity

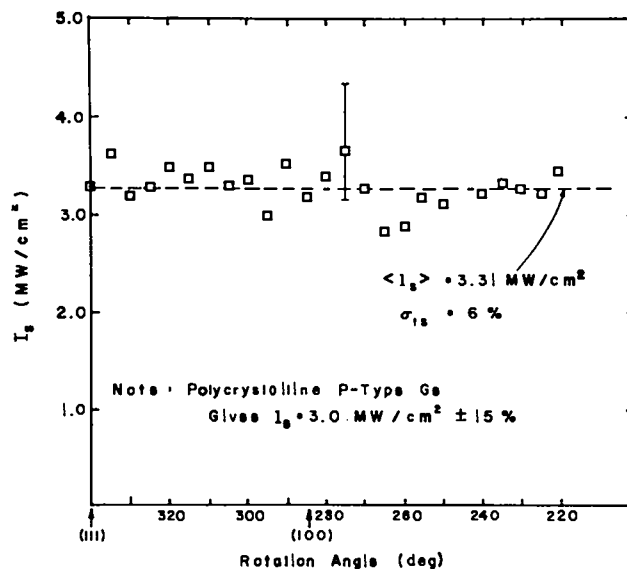


Fig. I-33.

Measured saturation intensity for various crystallographic orientations of germanium.

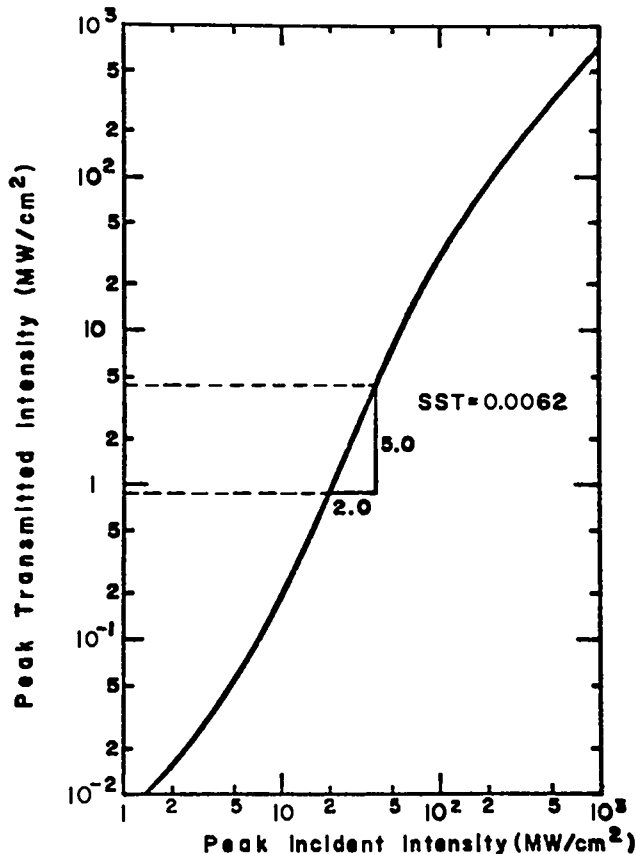


Fig. I-34.

Forward intensity transfer function calculated for typical p-type germanium sample.

transmission at the point of maximum pulse compression was 13%. No significant difference is seen in the effectiveness of pulse compression for single or multiline input spectra. Clearly, the p-type germanium absorbers represent a very simple method of obtaining moderate ratios of temporal pulse compression for 10- μ m regions predictably, whether in a single or multifrequency spectrum.

Faraday Rotator Development (R. Ahrenkiel).

General. The potential usefulness of Faraday rotators as 10- μ m isolators is being evaluated. The program is proceeding along two basic directions. First, in an in-house effort we have begun to extend the work of the Eastman Kodak group on the cobalt spinel family of ferrimagnetic rotator materials. This material is adaptable to hot-forging, which makes large devices possible. Also, because of its fer-

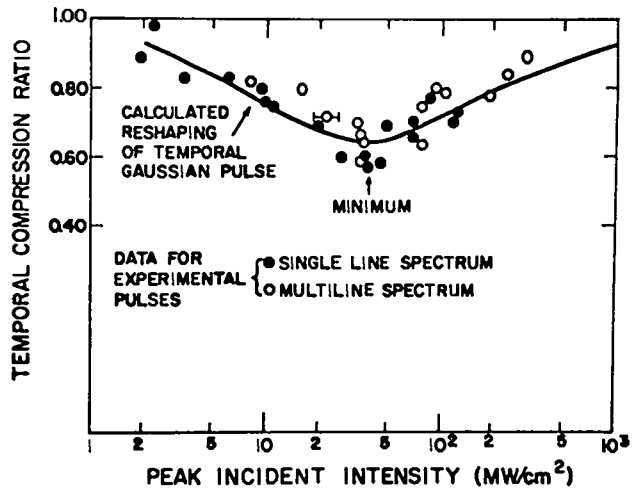


Fig. I-35.

Predicted and observed pulse shortening by p-type germanium sample.

rimagnetic nature, it requires modest fields (5 kG) of low spatial uniformity. Second, we are evaluating other prospective materials.

Cobalt Spinel Material. Samples of CoCr_2S_4 have been made by hot-pressing. The absorption coefficient of the first sample was $\sim 40 \text{ cm}^{-1}$. Analysis of the starting powder by various techniques showed several defects in this powder. It was $\sim 3\%$ chromium-rich, which is a sufficient departure from stoichiometry to produce this residual absorption, and it contained large crystals in addition to submicron crystallites. The latter condition usually results in poor densification of the hot-pressed product and in subsequent light scattering. New powders are being prepared in which this problem will be rectified.

We have also performed measurements on some Eastman Kodak samples of CoCr_2S_4 ($\alpha \approx 10 \text{ cm}^{-1}$), which have produced new parameters relevant to the Faraday isolator application.

- The specific Faraday rotation at P(24), $\lambda = 10.63 \mu\text{m}$, is 301.8 deg/cm at 7.2 kOe, which is well above magnetic saturation. Hence, the 45-deg thickness at this wavelength is 1.49 mm.

- The damage threshold on non-ar-coated samples with a medium-grade polish is $\sim 0.43 \text{ J/cm}$ or 400 MW/cm. This damage is purely surface damage and the threshold can probably be increased with better surface preparation. Antireflection-coated

samples will also be damage-tested to determine practical operating limits for a CoCr_2S_4 -based Faraday rotator.

Promising Faraday Rotator Materials. The II-VI periodic-chart material $\text{Hg}_{1-x}\text{Cd}_x\text{Te}$ has been suggested by Gullotti and Granneman of the University of New Mexico as a high-performance Faraday rotator for the CO_2 wavelength range. In particular they suggested that the interband rotation, which varies as $E_g^{-3.6}$, where E_g is the energy band gap, may be 10 times higher in $\text{Hg}_{0.63}\text{Cd}_{0.37}\text{Te}$ than measured in germanium.⁹

The Faraday rotation of these samples was measured with a cw 2.0-W CO_2 laser. The magnetic field was supplied by a 50-kG superconducting magnet with a "warm bore" for room-temperature operation. Four CO_2 lines were used so that the wavelength dependence of V , the Verdet coefficient, could be carefully determined. These lines were P(20) and P(18) of the 10- μm branch and P(26) and P(20) of the 9- μm branch.

The measured Verdet coefficients of the n- and p-type crystal are shown in Fig. I-36. Assuming a combination of the interband and free-carrier contributions to the Verdet effect, the total coefficient V is given by:

$$V = \frac{A}{\lambda^2} + B\lambda^2 = V_I(\lambda) + V_{fc}(\lambda), \quad (4)$$

where A is the interband component and B is the free-carrier component. For convenient use with wavelength expressed in micrometers, B is given numerically by:

$$B = 1.51 \times 10^{-20} \frac{N}{n_o m_*^2} \text{ deg cm}^{-1} \text{ kOe}^{-1} \mu\text{m}^{-2}, \quad (5)$$

where m_* is the effective mass, n_o is the index of refraction, and N is the carrier concentration.

The p-type crystal shows V to be very weakly wavelength-dependent, whereas V in the n-type crystal varies as $1/\lambda^n$ where $n > 2$.

Data fits of the points to Eq. (4) for the two samples give the results in Table I-VI.

We observe that the interband Verdet constant is comparable to that of germanium, but is much less

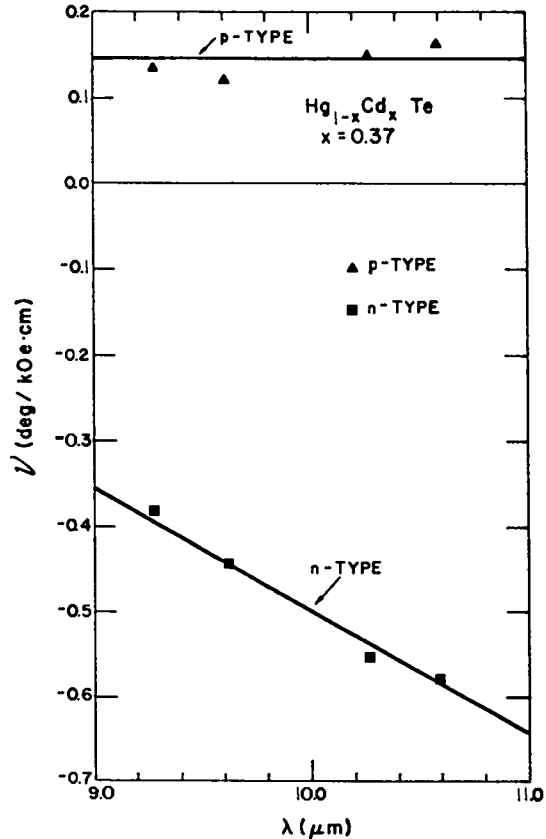


Fig. I-36.

Wavelength dependence of the Verdet coefficient for two mercury cadmium telluride samples.

than predicted. However, we see a large Verdet coefficient evolving from free-carrier absorption in n-type material. The rotation of n-type material per donor is ~ 77 times that of p-type material per acceptor. The physical origin of the difference is the very light mass of the donor. The figure of merit V/α (with V the Verdet coefficient and α the small-signal absorption coefficient) in n-type material is 0.76 deg/kOe , and is larger than that of other prospective materials except germanium and CdTe .⁹ More important, at this doping concentration, the room-temperature Verdet constant for n-type $\text{Hg}_{0.63}\text{Cd}_{0.37}\text{Te}$ is 0.58 $\text{deg/kOe}^1 \text{ cm}$, compared to 0.08 for germanium and 0.03 for CdTe . Because of the high Verdet coefficient, this n-type material may be useful for Faraday rotation devices in the 10- μm region.

TABLE I-VI

RESULTS OF HgCdTe STUDY^a

Sample	$ N_D - N_A $ (cm^{-3})	A ($\text{deg kOe}^{-1} \text{cm}^{-1} \mu\text{m}^2$)	B ($\text{deg kOe}^{-1} \text{cm}^{-1} \mu\text{m}^{-2}$)	m_*	$V_1(10.6 \mu\text{m})$ ($\text{deg kOe}^{-1} \text{cm}^{-1}$)
n-type	$4. \times 10^{18}$	10.7	-6.0×10^{-3}	0.053	0.095
p-type	3.8×10^{18}	7.1	7.3×10^{-4}	0.43	0.063

^a $|N_D - N_A|$ = Difference between donor and acceptor concentrations in the material.

A = Verdet constant, interband component.

B = Verdet constant, free-carrier component.

m_* = Effective mass of the carrier.

V_1 = Interband Verdet coefficient.

It would be very difficult and expensive to grow or hot-press large blanks of the material. Even 1.0-in.-diam crystals at constant composition and doping levels are difficult to fabricate. Application of this rotator in large systems will require further materials development. However, n-type HgCdTe represents a useful rotary medium for experimental and theoretical investigations in adjustable band gap Faraday rotators.

Evaluation of Optical Components.

Damage Tests of CdTe Antireflection Coating (E. J. McLellan, S. J. Thomas). Damage tests have been conducted to determine the damage thresholds of an ar-coated CdTe crystal. The results summarized in Table I-VII were obtained with a single 1.8-ns FWHM pulse of uniform peak intensity over the central 4.5-mm-diam part of the beam at the target.

The results show that, contrary to previous data, the crystal coatings should not be damaged by the peak power density typically available from an oscillator. Two possible mechanisms for damage seen in the past are dust particles on the crystal faces or an expansion/contraction mismatch between the crystal and its coating, causing the coatings to

buckle. Further tests will be conducted to determine crystal damage thresholds with a 50-ns oscillator pulse.

Damage Tests of Antireflection-Coated Germanium (C. Phipps, S. Thomas). Flux and intensity damage thresholds for antireflection coatings on germanium were determined in single laser shots. All samples had less than 2% surface reflection loss at the time of manufacture. Damage thresholds were measured with a beam whose intensity in a 0.4-cm-diam central region was uniform to within 1.5%. Pulse duration was 2.2 ns FWHM. Damage intensity was approached in a nine-shot surface-conditioning sequence of gradually increasing intensities. Results are summarized in Table I-VIII. Item 6 lists the damage data from the EBS polycrystal test piece reported elsewhere. We conclude that:

- Several responsible manufacturers produce good coatings, with little variation in quality.

- Because previous incidental data on Item 4 showed a 1.2-J/cm^2 damage threshold with a 1.0-ns FWHM incident $10.6\text{-}\mu\text{m}$ pulse, coating damage in the 1- to 2-ns range appears to be flux rather than intensity dependent.

More detailed tests of damage thresholds in germanium and other ir-transmitting materials are in progress.

TABLE I-VII
DAMAGE THRESHOLD OF CdTe ANTIREFLECTION COATING

Sample	No Damage		Damage	
	Power Density (MW/cm ²)	Energy Density (J/cm ²)	Power Density (MW/cm ²)	Energy Density (J/cm ²)
10-mm by 10-mm ar-coated CdTe modulator crystal (no visual imperfections).	470	0.89	740	1.40
Coated witness sample (no visible imperfections).	570	1.06	940	1.60
Coated witness sample (coating appeared scratched and damaged at scratch).	340	0.73	540	0.97

TABLE I-VIII
RESULTS OF DAMAGE MEASUREMENTS
AT 10.6 μm FOR ANTIREFLECTION
COATINGS ON GERMANIUM

Item	Date of Manufacture	Damage Flux (mJ/cm ² ± 10%)	Damage Intensity
1	March 1977	950	400
2	August 1974	650	400
3	August 1974	1000	370
4	August 1974	1000	490
5	August 1974	1000	440
6	March 1977	530	290

Measurement of (0,0°,2)→(1,0°,1) Gain in a TEA Double-Discharge Medium (B. Feldman, R. A. Fisher)

Introduction. We have studied the energy distribution in the asymmetric stretch mode (ASM) in a 600-torr CO₂ double-discharge laser system as part of an on-going program to determine the extent to which energy stored in levels other than (0,0°,1) can be extracted on a nanosecond time scale. In particular, we have measured the gain on nine lines in the (0,0°,2)→(1,0°,1) sequence band. Our measure-

ments indicate that it may be possible to construct a sequence-band TEA laser.

Sequence-Band Gain in a cw Probe Laser. We have constructed a cw sequence-band CO₂ laser operating on the (0,0°,2)→(0,0°,1) band. Similar to the work of Reid and Siemsen,¹⁰ we inserted a 50-cm-long heated (683 K) CO₂ absorption cell (pressure, 140 torr) into an otherwise conventional low-pressure cw CO₂ laser cavity. The absorption in the hot cell prevented the usual lasing from the (0,0°,1) level. The oscillator cavity consisted of a plane

grating (in Littrow) 1.5 m from a 5% transmitting output mirror with a 10-m radius of curvature. Identification of new lines was simple, using the interpretation in Ref. 11. As a further check, the laser-cavity grating settings required to obtain these lines and the conventional lines all correlated with the known wavelengths. We have obtained up to 170 mW in a single sequence-band line. The output power was limited by the current capacity of the power supply. These new lines also lased when the discharge was operated in the pulse mode.

Sequence-Band Gain in a TEA Discharge. The output of the new sequence-band laser was passed through a mechanical chopper (open 90% of the time), was then passed through a 1-atm TEA amplifier (active length, 90 cm), and detected by a S. A. T. detector. Maximum gain on the sequence band was $\sim 0.75\%/cm$, whereas the conventional band gain peaked at $\sim 3.2\%/cm$.

To verify that the sequence-band gains were not just off-resonant amplification due to the conventional bands, we calculated these off-resonant gain effects for each line. Typically, the conventional band gain at the sequence-band lines was only 0.05%/cm; no correction to our data was therefore necessary.

Relative number densities in $(0,0^{\circ},2)$ and $(0,0^{\circ},1)$ were established by using the ratio of measured gains and by assuming that the dipole transition matrix elements scale approximately as $\sqrt{\nu_s}$, where ν is the ASM quantum number. Although this assumption would be exact in the harmonic-oscillator approximation, there is some uncertainty about the dependence for CO_2 because of the complexities of vibrational mixing. From the gains reported above, we have established 1840 K (1570°C) as an effective vibrational temperature for the ASM; this corresponds to an $(0,0^{\circ},2):(0,0^{\circ},1)$ population ratio of $\sim 11\%$.

Disk Calorimeter Response Measurement (C. Phipps, S. J. Thomas, D. Watkins, F. B. Harrison)

We have measured the response of a 2.54-cm-diam Scientech disk calorimeter to an incident optical flux ranging from 0.01 to 3.0 J/cm² with 10.6- μm , 1.6-ns pulses. Incident flux was monitored with a second calibrated calorimeter and with a beamsplit-

ter. By comparing the energy transmitted through a small aperture in the center of the test beam with the energy of the input monitor signal, we calibrated the peak input surface-energy density in the test region.

In the experiment, the test calorimeter disk was freshly coated with "Nextel" paint and its response was determined at progressively higher fluxes. At the highest flux employed, brilliant plasma plumes were produced by irradiation of the disk coating.

The results of this test are shown in Fig. I-37. Prior to surface damage at 420 mJ/cm², the relative response of the test calorimeter showed a 2.6% deviation from linearity. At 1.0 J/cm², the relative calorimeter response is reduced to 0.76. Data scatter is due mainly to the details of plasma formation at each shot. Without recoating, the calorimeter subsequently returned to 98% of its response prior to damage, for input flux levels in the linear response region.

Gigawatt Test Facility (S. J. Czuchlewski, A. V. Nowak, E. Foley)

Several improvements were made in the Gigawatt Test Facility. A p-doped germanium isolator was installed between the amplifiers to control self-lasing and to reduce feedthrough to the design value of less than 1% of the signal pulse. Although the germanium is operated close to its damage threshold, its strong-signal transmission is only $\sim 25\%$, and the

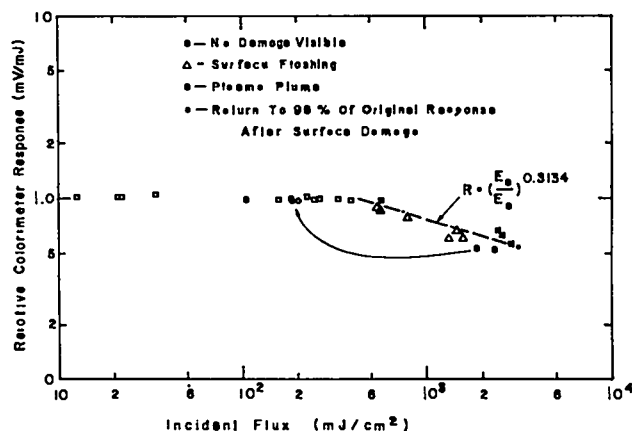


Fig. I-37.

Relative disk calorimeter response to incident flux at 10.6 μm .

final output of the system is reduced accordingly. Consequently, the germanium will eventually be removed and replaced by an SF₆ cell to control self-lasing, and by a multistage Pockels-cell switchout to provide the required contrast ratio. A final spatial filter has been installed after the second amplifier; it delivers a smooth, well-characterized pulse, free from any undesirable hot spots.

REFERENCES

1. E. Yablonovitch and J. Goldhar, *Appl. Phys. Lett.* **25**, 580 (1974).
2. F. Gires and P. Tournois, *C. R. Acad. Sci.* **258**, 6112, Paris, France (1964); J. A. Giordmaine, M. A. Duguay, and J. W. Hansen, *IEEE J. Quant. Elect.* **QE-4**, 252 (1968); T. W. Hansch, *Appl. Opt.* **11**, 895 (1972); R. A. Fisher and W. K. Bischel, *Appl. Phys. Lett.* **24**, 468 (1974); E. Yablonovitch, *Phys. Rev. A* **10**, 1888 (1974).
3. A. Gondhalekar, N. R. Heckenberg, and E. Holzhauser, *IEEE J. Quant. Elect.* **QE-11**, 103 (1975).
4. E. J. McLellan and J. S. Lunsford, Talk number 8.10, 1977 IEEE/OSA Conf. Laser Eng. and Appl., Washington, DC (unpublished).
5. M. Sirchis and R. Kung, AVCO-Everett Research Laboratory, have kindly advised us of their data on the saturation of FC-152a and dimethyl ether prior to publication of their work.
6. S. J. Czuchlewski, A. V. Nowak, and E. Foley, "An Efficient Gas Isolator for CO₂ 10- μ m P-Branch Laser Operation," submitted to the 9th Annual Electro-Optics/Laser Conference (October 1977); F. Skoberne, Comp., Los Alamos Scientific report LA-6245-PR (July 1976) pp. 35-37.
7. A. Javan and P. L. Kelley, *J. Quant. Elect.* **JQE-2**, 466 (1966).
8. F. Keilmann, *IEEE J. Quant. Elec.* **QE-12**, 592 (1976).
9. C. R. Phipps, Jr., and S. J. Thomas, *J. Appl. Phys.* **47**, 204 (1976).
10. J. Reid and K. Siemsen, *Appl. Phys. Lett.* **29**, 250 (1976).
11. M. C. Richardson, *Appl. Phys. Lett.* **25**, 31 (1974).

II. ANTARES—HIGH-ENERGY GAS LASER FACILITY

The High-Energy Gas Laser Facility (HEGLF) is built around a high-power (100- to 200-TW) short-pulse (0.25- to 1.00-ns) CO₂ laser, Antares, which is being designed to investigate laser fusion phenomena, with the objective of demonstrating scientific breakeven. A prototype module of the laser has been constructed and is being evaluated in extensive testing.

INTRODUCTION (J. Jansen, T. F. Stratton)

The objective of the High-Energy Gas Laser Facility Program (HEGLF), with its Antares Laser System, is to extend the present CO₂ laser capabilities to power levels at which fusion experiments can be expected to yield thermonuclear energy release in the range of scientific breakeven (defined as equality between the thermonuclear energy output and the laser-beam energy incident on target). The investigation of laser fusion phenomena at these levels will provide more complete understanding of the physics involved and allow laser and target design parameter requirements to be established with confidence. The program specifically calls for the construction of a six-beam, 100- to 200-TW CO₂ laser (100 kJ in 1 ns or 50 kJ in 0.25 ns) and of an associated target-irradiation facility.

We have undertaken a prototype program to verify experimentally the analytical conclusions to confirm from an engineering standpoint the design concepts before beginning procurement of the major laser hardware. We have concentrated especially on the fabrication and assembly of the prototype power amplifier (PA), which is being evaluated in extensive testing.

A major breakthrough was the successful production of NaCl boules of adequate size by the Kyropoulis/Czochralski process. Another significant achievement was the production of off-axis paraboloids of high optical quality.

Considerable effort was directed toward monitoring the experimental results obtained on the EBS and assessing their impact on Antares. Most signifi-

cant is the reduction of the maximum gain-length product to 6, which restricts Antares to a single-band system (10.6 μ m) and greatly increases the required output from the preamplifier.

These and other results are discussed in this section.

PROTOTYPE POWER AMPLIFIER

PA Status and Results (W. T. Leland, J. T. Ganley, D. Swanson, G. York)

General. The prototype PA program addresses design and performance questions associated with large cylindrical CO₂ laser amplifiers. Cylindrical geometry permits a very favorable ratio of total output to total space occupied and opens up a variety of design alternatives, many of which are heretofore untested.

Several alternative designs were studied and judged to be feasible, but for reasons of cost effectiveness and overall ease of assembly and maintenance, the design illustrated in Figs. II-1 and -2 was chosen.

The inner pressure vessel, which contains the electron gun and foil-support structure, represents the crucial part of the design. The electron gun is of the gridded cold-cathode type.

The particular design used here is similar to that produced for us by Systems, Science and Software, Inc., but the radii of the cathode and grid have been increased to reduce magnetic field effects in the gun. Energy is fed from one end via a coaxial cable whose outer sheath is used to make connections to the grid.

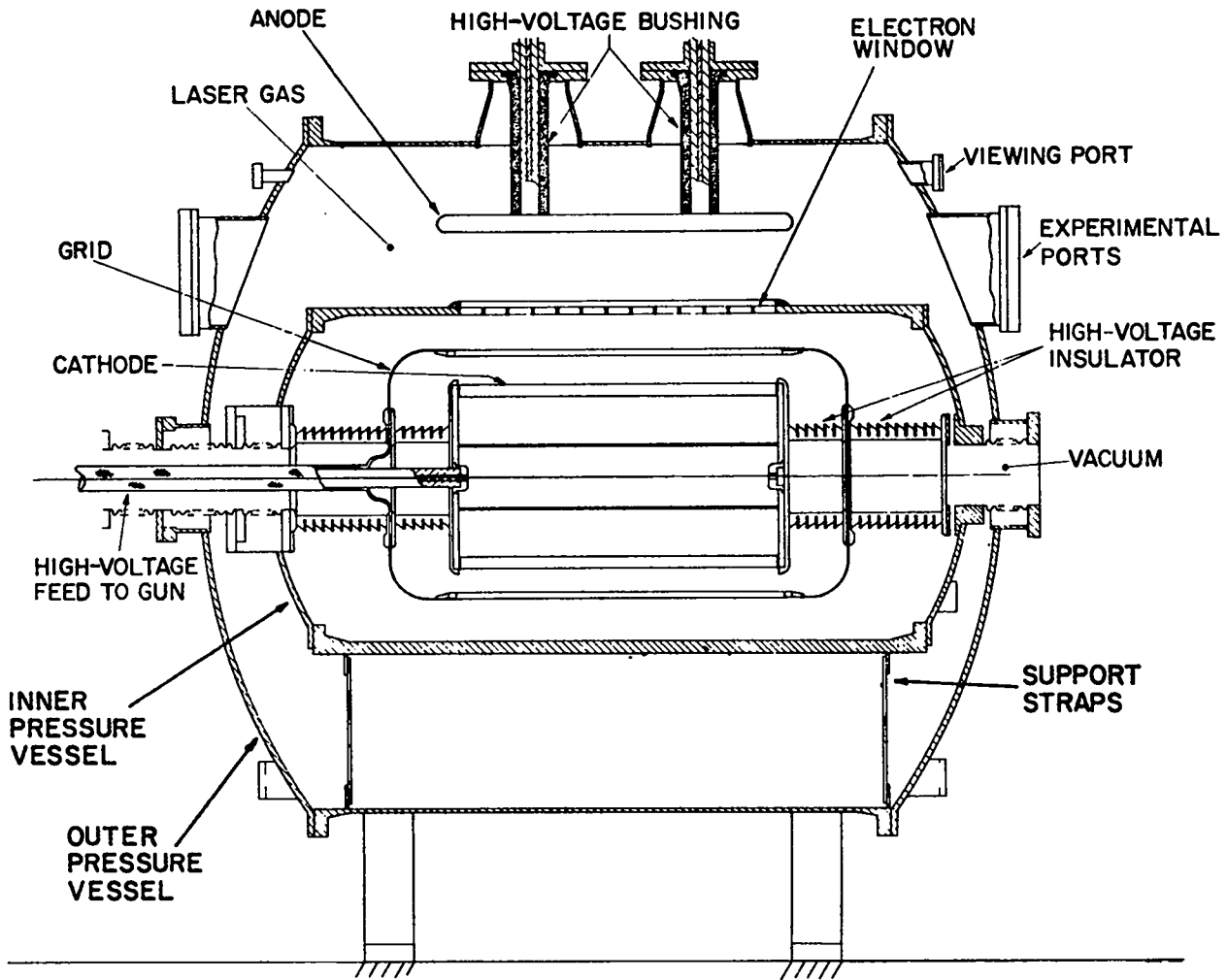


Fig. II-1.
 Transverse section of Antares prototype power amplifier.

The bushings and the energy feed passageway are filled with transformer oil to permit operation of the gun at 500 keV. A 2-mil-thick titanium window foil is supported by 6.3-mm- (0.25-in.-) thick ribs, spaced 50 mm (2 in.) apart, milled in the wall of the pressure vessel. With this support structure, the foil ruptures at ~120-psi differential, or about 3 times operating pressure. The entire inner pressure vessel is supported and centered in the outer pressure vessel by 12 support straps at each end. Tight end-to-end fabrication tolerances are avoided by using bellows at appropriate places.

Fabrication of the prototype components was essentially complete by the middle of May 1977, when the inner pressure vessel was delivered.

Assembly and Testing. Assembly and mechanical testing of the components occupied much of the remainder of the reporting period.

The prototype PA tests performed to date are listed below.

- The outer pressure vessel with its various instrumentation ports was checked for leaks and has

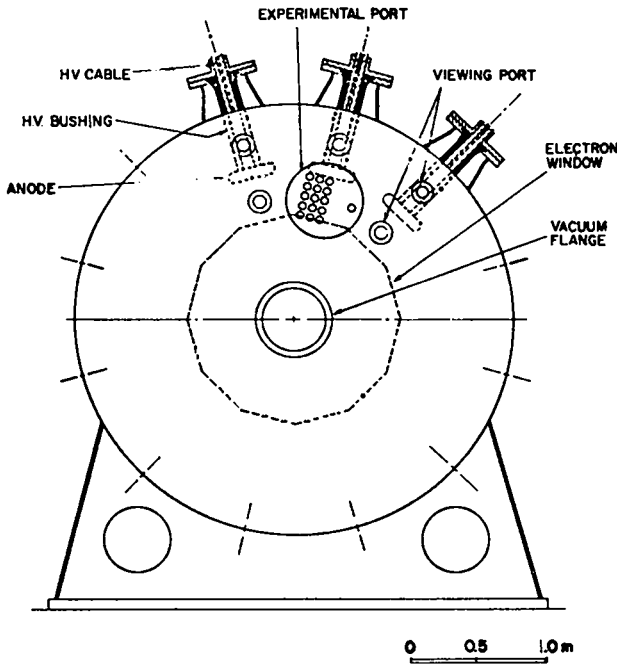


Fig. II-2.

End view of Antares prototype power amplifier.

been pressure-tested to 2250 torr (25% above design pressure of 1800 torr).

- The gas filling system has been tested by filling the vessel to the design pressure of 1800 torr with the specified gas composition (1:4::N₂:CO₂).

- The anode, bushings, and power cables have been installed and operated at design voltage (500 kV).

- The inner pressure vessel and the electron gun have been assembled with foils, installed, and checked for leaks.

- All the power supplies have been assembled and tested with dummy loads.

- All power supplies have been operated simultaneously with proper firing sequencing.

- The complete system has been assembled.

- The mapping of magnetic fields from the low-voltage power supply has been completed.

- The gridded cold-cathode gun has been operated from 300 to 500 kV.

- The primary gun current has been mapped in air (600 torr) at a gun voltage of 300 kV.

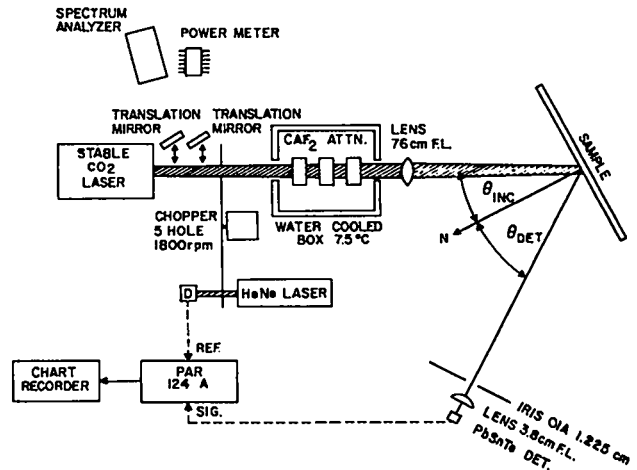


Fig. II-3.

Schematic of experimental setup for measuring surface reflection coefficients at 10 μ m.

Reflectance Measurements. An apparatus has been assembled to measure the absolute reflectance of CO₂ laser light from various surfaces. The experimental arrangement, shown in Fig. II-3, allows for independent variation of (θ_i, ϕ_i) , the angle of incidence, and of (θ_D, ϕ_D) , the angle at which the scattered light is detected. Quantitative measurements can be made of the energy scattered into any solid angle, $d\Omega$, at (θ_D, ϕ_D) . This makes it possible to experimentally characterize the reflection properties of any particular surface. These properties are conveniently summarized as a surface transfer function $f(\theta_i, \phi_i, \theta_D, \phi_D, B_p)$, which describes the scattering into any given angle from an arbitrary surface illumination, and for a beam polarization B_p .

A number of surfaces have been characterized for angles of incidence and reflection that may determine the parasitic oscillation characteristics of the Antares amplifiers. Of particular importance is normal reflection from surfaces at the ends of the gain medium. Measured values for specular reflectance and total integrated reflectance for near-normal incidence are listed in Table II-I. Data scans for three of these materials are shown in Fig. II-4; carbon-loaded polyurethane foam and lithium fluoride are clearly poorer reflectors than any of the other materials tested and are thus the best choices for minimizing end reflections.

TABLE II-I
REFLECTANCE OF VARIOUS
MATERIAL SURFACES

Material	Total Reflectance
Fiber glass Cloth I	0.13
Carbon cloth	0.12
Apiezon Q	0.056
Painted Nextel	0.055
Fiber glass cloth-Nextel Sprayed	0.045
Sprayed Nextel	0.043
Fiber glass Cloth II	0.032
25-PPI carbon polyurethane foam	0.015
Lithium fluoride (LiF) powder	0.0094
Polished LiF (specular reflection)	0.00041

Calculations and Analysis (W. T. Leland, M. Kircher, J. Comly)

Two-dimensional calculations have been carried out to predict the spatial gain distribution in large-aperture amplifiers. The departure from uniform gain is the result of a nonuniform deposition of energy by the primary electron beam, which, in turn, leads to a nonuniform discharge. The primary electron beam is injected from the cathode side of the discharge with initial velocities directed toward the anode. Scattering in the high-pressure gas and the effect of magnetic and electric fields result in complicated trajectories and energy deposition patterns. The energy deposition patterns are calculated on computers using Monte Carlo techniques. Once an energy deposition or ionization pattern is established, the discharge pattern is calculated by solving the equivalent of a nonlinear Poisson equation in two dimensions. The next step involves coupling-in the driving power supply characteristics to obtain voltage and current waveforms throughout the discharge. The final step involves CO₂ kinetics to obtain the gain.

Figures II-5 and -6 show the results of such calculations for the prototype. Voltage and current waveforms are shown in Fig. II-5; the power supply is simply 0.15 μF in series with 5.1 μH and 12.2 m

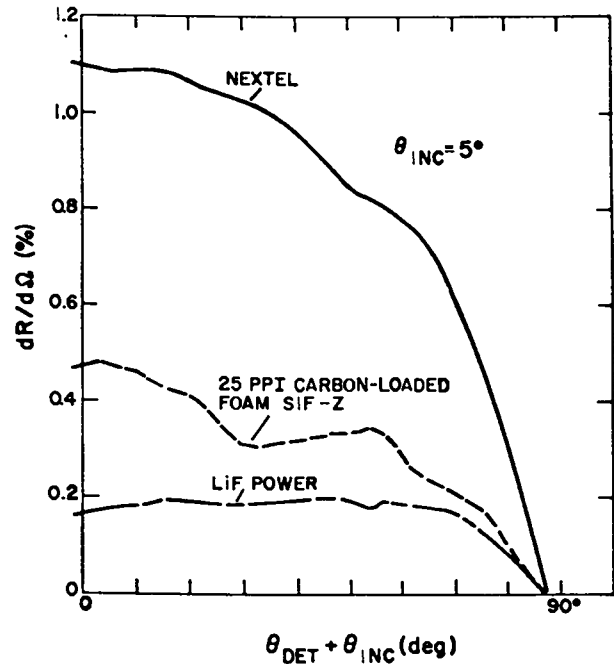


Fig. II-4.
Reflectance data scans for three materials.

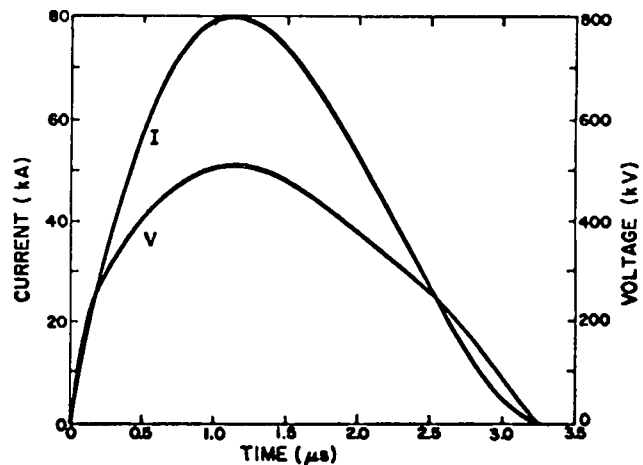


Fig. II-5.
Calculated voltage and current waveforms for prototype power amplifier.

(40 ft) of 8-Ω cable. Cylindrical geometry is used and two cases are presented in Fig. II-6: with fringing and without fringing. The numbers correspond to calculated small-signal gain at the points throughout the discharge cross section designated

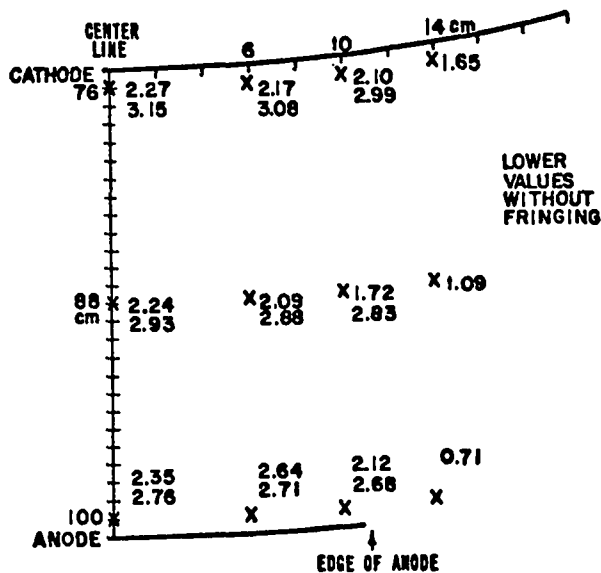


Fig. II-6.

Calculated gain uniformity in prototype power amplifier; upper values with fringing; lower values, without fringing throughout discharge cross section as marked by x's.

by the x's. The lower numbers differ from the upper numbers only in that no fringing has been allowed. In practice this corresponds to the use of a nonconducting barrier located at the desired boundary of the discharge. Clearly, elimination of discharge fringing substantially improves uniformity and overall performance.

Figure II-7 plots calculated gains along a 75-cm-long annular discharge. The fall off in gain near the

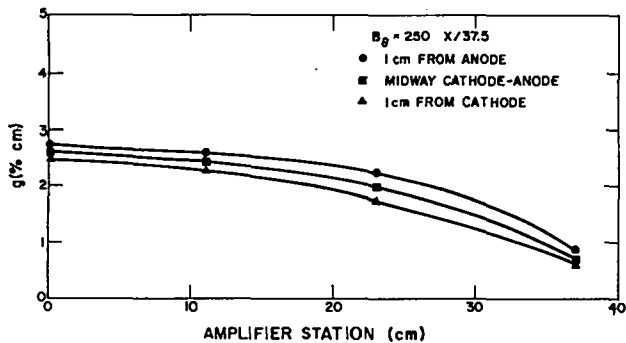


Fig. II-7.

Calculated gain along amplifier.

ends is largely caused by the magnetic field affecting primary electron trajectories. The field is an azimuthal field rising linearly to 250 G at the ends.

ANTARES DESIGN

Laser System Design (W. H. Reichelt)

Base-Line Design (K. C. Jones).

Front End (C. Knapp). The front end of Antares consists of a short-pulse generator and appropriate amplifiers. A detailed study of the system is in progress to determine the parameters of the amplifiers and isolators needed to meet the input requirements of the main PA. A conceptual design that meets these requirements has been completed.

Two major requirements are placed on the front end by the PA. To drive the PA to an output of 100 kJ in a 1-ns pulse, the front end must produce ~1 kJ in a 1.4-ns pulse, whereas for an output of 50 kJ in a 0.25-ns pulse, the front end must deliver ~25 J in a 0.31-ns pulse.

The parameters of this conceptual design are shown in Fig. II-8. The assembly consists of an oscillator/switchout (OSC/SO) and four amplifiers, three of which have associated p-doped germanium isolators.

The boxes show the pressure and cross-sectional area of the active regions in the amplifiers. The cross-sectional areas of each p-doped germanium isolator are indicated under their respective boxes.

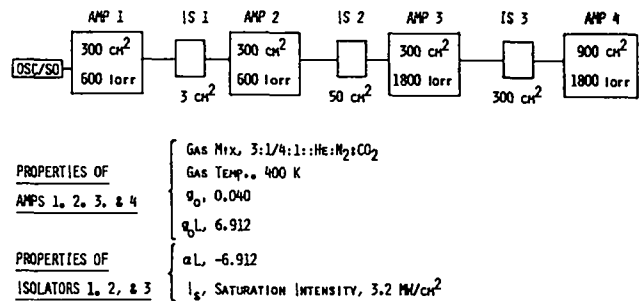


Fig. II-8.

Pressure and cross-sectional area of active region in each amplifier. The cross-sectional areas of the p-doped germanium isolators are shown under their respective boxes.

The pulse generator is a gain-switched oscillator with a smoothing tube and a cadmium telluride switch-out system. It is designed to produce a 0.5-MW pulse with 6 lines in the 10- μm band. The pulse is to have a specified pulse width and shape and is assumed to be spatially Gaussian.

Each amplifier contains a gas mixture of 3:1/4:1::He:N₂:CO₂, at a temperature of 400 K, and a gain-length product (g_0L) of 6.9. The p-doped germanium improves the contrast ratio and isolates the amplifiers to prevent prelasings. The absorption-length product (αL) is -6.9 . Thus, amplifiers and germanium isolators of the first three stages have a net small-signal gain of zero. The fourth stage is the only contributor from the front end to the system small-signal gain of $e^{6.9} \approx 10^3$.

The germanium saturation intensity has been verified experimentally to be 3.2 MW/cm², and the germanium damage threshold was taken to be 600 MW/cm². It was also assumed that the damage threshold is inversely proportional to the square root of the pulse width, although this is yet to be verified. As experimental data become available the calculations will be appropriately modified.

The calculations show that long-pulse operation requires 0.5 MW in a 13-ns pulse out of the OCS/SO. This pulse will produce a front-end output of 1.4 kJ in a 1.4-ns pulse, meeting the PA requirement mentioned above.

For short-pulse operation, the fourth amplifier will not be activated because less energy is required. The OCS/SO is expected to generate 0.5 MW in a 0.5-ns pulse. The output of the front end in this mode is 58 J in a 0.31-ns pulse, which will drive the main amplifiers to the desired 50-kg output, also mentioned above.

The contrast ratios for this conceptual design increase by 28.5 dB for energy and by 37.8 dB for power in passing through the amplifiers and saturable solid-state absorbers.

A study of the sensitivity of the PA output to OSC/SO input was conducted to determine the effects due to variations in the OCS/SO, for example, in output power, number of lines on the 10- μm band, and power distribution between lines. The results showed the long-pulse case is on a stable portion of the PA output curve. However, the short-pulse case was not as stable and requires some refinement.

A point design has evolved from this conceptual design. The point design defines the optical elements as to number, sizes, and focal lengths. In the point design the area of the fourth amplifier has been changed to 966 cm², so that associated optics will match those in the PA. The pressure has also been changed to 1677 torr, to maintain a constant area-pressure product. Thus, the stored energy remains the same. The areas of the third and fourth stages are split into three and six units, respectively. That is, the third stage consists of three amplifiers, each 100 cm² in cross-sectional area, whereas the fourth stage consists of six amplifiers, each 161 cm² in cross-sectional area.

The fourth stage will necessarily be an electron-beam device, because the rapid risetime of the gain is needed to help prevent prelasings between the PA and the fourth stage. Also, because of the pressures, both the third and fourth amplifiers of this point design are to be electron-beam devices. The first and second amplifiers, however, can be uv-preionized double-discharge devices.

Optical System Design (K. C. Jones, J. L. Munroe). The optical system described in this section is quite similar to previously presented designs, with a number of new features. Of the three basic input-optics schemes we have rejected the ring-focus geometry due to its extreme sensitivity to misalignment, and the point-focus scheme due to the larger input pulses required for the present PA design. With inputs on the order of several joules per segment it became highly impractical to form a real focus in the (unpumped) CO₂ medium and to keep energy densities below breakdown (5 to 10 J/cm²). Thus, we have elected to pursue the third alternative referred to as the narrow collimated beam configuration.

Additional factors which forced minor changes to the optical system design include:

- A 10% increase in the output beam cross-section area.
- Capability for spatially filtering each segment prior to PA input.
- Addition of one more electrode pair for a total of four.
- Additional plane mirror(s) for path-length adjustment prior to input to the PA.

- Use of a small NaCl window for the PA (as opposed to using the large window for both input and output) to minimize the possibility of retropulse damage to the large windows.

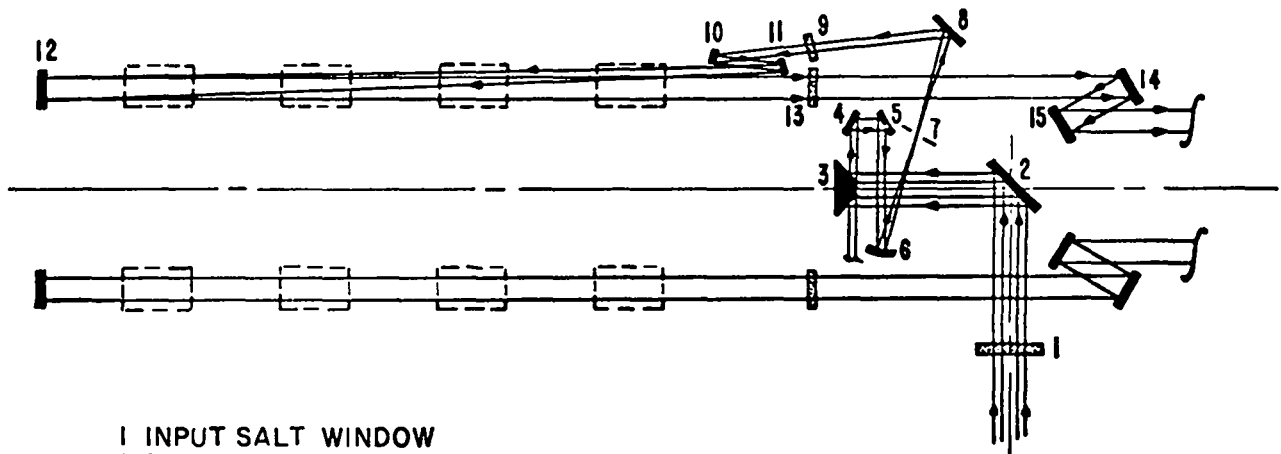
Figure II-9 illustrates the salient features of the power amplifier optical system. The input beam (either circular or annular) passes through the window (1) into the target-vacuum system space and is reflected by the plane mirror (2) to the polyhedron splitter (3). This mirror divides the beam into 12 identical segments per PA (for a total of 72). The plane mirror (4) is adjustable axially to allow equalization of the various beam paths. Adjustment range on this mirror will be large enough to allow staggering of pulses should this become desirable in the future for pulse shaping.

The concave mirror (5) focuses the flux through the spatial filter (6) that can serve simultaneously as a true spatial filter and as a field stop for both parasitic and retropulse suppression. The plane

mirror (7) directs the input pulse through a small NaCl input window (9) into the CO₂ gas medium where it is reflected by the plane mirror (9) to the convex mirror (10) designed to just slightly overfill the concave mirror (11), which collimates the pulse for a second pass through the gain regions to the output window (12). The two-mirror periscope radially translates each of the beams to reduce the size of the 12-beam array prior to entering the beam tubes to the target area.

The overlap region between the mirrors (9) and (10) is designed to provide retropulse protection for the small NaCl window (8) as well as other small elements farther from the target. The attenuation mechanism is inverse Bremsstrahlung and is based on experience gained from our TBS.

The design illustrated has very large f numbers and only small tilt angles. The aberrations introduced are exceedingly small and the system is very insensitive to minor misalignment. Note that



- 1 INPUT SALT WINDOW
- 2 TURNING FLAT
- 3 POLYHEDRON SPLITTER
- 4 85 PATH LENGTH ADJUSTMENT FLATS
- 6 FOCUS MIRROR
- 7 SPATIAL FILTER
- 8 TURNING FLAT
- 9 PA. INPUT WINDOW
- 10 FOLD FLAT
- 11 DIVERGING MIRROR
- 12 COLLIMATING MIRROR
- 13 PA. OUTPUT SALT WINDOW
- 14 & 15 PERISCOPE FLATS
- GAIN MEDIUM

Fig. II-9.
Optical schematic of Antares power amplifier.

the angles shown are not necessarily in the plane of the illustration and that some of the plane mirrors may have slight power for the purpose of balancing the very small residual aberrations. We are also actively examining the possibility of weakly focusing the beams as they exit the PA as well as of translating them radially inward to minimize the size of the target chamber.

Future efforts will concentrate on the details of the optical designs, including specification of alignment techniques, required degrees of freedom, adjustment ranges, adjustment resolution, and the location of baffles and stops. We have completed a first-order layout of the oscillator-preamplifier optical system to identify the number of required optical elements, their approximate locations, and potential alignment problems. This effort will continue.

For optical system modeling we continue to update and maintain various optical design and analysis codes, including several LASL-developed codes as well as ACCOS V, POLYPAGOS, and the University of Arizona-developed FRINGE II for interferogram reduction. Several of these programs are being modified for use with cathode-ray-tube interactive graphics, which will allow for more efficient use.

We have entered a contract with Hughes Research Laboratory to study the applicability of recent advances in the field of adaptive optics (deformable mirrors) to our laser system. Their effort will require extensive computer modeling of our optical system and should provide an opportunity for valuable design checks and suggestions for improvement. Hughes also has unique computer simulation codes for performing near-field diffraction calculations and "end-to-end" systems analyses. In addition to the Hughes contract we continue to receive excellent consulting support from the University of Arizona Optical Sciences Center.

Energy Extraction (P. N. Wolfe, H. C. Volkin, C. Knapp). To determine the optical energy and pulse shape delivered to the target by the HEGLF system, we continue to employ the coherent pulse-propagation code, described in previous reports, to model the two-pass propagation of an optical pulse through a typical sector of a PA. The initial objec-

tive of this effort was to determine a PA design that would meet Antares performance specifications. This task, essentially completed last year, identified the double-pass arrangement as preferred and provided information for project cost estimates. More recently, experimental results with the TBS and EBS have tightened constraints on Antares operating parameters. The objectives of the effort have consequently shifted to verifying acceptable performance under the new constraints and to maximizing design margins. Other new constraints have also been introduced as the overall Antares design became more detailed and subsystem interactions were identified. Two approaches have been followed in working toward these new objectives: the spectrum of PA operating parameters has been reexamined more carefully, and we have attempted to reduce uncertainties in the mathematical methods and in the values of fixed parameters in the PA code.

Most significant among the changed operating constraints is the single-pass gain-length product (g_0L) limitation of 6 that has been found necessary to prevent internal parasitic oscillations. As tentatively concluded in the previous report (LA-6834-PR), this change has forced us to abandon single-line operation for the 100-kJ, 1-ns design point. It first appeared that operating on the 9- μ m band in addition to the 10- μ m band would make up for the loss of gain, because under saturated conditions two-band operation with a common upper vibrational level may utilize $\sim 4/3$ of the inversion available on a single band. However, in reexamining the code parameters that contribute to 9- μ m gain we found, first, that our value for stimulated-emission cross section was too high, and, second, that the 9- μ m lower state (0,2^o,0) population at representative gas temperatures was not negligible as had been assumed, with the combined effect of reducing the gain on the 9- μ m band to $\sim 75\%$ of the 10- μ m value. (The revised values are in agreement with a recent measurement by Leland.) The low g_0L at 9 μ m (75% of 6) is insufficient to produce the first-pass output necessary to realize the $4/3$ factor on the second pass, unless impractically large first-pass inputs are employed. The two-band curve in Fig. II-10 shows that for 100-kJ output there is now no clear energy extraction advantage over single-band operation to

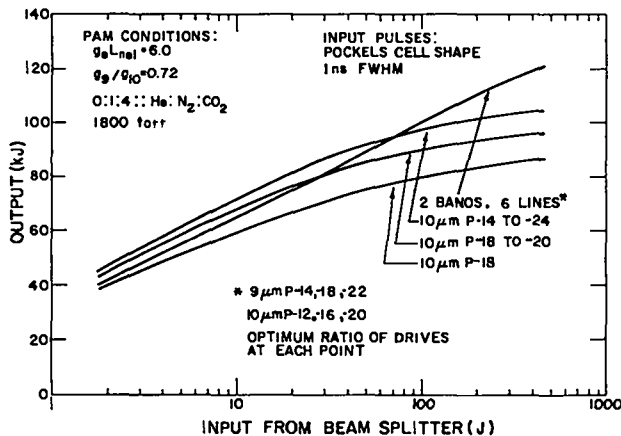


Fig. II-10.
Comparison of two-band and single-band output of power amplifier module.

justify the considerable additional complexity of a two-band front end.

This conclusion still leaves the alternative of operating with multiple rotational lines on 10 μm alone, to increase Antares output. Figure II-10 also shows output-vs-input characteristics for various numbers of lines on the 10- μm band alone. Because the gain on individual lines decreases as one moves away from P(18) and P(20), there is an optimum number of lines beyond which PA performance decreases because effective gain decreases. The optimum turns out to be rather broad, there being very little difference in performance for four or more lines. Even at optimum, however, the total drive required to produce an Antares output of 100 kJ now amounts to ~ 150 J, and the front end must supply considerably more energy than this to make up for beam splitting and shaping losses.

A somewhat simpler code, based on rate equations without coherent effects, is employed for energy extraction calculations for the TBS and EBS. To bolster confidence in both codes, several identical cases were run on both. At high saturations, excellent agreement was obtained for total extracted energy. Slight differences in output pulse shapes were noted, as expected. Also, in keeping with the nature of the coherent aspects of the PA code, this code predicted somewhat smaller outputs under small-signal conditions.

To further improve the accuracy of output calculations, the PA code was modified so that, in-

stead of generating its own input pulse (usually either Gaussian or one typical of a Pockels-cell pulse shape), it accepts the detailed pulse generated by the sister code used to calculate front-end performance. This feature was used extensively in detailing the point design described earlier.

Error Budget (J. L. Munroe).

Optical System Modeling. When system performance requirements are defined in terms of encircled energy, calculations must use this method also. Encircled energy is a far-field (Fraunhofer) diffraction calculation and can either be treated as a fast Fourier transform (FFT) problem, taking great care to avoid aliasing, or can be solved by quadrature of the diffraction integral. Both approaches have been used.

The NaCl windows effectively segment each annular aperture into 12 quasitrapezoidal, independent beams. It has been shown that this segmentation can be properly accounted for by incoherently summing the diffraction patterns for each individual segment. It has also been shown that, for encircled-energy calculations, the quasitrapezoidal aperture can be very accurately approximated by a square or a circle having the same area as the trapezoid (see Figs. II-11 and -12).

To calculate the effects of optical manufacturing error on the final wave front, we choose the

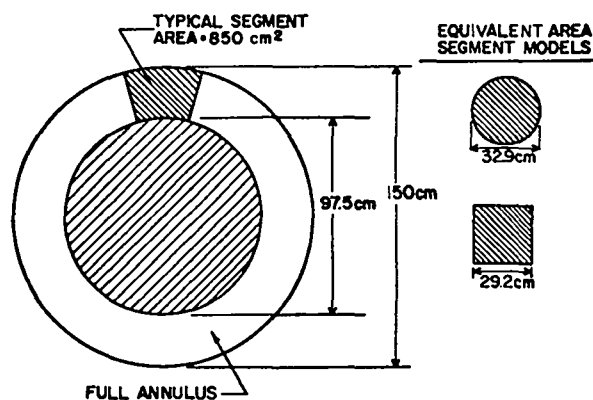


Fig. II-11.
Geometries used for comparative encircled-energy calculations to assess effect of optical manufacturing errors.

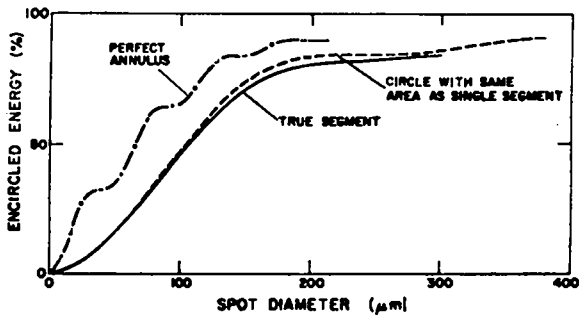


Fig. II-12.

Comparison of encircled-energy distributions for annular Antares power amplifier configuration and representations of a single segment of the annulus.

equivalent-circular-aperture model. The manufacturing error is modeled by analytically aberrating the final wave front and calculating encircled energy. Because the net wave-front error is caused by the entire optical train, there is no reason to assume any directional preference. In addition, the wave-front error should be distributed uniformly across the pupil. Balanced spherical aberration satisfies these requirements, rapidly deteriorates spot size, and maintains a reasonable analytic simplicity. Balanced spherical aberration is chosen as the analytical model for net optical manufacturing error. The results for calculated encircled energy for various amounts of root-mean-square (rms) net manufacturing error, modeled as balanced spherical aberration, are shown in Fig. II-13.

Quality of Optical Components. Reliable data are available for the optical quality of all components shown in the point design with the exception of the germanium saturable absorbers in the front end. The rms wave-front error contributions from the individual components can be root-sum-squared to calculate the net rms wave-front error. This calculational procedure is generally accepted as resulting in conservative performance predictions.

Available data and a conservative assumption for the quality of the saturable absorbers indicate that each of the 72 Antares beams will have a wave-front quality between $\lambda/14$ and $\lambda/20$ rms for $\lambda = 10.6 \mu\text{m}$. This quality is generally accepted as being diffraction-limited.

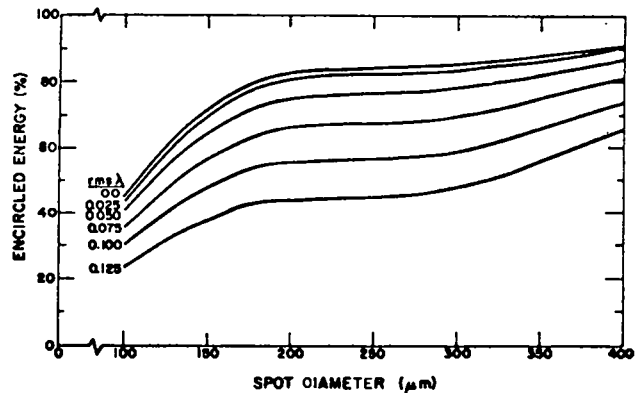


Fig. II-13.

Encircled-energy distribution for aberrated circular aperture with area of single power amplifier module segment.

Pulse Shaping (P. N. Wolfe). Antares output specifications to date have been based on short pulses of energy incident on target, typically ranging from 100 kJ in 1 ns to 50 kJ in 0.25 ns. However, in recent months, much longer pulses with controlled power-vs-time characteristics have become of interest. A typical case is a ramp rising linearly to a peak of 40 TW over an interval of 5 ns, perhaps preceded by a 10-ns "toe" of constant power of 40 MW (1000 times less than the 40-TW peak). The "toe" then contains a total energy of 400 J, whereas the main ramp contains 100 kJ. We have made a preliminary study of the feasibility of generating such a pulse in a highly saturated amplifier like the Antares PA. Since the 400-J "toe" of the pulse is more than three orders of magnitude below the Antares stored energy, it is clearly entirely within the linear, small-signal gain regime, and generating it is simply a matter of providing the appropriate constant power drive to the PA. Attention was therefore primarily put on means of generating the 100-kJ ramp.

At first thought one might suppose that a simple appropriately shaped pulse applied to the PA input would produce the desired result. However, because the PA has a small-signal gain about two orders of magnitude larger than its large-signal gain, the input pulse must rise very slowly throughout most of its duration, and then rapidly increase near the end. Unfortunately, correct output pulse shape turns out to be quite sensitive to small changes in the early

portion of the input pulse, so that simple pulse shaping, for example, with a Pockels cell, appears impractical.

A more practical input for generating the 5-ns ramp output is a series of narrow pulses of varying power, separated in time; for example, five 1-ns-wide pulses, each delayed 1 ns from the previous one, and of appropriately increasing pulse height, may be considered. Generating such a pulse train with precisely controlled delays and pulse heights is conceptually simple: a single pulse is switched out of an oscillator and is split into five beams, which are subjected to appropriate time delays and attenuations and are then recombined. The requirements on the attenuators may be relaxed by using different rotational lines for the various members of the pulse train, because the small-signal gain varies substantially from line to line.

Figure II-14 shows a calculated output pulse for such a pulse train applied to the input of the second pass of a PA. The input pulse train consists of the P-36, -32, -28, -24, and -20 lines, in that order, each

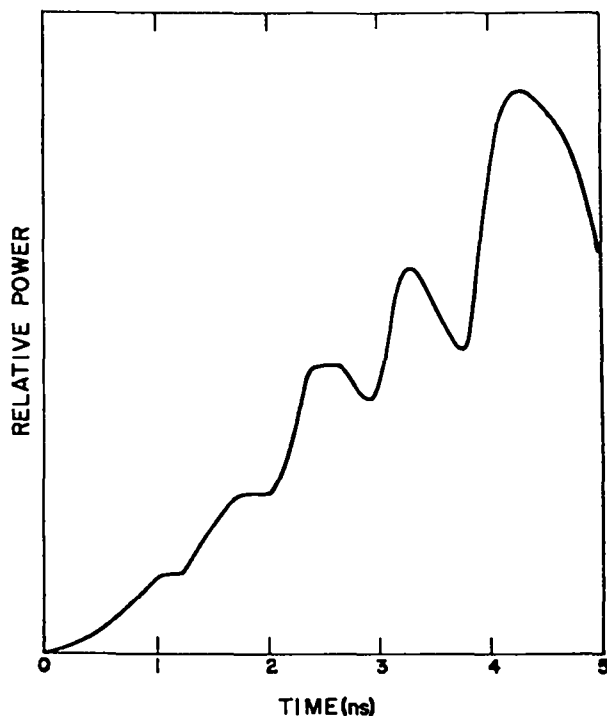


Fig. II-14.

Power amplifier output for second-pass input of five staggered P-branch lines. The input pulse train consists of P(36), P(32), P(28), and P(20).

pulse 1 ns wide and separated by 0.9 ns from its neighbors. The respective values of g_0L are 2.7, 3.6, 4.6, 5.5, and 6.0, and the respective relative pulse heights are 2, 2.5, 5, 10, and 70. The fine structure in the output pulse shape will probably not be objectionable for target effects. The ease of controlling pulse shapes by this technique appears encouraging, and we are proceeding with computer trials that model the overall Antares amplifier train.

Development of Optical Components.

NaCl Windows (W. H. Reichelt). About one hundred 45-cm-diam NaCl windows are required for Antares. At present, NaCl boules for large windows are grown by the Stockbarger process. It was soon recognized that both cost and time in any large-scale production of boules could be reduced significantly if an alternative growth process, the Kyropoulis/Czocharski process, could be scaled up to yield boules of adequate size. Under contract to LASL, Harshaw Chemical Co. has successfully grown crystals ~45 cm in diameter with excellent low-absorption characteristics ($\alpha = 6 \times 10^{-4} \text{ cm}^{-1}$). A boule grown by the Kyropoulis process is shown in Fig. II-15. These boules will subsequently be hot-forged into polycrystalline blanks for further tests and evaluation. Growing boules of such large size constitutes a breakthrough which could substantially reduce window costs for Antares.

Progress at Union Carbide Corporation's Y-12 Plant (W. H. Reichelt, D. Blevins). Union Carbide Corporation's Y-12 Plant at Oak Ridge, Tennessee, has been engaged in the development and production of mirrors for our CO₂ laser programs since 1972. Their main development areas include fixturing and mounting of mirrors for fabrication and inspection, copper plating on aluminum substrates, single-point diamond turning of optical surfaces, and optical inspection.

The University of Tennessee has been cooperating to determine the optimum support structure for the trapezoidal mirrors used in the annular Antares configuration. The SAP-IV finite-element program was used in the theoretical analysis. Typical results are shown in Figs. II-16 and -17. A comparison of the two figures indicates that the support points in Fig. II-17 cause a primarily spherical distortion whereas



Fig. II-15.

Salt crystals grown by the Kyropoulis/Czochralski method.

those in Fig. II-16 result in a far more complex distortion pattern, which would more seriously perturb the optical wave front.

In the past, electroplating of copper onto aluminum mirror substrate has been a costly process. Since then, process checks have been

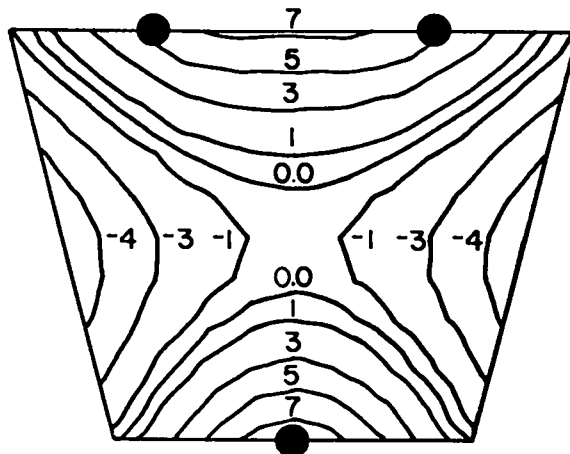


Fig. II-16.

Mirror deflections (in microinches) for indicated three-point suspension.

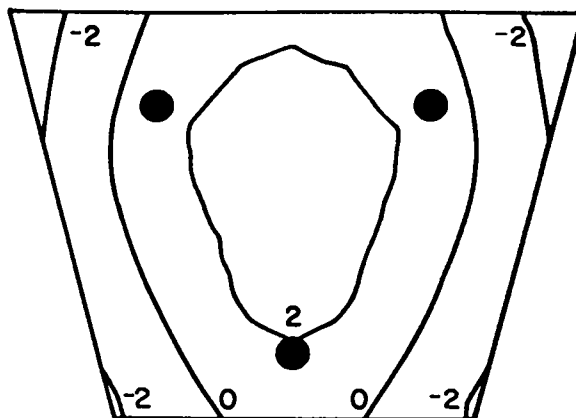
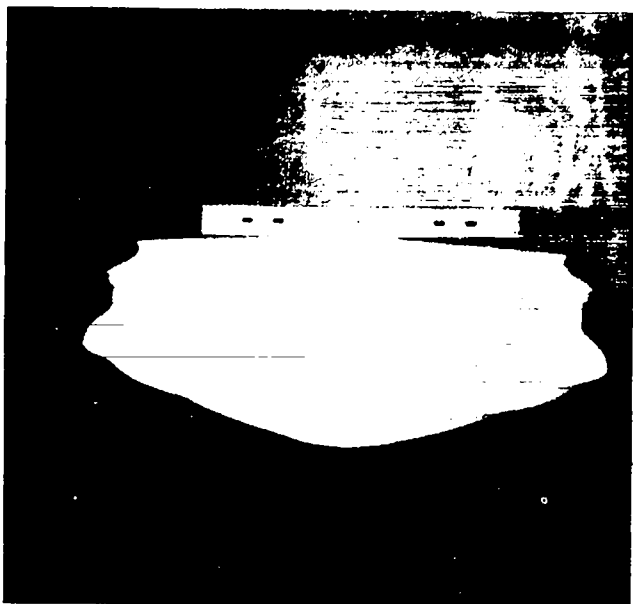


Fig. II-17.

Mirror deflections (in microinches) for indicated three-point suspension. Note reduced complexity of distortion pattern compared to Fig. II-16.

developed which ensure consistently good results. Industrial vendors who will ultimately perform the plating for Antares are being qualified by Y-12. Industrial participation will lead to a more cost-effective production.

A major breakthrough has been achieved in the diamond-turning of fast off-axis parabolas. Conventional optical fabrication techniques start out with a machined blank, which is worked to a point where the surface can be measured by optical techniques.

Once the optician can see the surface interferometrically he continues to work the surface by hand until he reaches the surface figure and finish he requires. This very time-consuming project has been made obsolete by Y-12 who succeeded in directly machining parabolic mirrors for our EBS. The mirrors are of such quality that good interferograms can be taken of their machined surfaces—a significant advancement of the state of the art. Figure II-18 shows the Excello machine used in the process, set up for simultaneously turning six paraboloids in a parent blank. An interferometer designed by the University of Arizona Optical Sciences Center is used to determine the surface figure while the parts are in the machine. Recent results indicate that the surface figure is on the order of 0.03λ rms at $10.6 \mu\text{m}$. However, the surface finish, although yielding good interferograms, still needs improving. The Optical Sciences Center has therefore developed a hand-polishing technique which smooths out the slight machining marks on the surface within a minimum of time.

The quality of the surface finish is at present limited by the runout of the lead screw on the Excello machine. A linear motor drive is being developed by Y-12 in a test bed configuration to replace the lead-screw drive. This drive is expected to ensure a better surface finish.

The optical inspection capability has been improved by the addition of a computerized inter-

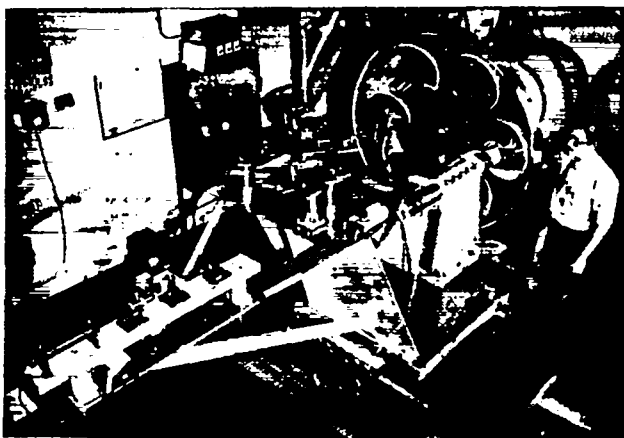


Fig. II-18.

Six parabolic mirrors in parent fixture of ex-cello machine with interferometer in place.

ferogram reduction program, FRINGE II. This program is capable of accepting interferometric data at $0.633 \mu\text{m}$ and expressing results at $10.6 \mu\text{m}$. It also yields optical path differences and aberration coefficients. All components produced for us by Y-12 are inspected interferometrically and are accompanied by the FRINGE reduced data package.

The objective of the Y-12 development program is the production of the many mirrors required for Antares at the fastest rate and lowest cost possible. The production program has been defined jointly by LASL and Y-12 and will be reviewed in a batch-prove-in process run early in 1978.

Fabrication (R. Williamson). Fabrication of 40-cm-diam NaCl windows for the EBS continues to improve. Recent measurements indicate a surface figure of 0.025λ rms at $10.6 \mu\text{m}$ to a best fit sphere with a focal length of $\sim 9 \text{ km}$. These windows were mounted in their support frames and the rms value therefore includes distortions due to mounts. Each window exhibits the classic hole-and-roll figure: convex at the edges and concave across the center.

Assembly of the 150-cm-diam annular lap ordered by LASL is proceeding at the vendor's plant. Delivery is scheduled for about September 1977. This polisher has been designed specifically for halide polishing. Temperature oscillations will be held to a minimum through careful venting, environmental control, and polishing speed control. The temperature differential between top and bottom surfaces of the pieces is a complex relationship between many parameters. We are developing a surface-temperature monitor, which will be embedded in a witness piece that closely duplicates the piece being processed.

Coatings (W. H. Reichelt). It has long been recognized that we can increase the output of the large PA by $\sim 8\%$ if we antireflection (ar)-coat the NaCl exit windows. This increased output is caused by the recovery of the Fresnel reflection at each window surface. We have developed adequate ar coatings on small samples. Recently we have entered into a contract with Optical Coatings Laboratory, Inc. (OCLI), to scale up these samples to diameters of $\sim 40 \text{ cm}$. The coatings will include TII (thallium iodide) to provide adhesion to the substrate, either in a sequence TII/NaF/ThF₄ or

TII/NaF/TII. Recent measurements on the latter coating indicate a damage threshold of $\sim 3 \text{ J/cm}^2$ for a 1.8-ns pulse at $10.6 \mu\text{m}$. Problems remaining to be resolved in the development program are whether the coated surface needs both polishing and cleaning beyond that the NaCl window received during fabrication; whether the coatings are suitable for 40-cm-diam mirrors; and whether the coatings are uniform and remain stable.

Handling the large NaCl windows during coating presents a formidable problem. Appropriate fixturing and handling techniques are therefore being investigated to minimize risks to the components. Test procedures for quality control and evaluation are also under development.

Diffraction Studies (J. E. Sollid). Preliminary experimental investigations of both near-field and far-field diffraction due to the 12 segmented windows in each of the 6 main beam lines of Antares are complete. The measurements were performed in visible light after scaling the linear dimensions.

For the near-field measurements, masks representing the scaled Antares aperture were made by chemically etching thin brass and copper foils. The near-field diffraction was photographed and measured photometrically at three distances from the window. These positions corresponded to the positions of the periscope, of the large turning flat in the beam tube, and of the target-chamber folding mirror. The smallest Fresnel number in the system, corresponding to the largest separation, is ~ 200 . If the entire annulus is to be considered rather than a single segment, the smallest Fresnel number is ~ 900 . Photometric scans show a diffraction spillover of $\sim 5\%$ at the final target turning mirror.

The far-field diffraction patterns were photographed to study the structure of the patterns. Irradiance measurements and encircled-energy measurements were also photographed.

Several conclusions were made. Phase shifts from the variable thicknesses of the salt windows will be unique for each segment. Measurements verify that the far-field irradiance distribution is the incoherent sum of the 12 single segments. As discussed earlier, it was also shown experimentally that a single quasitrapezoidal segment is well approximated by a square or circle of the same area for encircled-energy

considerations. Therefore, our segmented aperture may be reasonably approximated by the incoherent summation of 12 circular apertures of the same area as the window segments. Figure II-19 shows the measured encircled energy from a single segment and from a circular aperture of the same size. The solid lines are the calculated encircled-energy distributions.

Antares PA System (J. Jansen)

Parameter Studies (K. B. Riepe, M. Kircher).

Dependence of Gain on Cable Impedance.

Previous pumping-system analyses have assumed that the cables connecting the pumping pulsers to the laser are matched to the discharge resistance. However, because higher impedance cable, due to

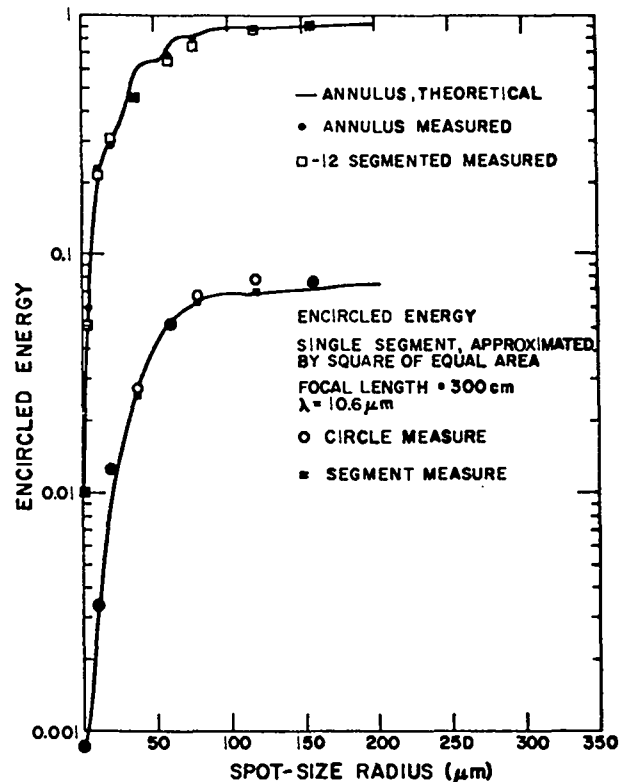


Fig. II-19.

Comparison of measured and calculated encircled energy for a single window segment and for a circular aperture of the same size.

its smaller center conductor, is both cheaper and easier to handle than lower impedance cable, we have investigated the possibility of using mismatched cables.

The following simple reasoning implies that cable mismatch will have a small effect. Pulser inductance will be $\sim 3 \mu\text{H}$. Each pulser will drive 12 anodes through 12 cables, each about 30 m long. The inductance of these 12 cables will be $0.5 \mu\text{H}$ if they have an impedance of 40Ω . If one adds this inductance to the pulser inductance, it will have an 8% effect on pulser impedance.

The laser gain was calculated for the following conditions:

Pulser charge voltage, MV	1.2
Pulser energy, kJ	200
Pulser inductance, μH	3.3
Amplifier length, m	3.2
Discharge area, cm^2	3.36×10^4
Discharge impedance per anode at 550 kV, Ω	33

The calculated g_0L for different cable impedances is shown in Fig. II-20. Clearly, cable impedance does not have a large effect. We will therefore favor the use of higher impedance cables in the 30- to $50\text{-}\Omega$ range.

Gain vs Charge Voltage. To determine how easily the gain of a PA can be controlled, we have calculated the gain as a function of charge voltage, all other parameters being held constant, including the gas discharge impedance. Both discharge

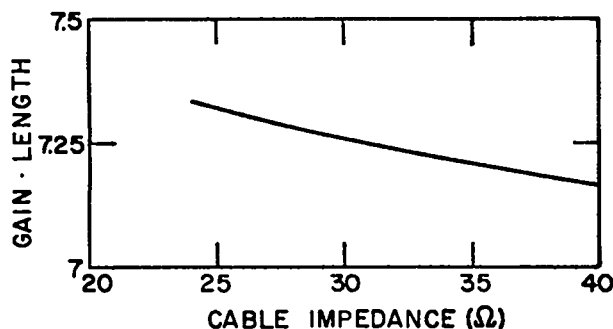


Fig. II-20.

Gain as a function of cable impedance.

voltage and current will thus decrease with decreased charge voltage. The parameters were:

Pulser capacitance, μF	0.42
Pulser inductance, μH	3.0
Amplifier length, m	3.2
Discharge area, cm^2	3.36×10^4
Discharge impedance, 550 kV, Ω	2.2

The gain as a function of charge voltage is shown in Fig. II-21. Note that the gain is almost proportional to stored energy.

Gain as a Function of Gas Impedance. It may be expected that gas impedance will vary, both between amplifiers and from shot to shot. These variations will be due primarily to variations in the electron-beam current density, caused, for example, by differences in grid bias resistors. We calculated PA gain as a function of gas impedance, for the following parameters:

Pulser charge voltage, MV	1.05
Pulser stored energy, kJ	230
Pulser inductance, μH	3.0
Amplifier length, m	3.2
Discharge area, cm^2	3.36×10^4
Cable impedance, Ω	50
Cable length, m	30
Discharge impedance	2.44, 2.75, 3.14

The variation in impedance caused the voltage to range from 512 to 573 kV, the current to range from 202 to 185 kA, but the gain variation, shown in Fig. II-22, was only 3%. This result was expected because the peak load power generated by the single-mesh network is relatively insensitive to load impedance.

Because the recombination-limited discharge current at constant electric field vs pressure (E/P) is proportional to the square root of the electron-beam current density, the specified impedance change would be due to a 50% change in electron-beam current.

Gridded Gun (G. Allen, G. Ross—Systems, Science and Software). The E-beam gun to be used in the PA Module is a cylindrical gridded cold-

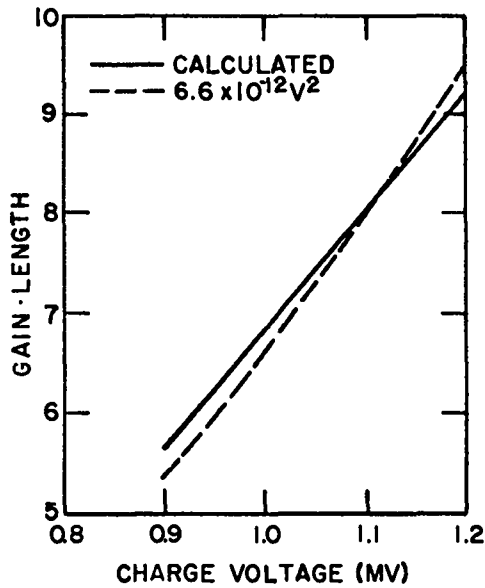


Fig. II-21.

Gain as a function of charge voltage.

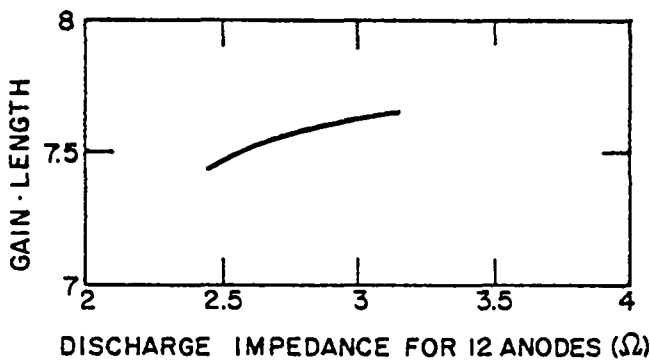


Fig. II-22.

Gain as a function of discharge impedance.

cathode type. The base-line design calls for the following parameters:

Cathode radius, m	0.39
Grid radius, m	0.53
Window radius, m	0.68
Operating voltage, kV	500
Cathode current, kA	8
Current density, mA/cm ²	50
Gun impedance, Ω	63
Grid resistor, Ω	285

Because the Systems, Science and Software (S³) study has established that the self-biased grid arrangement is effective in controlling the current density and in preventing the typical gun impedance collapse associated with a diode, the primary concerns remaining are the beam deflection due to self-generated magnetic fields, and gun emission uniformity.

Two approaches are being used to minimize the effect of the self-generated magnetic field. First, the S³ study used a rail support structure for each of the 12 cathode blades which resulted in high localized magnetic fields around each blade. However, by changing the cathode structure to a continuous cylinder, these localized magnetic fields are reduced for the same cathode current. Using the Stanford Linear Accelerator (SLAC) beam trajectory code, we modeled both the rail structure and the continuous cylinder structure; the latter showed a 50% reduction in beam deflection. An experimental program to verify this result is in progress at S³.

The second approach to minimize magnetic deflection is to use multiple gun feeds, which essentially reduces the magnetic field in any gun section by the number of feed points used. Because electrical access to the gun is limited to one end, the multiple feed concept must be accomplished through the use of a multicoaxial cable. Such a multicoaxial feed arrangement is shown in Fig. II-23. Note that, ideally, the peak magnetic field at any point along the gun is one-fourth that produced by a single-feed point. Although the configuration shown in Fig. II-23 would reduce the magnetic deflection to one-fourth of the single-feed arrangement, it is quite complex both mechanically and electrically. As a compromise, we chose the single-section center-fed

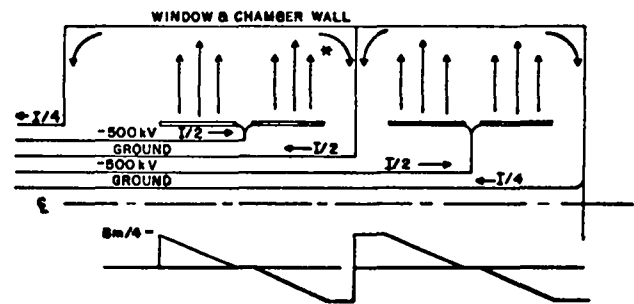


Fig. II-23.

Magnetic field distribution of multicoaxial end-fed electron-beam gun.

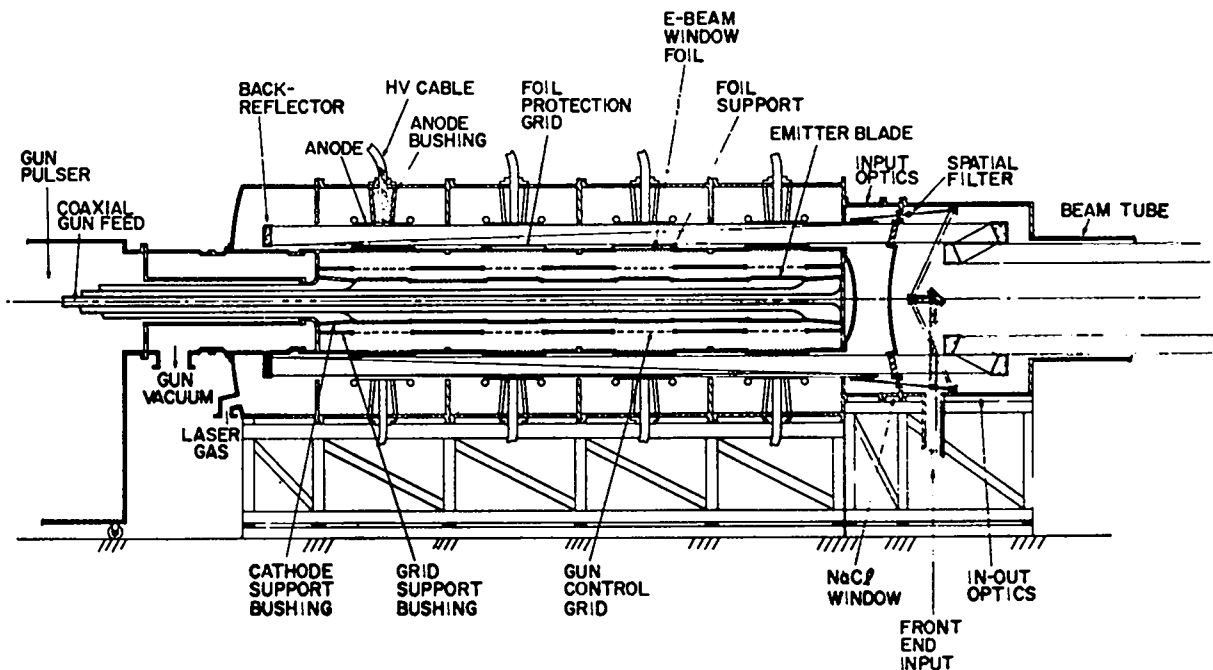


Fig. II-24.
Longitudinal section of Antares power amplifier.

arrangement shown in Fig. II-24, which reduces the magnetic deflection by 50%.

In present estimation magnetic deflection has been reduced over previously reported S^3 results by about a factor of 8: by a factor of 2 due to the cylindrical cathode structure, a factor of 2 due to the feed arrangement shown in Fig. II-24, and about a factor of 2 due to the increased gun dimensions of the PA gun over the S^3 experimental gun.

The concept of using internal pulse transformers to reduce magnetic field deflections of the electron beam has been abandoned primarily because the gun pulse-width requirement of $5 \mu s$ makes the transformer core too large to fit inside the cathode cavity. In addition, the multicoaxial feed arrangement should be equally effective, less expensive, and simpler.

Gun emission uniformity is directly related to the number of cathode-blade emission sites generated per unit length. The number of emission sites is, in turn, related to the rate of change of the electric field, and thus of the voltage (dV/dt), at the tip of the blade. Data obtained from the S^3 study show that emission sites are spaced about every 10 cm

along the blade when the applied voltage rises at 3 kV/ns. Because other values of dV/dt were not used during the S^3 study, an accurate relation between dV/dt and the number of emission sites for the type of gun being used is not available. However, one may safely assume that the number of emission sites will increase with increasing values of dV/dt similar to multichannel arc generation in rail-type spark gaps. Therefore, the PA electron-beam pulser is being designed to provide a dV/dt of 20 kV/ns.

Mechanical Design (L. Fuka, W. O. Miller, G. Ross, E. Yavornik, V. L. Zeigler).

General. A concept of a four-section PA has been developed to provide the space and support needed for the optical and high-voltage equipment and for functions required in the PA. This concept is shown in Fig. II-25. The PA will consist of four pumping sections with input and output optics sections on the forward end and with reflecting optics, high-voltage sections, and vacuum sections on the back end. Tentative assembly procedures have been considered, to be compatible with the overall concept arrangement.

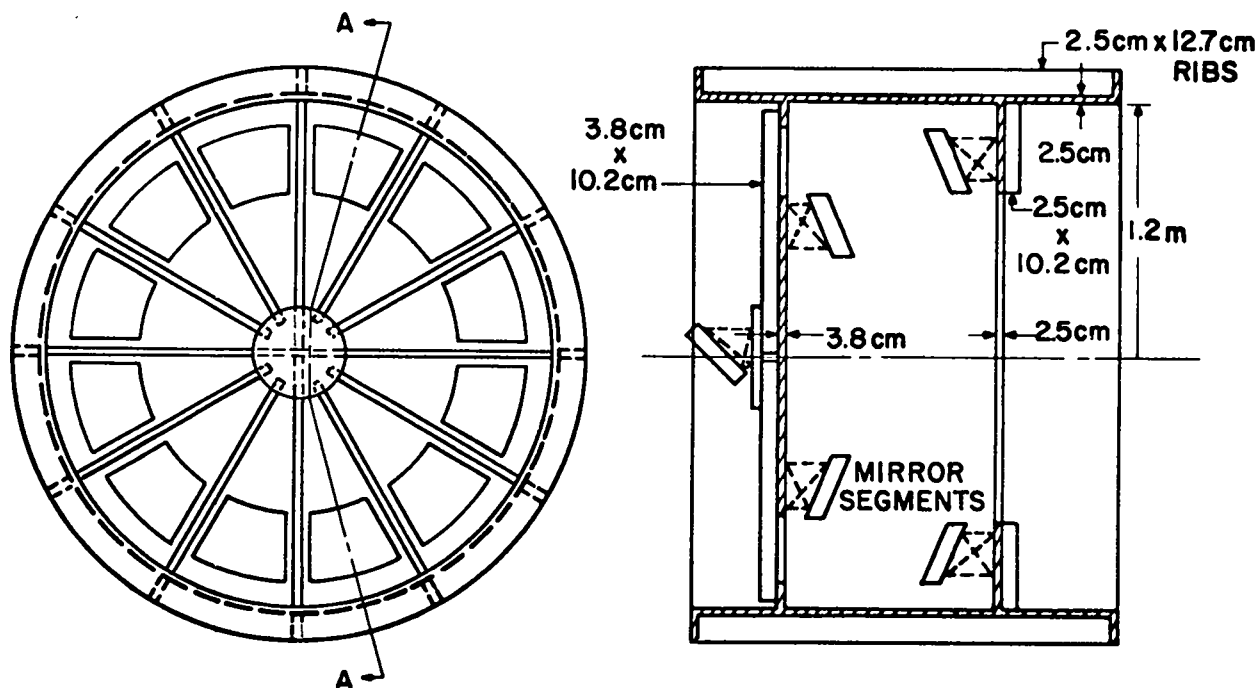


Fig. II-25.

Power amplifier support structure for input-output optics (Arrangement 1).

Vibration Analysis. A finite-element-method (FEM) analysis of the initial preliminary designs of the PA structure was performed. The lowest frequency for a support structure made of 10-in. (25.4-cm) aluminum box beam sections was ~ 75 Hz and depended on the end rotational fixity at the base of the support-stand columns. The next five higher frequencies increased with increments lying between 5 and 10 Hz.

The results of this analysis suggested modification of the initial support-stand design. A new FEM model of the support stand and PA was therefore created by using estimated weights and weight distributions of components in the PA. The lowest frequency determined for this composite structure was ~ 13 Hz and was primarily a response in the longitudinal direction, with the vertical response about 1/10 of horizontal. The second frequency was ~ 19 Hz, with its primary response in the lateral direction where the lateral translation of the mirror mounts and concentrated masses representing the electron-beam gun were in phase. The third frequency occurred at 23 Hz and was primarily a

lateral motion in which the mirror mounts moved out of phase but in which the rotations about the vertical axis were in phase. The fourth through seventh frequencies ranged from 25 to 35 Hz and were primarily longitudinal motions of the masses representing the electron-beam gun.

The stiffness matrix and estimated weights of the PA and its support structure were determined and transmitted to Mechanics Research, Inc. (MRI), Santa Monica, California, for use in their analysis of the dynamic response of the building floor supporting the PA. Their results will be used as a forcing function input to the PA support to determine the actual dynamic rotations and displacements of the optical components contained in the PA.

Pumping Chamber. A preliminary design of the four-chamber module shell has been initiated, with the length being set and material tradeoff studies nearly complete. The outer diameter and high-voltage (HV) bushing feed to the anode are currently being evaluated for HV considerations and economic tradeoffs of several arrangements. As soon

as these studies are complete, a final design for all interfaces will be started.

A concept for electron-beam gun support has been developed, leading to continuous rails mounted within the chamber (see Fig. II-26). Structural and HV analyses have determined the feasibility of this concept and its compatibility with the rest of the system.

Electron-Beam Gun Structure. The electron-beam window support has been modeled mathematically. The windows are supported on a ribbed structure that is part of the vacuum vessel. Two problems concerning the mechanical design of the electron-beam window support are how to insert and remove the electron-beam gun readily, and how to design the vessel and foil to withstand external pressure loads of 3 atm. The first problem results in concentrated bearing support loadings on the bottom edge of the electron-beam gun as it is moved in and out of the pumping chamber. During this translation the entire weight of the gun is cantilevered from the bearing support, which produces a complex stress pattern in the multiribbed window supports.

The second problem produces a compressive stress loading throughout the structure and poses buckling stability problems of the ribs and shell structure.

To address these problems, we created a finite-element model of the prototype vacuum vessel. Individual beams represent the rib structures (hibachi grill) which support the reinforced titanium foil windows. Beams were also used to simulate the longitudinal sections and circumferential flanges which were overlaid with plate elements. A static stress analysis is being performed with the computer code SAP IV. This analysis is readily extendable to the proposed Antares design by changing grid-point locations and inserting appropriate boundary conditions at the nodal points located at the ends of the model. These different boundary conditions will represent the effects of adjacent similar sections that are continuously attached to the Antares vacuum-vessel window support.

The preliminary design of the structure (as used on the prototype) is also being reviewed for materials processing to facilitate assembly. Alternatives are being investigated for economic fabrication of sizes.

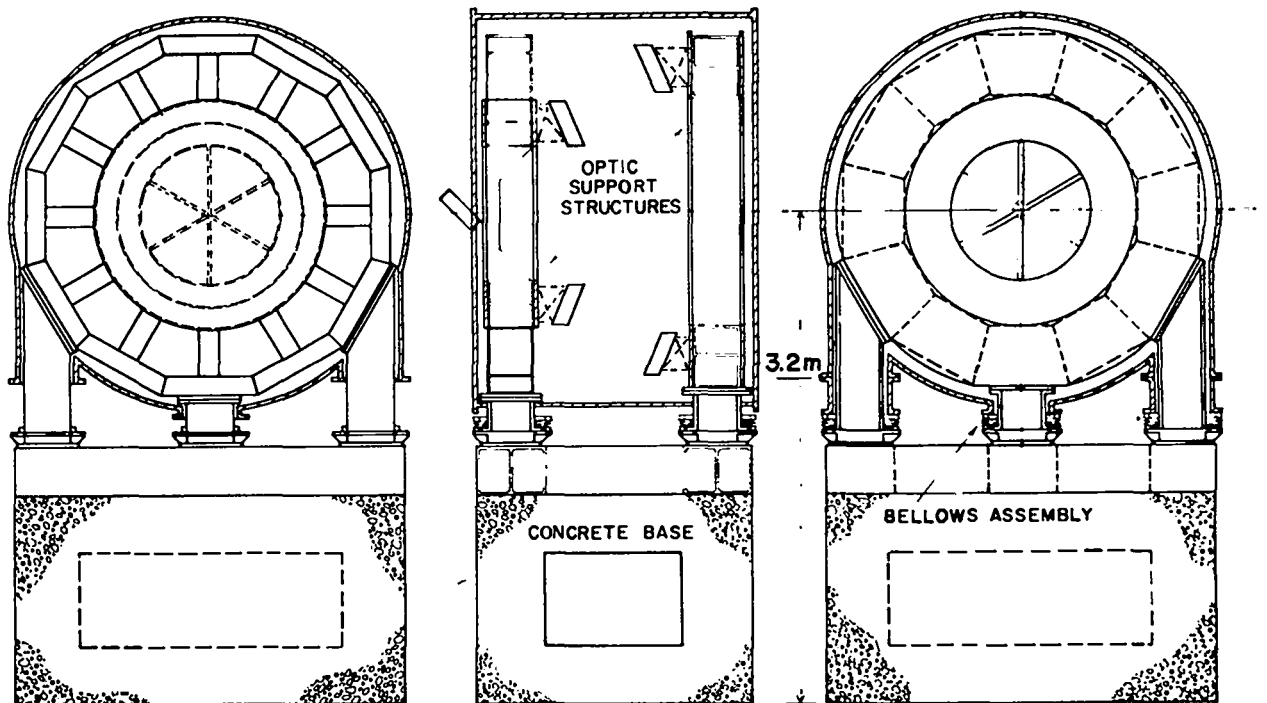


Fig. II-26.
Power amplifier support structure of input/output optics (Arrangement 2).

PA for Optical Support Structure. Preliminary design studies have been completed for two PA optical support structural arrangements. The first arrangement, shown Fig. II-25, is composed of transverse plates integrally mounted to the PA shell structure. Figure II-26 depicts the second arrangement where the optical support structure is secured directly to the floor of the laser hall. Presently, both concepts are undergoing continuing analysis and design because it is possible that the PA may require both concepts to satisfy the diverse mirror mounting requirements.

Making the optical support structure an integral part of the PA results in a simple, relatively inexpensive structural arrangement for mounting the optics. The small mirror segments which are close to the shell are best suited to this form of support. Chief areas of concern in such a support arrangement are:

- mirror movement due to support-structure distortions (creep) under shell pressure loads,
- a low natural frequency of the optical support structure stemming from low flexural rigidity of the shell, and
- larger dynamic beam motion due to low-frequency bending modes within the PA structure and support frame.

Preliminary structural analyses indicate that sufficient rigidity can be achieved in the shell and transverse mounting plates through simple rib reinforcements (Fig. II-25). These ribs will ensure that the internal plate structure will not resonate in the low-frequency range (<50 Hz). Although secondary plate deflections (warping) are expected to be within acceptable limits, this assumption must be confirmed with a rigorous structural analysis using finite-element methods. The preliminary analysis, which provided initial plate sizes, is the first step in employing this method.

The Antares model is being updated to assess the effect of foundation motion on the PA and other critical assemblies. These data, in the form of base acceleration inputs, are critical to our structural response analyses of the optical support structures. In particular, the PA, with the integrally supported optical structure, is massive ($\sim 40\,000$ kg), making it reasonable to expect a low first-vibration mode (≤ 20 Hz). Structural bending modes are likely to be ex-

cited in this frequency range and would contribute significantly to the target dynamic error. Significant structural changes have been introduced to the foundation design beneath the PA for isolation of vibration sources. These changes are expected to reduce the base acceleration to negligible levels; this reduction is of major importance.

PA shell penetrations to accommodate independently mounted optical support structures introduce added complexity and cost. However, the supported mass is comparatively small and the structural stiffness is essentially unchanged. Consequently, the first vibration mode is much higher. As shown in Fig. II-26, an optical ring mount of sandwich construction is supported on three short pedestals which, in turn, are mounted to a large concrete base. The composite ring construction was selected to achieve high ring bending stiffness. The pedestal support lengths were minimized to stiffen the axial vibration mode. The fundamental mode is >40 Hz, well above the lowest frequency expected for the PA structure.

We recently measured the vibrations on the EBS floor and optical support stands, and reviewed these results for their general applicability to Antares. They typify responses of various structural stands and will be useful in interpreting the Antares vibration predictions discussed above. An example is shown in Fig. II-27 where structural response to the low-frequency random vibration is evident. As mentioned earlier, the magnitude of the structural response can be reduced by achieving a first structural mode of higher frequency, preferably above 40 Hz.

Bushing Design (PA System) (R. Lindstrand).

The bushings are being designed in a sequential manner. The initial anode and gun bushings have been developed for the prototype system. Experience gained will then be used to obtain an improved design for Antares.

Gun bushing designs have been modeled in a small-scale test fixture. In the fixture, individual sections from the entire graded ring vacuum bushing may be tested. Tests have been conducted to determine the breakdown voltage for inner and outer bushing surfaces. Several configurations were examined for simultaneous electrical and

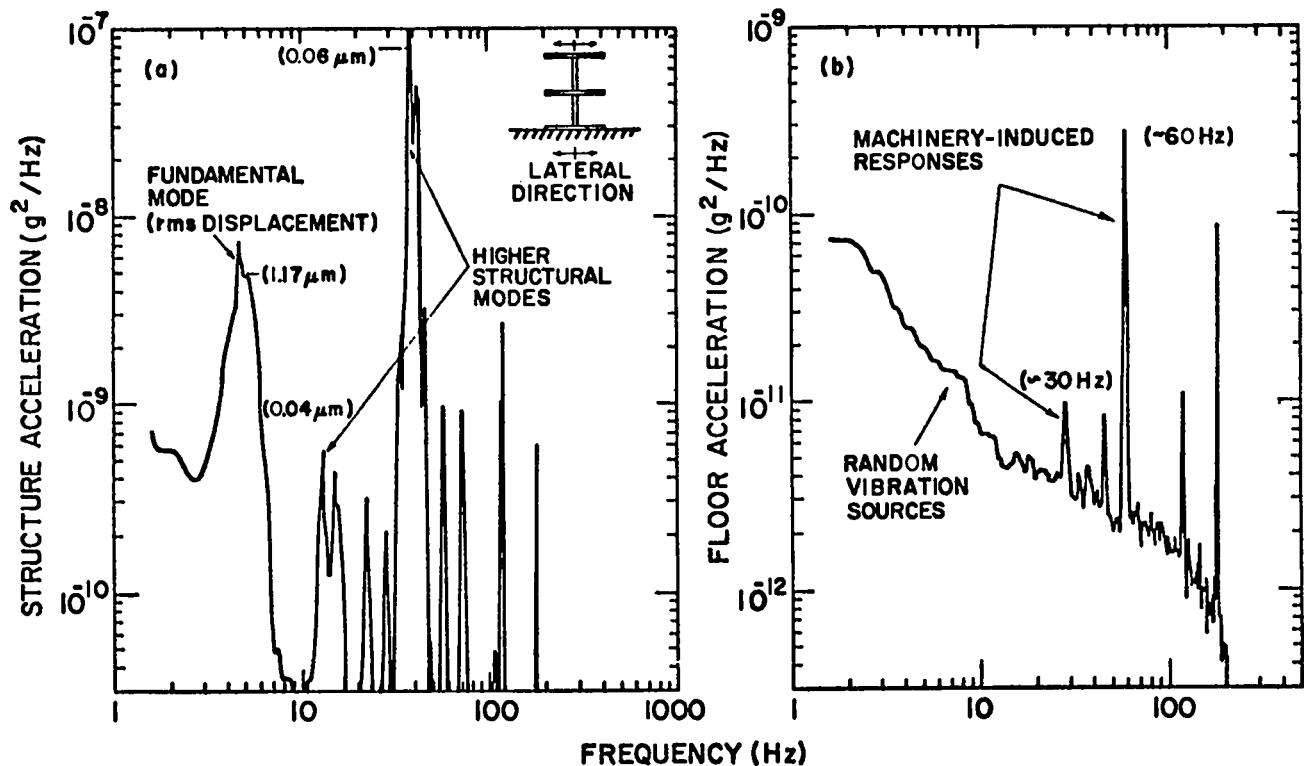


Fig. II-27.

Structural acceleration response and base accelerations for EBS optical support stands evaluated for Antares applicability.

mechanical strength. Results indicate that the chosen bushing design will withstand twice the electrical operating stress of 50 kV/section. In addition, the prototype grid-to-gun cable termination has been tested successfully to levels 50% above operating voltage.

To reduce material and machining costs for the gun bushing, an attempt is being made to develop a straight vacuum bushing. Unlike the graded ring vacuum bushing, the straight bushing does not provide uniform field grading. For such a design, high-voltage breakdown typically occurs at the common intersection of bushing, vacuum, and negative electrode. Experiments attempting to reduce the stress at the intersection by shielding are under way. Two designs have been tested which achieve a 20 to 30% safety margin at maximum voltage. The goal is to achieve at least a 50% margin.

The anode bushing developed for the prototype is ~ 60 cm long, contains water, and uses an ungraded

cable termination. Water was chosen initially as a medium because of its high dielectric constant relative to the cable insulation. In addition, the water used has a typical resistivity of $50 \text{ k}\Omega \text{ cm}$ to provide grading of the axial electric fields. Such bushings and cable terminations have been tested to peak voltages in excess of 750 kV.

Because of maintenance problems, the anode bushings for Antares will preferably not involve liquids such as water or oil. A gas-filled bushing utilizing a graded cable termination has been tested and found unsatisfactory. The grading was accomplished by using the outer semiconducting layer of the cable. Nonuniformities in the carbon-loaded polyethylene lead to voltage breakdown along the surface of the cable. Other designs now being considered involve solid dielectric grading sleeves for the cable and/or external field-shaping structures.

A LASL computer program for electrostatic field calculations has been used extensively to evaluate

designs of various bushings. When combined with experimental data, reasonably accurate performance predictions of proposed bushing designs are possible. Numerous subsections of the prototype underwent such analysis prior to assembly. Currently, the computer is being used to aid in the development of a straight vacuum bushing and of a nonliquid-filled anode bushing.

Energy Storage System

Gas Pulsar Design and Development (K. B. Riepe). The gas pulser circuit was described in the last progress report (LA-6834-PR). Briefly, it is a matched single-mesh inductance capacitance (LC) circuit, the capacitor being a Marx generator and the inductance being the internal inductance of the Marx. The Marx is a double-folded design, shown in Fig. II-28, which will have an inductance of $\sim 3 \mu\text{H}$ for a 1.2-MV open-circuit voltage. A prototype of this circuit will be built for component development and reliability testing, and will be operated into a dummy load.

The capacitor chosen for the prototype design is the 2.8- μF , 60-kV unit which has been tested at LASL in the Scyllac facility. Three of these units in parallel, with 20-series stages, provide 300 kJ at 1.2 MV. One of these Marx generators will drive 12 anodes with energy to spare.

The capacitors will be mounted in racks. Because we will be using a plus-minus charging circuit, a rack will contain six capacitors (Fig. II-29). The racks will be suspended from each other by insulating rods.

The short-circuit current in this Marx generator is $\sim 400 \text{ kA}$, with a total charge transfer of 6 C, assuming a circuit quality factor Q of 20. Normal discharge current is $\sim 200 \text{ kA}$, with charge transfer of 1 C. We have ordered spark gaps from three vendors for qualification testing. (The test system is described below.)

We have studied a few aspects of the fault protection problems. There are two cases to consider: overvoltage due to high impedance in the discharge, and arcs that are not preceded by a significant overvoltage. It is presumed that a significant overvoltage will lead to electrical breakdown somewhere, most likely in the discharge chamber.

An overvoltage will be caused by high impedance in the discharge due to low electron-beam current. This low may either occur during the discharge pulse or the electron beam may not have turned on at all. If the gas pulser is fired without the electron gun on, the cable voltage will ring up to twice the

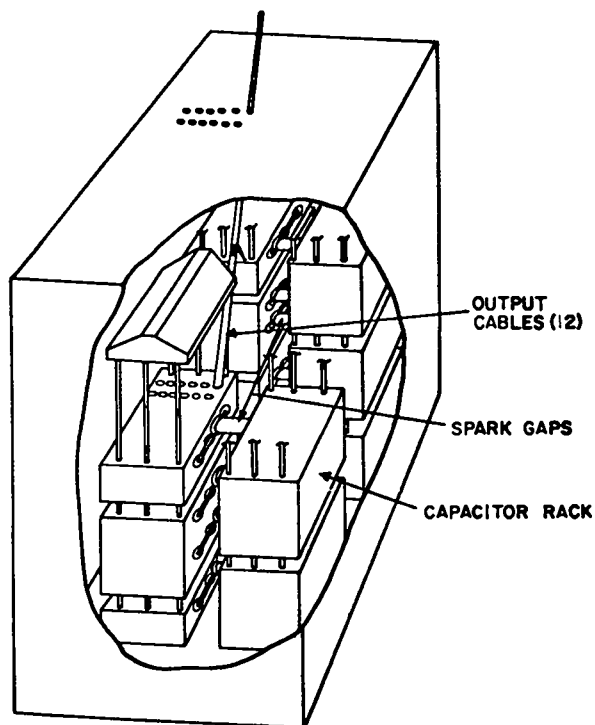


Fig. II-28.
Marx pulse generator.

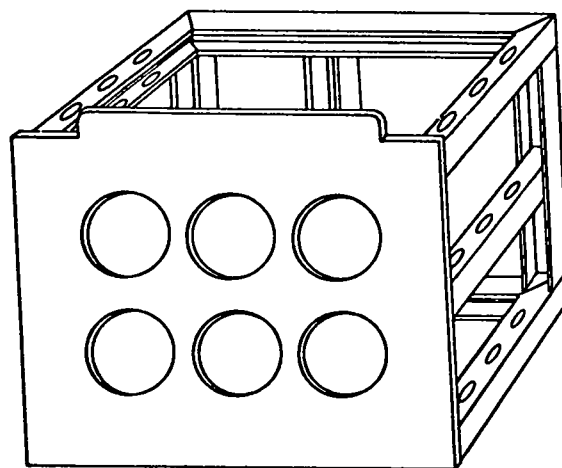


Fig. II-29.
Capacitor rack.

pulsar charge voltage, for example, 2 MV, in a time given approximately by

$$T = \pi\sqrt{LC},$$

where L is the pulser inductance and C is the cable capacitance. Assuming twelve 50- Ω cables, ~ 30 m long, this time is $\sim 1 \mu\text{s}$. The time to 0.5 MV is then $\sim 0.25 \mu\text{s}$. It seems possible in this case to use either an active (triggered) or a passive (self-breakdown) diverter gap to reduce the voltage to a safe level. If the electron beam goes off during the discharge pulse, it is expected that the impedance will change by a significant factor in $\sim 0.25 \mu\text{s}$. This would cause the cable voltage to nearly double. It is again possible that an active diverter system could sense the fault and trigger a spark gap on this time scale, but a passive system is probably better. This system would have to be located at the discharge chamber rather than at the pulser because by the time the overvoltage wave reaches the pulser, the voltage at the load may be up to 1 MV. A passive diverter system, namely a high-pressure point-plane spark gap, has been in operation on the EBS for a year. Laboratory tests had shown that this gap broke down in 50 ns with a 20% overvoltage. In practice, it has successfully protected against overvoltage.

In the event of an arc in the discharge chamber, the voltage will drop very quickly, most likely in less than 100 ns. This time holds if the voltage drop is due to a diverter gap firing. Because the pulser inductance corresponds to a high impedance on this time scale, the voltage wave in the cables will reflect from the pulser and put full voltage reversal on the cables and terminations. Cables and terminations will have to be tested to determine the effect of this voltage reversal. If it will reduce cable life significantly, two possibilities exist to prevent the reversal. One is a series resistor at the load end of each cable. A 12- Ω resistor will reduce the fast reversal of ~ 145 kV, but requires 765-kV operating voltage on the cable and 30% additional energy stored in the pulser to reach the same gain. Less resistance requires lower operating voltage but gives higher reversal. Another possibility is to utilize the polarity dependence of the point-plane high-pressure gap. In air at 60 psia, the breakdown voltage is almost two times higher for a negative

point than for a positive point. A series resistor in the Marx generator will probably still be desirable to damp ringing in the Marx.

Experiments are being designed to determine the effect of voltage reversal on cable life.

Electron-Gun Pulsar Design and Development (G. Allen). Three electron-beam pulser configurations have been considered, each with a set of advantages and disadvantages. The primary factors affecting the selection of a suitable electron-beam pulser are given in Table II-II.

Of the three pulser arrangements considered, the high-voltage PFN appears to be the most attractive. A suitable choice for such a PFN is a two-section Type-A Guillemin network as shown in Fig. II-30.

The values given are for a 5- μs (at 90% peak) pulse into a 63- Ω load. The Type-A network offers the advantage that the series inductance, L1, can be used for pulse-shaping. This allows the Marx generator, C1, to be highly inductive and of simple construction.

A computer simulation of such a network was run with the circuit analysis code NETTWO. The network model used is shown in Fig. II-31.

The capacitor C4 (dotted in Fig. II-31) may be used to achieve a high dV/dt without the use of a peaking gap. With $C4 = C3$, $dV/dt = 20$ kV/ns. However, because the L2-C4 section must withstand a peak voltage of ~ 1 MV, a peaking gap may be more practical. The peak voltage across the pulse-shaping section L3-C2 is only 250 kV, thus C2 may be more easily constructed.

A typical NETTWO load-voltage waveform based on our model is shown in Fig. II-32. Although the rise and fall times are not very fast, the pulse is sufficiently well shaped to completely envelop the gas pulser waveform at the 90% peak voltage points. Also, with the addition of a peaking gap (or C4) the rate of voltage change will be quite sufficient to ensure good gun ignition. In addition, the low-energy requirements of the PFN (25 kJ vs 95 kJ for resistively discharged Marx) reduce the cost of both the pulser and the charging supplies.

The major uncertainty remaining in the design of the gas pulser is the possibility of a pumping-chamber arc due to decreased electron-beam ionization range as the electron-beam pulser voltage falls

TABLE II-II

FACTORS AFFECTING SELECTION OF ELECTRON BEAM PULSER

	<u>Advantages</u>	<u>Disadvantages</u>
Rundown Marx	Fast risetime. 500 kV peak voltage. Simple construction.	Diverter gap required. Large energy storage required (95 kJ for 10% droop). ^a
Low-voltage PFN with pulse transformer	Air-insulated PFN. Pulse transformer saturation could be used instead of a diverter gap.	Expensive (transformer alone ≈\$25 k). Peaking gap required. Very low impedance PFN required (≈0.15 Ω).
High-voltage PFN	Diverter gap may be eliminated. ^b Relatively low energy storage required (≈25 kJ).	1-MV PFN open-circuit voltage to achieve 500 kV at cathode. More complex than simple Marx generator.

^aThis also affects the size of the charging supply.

^bDepends on required voltage rate-of-fall.

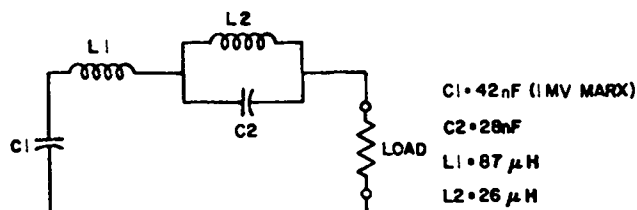
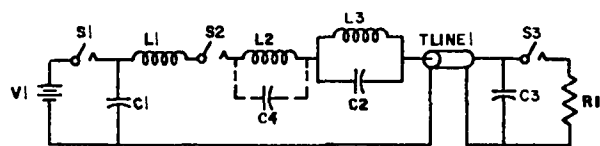


Fig. II-30.

Two-section, Type-A Guillemin pulse-forming network.



- C1 = 1 MV MARX
- L1 = MARX INDUCTANCE
- L2 = ADDED SERIES INDUCTANCE
- L1 L2 = TOTAL SERIES INDUCTANCE (87 μH)
- TLINE = 50 Ω, 14-m TRANSMISSION LINE
- C3 = GUN CAPACITANCE
- R1 = GUN IMPEDANCE
- S3 = VOLTAGE CONTROLLED SWITCH TO SIMULATE GUN IGNITION

Fig. II-31.

NETTWO model of two-section Guillemin Type-A pulser.

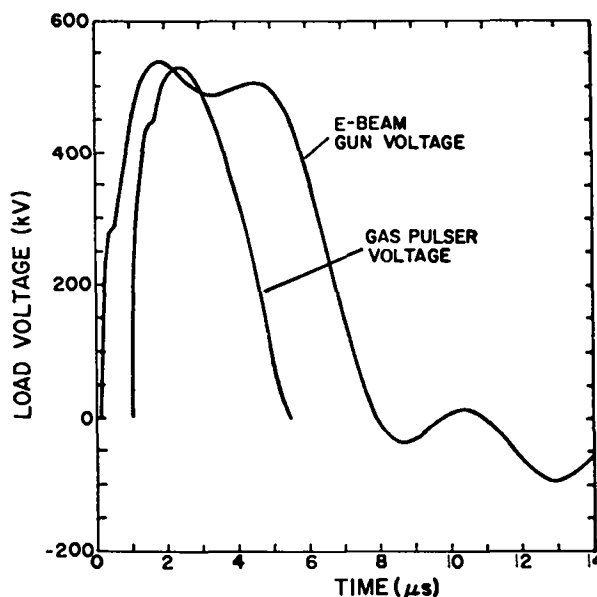


Fig. II-32.

Comparison of gas pulser and electron-beam pulser voltages.

off. However, because the gas pulser voltage is passing through zero when the electron-beam voltage begins to drop below 90% peak, a pumping-chamber arc is considered a remote possibility. Nonetheless, an experiment has been designed using the test vehicle to determine the effect of electron-beam pulser fall time on pumping-chamber arcs.

Component Testing and Evaluation (K. J. Bickford). Electrical testing of high-voltage components of the energy storage system has begun. The internal swaging of the 2.8- μ F, 60-kV capacitors has been tested at high currents because it was thought that this swaging might deteriorate at currents above 150 kA.

The capacitor tests have been implemented as follows. Two capacitors, isolated by a triggered spark gap, are slowly charged to ± 50 kV with a circuit inductance of 300 nH. The spark gap is triggered and the system rings down with a peak current of 200 kA. This is repeated with a repetition interval of 35 s.

During these tests the spark gap is also heavily stressed by the 200-kA peak currents and 100-kV holdoff requirements. Heavy-metal alloys for the electrode material (for example, Elkonite) are reasonably effective in reducing surface erosion and cracking, although at higher currents these metals could be less effective. Efforts have been initiated to obtain a metallurgically superior heavy metal.

During the capacitor tests we discovered that some problems exist in the fabrication of high-current connections between two metal surfaces. Efforts to develop more reliable current joint technology are continuing.

Special high-current spark gaps are on order from three vendors for evaluation and development. Testing will commence upon receipt, probably in a few weeks. The test system will be similar to that of the capacitor test, with the exception that eight capacitors will be used to provide up to 400-kA peak.

A testing program for evaluating high-voltage and energy effects on two types of commercially available solid resistors is under way.

Target System (V. L. Zeigler)

Focus and System Layout (V. L. Zeigler). The layout of the target system optics is shown in Fig. II-33. The six segmented annular beams from the PAs enter the target area roughly parallel to each other and are turned by six turning mirrors so that three beams enter the target chamber from each end. Each of the six beams is then reflected from a turning-mirror array, and then from a focusing-mirror array, as illustrated in Fig. II-34. The focusing arrangement is such that pairs of beams approaching the target from opposite directions lie in the same plane; the three pairs of beams are then separated by 120° around the longitudinal axis of the target chamber.

The aggregate of beams, mirrors, and supporting structure (space frame) is shown in Fig. II-35. This space frame is a separate entity from the target chamber and can be removed from the chamber for mirror replacement or other maintenance work.

Mirror Cells (D. Blevins).

Mirrors. It was decided to use solid aluminum-alloy substrates with copper-plated faces. A typical mirror is shown in Fig. II-36. These mirrors weigh

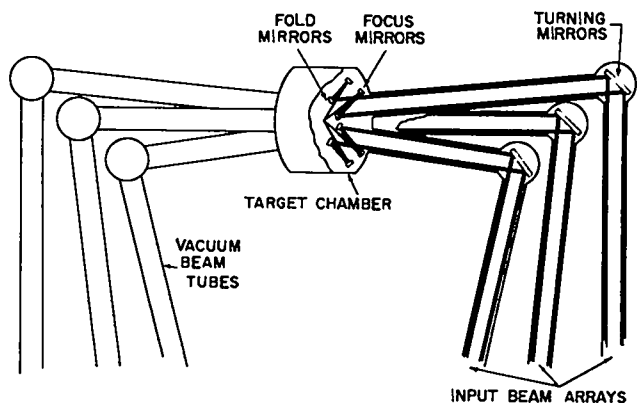


Fig. II-33.
Layout of optics in Antares target area.

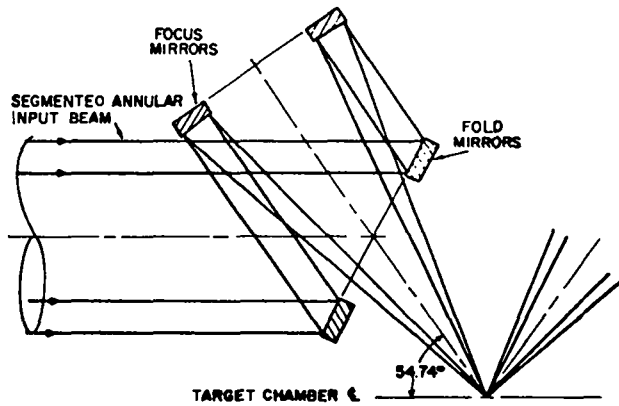


Fig. II-34.

Antares target focusing arrangement (one beam).

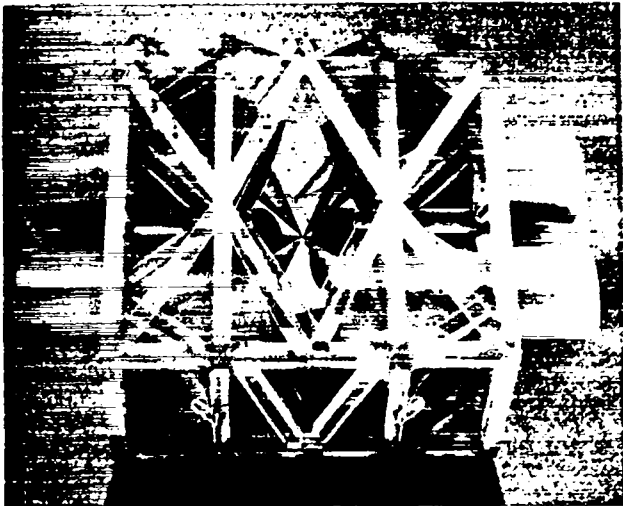


Fig. II-35.

Antares target focusing system and space frame.

~23 kg (50 lb) and have a diameter-to-thickness ratio of ~5.

Alloys being considered for substrates are 5456, 6061, and 2219. Prime requirements are dimensional stability, ease of plating, strength, and weldability. Selection of materials will be based on a materials stability test program that has been initiated by contract with Southwest Research Institute, San Antonio, Texas. In addition to the aluminum alloys, they will investigate the temporal dimensional stability of several copper alloys and of 304 L

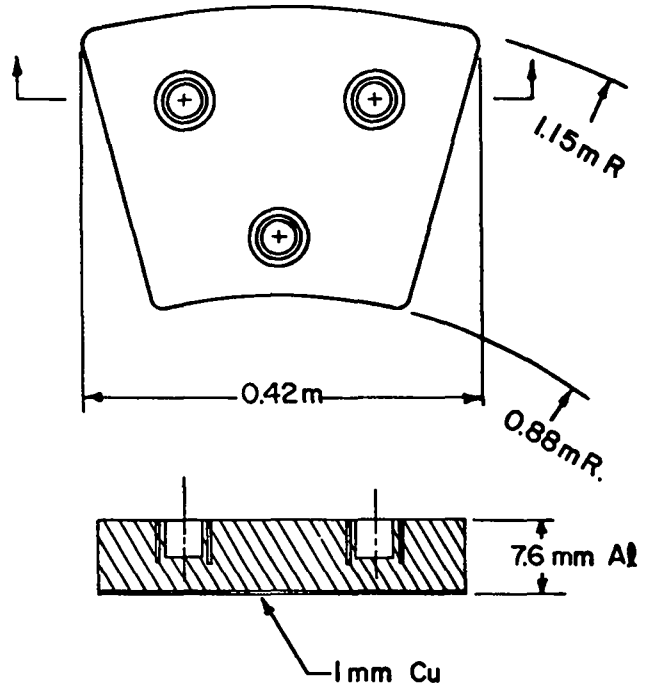


Fig. II-36.

Typical copper-plated solid aluminum mirror.

stainless steel. They have procured the necessary materials and equipment and are machining blanks and plating some coupons.

Preliminary finite-element analyses of a typical mirror indicate that a three-point kinematic support registering in pockets in the mirror will support the mirror with deflections of $0.04 \mu\text{m}$ or less.

Hardware for a kinematic mount for a test mirror has been designed and is being procured. A support test mirror is also being procured. With this test gear, the mirror support system will be tested at various attitudes, and mirror distortion will be measured. The ability of the kinematic support system to absorb large mounting-system errors without distorting the mirrors will also be evaluated.

Mirror Positioner. Several mirrors in each of the 72 beam lines will be steered remotely with individual mirror positioners. A prototype positioner has been designed and procurement has been initiated (Fig. II-37). It consists of a fixed base plate, a tiltable face plate pivoting on a central gimbal bearing, and two linear actuators that tilt the face plate

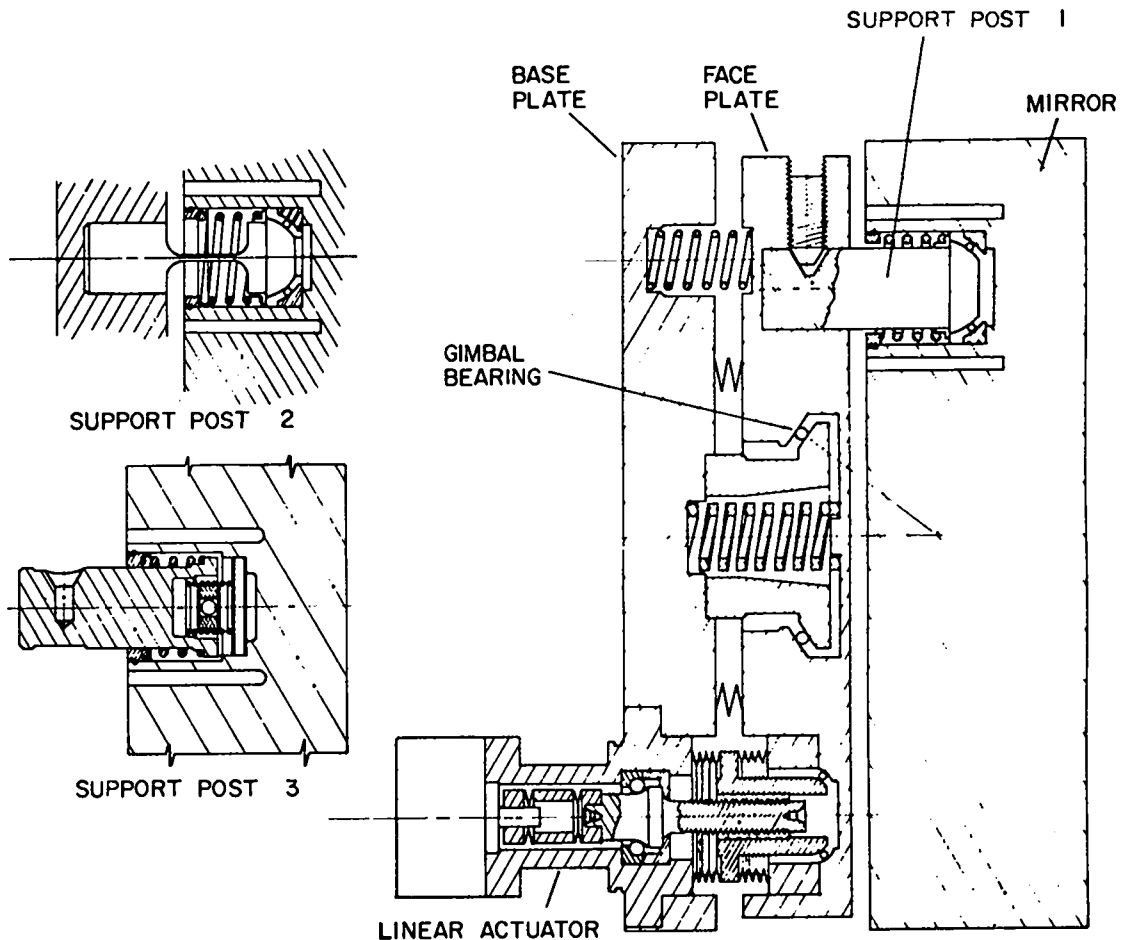


Fig. II-37.
Antares mirror positioner.

about orthogonal axes. Two different linear actuators have been designed and will be developed. One utilizes a 1000-step-per-revolution stepping motor driving a simple screw and nut. The other incorporates an inexpensive 200-step-per-revolution stepping motor driving a new type of ball screw and nut. This new ball screw will provide an effective lead of $20\ \mu\text{m}$. With the ball-screw actuator, tilts of $1\ \mu\text{rad}$ per motor step are expected compared to $10\ \mu\text{rad}$ with the simple screw.

Ten-microrad steps provide adequate steering for all but final turning mirrors, which require $1\text{-}\mu\text{rad}$ steps.

Vibration Analysis (L. Fuka). One of the most important actions in beam alignment is the

minimization of the dynamic response of critical optical components to vibrations caused by external sources. These sources include compressors, motors, and miscellaneous background seismic noise. In addition to minimizing the vibrations from the first two sources by proper vibration isolation techniques, it is important to design the optical components and their supports in such a way that the natural frequencies of the supports are as far away from the exciting vibration frequencies (preferably higher) as possible. To do this, a dynamic analysis is being performed to determine the frequencies and mode shapes of the target system space frame (Fig. II-35). These frequencies and mode shapes will be used to modify these structural members which may

adversely affect the frequencies of the overall space-frame structure.

The stiffness matrix of the space-frame structure was determined and will be provided to Mechanics Research, Inc. (MRI) for their dynamic analysis of the floor structure. Using these data in their dynamic model, MRI will determine the forcing function to the base of the space-frame structure. This forcing function will then be used with our analytical model to determine the dynamic response of the optical components mounted in the space-frame structure.

Target Vacuum System (N. G. Wilson). The target vacuum system will be contracted from Department of Energy (DOE) as a single package including design engineering, fabrication, erection, and installation of all equipment required to provide an operational vacuum system. The DOE Project Engineer will work closely with LASL. The target chamber, turning-mirror chambers, beam tubes, mechanical and electrical equipment, and civil construction required for the complete installation are the principal elements of the contract. Antares is configured around a vacuum-system concept that utilizes cryogenic high-vacuum pumping as the principal pumping mechanism, with additional turbomolecular pumping of noncondensibles and Roots blower/mechanical-pump roughing systems. A draft of design criteria for the system has been completed and reviewed internally.

Control System (B. G. Strait)

Hardware.

PA Controls (M. Thuot). The PA will be controlled by three subsystems: the mirror-positioning system, the anode current monitor, and the vacuum-gas controller.

The function of the anode current monitor is to collect data from the 48 anodes in the PA and either present the data locally as a plot on a CRT terminal or send the information to the control room. The anode current information will be transmitted by analog fiber-optic links to the local screen room. There the data will be captured at a 12-MHz rate and will undergo time-base expansion by a serial

analog memory circuit which is now being developed. A microprocessor controller will operate an analog-to-digital converter to digitize the time-expanded data and format them for display or transmission.

The vacuum-gas controller will be a table-driven microcomputer control system. It will operate with an interactive CRT display to allow the operator to check out any system component or to automatically arrive at a commanded vacuum or gas pressure level. Full operational and safety interlocks will be incorporated in the system.

A basic component of the Antares distributed task microcomputer network is the communication and data fiber-optic links. The control system will be subjected to high-level electromagnetic interference (EMI) generated by the pulse-power supplies. The network microcomputers are locally shielded and grounded to a distributed ground mesh. This mesh provides local common grounds, but cannot ensure a common ground for the facility. Communication to various areas of the facility must be done through a nonconductive, EMI-immune medium: fiber optics. In the Antares control system, fiber optics will be used for three purposes: digital asynchronous communication between computers, analog data acquisition, and control of elements in various subsystems, for example, valves and contactors.

The realization of the first function was reported in LA-6834-PR. Recently, we have improved the digital data communication links through the use of a new pure silica cable. This cable has low attenuation, ~ 100 dB/km, and is very rugged. The average operating length limit with this cable and our fiber-optic transceiver is 86 m. We have tested this type of fiber-optic link for 10^{10} bits with no errors at the design-length limit and 38.4 kbps.

The second function, analog data transmission, when tested over a 17-dB current range, was linear within a few per cent. The length limit for analog transmission is ~ 30 m where the full dynamic range is important. The signal bandwidth is 10 MHz. Fifteen of these units have been installed in the Antares prototype where they are working well in the severe EMI environment and have rejected common-mode voltages up to 640 kV.

The third function, remote control, has been accomplished with a solid-state relay which has a

fiber-optic input. This relay is powered by the circuit being controlled; no external power supply is required. The relay, operating on the 117-Vac line, can switch a 1000-W load with a 1.5- μ W input from the fiber-optic cable. The circuit is immune to line transients because it is a fully floating two-terminal device. The relay has been tested for 5×10^4 operations without malfunction. This device will be used wherever a solenoid valve, motor, or contactor will be controlled by the output of a microcomputer.

Used in these ways, fiber optics will eliminate the need to route wiring into the shielded microcomputer enclosures. This will improve the reliability of the system and increase the resistance to the EMI environment.

Pulse-Power System (D. L. Call). The instrumentation and the controls for the pulse-power system (PPS) have been defined. We have changed an earlier concept of small separate screen rooms for each of the PA controls and one large isolated screen room for all six PPS controls. The new design is a medium-size screen room located near each of the six PAs. Each screen room will contain instrumentation and controls for that PA and its PPS. This change is due to the necessity of having a viable control system during the three years of assembly and testing. Each of the six PPSs must be operable independently of the others, with the exception of safety considerations. The central laser control computer (LCC) will be used in a time-shared mode for this 3-yr period. However, operation of any of the six subsystems in a limited graphics mode is possible if the LCC is not available.

Each screen room will contain a local sequencer, local safety system, graphics display unit, fast timing system, slow analog-to-digital converters, spark-gap pressure controller, spark-gap monitor system, and transient recorders. Near the high-voltage power supplies are controls and monitors for those units. The trigger system and the high-voltage relays are located in the Marx generator tanks. All interconnections are by fiber-optic cable.

Beam Alignment (D. Gutscher). The design of the stepping-motor controller has been changed to allow use of Motorola's MM01A microprocessor card in place of a custom card. The new controller will drive eight stepping motors, five more than in the

earlier design. Two additional custom cards are required in the controller: the motor driver card and a CMOS memory card. The CMOS memory card contains a memory-protect circuit with a battery to preserve critical parameters (for example, motor position information) when the power is turned off. The memory card also contains an 8-channel, 8-bit analog-to-digital converter which is used to measure the power-supply voltages and the box temperature. These features will aid in monitoring the controller's state of readiness.

Steps taken to reduce the susceptibility of the controller to external noise include filtering the power input, using a shielded power supply with very low coupling between input and output, using optoisolators between the motor drive transistors and the microprocessor, and including in the shielded box a separate compartment for the more sensitive electronics.

Evaluation of sensor types for detecting the laser-beam position has begun.

Software (J. P. Hong, F. McGirt).

General. The control computer was acquired, installed, and is operational. Software development on the HP 3000 is progressing and a study on how to develop software for the microcomputers is under way. Software task management efforts yielded an estimate and a PERT diagram which require us to reduce our software needs.

Procurement and Installation of the Control Computer. Preliminary specifications for the control computer were approved by LASL's Coordinator on Automatic Data Processing (CADP) in January 1977, and requests for proposals and quotations went out in early February. By mid-March a computer system was selected and by the end of April LASL CADP obtained Albuquerque ERDA approval for the computer system selection. On May 6, a purchase order was placed for an HP 3000, Series II, Model 8. The system arrived at LASL on 24 May and power was applied on June 1, 1977. The system was operational 8 min after application of power and has remained operational since. The HP-3000 computer is shown in Fig. II-38.

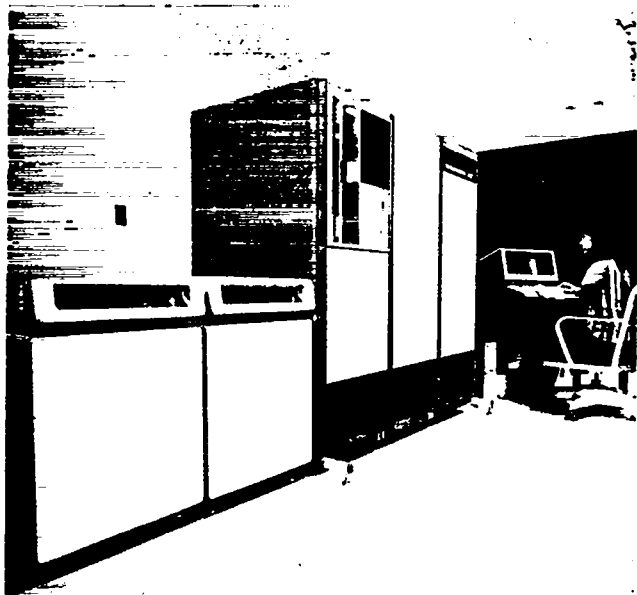


Fig. II-38.
Antares HP-3000 control computer.

The system comprises:

- 512 x 1024 bytes (8 bits) of error-correcting main memory,
- 100 x 10⁶ bytes of disk storage,
- 9-track 45-in./s, 1600-bpi magnetic tape,
- 16 terminal ports, each up to 2400 bps, and
- U3 CRT terminals.

The system was configured to maximize concurrent (multiprogram) programming; its time-sharing capability is important to Antares.

Software items included in the system are:

- SPL, a structured ALGOL-like language with complete FORTRAN-like formatted input/output,
- IMAGE and QUERY, a data-base management system similar to System 2000, and
- MPE, a time-shared, multiprogramming executive that enables process creation and management.

Control Computer Software. The software previously developed has been interfaced with the Antares Hewlett Packard HP-3000 computer.

The HP 3000 interactive program using the HP 2645 terminal (SED) is nearing completion. Most of the top-level program modules are operational and

many of the stubs have been replaced by working programs including cursor motion left, right, up, and down, as well as file access commands. An SED-like approach will be used in the simulator of the M6800 microprocessor.

We have decided that structured programmings will be adhered to on this project. Functional requirements and design of the software in a Procedure Description Language (PDL) must be defined before coding of a program may begin. A PDL standard has been published. Also, a collection of software notes (29 to date) has been published to document present programming efforts.

Microprocessor Software Development. We are studying five ways of writing software for the microcomputer:

1. Write in assembly code.
2. Write in MPL, which is a high-level compiler with incomplete structure.
3. Write in an extensible self-defining compiler-emulator, such as FOURTH.
4. Emulate portions of HP 3000 on the M6800 to run a transposed form of the HP 3000 object code originally coded in SPL.
5. Write a structured compiler that produces the M6800 object code.

Method (1) can be supported now on EXORCISOR, the CCF computers, and CTR's DEC-10 system. Such capacity can also be built on the HP 3000. But assembly programming is time-consuming, error-prone, and hard to maintain, even for short periods of a few months.

Methods (2) and (3) are state of the art. An MPL compiler is operational on the CCF and an extensible compiler is on the market for the M6800. These methods are unattractive because they are both based on incomplete structures.

Method (4) is unattractive because of the potentially slow algorithm, but it is also attractive because the same code runs on the HP 3000 and M6800. Such a code would be the easiest to generate and to debug.

Method (5) produces the best run time. But the calendar time needed to write a compiler appears incompatible with project requirements.

We will decide during the next six months which method to choose and will start the coding.

Diagnostics (B. C. Strait). A review of space requirements resulted in separate shielded control rooms for laser control and for target diagnostics. Each will be equipped with independent isolated power, air conditioning, and terminal boxes.

Site and Structures (E. O. Swickard)

Design (J. Allen). The HEGLF project comprises two efforts: site and structures and the laser system. Five major buildings are included in site and structures: the laser building, target building, mechanical building, office building, and warehouse. Because of budgetary constraints, the site and structures effort has been divided into two construction packages; Package I is to be obligated in FY 1978, and Package II in FY 1979. Package III, the target-vacuum system, will also be obligated in FY 1979. Package I includes the laser building,

mechanical building, office building, warehouse, and some site and utilities work. Title II design for this package has been completed and the bid package has been sent to interested contractors. Bid opening is scheduled for July 7, 1977.

The Title II design for Package II, the target building and the remaining site and utilities work, has been completed and reviewed internally. A review with the Architect-Engineer is scheduled for early July. Following any review changes, the drawings and specifications will be assembled into a bid package and held until FY 1979 funds are available.

Preliminary Safety Analysis Report (PSAR) (J. Graf, E. O. Swickard). The PSAR draft has been reviewed by both LASL and ERDA personnel and, after a few minor changes, will be ready for publication. Approval of the PSAR prior to the expected start of Package-I construction is assured.

III. LASER FUSION THEORY, EXPERIMENTS, AND TARGET DESIGN

In an integrated program of theory, target experiments, and target design, we are establishing a fundamental understanding of laser-target interactions, particularly of the relevant plasma physics and hydrodynamics. Both the experimental and the theoretical efforts have concentrated on studying the wavelength dependence of laser-plasma interactions. The close coupling of theory and experiment has made it possible to eliminate theories that are not supported by experiment. In general, basic studies of laser-plasma interactions have shown that the design difficulties associated with long wavelengths are less severe than believed earlier, and that breakeven target designs are attainable even in the presence of a hot-electron spectrum. These results have given us new confidence that significant yield can be obtained from more efficient, less expensive CO₂ lasers.

LASER FUSION EXPERIMENTS

Introduction (R. F. Benjamin, D. V. Giovanielli)

Many programmatic experiments have been performed successfully on the SBS, as summarized below.

We have collected data in essential target studies involving vacuum-insulation concepts and absorption measurements. The vacuum-insulation study was preceded by conductivity measurements of target-mounting stalks and by comparison of the hot-electron temperatures as determined by x-ray and ion measurements. We then carried out vacuum-insulation experiments with a double foil, with and without a short circuit. The absorption measurements used a novel light collector to study flat-target absorption by collecting all the scattered and reflected 10.6- μ m light.

Several support experiments were also performed. Layered-target experiments produced evidence for laser intensity-dependent electron spectra, whereas the thin-foil (100 to 1000 Å) absorption measurements corroborated recent theories on wavelength scaling. Visible-probe measurements on the thin-foil experiment demonstrated the usefulness of this new method for measuring plasma expansion and profile modification.

In addition to these studies, we made several measurements related to CO₂ laser technology and laser-beam diagnostics. The vacuum-aperture retro-pulse isolator, using a plasma shutter based on ablation of an aperture's edge, was tested at higher energies than previously and displayed useful characteristics. Infrared calorimeters, including prototypes for the EBS, were studied carefully. Several calorimeters were cross-calibrated and tested for damage threshold and linearity. Another test involved comparing a microscope and an autocollimating mask test for purposes of aligning and focusing the 10.6- μ m beam on target. Both systems utilize pyroelectric vidicon detection of the ir beam. These tests depended on the beam's spatial profile. Both the calorimetry and target-alignment tests had an immediate impact on EBS development. Another test measured the damage threshold of a metallized plastic-foil beam splitter/attenuator. We also explored the possibility of using a multiple-pulse technique to monitor the efficiency of attenuators and isolators.

The TBS was used successfully for imploding spherical glass microballoons filled with 1 to 10 atm of DT fuel. With total laser output powers of 0.16 to 0.40 TW, we obtained neutron yields as high as 5×10^6 , similar to the yields obtained with Nd:glass lasers operating at the same peak power levels.

A variety of x-ray spectral and imaging diagnostics, charged-particle diagnostics, and scattered-light diagnostics were used to compare target performance to predictions of LASNEX and PIC simulation codes.

SBS Experiments

Transmission of 10.6- μm Laser Light Through Plasmas from Thin Targets (K. B. Mitchell). We conducted an experiment to measure, for the first time, the absorption depth of 10.6- μm laser light in plasmas formed on thin Formvar foils ranging in thickness from 150 to 700 \AA . Target thickness was measured interferometrically. This experiment was conducted with a laser irradiance of $3 \times 10^{13} \text{ W/cm}^2$ for a laser pulse width of 1.6 ns FWHM. The 10.6- μm light passing through the plasma was collected by an f/1.2 mirror and measured with a disk calorimeter. Figure III-1 shows the ratio of the transmitted energy to the energy incident on target plotted against foil thickness. The best fit to this curve is that the transmission

$$T \cong \exp^{-0.0055 d(\text{\AA})}$$

where the $1/e$ absorption depth is 180 \AA . As measured from layered-target experiments the absorption depth was twice the penetration depth. For the Formvar foil target, free plasma expansion was both toward and away from the laser; whereas with the layered target, free expansion was toward the laser only. Therefore, the penetration depth of the plasma is equivalent to the absorption depth of laser light. Wavelength-scaling comparisons to 1- μm experiments suggest that

$$T = \exp - \frac{(\kappa \lambda^2 d)}{\tau}$$

where κ is a proportionality constant, d is the film thickness in (\AA), and τ is the laser-pulse width.

Transmission of Green (0.5- μm) Light Through Thin Target Plasma (R. F. Benjamin). As part of our experiments with thin target foils, we monitored the transmission of green laser light from a 0.515- μm

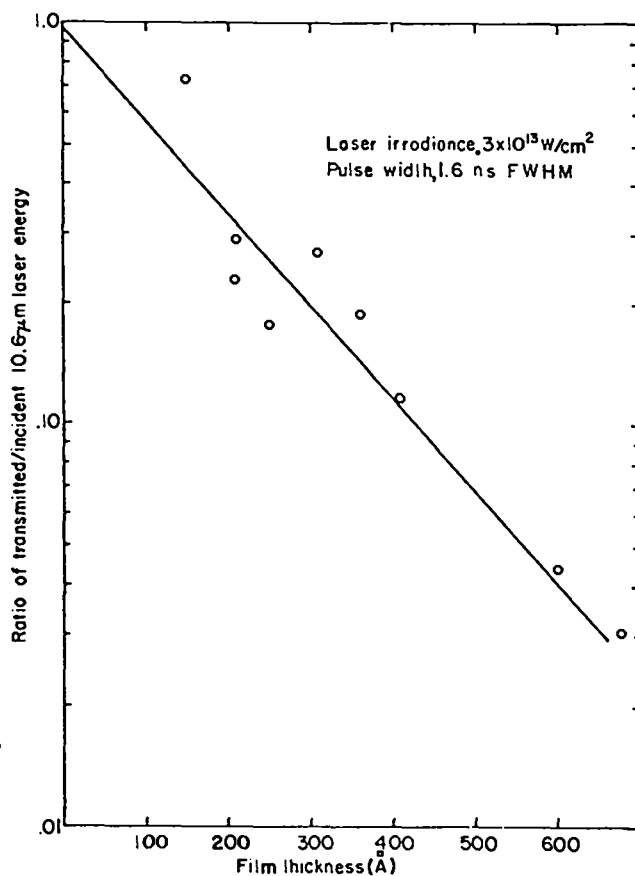


Fig. III-1. Transmission through 10- μm -produced plasmas for thin slab targets of Formvar. Laser irradiance, $3 \times 10^{13} \text{ W/cm}^2$. Pulse width, 1.6 ns FWHM.

argon-ion laser passing through the plasma. The critical density for this probe beam is $4 \times 10^{21} \text{ cm}^{-3}$. The green pulse was strongly attenuated for a time comparable to the duration of the main CO_2 pulse ($\sim 1.5 \text{ ns}$), which indicates the presence of an over-dense or strongly refracting plasma. The time during which the 0.5- μm beam was attenuated varied directly with the target foil thickness. Measurements of 0.5- μm attenuation duration as a function of foil thickness were consistent with a one-dimensional LASNEX calculation describing the CO_2 beam transmission and the ion data. However, for a good comparison with theory, we have to improve the time resolution. We need a probe laser of

constant intensity, and subnanosecond resolution in the detection system, to obtain improved time resolution of the transmitted 0.5- μm beam. Detector resolution better than 200 ps was obtained with a fast biplanar vacuum photodiode (ITT F4014) and an oscilloscope equipped with an intensified cathode-ray tube. The argon-ion laser used as a visible probe exhibited intensity modulations at frequencies up to 5 GHz due to beating between the laser's longitudinal modes. By inserting an intracavity etalon, we successfully suppressed this high-frequency modulation. The 5-GHz noise is consistent with the gain-bandwidth of the argon-ion laser. We will study the effect of beam profile modifications in these targets when the thin-foil experiments are rerun with this improved diagnostic.

Experiments on Vacuum Insulation (T. H. Tan). In laser fusion, high-energy electrons must be prevented from entering the target fuel if near-isentropic target compression is to be obtained. A fuel preheated by high-energy electrons will require much more energy for compression. The electron flow to the fuel can be inhibited by various schemes, for example, by separating the absorption surface from the interior of the target by a vacuum gap. Ordinarily, energetic electrons have little difficulty penetrating and heating target material to great depths, but they cannot cross the vacuum gap in large numbers due to the high magnetic fields set up in that region after the passage of relatively few electrons. The high field is maintained because the return current across the vacuum is limited to the relatively small value determined by the Langmuir-Child law. Figure III-2a shows a schematic of the experiment performed to test this design. Two plastic foils 0.1- μm and 3.75- μm thick, were used as the targets at various separation distances, with the laser pulse impinging on the 0.1- μm foil. The accelerated ions resulting from the hot electrons were observed on both sides. At foil separations sufficiently wide to prevent the plasma from the first foil from colliding with the second foil during the laser pulse, no fast ions were accelerated from the back face of the second foil as illustrated in Fig. III-2b (data points marked x and o), which shows that the rear ion velocity drops abruptly at a foil separation distance of ≥ 1.0 mm. Only ions from the first foil were observed in the rear, with a characteristic

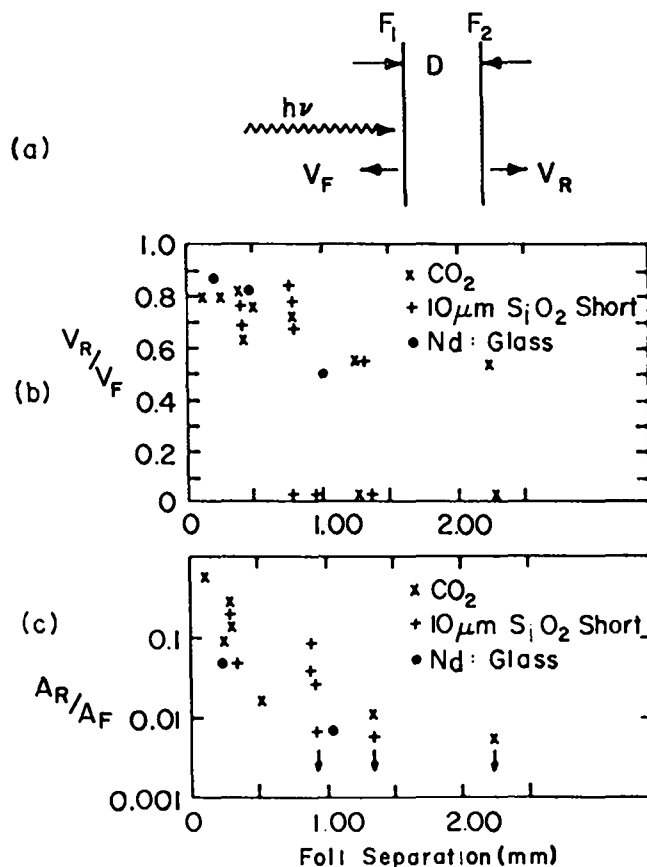


Fig. III-2.

Double plastic-foil experiments and data showing effect of foil separation on electron flow. (For explanation of results, see text.) (a) Schematic. (b) Ratio of maximum back-emitted ion velocity V_R to maximum front-emitted ion velocity V_F as a function of foil separation. Data were chosen from shots of approximately equal laser power on target, resulting in almost constant V_F . (c) Ratio of back-emitted ions at maximum velocity A_R to front-emitted ions at maximum velocity A_F as a function of foil separation.

energy loss suffered in passing through the second foil. The foil separations needed to inhibit hot-electron flow (that is, to prevent shorting while the laser is still on) scaled linearly with laser-pulse length. At intensities of $\sim 10^{15}$ W/cm², a characteristic gap closure velocity of $\sim 1 \times 10^9$ cm/s was obtained for both CO₂ and Nd:glass laser experiments.

Note that the number of ions emitted from the back also decreases rapidly as the foil separations increase.

If these foils were spherical, as in a compression target, supports would be needed to hold the inner sphere in place. However, they might ionize and rapidly expand to fill the void between the spheres and defeat the insulation properties of the vacuum. To examine the effect of supporting struts, the flat-foil experiment was repeated with a glass fiber shorting the two foils, as shown in Fig. III-3. The end of the fiber was struck directly by the incoming laser. No apparent difference was observed in the behavior of the ion expansion in the rear of the target when the supporting fiber was added, as indicated by the data marked by crosses (+) in Figs. III-2b and -2c. No x-ray emission along the fiber was observed by the x-ray pinhole camera (25- μm aperture) even when the separation was smaller than 1 mm. We conclude, therefore, that vacuum insulation effectively minimizes target preheating, and that the presence of supporting SiO_2 fibers of very small diameter (typically $\sim 2 \mu\text{m}$) should not significantly affect the irradiation properties.

TBS Experiments

Compression Experiments (D. Bannerman, P. Lee, J. L. Shohet, T. H. Tan, D. vanHulsteyn, A. Williams). We successfully conducted the first compression experiments using 10.6- μm laser radia-

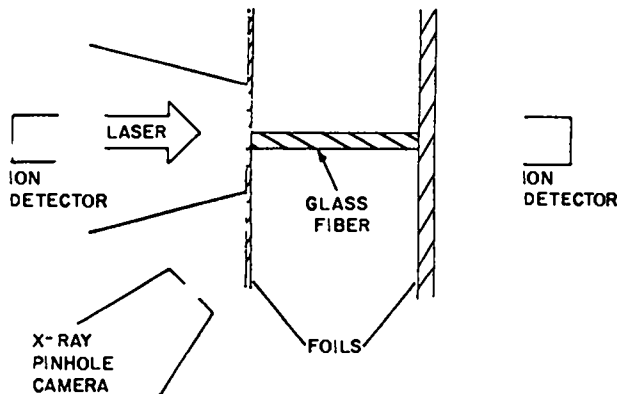


Fig. III-3.

Schematic of experiments to examine ionized effect of supports between separated foils.

tion early in 1977. The implosions were imaged on Kodak 2490 film both with pinhole cameras and with Bragg-crystal x-ray spectrographs. Plastic scintillators and silver counters were also used to detect neutrons produced in fusion reactions as another technique for inferring compression.

The targets irradiated were glass microballoons with nominal wall thicknesses of 1 μm , and whose diameters ranged from 90 to 100 μm . These balloons were filled with DT or DT-neon mixtures varying in total pressure from 1 to 10 atm.

Some of the spheres of the ball-and-disk variety (Fig. III-4) were suspended between thin layers of cellulose acetate stretched over a frame formed by glass fibers of 10- μm diameter. Typical foil thicknesses were 0.05 μm . Targets in which the supporting foils were not bounded by the glass fiber frame, but extended several millimeters to the edge

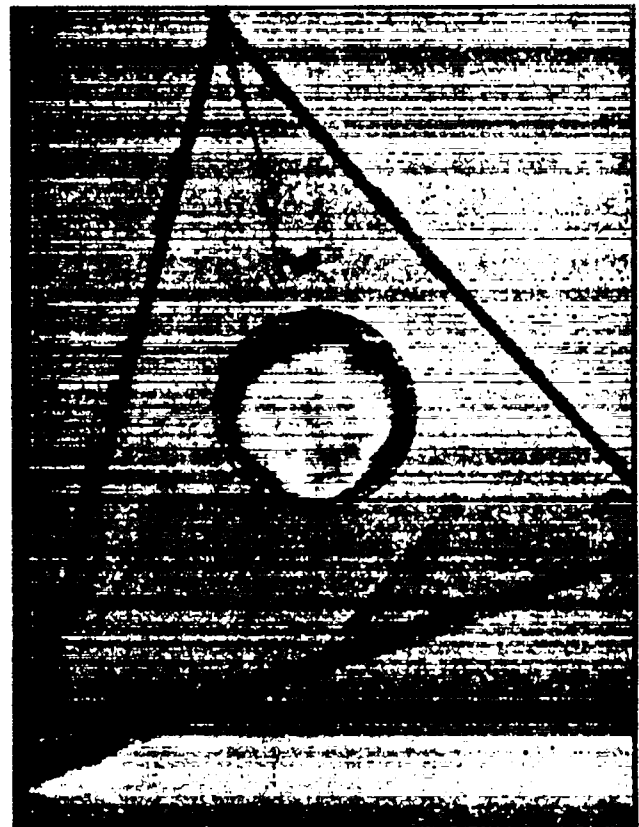


Fig. III-4.

Glass microballoon suspended between cellulose acetate films.

of a target mount, were also irradiated. The yield and the x-ray images of these unbounded targets were the same.

A representative neutron-producing shot yielded the pinhole x-ray images presented in Fig. III-5. The target was identical to that shown in Fig. III-4. Images of the supporting glass fibers are faint, but perceptible. A ring inside the microballoon shows the degree of compression.

Other targets were of the ball-on-stalk configuration with the microballoon mounted on a glass stalk whose diameter at contact with the ball was typically $3\ \mu\text{m}$.

The densitometer trace of an x-ray pinhole photograph from a typical ball-on-stalk target shot is presented in Fig. III-6. The profile is consistent with LASNEX predictions for simulated pinhole picture densitometer scans, as shown in Fig. III-7. The neutron yield, as determined from the silver activation counter, was 5×10^{-6} . Table III-I shows good agreement with LASNEX-predicted neutron yields for three groups of target experiments, all of which were expected to have identical yields. Time-of-flight measurements obtained with the scintillation detectors show that 14-MeV DT fusion neutrons were produced in these shots.

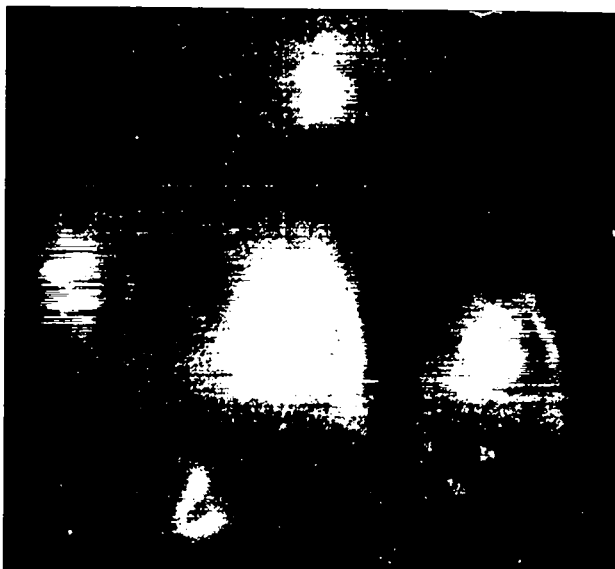


Fig. III-5.

Pinhole x-ray image of a target similar to that shown in Fig. III-4.

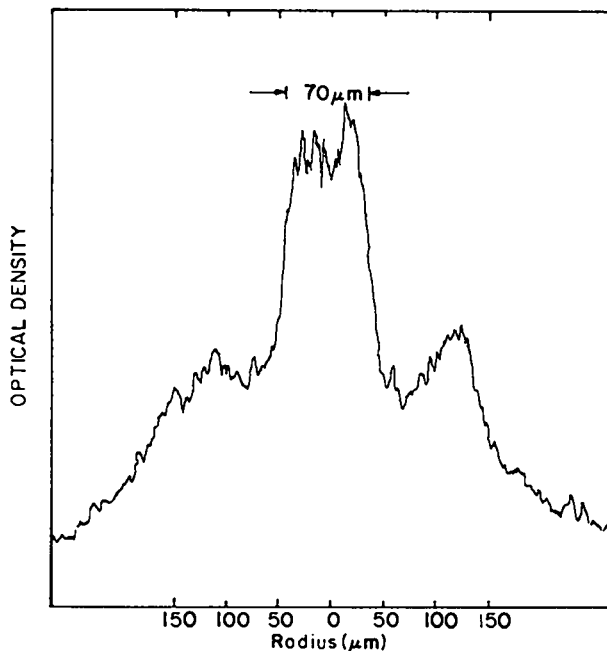


Fig. III-6.

Densitometer trace from x-ray pinhole photograph of a typical ball-and-stalk target.

In these examples, neutron measurements together with pinhole photographs indicate that compression is taking place. Furthermore, the x-ray images confirm the centering of the two incident beams, as illustrated in Fig. III-8, which shows the irradiation of a $500\text{-}\mu\text{m}$ magnesium-coated solid copper sphere.

A second example of neutron-yielding compression is shown in Fig. III-9. This example is of interest because it shows the irradiation of a $100\text{-}\mu\text{m}$ -diam sphere. Note that the outer region is illuminated very uniformly, indicating that energy deposition into the shell was uniform.

More recently, we have used spatially resolved x-ray spectroscopy to obtain spectrally resolved images. One example, in which a $25\text{-}\mu\text{m}$ -wide slit was used on a flat crystal diffraction instrument to provide the resolution, is shown in Fig. III-10. This image is very similar to the corresponding pinhole photograph of Fig. III-9 except that it does not show the central region. This indicates that the intensely glowing central region is not produced by the helium-like resonance transition, but rather by

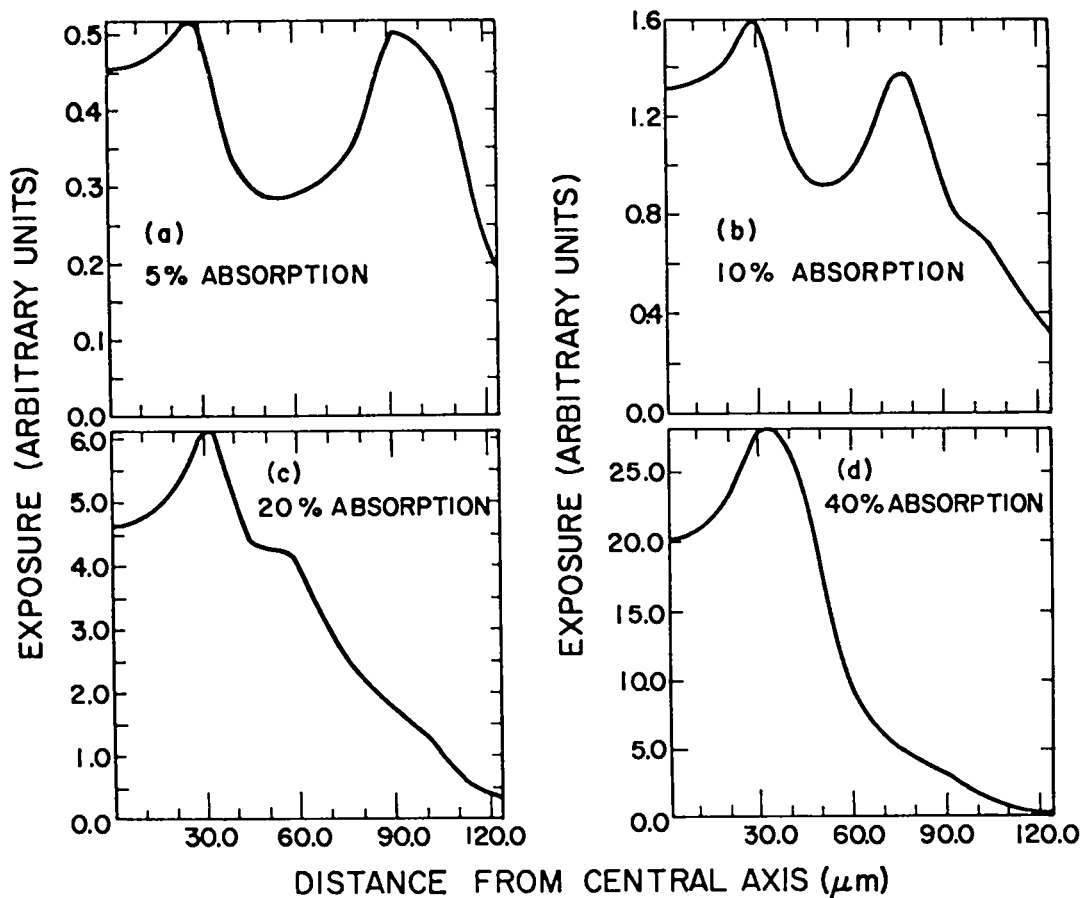


Fig. III-7.

Theoretical prediction of soft x-ray pinhole pictures (10- μm resolution).

TABLE III-I

EXPERIMENTAL RESULTS COMPARED WITH LASNEX
PREDICTIONS OF NEUTRON YIELDS^a

Experimental Group	No. of Shots	Initial Radius (μm)	Wall Thickness (μm)	Fuel Mass (ng)	Peak Laser Power (TW)	Neutron Yield (10^6)
I	6	75.8 ± 0.8	1.0 ± 0.1	3.9 ± 0.2	0.25 ± 0.06	1.4 ± 0.4
II	7	98.5 ± 1.8	0.8 ± 0.1	8.5 ± 0.5	0.24 ± 0.05	1.4 ± 0.8
III	2	47.8 ± 2.2	0.65 ± 0.1	0.11 ± 0.02	0.27 ± 0.06	1.5 ± 0.8
LASNEX	---	75.0	1.0	3.78	0.25	1.35

^aAbsorption fraction, 0.16 at critical surface. Ponderomotive force and improved hot-electron prescription included.

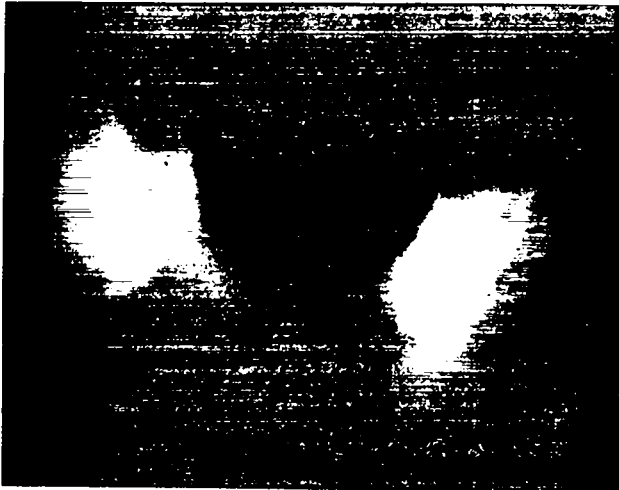


Fig. III-8.

Both laser beams of TBS irradiating a magnesium-coated 500- μm -diam copper sphere. The beam on the left is well centered; the other is about 70 μm high.

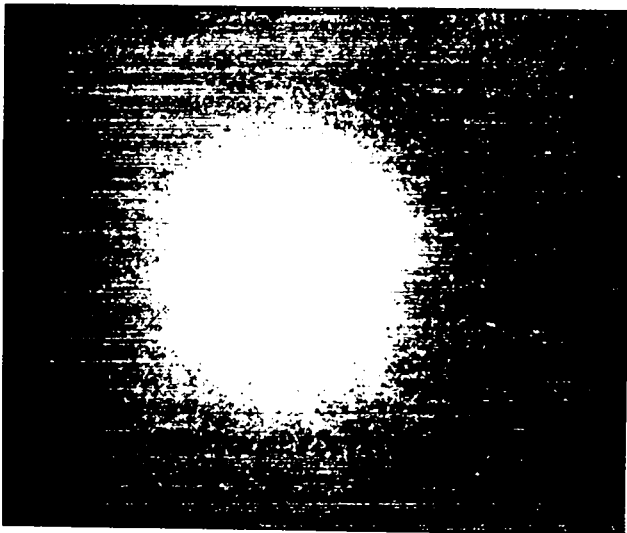


Fig. III-9.

X-ray pinhole image of irradiated 100- μm -diam sphere.

some other portion of the spectrum. We are attempting to identify the source of this radiation.

We also established that spectrographic data can be used to measure the density of the electrons in the x-ray-producing plasma. This is achieved by



Fig. III-10.

Spatially resolved image of an irradiated sphere, using a 25- μm wide slit on a flat crystal diffraction instrument.

measuring the spectral widths of the individual lines and subtracting the effects of source-broadening and crystal-rocking angles. The difference is attributed to Stark-broadening which, in turn, is directly related to the electron densities. Recent measurements indicate electron densities of $\sim 10^{23}/\text{cm}^3$, which is consistent with shell densities calculated for the implosion phase of the experiment. Imaging of the x-ray emission lines also indicates that these emissions came from the region between the original microballoon radius and the minimum implosion radius. Doppler-broadening of these lines was small for temperatures < 500 eV. Temperatures determined from line-ratio measurements in our experiments ranged from 100 to 300 eV, and were consistent with LASNEX calculations.

Thomson Parabola Measurements of Fast-Ion Distributions (F. Young). The kinetic energy in a plasma expanding from a target is usually determined with a charge cup, which measures electron current as a function of the time of flight. However, determining the plasma energy requires that both the ion mass and the charge be known, both of which are frequently derived either by calculation or by fiat. To determine the accuracy of these measurements, one has to find both the velocity distribution and the charge distribution of the ions in the expanding plasma.

We have used a Thomson parabola ion analyzer¹ to measure charge species and the distributions of

fast ions emitted by laser-produced plasmas. A cellulose-nitrate foil² was used as a particle counter. Typical track densities were $\sim 10^6/\text{cm}^2$. Space-charge distortions of the ion-velocity distributions and effects of sheath fields at the entrance aperture of the Thomson mass analyzer were shown to be negligible.

The passage of heavily ionizing nuclear particles through a cellulose-nitrate foil produces narrow paths of intense damage on the atomic scale. These tracks can be seen with a microscope on the processed film.³ This film meets the need for a 100- μm nonphotographic detector capable of recording strongly ionizing radiation (that is, protons, alpha particles, heavy ions, and neutron-induced charged particles) in the presence of weakly ionizing radiation (light, x rays, gamma rays, and electrons). The film has a track-registration threshold⁴ of 0.35 MeV/mg/cm², the highest sensitivity of all known dielectric track detectors. At the upper range, track-registration in cellulose nitrate for protons ranged from 500 keV to 1.6 MeV (Ref. 5).

Several computer programs are aiding us in analyzing the Thomson parabola mass-analyzer data. These programs

- test and correct the experimental orientation of the coordinate system used to analyze the raw data;
- calculate ion-velocity distributions;
- calculate volume number-density distributions;
- calculate electron temperatures, assuming isothermal expansion;
- calculate total energy and total volume number-density for each parabola; and
- calculate current densities, which are used to test the correlation between the Thomson data and the scintillator and ion-probe data.

Figure III-11 shows a composite of ion data from a CH₂ plasma recorded on a cellulose nitrate foil. Other parameters and a summary of the experiment are listed in Table III-II. Note that the maximum velocity cutoff of the carbon-ion distributions is a straight line with the slope

$$\frac{z}{y} = \frac{k_1}{v},$$

where z is the vertical axis, y is the horizontal axis, and $k_1 = V/mcBd$ with v the ion velocity, V/d the electric field, m the ion mass, B the magnetic field,

and c the velocity of light. Constant values of k_1 and z/y imply that the asymptotic value of the velocity for all carbon-ion species is a constant.

Other features of the ion data in Fig. III-11, not discussed in this report, include periodic "bunching" in the proton number and energy distributions, track extension near and into the origin of the parabolas, and range-energy analysis of ions in the cellulose-nitrate foil.

If we assume that $\sim 50\%$ of laser energy is absorbed and that the emitted ions have a $\cos(\eta\theta)$ distribution with $4 \leq \eta \leq 10$, in agreement with charge-cup data, then $\sim 10\%$ of absorbed laser energy is partitioned into the production and acceleration of these ions.

Figure III-12 shows a correlation of current density plotted for time-of-flight scintillator measurements and for Thomson parabola data. The Thomson data, which are a composite of the seven lines in the CH₂ plasma, showed that the early peak was due to protons only (Fig. III-13), whereas the later peak was due to both protons and carbon ions. Figure III-14 shows the contribution from carbon ions only.

In an experiment we tried to test the validity of the isothermal expansion model used by Crow, Auer, and Allen,⁶ who reported calculations of the collision-free expansion of a plasma in vacuum. This experiment was also designed to investigate the production of neutrons in a D-D fusion reaction. Figure III-15 shows the impinging CO₂ laser beams and the two thin CD₂ target foils suspended in vacuum at a separation distance of 2.7 mm. A specific neutron yield (number of neutrons per initial ion density) was calculated and plotted (Fig. III-16) as a function of electron temperature.

The measurements of neutron and deuteron velocity distributions suggest that an isothermal deuteron distribution (see Fig. III-17) is formed near the surface of one of the CD₂ foils and expands into the adjacent CD₂ foil where D-D fusion reactions occur. The observed values for initial ion density ($\approx 10^{19}$), electron temperature (~ 25 keV), and neutron yield ($\sim 10^7$) agree with the predicted values shown in Fig. III-16.

Figures III-18 through -20 summarize the correlation of current density versus time for the Thomson ion data and ion-probe current data. They show that the ion current consists primarily of protons. The contribution to the ion current from

TABLE III-II
DATA SUMMARY FOR CH₂ EXPERIMENT

Laser Type: two-beam CO₂
Target: 50- μ m-thick CH₂ foil

Incident laser energy, J	
North beam	245
South beam	0
Laser pulse width, ns	~1
Absorbed laser energy, J	~123
Target chamber vacuum, torr	~10 ⁻⁶
Target-analyzer axis-to-target normal angle, deg	29.2
Target-to-analyzer entrance aperture distance, cm	150
Analyzer entrance aperture width, cm	0.02
Analyzer magnet field, G	385
Analyzer electric field, V/cm	600

<u>Ion Type</u>	<u>E_{min}</u> <u>(keV)</u>	<u>E_{max}</u> <u>(keV)</u>	<u>Ion Energy (J)</u>
H ⁺	44 ± 2	653 ± 26	3.6 ± 0.15
C ⁺¹	144 ± 6	1543 ± 62	1.55 ± 0.06
C ⁺²	231 ± 10	1746 ± 70	2.26 ± 0.09
C ⁺³	235 ± 6	1771 ± 71	1.15 ± 0.05
C ⁺⁴	572 ± 23	1709 ± 68	1.32 ± 0.05
C ⁺⁵	524 ± 21	1674 ± 67	1.98 ± 0.08
C ⁺⁶	855 ± 34	1651 ± 66	0.528 ± 0.02
Total			12.4 ± 0.50

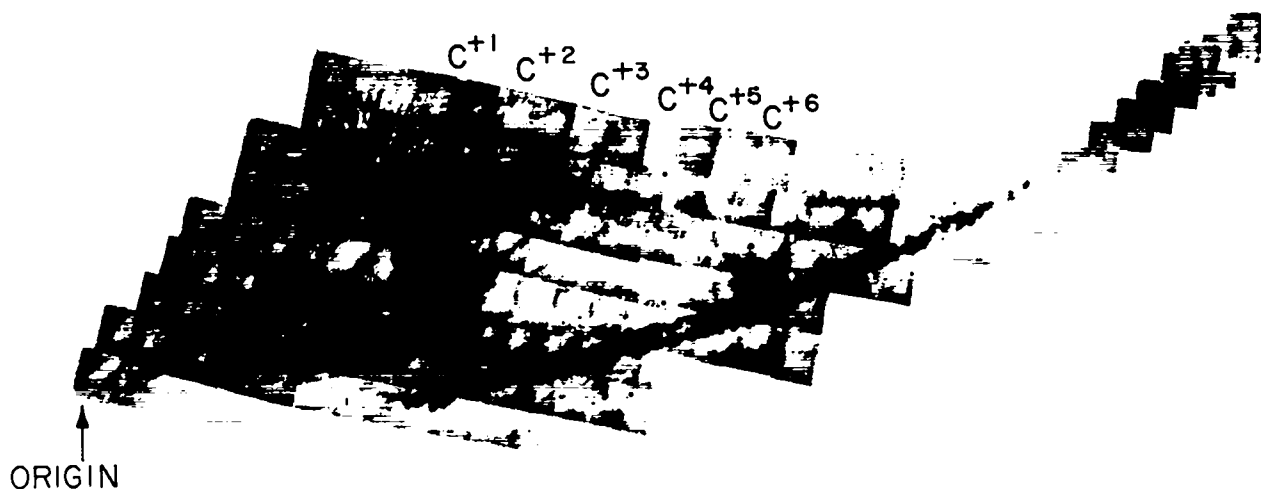


Fig. III-11.
Photomicrograph of data from CH₂ plasma recorded on cellulose nitrate film. The lower right parabola is due to protons; the parabola adjacent to the proton curve is due to C⁺⁶ ions.

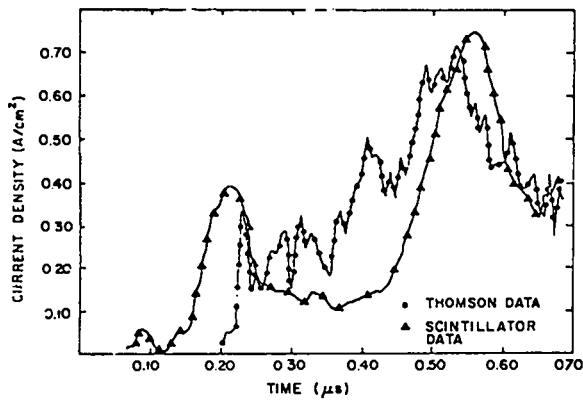


Fig. III-12.

Comparison of scintillator data with Thomson data (protons and carbon ions) for CH_2 plasma.

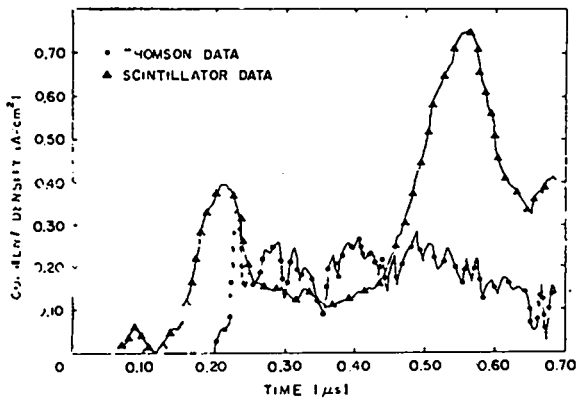


Fig. III-13.

Comparison of scintillator data with Thomson data (protons only) for CH_2 plasma.

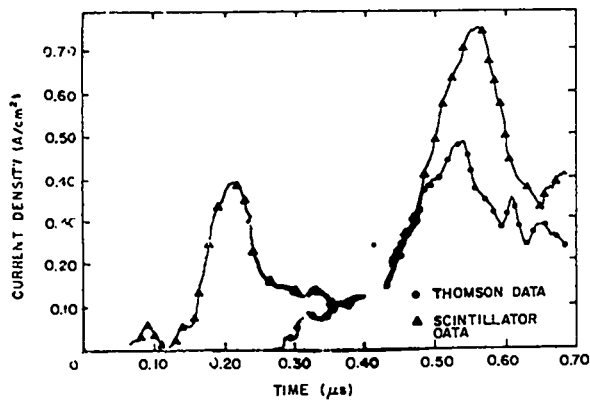


Fig. III-14.

Comparison of scintillator data with Thomson data (carbon ions only) for CH_2 plasma.

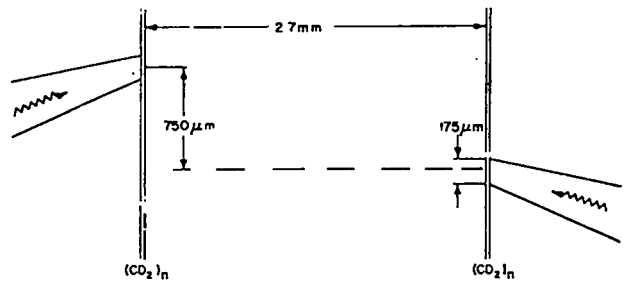


Fig. III-15.

Foil and laser-beam geometry for double CD_2 foil experiment.

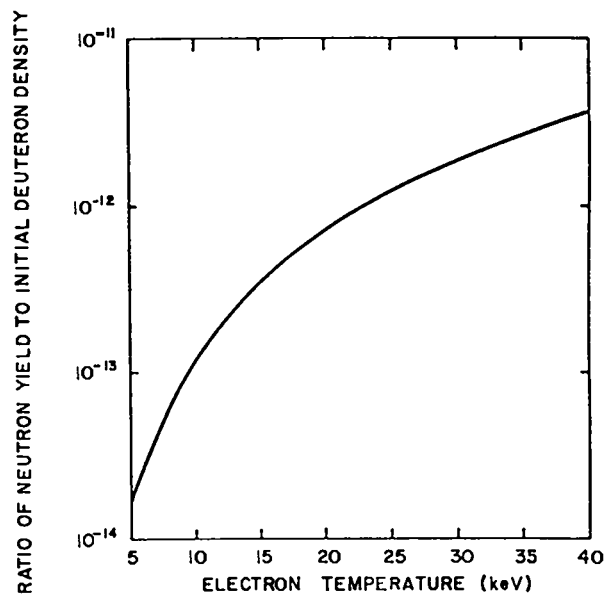


Fig. III-16.

Plot of specific neutron yield vs electron temperature.

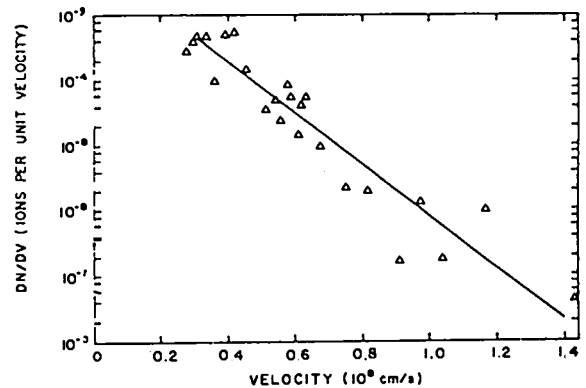


Fig. III-17.

Deuteron velocity distribution from CD_2 plasma; electron temperature, ~ 25 keV.

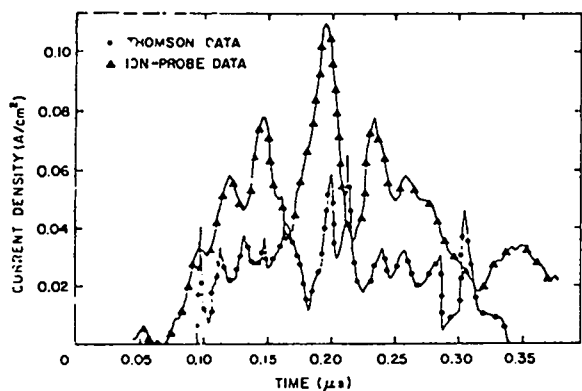


Fig. III-18.

Comparison of ion-probe data with Thomson data (protons only) from CD_2 plasma.

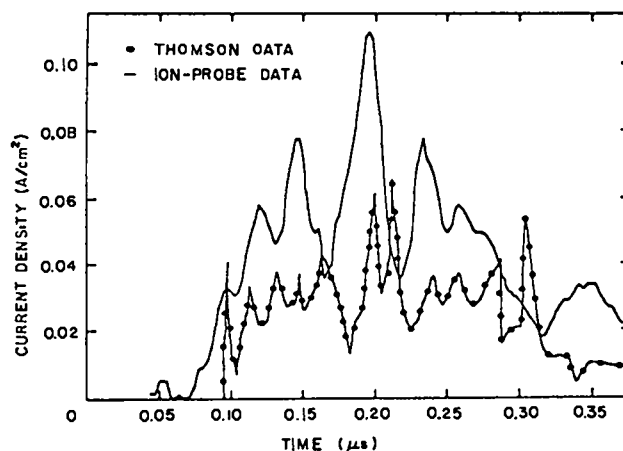


Fig. III-20.

Comparison of ion-probe data with Thomson data (protons and deuterons) from CD_2 plasma.

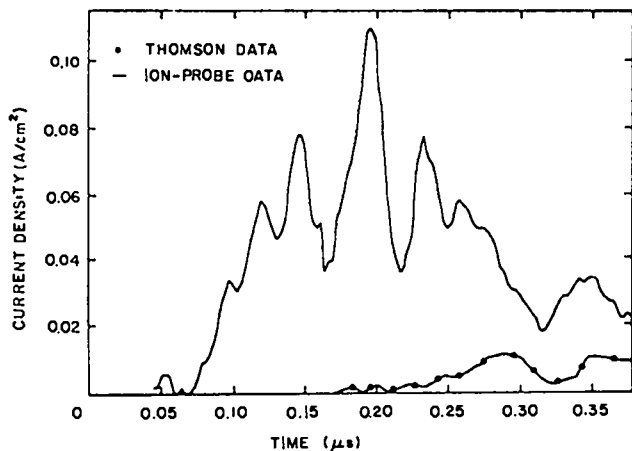


Fig. III-19.

Comparison of ion-probe data with Thomson data (deuterons only) from CD_2 plasma.

the deuterons occurs at later times (Fig. III-19). Furthermore, time-of-flight scintillator measurements show that the contribution from carbon ions occurs later than that from the deuteron current density (Fig. III-12). These measurements show that the fast-ion energy is lower than believed earlier. The importance of accurate charge-to-mass ratio and velocity distributions is also evident.

MILITARY APPLICATIONS EXPERIMENTS AND STUDIES

Introduction (L-Division's A. G. Engelhardt, R. Robertson, J. H. McNally)

We are conducting laser experiments to simulate and study, on a miniature scale, the blast- and shock-wave phenomena of nuclear explosions. These experiments, performed almost exclusively on our Nd:glass laser system, include equation-of-state studies, multiburst simulations, and opacity experiments as described below. These weapons applications are dependent on short-pulse laser technology that has been developed for, and is being used in, our laser fusion program. The laser used in these applications is supported by laser fusion funding; but the experimental work is supported by weapons programs funding.

Equation-of-State Studies (P-Division's L. Veerer, J. Solem)

We are exploring the feasibility of using lasers to measure high-pressure equation-of-state (EOS)

parameters. Although there have been experiments to observe shock compression by laser ablation,⁷ no EOS parameters have been measured.

We plan to obtain points on the Hugoniot of a test material by impedance-matching and to compare the data with those for a standard. This approach will involve measuring shock velocities in multilayered foils by observing radiation at shock breakthrough. Shocks will be generated by depositing laser energy in a substrate of standard material.

In designing a foil, we face two constraints: (1) the substrate must be thick enough to reabsorb most of the hot electrons generated at the ablation surface, and (2) the substrate and test layers must be thin enough to allow passage of the shock through all parts of the system before it is overtaken by a rarefaction. The second consideration is dependent on pulse length and laser energy.

In our base-line target design (Fig. III-21), we hope to measure the time of shock emergence from the substrate, of two shock emergences from the 5- μm layers of aluminum, and of the shock emergence from the platinum. The two timing signals from the aluminum are to ensure a flat-topped shock.

Calculations show that for a 20-J, 1-ns pulse with 500- μm spot diameter, the shock should be flat-topped through all the layers. The pressure should be ~ 1.5 Mbar in the aluminum and ~ 3.0 Mbar in the platinum. Shock emergence times are 1.2 ns for the substrate, 1.7 ns for the first aluminum layer, 2.2 ns for the second aluminum layer, and 3.1 ns for the platinum. The streak camera we are using should give ~ 15 ps resolution, allowing us to measure shock velocities to within a few per cent. The temperature at shock breakthrough is 0.33 to 0.5 eV, which we expect to see with the S-1 photocathode. With 100-J pulses, calculations show that we should reach pressures of ~ 4 Mbar in the aluminum and breakthrough temperatures of ~ 1.0 eV.

The substrate standard material for our EOS target is aluminum and the test material is platinum. In these first proof-of-principle experiments, we intend to obtain data in the pressure regime of 1 to 5 Mbar, which has already been partially explored with gas guns. At much lower pressures, our data will be obscured by viscosity and other dissipative mechanisms that give shock fronts

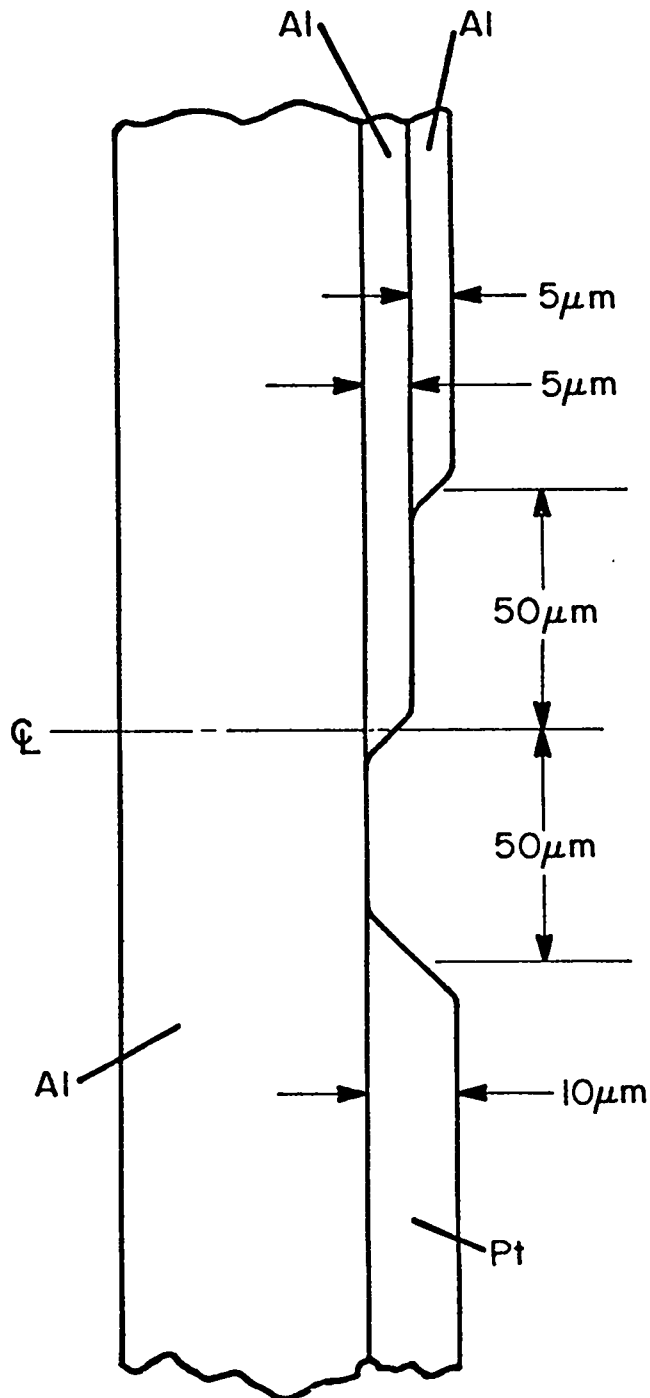


Fig. III-21.

Proposed target design for laser EOS measurements. A laser beam 200 to 400 μm in diameter impinges along the center line. Shock emergence is observed at various depths in aluminum and platinum to determine the relative shock velocities in the two materials.

finite widths. At much higher pressures, no experimental data are available for comparison. If our technique is viable, we will use molybdenum as the substrate standard and will extend into the 10- to 100-Mbar regime, depending on the state of laser development at that time. We note that, by then, molybdenum will have been well characterized in nuclear tests.

Despite several weeks of experimenting, our instrumentation did not work well enough to measure shock velocities in metal foils reproducibly and convincingly. However, we believe that we are closer to understanding the source of our difficulties. The main problem appears to be the limitation of the image-tube-based streak camera. The streak circuitry seems to be subject to an intolerable amount of drift and jitter, and the image tube is severely limited in sensitivity and dynamic range.

The jitter and drift have been a continuing frustration. A large number of laser shots were wasted when the sought-after image spontaneously drifted out of the time window. We may have to solve this problem by investing the time and money needed to incorporate a state-of-the-art trigger system using a Mylar spark gap rather than a photodiode.

We used a ruby laser and a joulemeter to test the sensitivity and dynamic range of the camera. We found the camera threshold to be higher than 100 W/cm² and the dynamic range only one third of normal, which is apparently symptomatic of an image tube at the end of its life. While the sensitivity may be tolerable, the severely limited dynamic range is not. The light intensity from an emerging shock varies approximately as the fourth power of the postshock temperature; hence, a 30% variation in this temperature could cause the image tube to change from gross overexposure to no streak at all.

We are now set up to look at targets with thicknesses varying in steps as small as 1 to 3 μm . We hope that temperature difference across the stop will be so small that we will obtain equal exposure on both sides, even if the shock is being overtaken by rarefaction, or the primary source of heating is fast electrons. We also put a beam splitter in our optics and are monitoring the spatially integrated light output. We hope to learn something about the signals we have lost to drift and jitter. So far, the effort has been unrewarding.

Multiburst Simulation: Blast-Wave Interactions (J-Division's G. E. Barasch, S. N. Stone).

We have developed diagnostic techniques and experimental procedures for simulating nuclear multiburst hydrodynamics by using our two-beam Nd:glass laser system. Single-beam experiments have previously demonstrated the usefulness of high-speed framing photography of fireball and blast-wave phenomena in emission and shadowgraph modes. These data resulted in the choice of target configuration (small, hollow spherical shells) and verified that the single laser-produced blast waves obey the Taylor-von Neumann-Bethe (ϕ^5) scaling law for strong explosions—as do those generated by low-altitude nuclear explosions. We have now observed interactions between blast waves in two types of experiments.

In the first series of experiments, a single blast wave was generated adjacent to a planar surface to simulate a near-surface nuclear explosion. Interactions between the incident and reflected blast waves were observed by shadowgraphy. Figure III-22a shows a shadowgraph recorded 17 μs after laser energy deposition. The incident blast wave was produced by a 0.3-ns laser pulse of 24 J incident on a spherical shell target 0.9 cm from the plane. The blast wave energy was ~ 6 J, and the ambient air pressure was 40 torr. The positions of the incident blast wave and a well-formed Mach stem propagating along the reflecting surface are clearly evident. The general appearance of this record is very similar to that of Fig. III-22b which was recorded 170 ms after Event Teapot/Met (22 kt on a 122-m tower).

Whereas the same phenomenology applies to laser-driven and nuclear blast waves, the large-scale differences between the two types of experiments preclude matching of all blast-wave parameters simultaneously. Consequently, the scaling by which a particular laser event can simulate a specific nuclear event is not well defined, and the use of hydrodynamic codes will be required to make the simulation complete. To a first approximation, however, we have found a method to scale between laser-driven and nuclear blast waves, and to account for many of the blast-wave parameters. We use ϕ^5 scaling, combined with the assumption that average energy densities per unit mass of engulfed

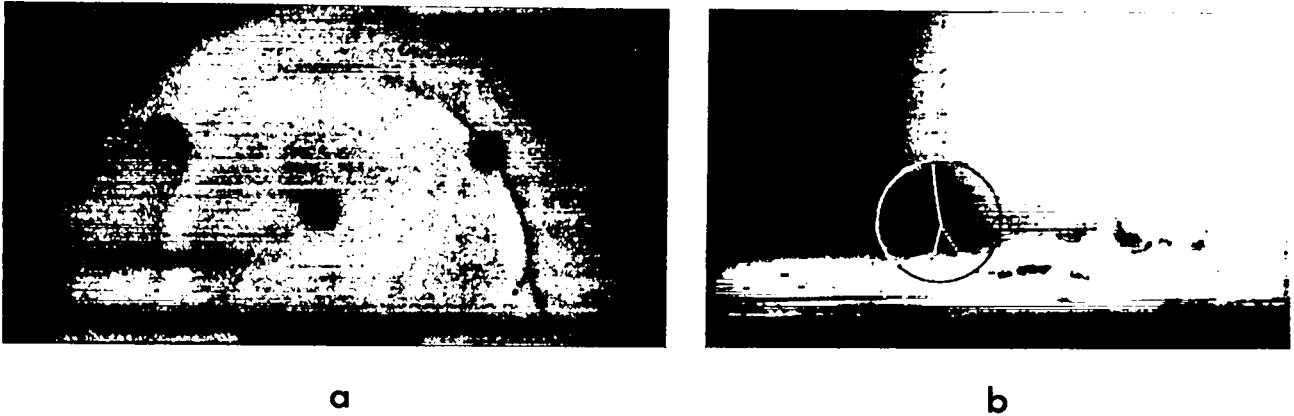


Fig. III-22.

Interaction between incident and reflected blast waves; (a) laser shadowgraph simulates blast wave of 22-kt nuclear explosion on an 86-m-high tower; (b) photograph of a nuclear blast (TEAPOT/MET, 22 kt on a 122-m-high tower).

air are the same for the two cases. Other parameters are thereby also matched: blast-wave velocities, temperatures, heat-capacity ratios, and density ratios across the shock front. Absolute pressure and density agreement is not achieved.

Using this approximate simulation method, we can show that the laser blast wave in Fig. III-22a simulates a 22-kt nuclear blast wave on an 86-m tower, rather than on the 122-m tower of Teapot/Met (Fig. III-22b). Computer calculations in progress will describe the two events in more detail for further comparison.

The sequence of shadowgraphs in Fig. III-23 shows the interaction of two blast waves produced by a pair of simultaneous laser pulses, each of 0.3-ns duration and ~ 30 -J energy. The targets were again spherical shells and were separated by 1.8 cm in 50 torr of air. Blast-wave energies were ~ 7.5 J each. The formation and development of the Mach stem between expanding blast waves are clearly visible. To first approximation, this laser multiburst event simulates sea-level nuclear multiburst environments for which $Y/S^3 = 4.6 \times 10^{-6}$, where Y is the yield of each nuclear event in kilotons, and S is the separation of the burst in meters. An example of the simulation specifies 130 m separation between 10-kt detonations.

This two-target experimental arrangement will serve as the principal geometry in experiments to be conducted for validation of existing hydrodynamic computer codes.

Opacity Experiments (J-Division's N. Hoffman, J. Mack, and L. Miller)

We carried out time-integrated spectroscopy of the emission from both sides of thin aluminum targets. Our goals were (a) to determine whether the emission from the backside had a Planckian spectrum, as expected for a shock-heated plasma in local thermodynamic equilibrium, and (b) to determine whether our back-side observations might be responding to front-side emission transported through the target.

Our back-side spectra are apparently contaminated by continuum emission from the laser-amplifier flash lamps, and goal (a) therefore has not yet been satisfied. Future efforts will include time-resolving the spectra by using a streak camera or optical gate and moving the spectrograph off the laser-beam axis.

Our back-side spectra show broad ($\sim 10 \text{ \AA}$), intense A/I resonance lines at 3944 and 3961.5 \AA . These lines seem to be formed on the front side of the target, and goal (b) therefore has been satisfied; front-side emission does indeed propagate through the target. The A/I lines generally show a central absorption feature, blue-shifted by as much as 1 \AA , indicating cool material traveling toward the spectrograph. This is evidence for the presence of unloading shocked material at the backside of the target.

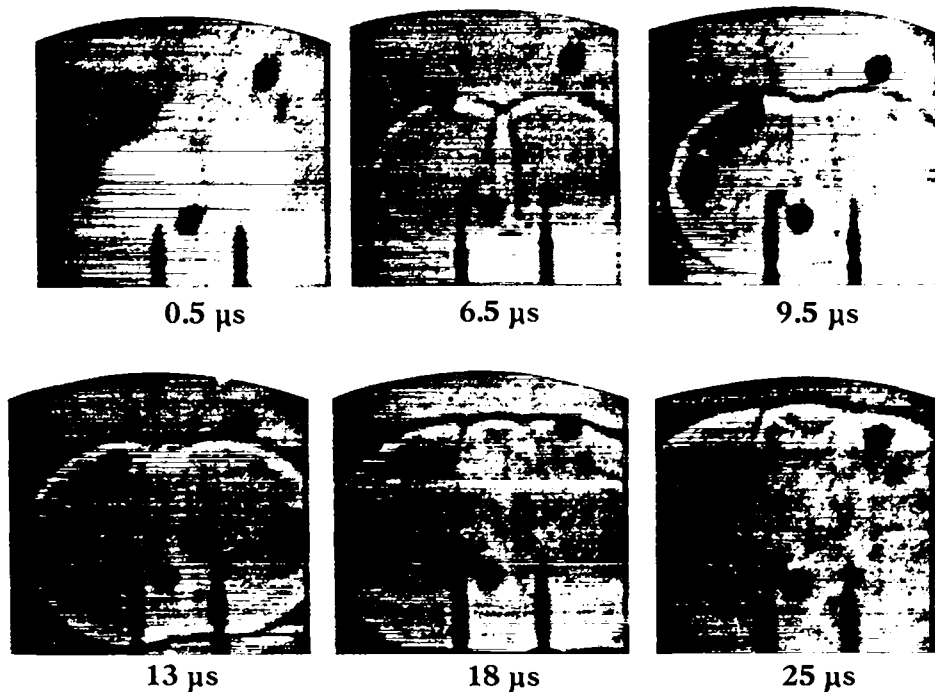


Fig. III-23.

Blast waves and Mach stems produced by two simultaneous laser-driven microfireballs of about equal yields.

We considered problems of transferring radiation whose frequency is near the plasma frequency, so that the refractive index of the plasma is significantly different from unity. This difference may arise in the emission of radiation by unloading shock waves. We also performed a derivation of the time-dependence of the brightness temperature of an unloading shock wave. The derivation is based on a discussion published by Zeldovich and Raizer.⁸ The authors suggested that observations of brightness temperature vs time in an unloading shock wave would allow an experimental determination of the material opacity. This is the technique we hope to use eventually.

THEORETICAL SUPPORT AND DIRECTION

Introduction

Our studies continued in areas of hot-electron generation, hot-electron transport, and critical-

surface stability. Careful LASNEX modeling has demonstrated that strong ponderomotive force effects can explain experimental results which, originally, had been thought to be evidence for anomalously inhibited electron thermal conduction. Calculations on vacuum insulation have been extended to spherical geometry with a self-consistent treatment allowing for return-current electron flow across the vacuum. Simulation studies of hot-electron generation by resonant absorption have been refined; and simulation studies and fluid modeling of critical-surface rippling phenomena have continued.

Reexamination of Strongly Flux-Limited Thermal Conduction in Laser-Produced Plasmas (S. J. Gitomer, D. E. Henderson, R. N. Remund)

General. In the following, we will construct a concept of laser-plasma interaction based on the effects

of ponderomotive forces. By using this *a priori* ponderomotive force and suprathreshold electrons generated by resonant absorption near the critical surface, we obtain very satisfactory agreement to the experimental data without invoking an anomalous flux limit or other nonclassical mechanism. The data include the x-ray and ion spectra produced and the fraction of laser light transmitted through thin foils. We have simulated these data for a variety of conditions at both 1.06 and 10.6 μm with the LASNEX code, modified to include the ponderomotive force and some simulation instruments. The classical nature of the model itself enhances its credibility.

There are two basic effects of long laser wavelengths: (1) the critical density at which the light is reflected is lower by a factor of wavelength squared (λ^2), and (2) the oscillating energy of a free electron in the wave field is higher, also by a factor of wavelength squared. It was previously believed that for longer wavelengths the lower critical density would occur much farther out in the plasma blown off the target, requiring the absorbed power to be transported farther through lower density plasma. Adequate thermal conductivity was thought to pose a problem so that the usefulness of longer wavelengths suffered, because greater oscillating energy provides a higher free energy to be converted into a hard, nonthermal tail on the electron distribution through a variety of detailed mechanisms. Remember that fuel compression must be nearly isentropic. By depositing heat in the fuel, the hot electrons make it more difficult to compress the fuel to the required ρR of 1.0g/cm². If the fuel is to be protected by a layer of high-Z material, this shielding material must also be heated and thus affects the energy economy or the efficiency of the pellet process. The numerical evaluation of these efficiencies is an objective of our target design work. The production of suprathreshold electrons, the absorption of laser energy, and the transport of both the heat energy and of those suprathreshold electrons are features of the interaction model discussed here.

Energy Transport. We began our experiments on thin plastic foils in 1973 with 1.06- μm Nd:glass lasers, and continued these experiments with 10.6- μm CO₂ lasers. The measured quantities, indicated

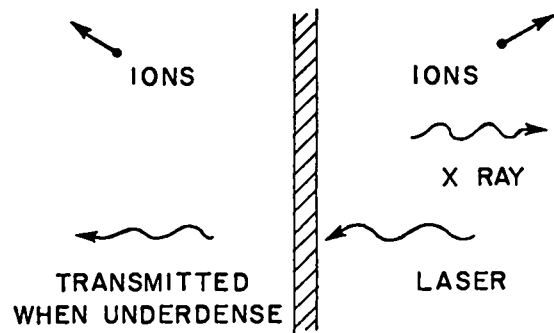


Fig. III-24.

Illustration of energy-transport in thin-foil experiments.

in Fig. III-24, included the x-ray Bremsstrahlung spectra emitted, the plasma ion current collected as a function of time of flight, and the amount of light that eventually penetrated the thin foil. The first finding, then a new phenomenon, revealed that very fast ions were produced from both sides of the thin film. Because the energy was sufficient to penetrate the film's areal mass, we concluded that they were produced on both surfaces by nonthermal electrons, which were themselves inferred to exist from x-ray spectra. Charge and mass were assigned to portions of the ion time-of-flight signal, and we concluded at that time that 90% of the laser energy resided in these fast ions.⁹

The fraction of laser light transmitted was compared with that calculated, assuming that all the light intensity was transmitted after the film had ablated away to become subcritical and that none had been transmitted before. (The experiment was not time-resolved.) The conclusion was that disassembly was too slow: the calculated fraction of light transmitted was too high. A hypothesis advanced at that time suggested that the heat flux was "anomalously" reduced to some value below the usual Spitzer formula and below the usual kinetic limit.^{9,10} According to this hypothesis, only a thin layer was heated to a very high temperature. The layer ablated away as hot ions. With less heat transmitted into the bulk material, the film took longer to become underdense and to transmit the light.

Soon after obtaining the LASNEX code from Lawrence Livermore Laboratory, we used its hot-electron capability to model this problem. Our finding was that the presence of hot electrons alone was sufficient to produce the fast ions and that no special reduction in conductivity was needed.¹¹ An equally important development was the experimental determination of the various masses associated with the time-of-flight data. We have concluded in the meantime that the previous interpretation was in error. Our present belief is that only 10 to 20% of the laser energy is found in the fast ions.¹²

The LASNEX Code. Our main hydrodynamics tool is now the LASNEX code. We have added several "instrument" packages to simulate time-of-flight ion signals and to measure the fraction of the light transmitted through the target. We have modified the code to include the ponderomotive force:

$$F = -(\omega_p^2/\omega_0^2) \Delta \left(\Psi_T/2c \sqrt{1-\omega_p^2/\omega^2} \right). \quad (1)$$

Here Ψ_T is the total intensity due to the many rays which may pass through a given spatial zone in various directions. The radical is the dielectric coefficient which swells the electric part of the wave.

This form for the ponderomotive force results in a delta-function force inward at the critical point R_c . It also results in a distributed outward force outside this point. The effect helps to "dig out" a lower plateau. The jump in pressure is matched to the momentum from the laser and so must come out correctly. The separate upper and lower density plateaus are found to be in agreement between LASNEX¹¹ and our WAVE¹³ simulations. It is important to verify these results experimentally by using synchronized interferometers. Analogous experiments with microwaves rather than lasers are under way at University of California, Davis, and at the University of California, Los Angeles/TRW.

The steep profile and its trajectory are clearly illustrated in Fig. III-25. Here the Lagrangian mass points obtained in a one-dimensional calculation are plotted against time. (The laser is impinging from the right.) Without ponderomotive force these hydrodynamic calculations do not produce such a steep gradient.

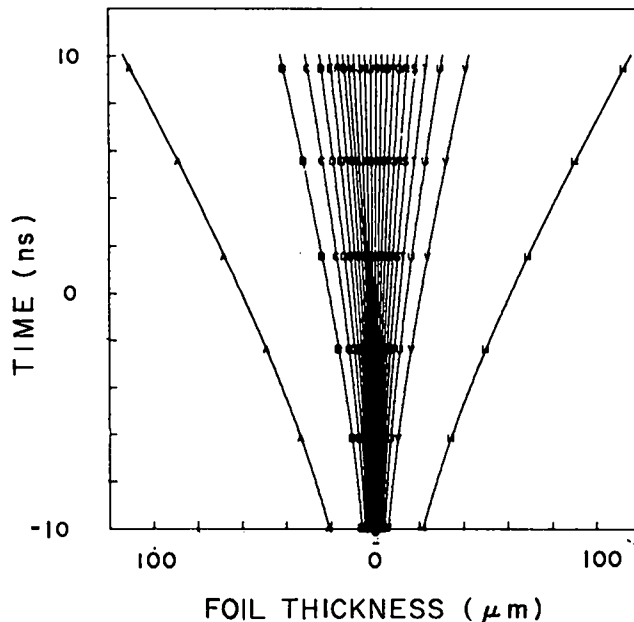


Fig. III-25.

A time-vs-position plot from a LASNEX calculation of a thin-foil experiment.

The hot-electron generation is associated with resonant absorption at the steep (modified) gradient.¹⁴ Resonant absorption was considered early in the program but was neglected because it requires a steep profile to be significant. There are angular and polarization dependences that have been used to infer the scale of the steep gradient and to verify the model. At the intensities of interest we find the scale lengths for 1.06 μm coincidentally equal to one wavelength. For 10.6- μm experiments the scale length is shorter, much less than a wavelength. This means that in some ways it is accurate to consider a skin effect, such as the reflection of a long radio wave from the steep interface at a metal surface. Our WAVE plasma simulations show that the hard spectrum is Maxwellian at a hot temperature of

$$T_h = |\alpha| [P\lambda^2/10^{17} \text{ W}\mu\text{m}^2/\text{cm}^2]^{1/4} [T_c/1 \text{ keV}]^{1/2} \text{ keV}. \quad (2)$$

Here T_c is the temperature of the cold (background) distribution and $|\alpha|$ is a parameter. With $|\alpha| = 20$, we obtain a good fit to both the WAVE simulations and the experimental data. A fraction of the laser

energy that reaches the turning point is dumped into the hot distribution. This fraction is taken to be about one-quarter to one-third, again in agreement with both plasma simulations and experiments.

Results. Results obtained with our model in LASNEX calculations were compared with experimental data. The application of the results to the light-transmission data is indicated in Fig. III-26. Here the intensity from the laser and that calculated to be transmitted are plotted as a function of time. This form taken is $[\sin(\alpha t)/(\alpha t)]^2$, which is appropriate for the modelocked Nd:glass laser; it results in the small pulses after the major pulse at time zero. Fig. III-27 illustrates that the ponderomotive force has little effect until the intensity rises. This point in time coincides with the optical pressure driving a shock wave on the upper plateau. Once the light has burned (ablated) through the foil, the ponderomotive force disappears and the more rapid drop in maximum electron density resumes. The laser is transmitted through the foil when the electron density drops below the critical value of $10^{21}/\text{cm}^3$.

The good fit obtained to the fractional transmitted energy data for foils of various thickness is shown in Fig. III-28. Only the case calculated with

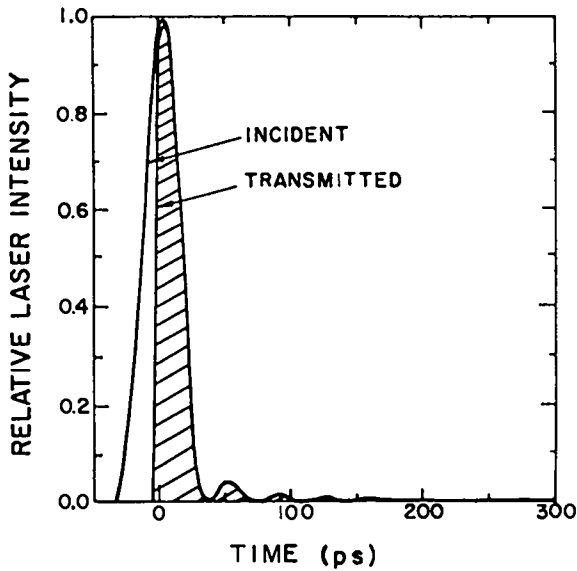


Fig. III-26.

Time history of incident and transmitted laser intensity in calculated thin-foil experiment.

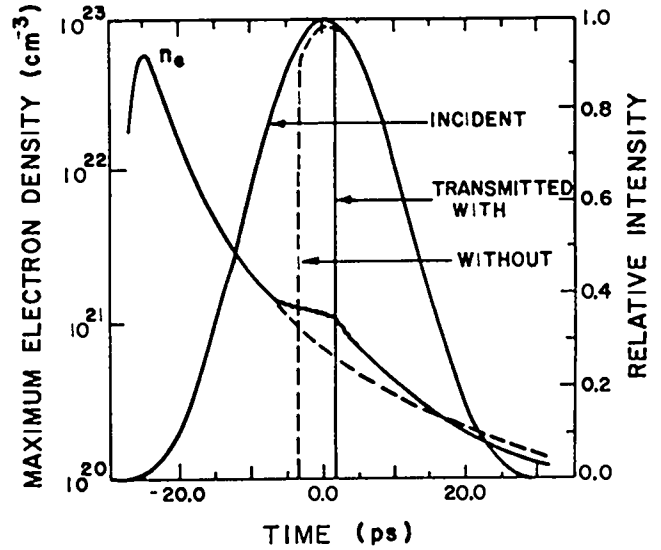


Fig. III-27.

Detail of a portion of Fig. III-26 for calculations with and without ponderomotive force.

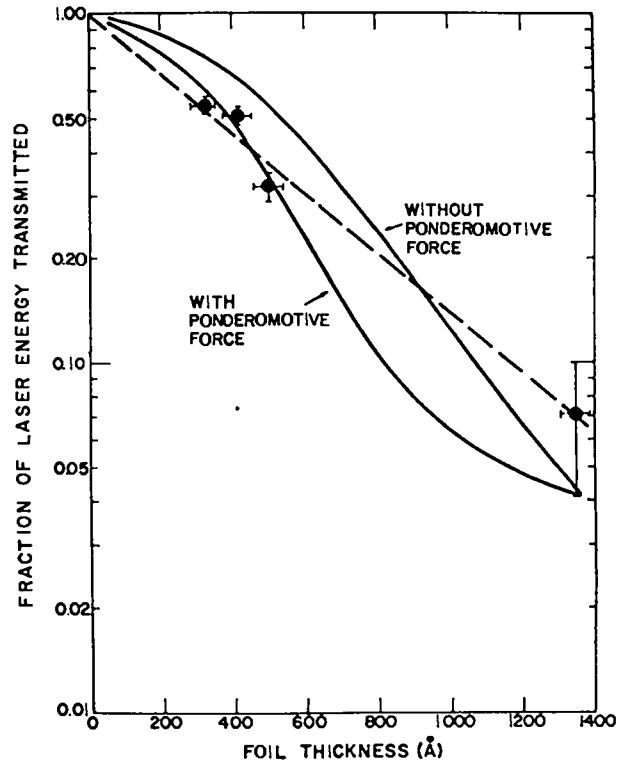


Fig. III-28.

Comparison of calculated net transmission fraction vs foil thickness with experimental data.

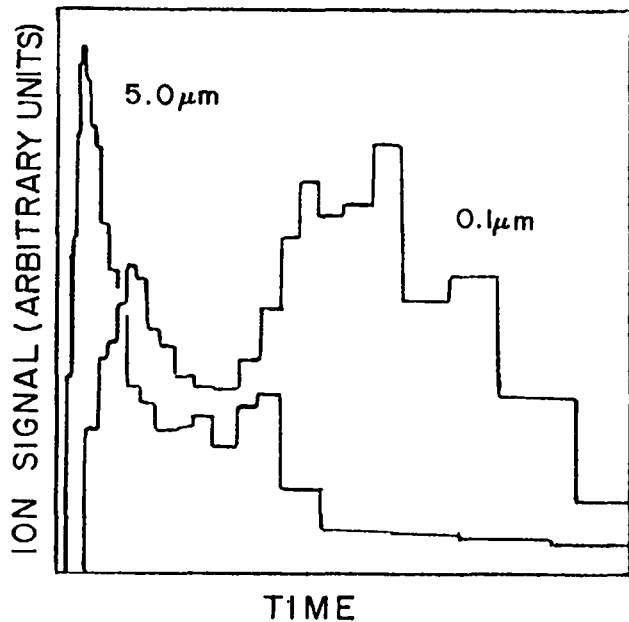


Fig. III-29.

Computed ion time-of-flight data for 10- μm irradiation. (The arbitrary scales are different for the two plots.)

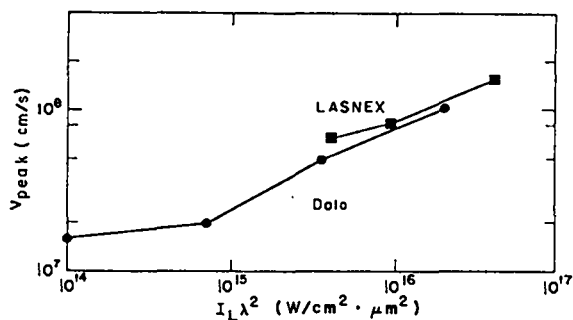


Fig. III-30.

Velocity of peak signal vs intensity times wavelength-squared ($I\lambda^2$) from LASNEX modeling and from experimental data.

ponderomotive force has the shape of the experimental data curve. The straight dashed line is a least square error fit to an exponential form. The effect of the ponderomotive force is easy to understand: with pressure on one side, disassembly can proceed only through the other side and it takes longer. Incidentally, the thickest data point in the simulation corresponds to the transmission of the

subsequent pulses in the modelocked laser pulse train shown in Fig. III-26. No *ad hoc* adjustment of the pulse shape, of the transport coefficients, or of the flux limit is required.

Some calculated ion time-of-flight data for the 10.6- μm laser irradiation are shown in Fig. III-29. The familiar two-humped distribution is found to depend upon the distribution of suprathermal electrons, on laser intensity, and on material thickness. Figure III-30 illustrates the good match of LASNEX and experimental data. Originally, we obtained such agreement by *adjusting* the hot-electron strength, as noted herein. Here, we have implemented an *a priori* algorithm from theory and simulations which produce the hot-electron distribution automatically. This approach is successful as shown by the LASNEX points in Fig. III-31. These points were found indirectly, being hot-electron temperature. The bremsstrahlung x rays from which they are primarily deduced are also in agreement with the data, as shown in Fig. III-32.

The objective of our thin-film experiments was the production of films thin enough to heat through before any hydrodynamic response occurred. At high temperature, the conductivity is high, and the foil therefore should be isothermal and disassemble symmetrically. This did not happen: the thinnest foils just moved away from the laser. As already discussed, we thought at that time that the conductivity was not high enough. Our present analysis, however, shows that the thin films were isothermal after all, but that the density was not symmetric and that, consequently, the flow field was also

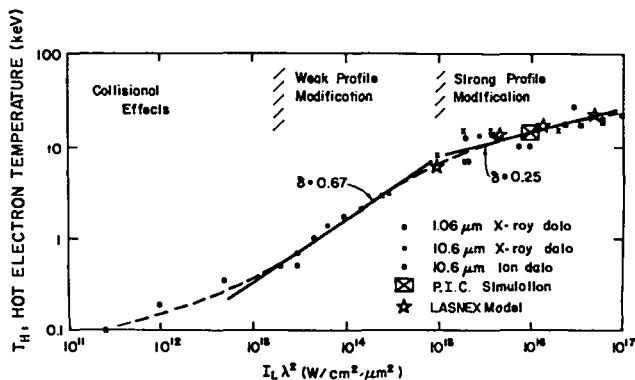


Fig. III-31.

Suprathermal electron "temperature" inferred from experiments and simulations vs $I\lambda^2$.

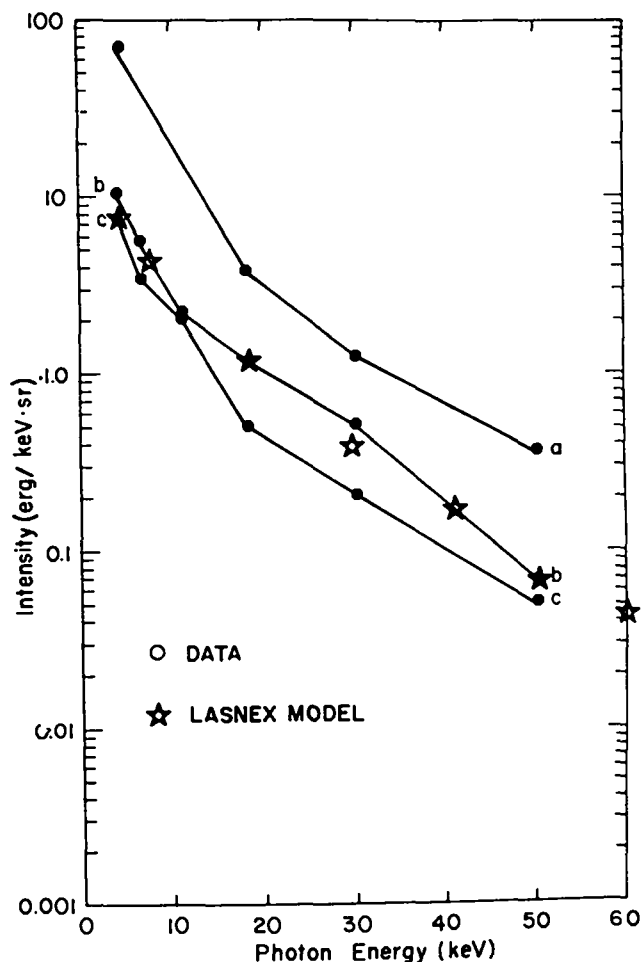


Fig. III-32.

Differential x-ray spectra calculated with the LASNEX model and from experiments.

asymmetric. As the films are made successively thinner, the center-of-mass motion from the ponderomotive force becomes more significant. As an extra success of this model, we show in Fig. III-33 the speed of the fastest ions seen from the side turned away from the laser to that on the laser side. The eventual falloff at $\sim 1.0 \text{ mg/cm}^2$ is interpreted to imply that the hot electrons have temperatures of 10 to 20 keV. Calculated and experimental data agree well. Note, though, that the low-mass intercept does not go to unity as the explanation would require. This deviation is due to the acceleration of the center of mass of the whole film by the ponderomotive force. Indeed, experiments with the thinnest foil

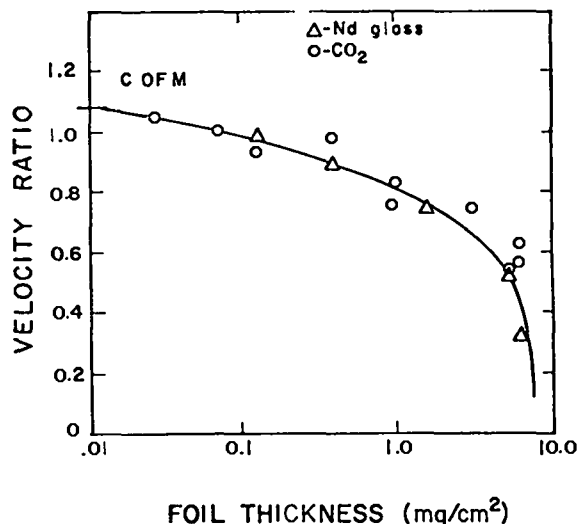


Fig. III-33.

Plot of ratio of maximum ion velocity on the two sides of the foil vs foil thickness.

show only that the whole mass is driven away, with no signal on the laser side.

Vacuum Insulation in Spherical Geometry (K. Lee)

Introduction. It is generally agreed that resonant absorption is the dominant absorption mechanism in current high-power laser-target interaction experiments. Simulations show that the absorbed laser light energy is carried away from the absorption region by suprathermal electrons. These electrons can adversely affect target performance by preheating the fuel and/or degrading pusher action. The fuel can be shielded against suprathermals with high-Z material, but the additional mass can degrade target performance. Without suffering a mass penalty, a vacuum can be an effective insulator against suprathermal electrons. Vacuum insulation has been analyzed in previous reports for plane geometry. The analysis is extended here to spherical geometry.

Discussion. If hot electrons are generated at radius r_H with a temperature T_H and density n_H , their transport from shell to shell across the vacuum

is inhibited by a potential well created by the electron space charge. Consider the case in which the inner pellet consists of a cold plasma with electron density n_c and electron temperature T_c at radius r_o . The electrical potential distribution between r_m and r_H , where r_m is the location of the maximum potential and is governed by

$$\frac{\partial}{\partial r} (r^n \frac{\partial \phi}{\partial r}) = \frac{J_H^* r_H^n}{2} \left\{ e^{(\phi - \phi_m)} \left\{ 1 + \text{ERF} [(\phi - \phi_m)^{0.5}] \right\} + \alpha e^{\alpha^2 (\phi - \phi_m)} \text{ERFC} [\alpha (\phi - \phi_m)^{0.5}] \right\}; \quad (3)$$

and the potential distribution between r_m and the inner-pellet radius r_o is governed by

$$\frac{\partial}{\partial r} r^n \frac{\partial \phi}{\partial r} = \frac{J_H^* r_H^n}{2} \left\{ e^{(\phi - \phi_m)} \text{ERFC} [(\phi - \phi_m)^{0.5}] + \alpha e^{\alpha^2 (\phi - \phi_m)} \left\{ 1 + \text{ERF}[\alpha(\phi - \phi_m)^{0.5}] \right\} \right\} \quad (4)$$

where

$$J_H^* = en_H \left(\frac{T_H}{2\pi m_e c} \right)^{0.5} e^{\phi_m}$$

$$\text{ERF}(x) = 2/\sqrt{\pi} \int_0^x e^{-t^2} dt$$

$$\text{ERFC}(x) = 1 - \text{ERF}(x)$$

$$\alpha^2 = T_H/T_c$$

Also, the potential is normalized to T_H , and the maximum normalized potential ϕ_m is negative. The radius r is normalized by the nonelectron Debye length; and J_H^* is the hot-electron current density transmitted across the vacuum.

The above equations assume that the electrons have only radial motion with no transverse velocity. The current transmitted across the vacuum gap calculated by the above equation represents an upper limit. For a vacuum gap large compared to the inner pellet radius simulations show that the transmitted current corresponding to an isotropic

electron distribution can be reduced by more than 50% from that calculated here.

For plane geometry the power coefficient n is equal to zero, and both equations can be analytically integrated once. For spherical geometry ($n = 2$), the above equations can only be solved numerically by iteration. For $T_H/T_c \gg 1$, r_o is nearly equal to r_m ; thus, the vacuum-gap distance is well approximated by $(r_H - r_m)$ and only the first equation needs to be solved. In the previous report (LA-6834-PR) we found for plane geometry that the transmitted current across the vacuum is insensitive to the ratio of T_H/T_c and N_c/N_H , provided $T_H/T_c \gg 1$. This is also the insensitivity for spherical geometry. Figure III-34 shows the normalized transmitted current density at the inner pellet radius as a function of vacuum gap for plane geometry and spherical geometry with inner pellet radii of 100 and 400 hot-electron Debye lengths, respectively. For a hot-electron temperature of 30 keV and a density of $10^{16}/\text{cm}^3$, 100 D corresponds to 175 μm . Figure III-35 shows the normalized transmitted-current density at the inner pellet radius vs the ratio of vacuum gap and inner pellet radius for vacuum gaps of 50, 100, and 200 hot-electron Debye lengths.

Due to electron space charge in the vacuum-gap region, the current density at the inner pellet radius increases only as $1/r_o$, which is weaker than the $1/r_o^2$ dependence expected for free-streaming electrons. If the transmitted current density at the inner pellet radius is normalized to its plane-geometry value the dependency shown in Fig. III-35 can be given by one universal curve shown in Fig. III-36.

In conclusion, Fig. III-36 shows that the transmitted current density for spherical geometry deviates only slightly from that for plane geometry if the vacuum gap does not exceed the inner pellet radius. Our conclusion that vacuum insulation is effective for plane geometry is also true for spherical geometry.

Hot-Electron Modeling (D. W. Forslund, J. M. Kindel, and K. Lee)

The model for the absorption of very intense laser light into a suprathermal electron tail in the

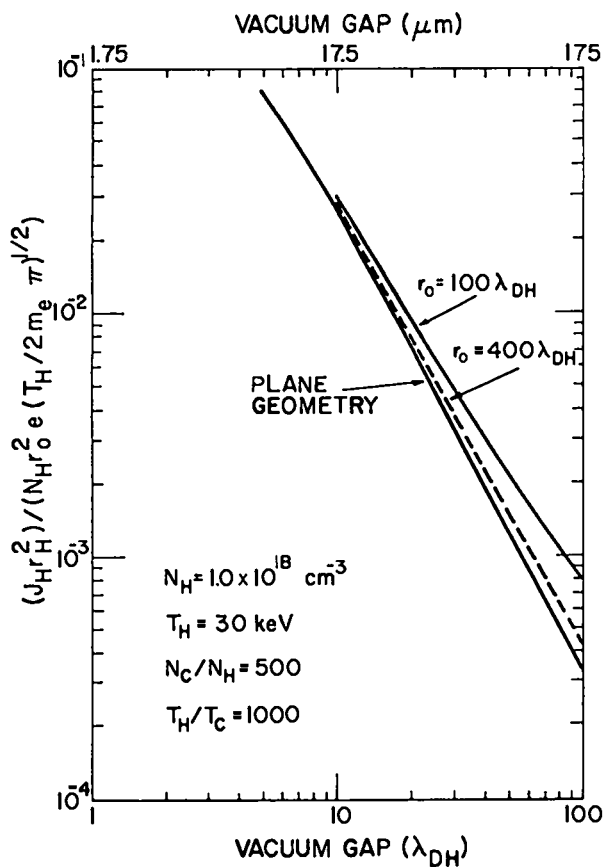


Fig. III-34.

Ratio of current density incident on inner pellet radius to emitted current density as a function of vacuum-gap size for inner pellet radii of 100 and 400 D . The corresponding dependence for plane geometry is also plotted.

presence of the self-consistently steepened electron density profile has been refined continually to understand the microscopic process and to use the model in hydrodynamics calculations. The electron distribution has been characterized more precisely; more simulations have been done to obtain a statistically more accurate scaling law; and the scaling laws for the structure of the localized plasma wave, which is providing the absorption, have been measured.

We find that the high-energy electron distribution deviates only slightly from a Maxwellian over a wide range of energy as shown in Fig. III-37. This finding has important implications in target design and apparently is due to the fact that the coherent electron acceleration is localized. Because the distribution is

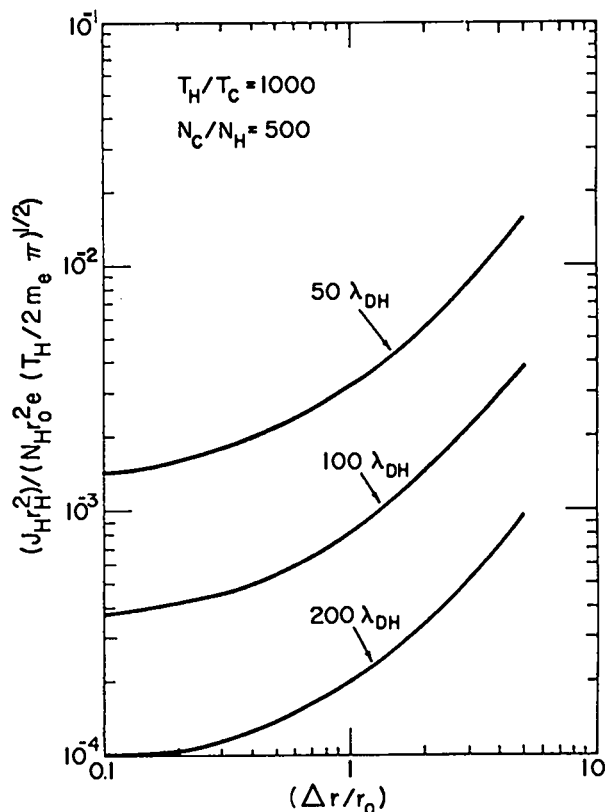


Fig. III-35.

Ratio of current density incident on inner pellet radius to emitted current density as a function of ratio of vacuum-gap size to inner pellet radius.

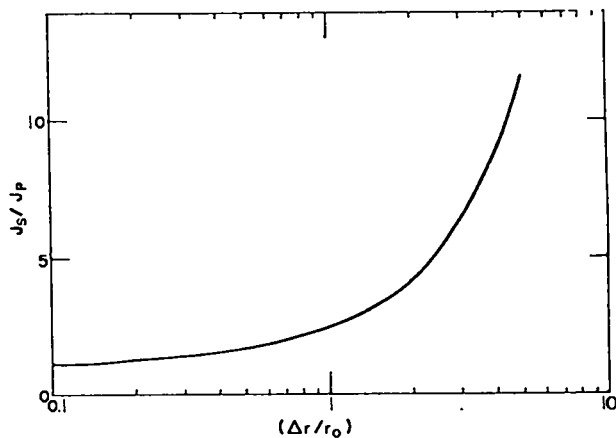


Fig. III-36.

Ratio of transmitted current density in spherical geometry to plane geometry as a function of ratio of vacuum-gap size to inner pellet radius.

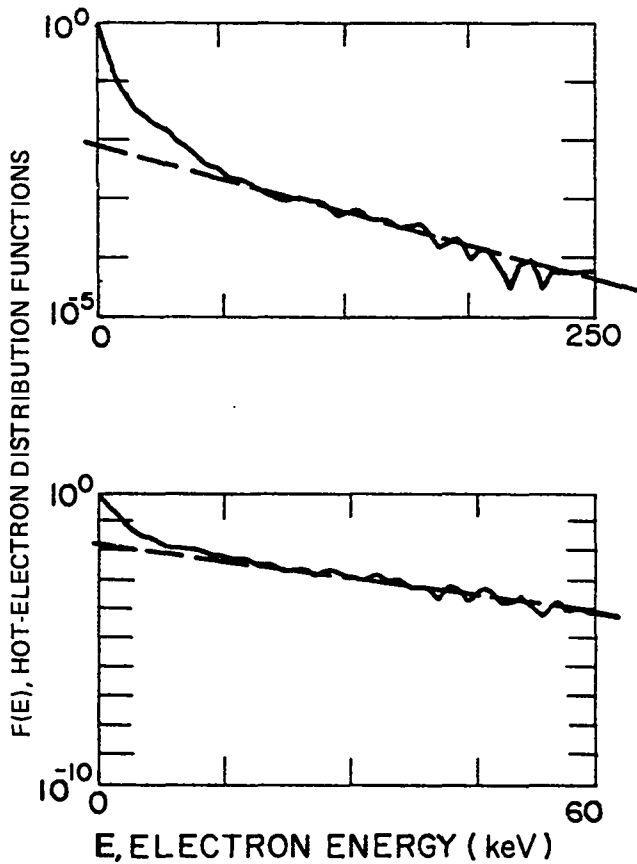


Fig. III-37.

Typical hot-electron distribution functions $F(E)$ vs E . Note the excellent fit to a Maxwellian distribution at high energies.

essentially Maxwellian, the hot-electron temperature-dependence wavelength for an intensity of 10^{16} W/cm² can be plotted as shown in Fig. III-38. The best fit to these data is

$$T_H = 14(I\lambda^2)^{1/3} T_C^{1/3}, \quad (5)$$

where the T_C dependence is obtained by varying the background temperature; $I\lambda^2$ is in units of 10^{16} W · μm/cm²² and T_C is in keV. This scaling law would predict a more rapid dependence on $I\lambda^2$ than experimentally observed for a fixed T_C . However, T_C itself may not be independent of intensity. In fact, the deviation of this scaling law from the experimental points is not statistically significant, as can be seen in Fig. III-39 where the simulation points are plotted along with the experimental data. Using power

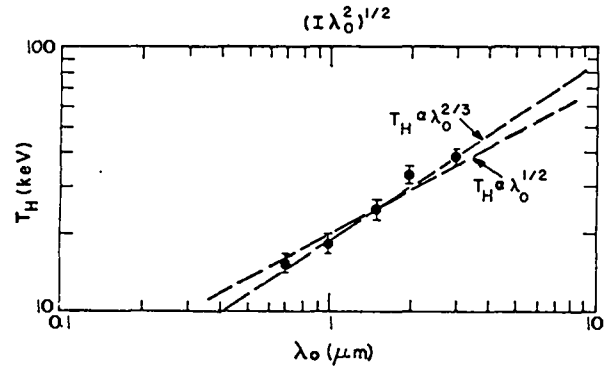


Fig. III-38.

Measured hot-electron temperature as a function of laser wavelength for simulations with intensity equal to 10^{16} W/cm² and a background electron temperature $T_C = 2.5$ keV, the light wave incident at 20° to the electron density gradient and polarized in the plane of incidence.

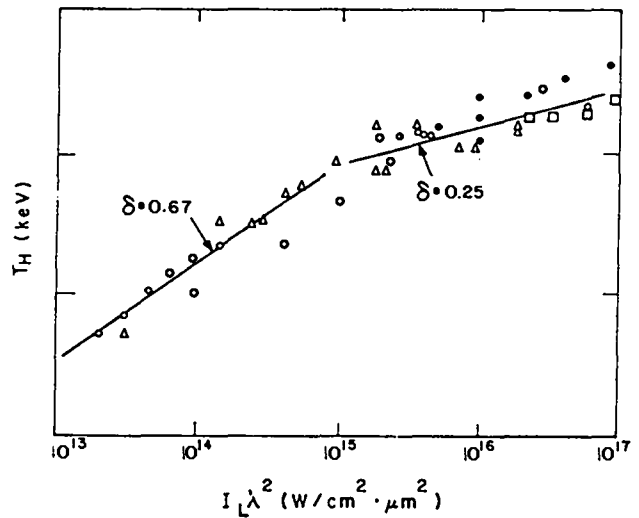


Fig. III-39.

Hot-electron temperature as a function of laser intensity times the square of the wavelength. The measurements obtained from x rays are shown with triangles for 1.06 μm and with open circles for 10.6 μm. The squares correspond to temperatures for 1.06 -μm ion data. The closed circles correspond to the simulation results. The solid curves are fit to the data of the form $T_H \propto (I\lambda^2)^\delta$.

balance to determine the hot-electron generation density n_h , we find

$$\frac{n_h}{n_c} = 2\alpha \left(\frac{I\lambda^2}{T_c} \right)^{1/2}, \quad (6)$$

where n_c is the critical density and α is the absorption coefficient, typically $\sim 1/3$. The sharp density equilibrium appears to persist even when $n_h \sim n_c$ in the simulations. In fact, the experimental data indicate that above $3 \times 10^{18} \text{ W} \cdot \mu\text{m}^2/\text{cm}^2$ the hot-electron temperature produced is less than that which would be produced by the classical flux limit.

Careful measurements of the plasma-wave structure in a sharp density gradient have been completed as illustrated in Figs. III-40 and 41. In Fig. III-40, we show the dependence of the plasma-wave scale length on $I\lambda^2$ and find that $L_p/\lambda_0 \approx (I\lambda^2)^{-1/4}$. In addition, we find that L_p is proportional to $T_c^{1/3}$, as shown in Fig. III-41. Both scalings tend to support the hypothesis that $T_H \sim E_p L_p$ in the localized plasma wave when one compares to the empirical form for T_H .

The above scaling law of T_H with intensity and temperature has been used in the LASNEX simula-

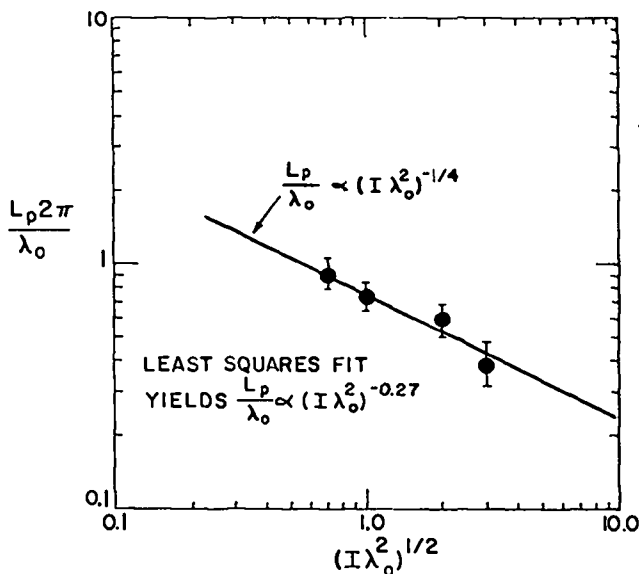


Fig. III-40.

The excited-plasma-wave scale length as a function of $I\lambda^2$ as measured from plasma simulations.

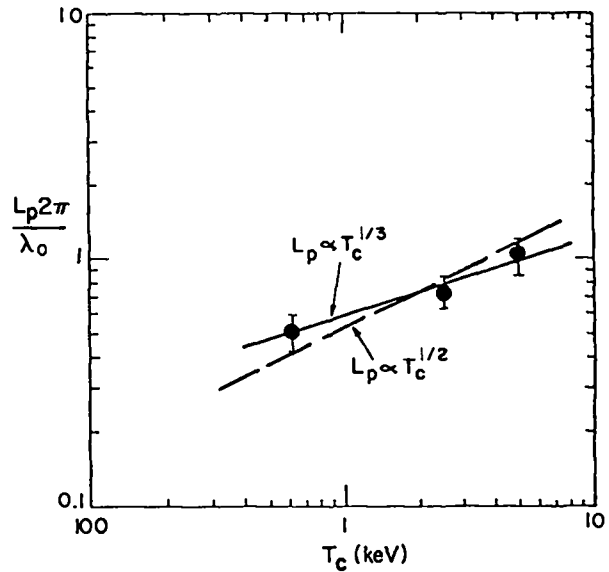


Fig. III-41.

The excited-plasma-wave scale length as a function of cold-electron temperature T_c as measured in plasma simulations.

tion code to obtain better agreement between hydrodynamics calculations and experiments.

Critical-Surface Stability (D. W. Forslund, J. M. Kindel, E. L. Lindman)

At a high laser intensity the laser ponderomotive force leads to a highly steepened laser-plasma interface, that is, the critical density resides in a region in space where the density rises from subcritical values to as much as several hundred times critical density over a distance of a few micrometers. We have previously mentioned (LA-6616-PR, p. 47) our initial efforts to understand the plasma stability of such an interface. Here we summarize our understanding of the linear and nonlinear properties of this instability.

We consider a surface displacement $\xi(x)$ of wave number K_y , where x is the direction of the density gradient and y is the infinite homogeneous or periodic direction. This is shown schematically in Fig. III-42. The shaded region is the plasma and the incoming laser light is shown propagating through the vacuous or subcritical plasma toward the laser-plasma interface; $E_0 \approx E_0 \hat{e}_z$ is the laser electric field,

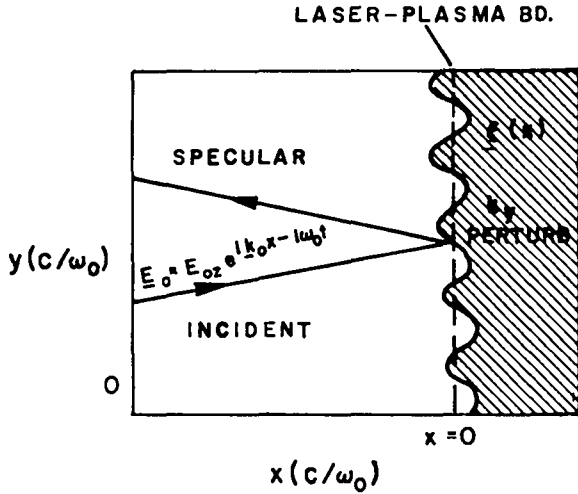


Fig. III-42.

Diagram of geometry for sharp-boundary stability calculation showing the perturbation at the laser-plasma interface.

k_0 is the wavenumber, and ω_0 is the frequency. For polarization out of the plane of incidence our understanding of the linear properties of the instability may be summarized as follows:

- The instability for $cK_y/\omega_0 \leq 1$.
- The growth rate $\gamma \sim (M_i)^{-1/2} E_0$.
- The real part of the ion wave frequency is zero for normally incident laser light, nonzero for oblique incidence.
- A theory with no dissipation predicts instability of polarization in and out of the plane of incidence.

Instability is determined by solving in zero and first order the vector wave equation for the electric fields and the ion density fluctuation. Either one solves the equations with first-order time variations in the electric field and with second-order time variations in the quasineutral ion equation, or one solves the equations by Fourier-analyzing in time. The latter method automatically allows a determination of the conditions for absolute instability.

Typical eigenfunctions for this instability, which ripples the laser-plasma interface, are shown in Fig. III-43. The self-consistent density profile is shown in Fig. III-43a, the low-frequency density-fluctuation amplitude n_L in units of critical density n_c is shown in Fig. III-43b, and the amplitude of the scattered wave is shown in Fig. III-43c. Parameters for the calculations are as follows:

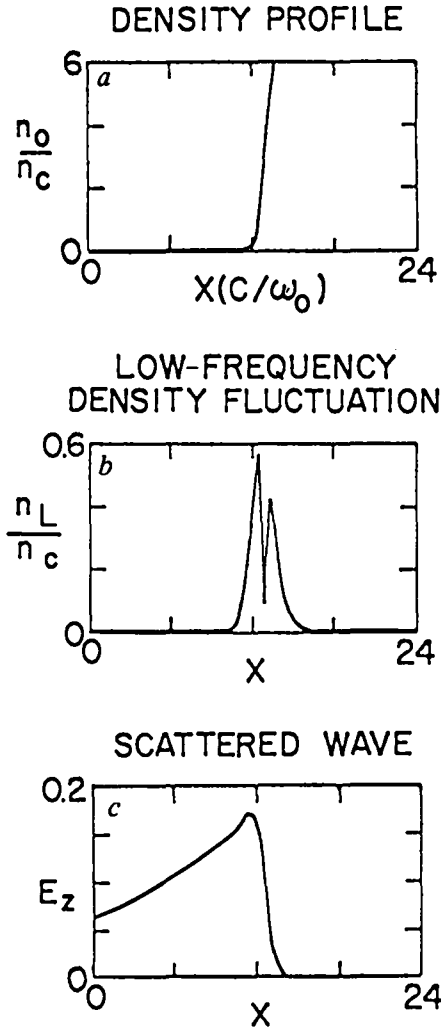


Fig. III-43.

Typical eigenfunctions for the instability; (a) the equilibrium density profile; (b) the low-frequency fluctuating density amplitude; (c) the amplitude of the scattered wave.

$$v_0/v_e = \frac{eE_0}{m_e \omega_0 v_e} = 2.4 ,$$

$$cK_y/\omega_0 = 0.6 ,$$

$$M_i/M_e = 25 , \tag{7}$$

and the laser light is normally incident.

For the same conditions as in the previous calculation, we can plot in Fig. III-44 the growth rate as a function of perpendicular wave number.

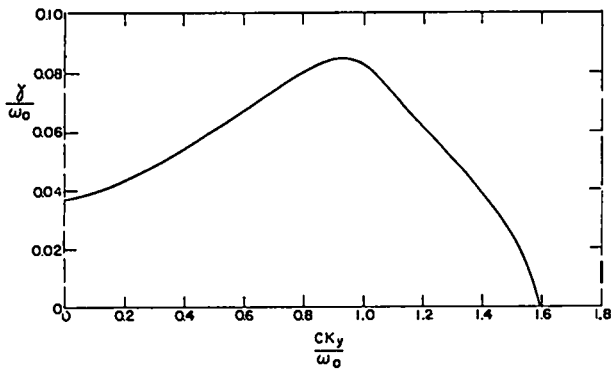


Fig. III-44.

Growth rate of the most unstable mode vs perpendicular wave number of the excited low-frequency wave.

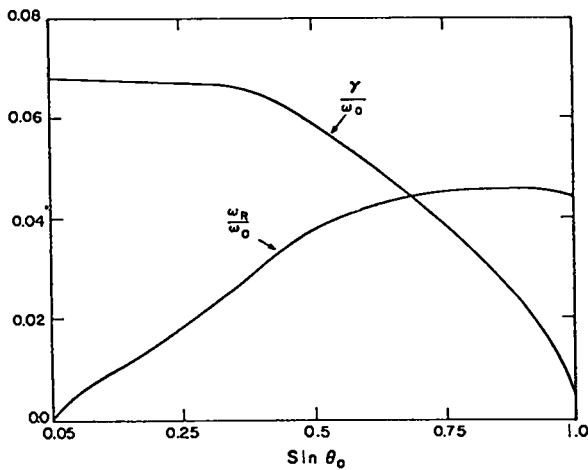


Fig. III-45.

Growth rate and real frequency of most unstable mode as a function of angle of incidence.

Note that the growth rate sharply cuts off for ck_y/ω_0 near 1.0. In Fig. III-45 we plot the growth rate and real frequency in units of ω_0 as a function of $\sin \phi_0$ where ϕ_0 is the angle of incidence of the incoming laser light. The real frequency becomes as large as the ion acoustic frequency, whereas the growth-rate curve stays relatively flat over typical angles of incidence in experiments.

Finally, several simulations have been carried out to isolate the nonlinear behavior of this instability. Simulations in this regime, however, are difficult because of the large amounts of computer time required. Typically, the noise levels in the simulations are high enough that growth rates at the onset are

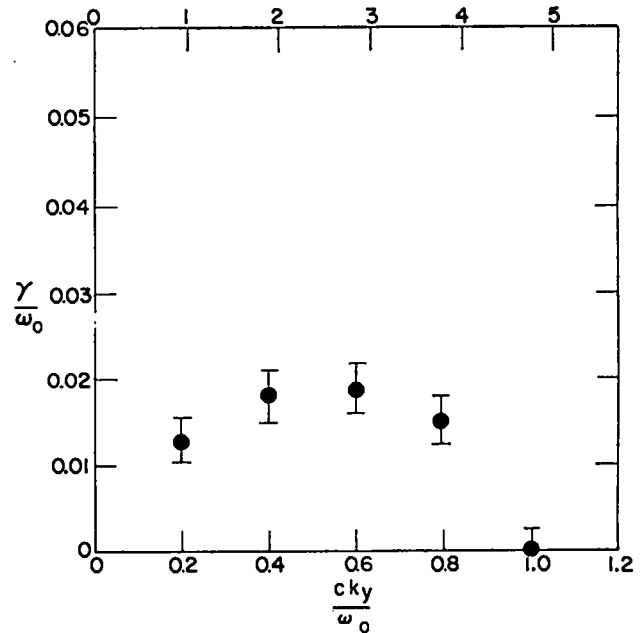


Fig. III-46.

Growth rates as a function of perpendicular wave number as determined by simulation.

somewhat reduced over those predicted in linear theory. Some effort is being made to remedy this situation. The growth rate in a simulation corresponding to the previous set of parameters is shown in Fig. III-46 as a function of perpendicular wave number or equivalently perpendicular mode number. Growth rates are more than 50% less than predicted by theory. Additionally, growth rates peak near $ck_y/\omega_0 \approx 0.5$.

Previously (see LA-6616-PR, p. 47, and LA-6510-PR, p. 88) we have presented simulation results which showed bubble formation as one nonlinear state of this instability. This was only true for polarization out of the plane of incidence. For polarization in the plane of incidence, no stability developed. We cannot yet explain the difference between polarization in and out of the plane of incidence although we suspect the difference is due to the added kinetic dissipation of the excited high-frequency waves in the plane-of-incidence case. Finally, for arbitrary polarization with equal components in and out of the plane of incidence, we observe saturation of the instability as soon as a significant component of the high-frequency electric field exists along the gradient of the excited low-frequency density fluctuation.

REFERENCES

1. J. N. Olsen, G. W. Kuswa, and E. D. Jones, *J. Appl. Phys.* **44**, No. 5, 2275 (1973).
2. R. L. Fleischer, P. B. Price, and R. M. Walker, *Nuclear Tracks in Solids; Principles and Applications* (University of California Press, 1975).
3. Kodak Pathe Nitrocellulose Film CA 80-15 is available from Eastman Kodak Co., Scientific Photography, 343 State Street, Rochester, New York.
4. W. D. Jones and R. V. Neidigh, *Appl. Phys. Lett.* **10**, 18 (1975).
5. H. B. Luck, *NIM* **119**, 403 (1974).
6. J. E. Crow, P. L. Auer, and J. E. Allen, *J. Plasma Phys.* **14**, 65 (1975).
7. C. G. M. vanKessel, "Shock Compression of Plane Targets by Laser Ablation," *Z. Naturforsch* **30a**, pp. 1581-1593 (1975).
8. Ya. B. Zeldovich and Yu. P. Raizer, *Physics of Shockwaves and High-Temperature Hydrodynamic Phenomena, II, XI* (Academic Press, New York, 1966).
9. A. W. Ehler, D. V. Giovanielli, R. P. Godwin, G. H. McCall, R. L. Morse, and S. D. Rockwood, Los Alamos Scientific Laboratory report LA-6511-MS (1974).
10. R. C. Malone, R. L. McCrory, and R. L. Morse, *Phys. Rev. Lett.* **34**, 721 (1975).
11. S. J. Gitomer, D. B. Henderson, and R. N. Remund, *IEEE Int. Conf. on Plasma Science*, 77CH1205-4NPS, Paper 403, p. 144 (IEEE, New York, 1977).
12. D. V. Giovanielli, D. B. Henderson, G. H. McCall, and R. B. Perkins, *IEEE/OSA CLEA conference paper* (1977).
13. D. W. Forslund, J. M. Kindel, K. Lee, and E. L. Lindman, *Phys. Rev. Lett.* **36**, 35 (1976); D. W. Forslund, J. M. Kindel, K. Lee, E. L. Lindman, and R. L. Morse, *Phys. Rev.* **A11**, 679 (1975); K. G. Estabrook, E. J. Valeo, and W. L. Kruer, *Phys. Fluids* **18**, 1151 (1975).
14. D. W. Forslund, J. M. Kindel, and K. Lee, *Phys. Rev. Lett.*, to be published.

IV. LASER FUSION TARGET FABRICATION

Our pellet fabrication effort, supported by extensive theoretical investigations, supplies the thermonuclear fuel packaged in a form suitable for laser-driven compressional heating experiments. These targets range from simple deuterated-tritiated plastic films to frozen DT pellets to complex DT-gas-filled hollow microballoons, mounted on ultrathin supports and coated with various metals and/or plastics. Numerous quality-control and nondestructive testing techniques for characterizing the finished pellets are being developed.

INTRODUCTION (R. J. Fries)

In our target fabrication effort, we are developing techniques and methods to fabricate spherical targets containing DT fuel in a variety of chemical and physical forms. High-pressure DT gas has been used extensively as the fuel because it can be packaged conveniently in glass or metal microballoons for use as laser fusion targets. However, the designers and experimentalists would prefer a higher density of DT fuel than can be obtained conveniently in gaseous form. In addition, significantly better yields are predicted if the fuel can be formed as a high-density shell surrounding either a vacuum or a low-pressure spherical core because it is then unnecessary to work against the high pressure of the inner fuel core during the compression of the spherical fuel shell. These considerations have led to our development of methods to condense layers of cryogenic DT, either liquid or solid, onto the inside surfaces of microballoons. In addition, we are developing techniques to prepare room-temperature solids containing fuel atoms at high density (for example, polyethylene, lithium hydride, and ammonia borane, in each of which the hydrogen has been replaced by an equiatomic mixture of deuterium and tritium) and to form these into microspheres and/or microballoons. The non-fuel atoms in these room-temperature solids (carbon, lithium, nitrogen, and boron) must also be compressed and heated to fusion conditions along with the deuterium and the tritium, but, because they do not participate in the fusion reaction, they

act as diluents of the fuel. As a result, targets fueled with these room-temperature solids are not expected to perform as well as those with cryogenic DT fuel shells. However, the fuels that are solid at room temperature are considerably easier to work with, both in target fabrication and in laser-target interaction experiments; they also enlarge the parameter space available for exploration in our laser-target interaction experiments.

Along with the development of techniques to fabricate the fuel pellets, we also are developing methods to apply a wide variety of coatings to the fuel pellet and to support the pellets for irradiation by the laser beam, using thin plastic films or glass fibers so as to introduce a minimum of extraneous material into the system. Finally, we are continuously developing techniques to select, characterize, and measure the various pieces of the target both before and after assembly.

MICROBALLOON SEPARATION, MEASUREMENT, CHARACTERIZATION, AND FABRICATION (R. J. Fries)

General

Almost all our DT-filled targets use a microballoon as the central fuel-filled core. We, therefore, devote considerable effort in developing methods for the separation, quality selection, measurement, and characterization of glass or metal microballoons. In addition, we are developing

techniques to alter the size and/or quality of existing microballoons, as well as to directly fabricate microballoons.

Separation Techniques

General. Commercially available microballoons, both glass and metal, are generally of very poor quality, with perhaps only one in a million possessing the sphericity and wall-thickness uniformity required for laser fusion targets. We have, therefore, developed and are using elaborate procedures to find and recover the few high-quality microballoons.¹ At the same time we are investigating other techniques that might speed up and refine the separation and recovery operation.

Surface Acoustic Wave Separator (W. Bongianni, Rockwell International, Electronic Devices Division). We are evaluating the use of surface acoustic waves (SAWs) to separate microballoons according to their size and geometric perfection. Consideration of the electrostatic forces acting on glass microspheres led to the development of a multiple-contact adhesion model (based on the work of Kunkel²), which provides good agreement with the observed adhesion of microspheres and microballoons. This model permits us to predict the amount of charge on a given glass microballoon (GMB), which, in turn, allows us to estimate the ultrasonic force required to overcome such adhesion.

These theoretical analyses led us to conclude that surface acoustic waves (SAWs) could overcome the electrostatic adhesion between a particle and a surface and could be used to move the particle along

the surface in a controlled fashion. This possibility has been demonstrated experimentally by using a SAW transducer deposited on a single-crystal bismuth-germanium-oxide substrate. Unfortunately, we also found that, in this geometry, colliding particles agglomerate into clumps that could not be broken apart with SAWs.

In an inverted geometry, we found evidence for resonance in the hollow microballoons. Two distinct modes were observed: the "breathing" mode and the Lamb-wave mode associated with resonance of the walls. The measured Lamb-wave velocity was 6.15×10^6 cm/s. This Lamb-wave resonance is particularly important because it allows the selection of microballoons with predetermined parameters using microballoon velocity on the SAW plate as a sorting mechanism, provided the GMBs are fed to the SAW plate slowly enough to prevent agglomeration. By controlling the bandwidth of the rf signal, a narrowing of the distribution of outside diameters was observed. The quality (that is, wall-thickness uniformity) of the removed microballoons was much improved over the normal distribution, as shown in Table IV-I.

We intend to combine a one-at-a-time particle feeder (see below) with the SAW transducer to provide a continuous separator for microballoons.

One-at-a-time Microballoon Feeder (J. Miller, S. Butler). Motivated by Rockwell International's successful demonstration of GMB size and quality separation by SAWs and by their need for a fast, reliable, one-at-a-time microballoon feeder that would allow the SAW device to be used as a production-line-type microballoon separator, we developed the feeder illustrated in Fig. IV-1. This

TABLE IV-I
EFFECTS OF SURFACE ACOUSTIC WAVES
ON GLASS MICROBALLOONS

	Starting Material	SAW-Processed Material
Diameter (μm)	62.4 \pm 4.4	66.1 \pm 1.8
Wall thickness (μm)	0.78 \pm 0.13	0.71 \pm 0.23
% of good quality	26	91

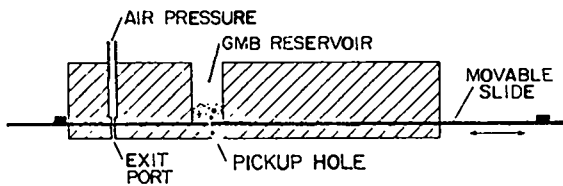


Fig. IV-1.
One-at-a-time microballoon feeder.

device, resembling a corn planter, operates effectively and reliably.

GMBs presized with standard testing sieves are loaded into the reservoir. A movable slide below the reservoir, ~25% thicker than the GMB, contains a pickup hole ~25% larger than the GMB. When the hole in the slide is positioned under the reservoir, a single GMB falls into the hole. The slide is then moved to position this GMB over the exit port where a puff of compressed gas blows the GMB out of the slide hole onto a receiver. The air entrance hole must be smaller than the GMB diameter to prevent the GMBs from jumping upward when the slide hole moves under the air port. This simple feeder is effective and delivers single, unbroken GMBs with better than 90% reliability at rates up to one per second.

This feeder can also be used to deliver GMBs one at a time into a liquid column for buoyancy measurements and/or separations. The entire feeder assembly is simply inverted, and any air captured under it is carefully removed. Natural buoyancy is sufficient to drive the GMB out of the hole in the slide and through the exit port; no air pressure is needed.

Microballoon Measurement Techniques

General. We must be able to measure the size and uniformity of laser-target microballoons to a resolution at least as good as the required level of uniformity, estimated at 1% for sphericity, from 1 to 10% for wall-thickness uniformity, and from 1 to 100 nm for small-scale surface defects such as dimples and warts. Optical interferometry is a very useful technique for GMBs, but it cannot be used for metal or other opaque targets, for which we are using x-ray

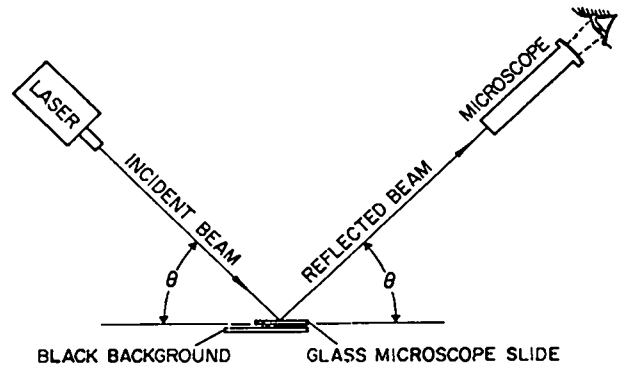


Fig. IV-2.
Simple, useful shearing-plate interferometer.

microradiography, a technique we are refining for easy and convenient use with a resolution sufficient for our needs.

Optical Interferometry (D. Stupin, D. Kohler).

We are supporting the work of several contractors to develop a quality separator for microballoons and to devise a technique for reworking existing ones to increase their aspect ratio and/or to improve their surface finish, strength, and quality. Because an inexpensive optical interferometer was needed to assess the quality of GMBs being separated or reworked, we developed the simple, effective, inexpensive shearing-plate (or Murty) interferometer illustrated in Fig. IV-2.

A low-power (~1.0 mW) cw laser beam is reflected from both surfaces of a flat glass microscope slide into a microscope, as shown in Fig. IV-3. An object at A, illuminated by light rays near Path b, will produce one image at B, due to its reflection in the first surface of the microscope slide (Path b - b'), and another image at C, due to the reflection at the second surface (Path b - b''). The images B and C will be superimposed on light from paths near a - a' and e - e', which has not passed through the object. The superposition will cause an interference pattern at B and C. However, the interference pattern at C will not be as distinct as that at B because of the distortion of the image by both surfaces of the glass slide. Also, if the beam is not wide enough or if the object is in the wrong place, the rays a - a' or e - e' may not exist, and the corresponding interference patterns will not be seen.

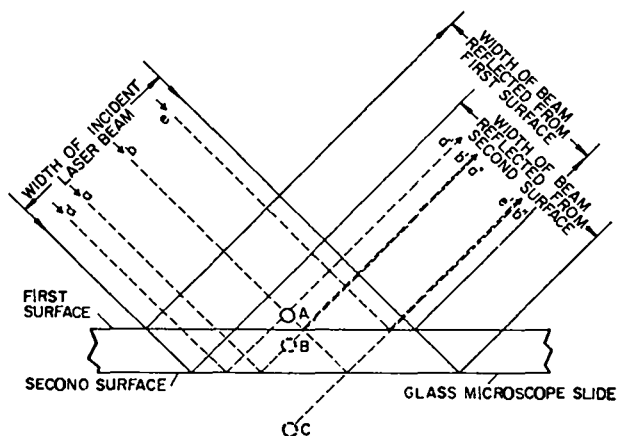


Fig. IV-3.
Shearing-plate interferometer.

Another interference pattern will be seen at A, due to light scattered from the object along Path b - d' interfering with light along Path d - d', but will not be as distinct as at B.

If the glass microscope slide is not uniform, it will produce interference fringes of its own. Therefore, an area must be found on the slide which does not produce interference fringes. If this area is large compared to the size of the object, the microscope slide will not contribute significantly to the interference pattern of the object. The background (whatever is seen through the microscope slide) should be black or void for best visibility (see Fig. IV-2).

If the GMB touches the first surface the images at A and B will overlap when viewed in the microscope. Alternatively, the GMB may be supported slightly above the surface and two images will separate. The entire interference pattern of the GMB can be examined by rotating it about an axis parallel to the surface of the microscope slide. The quality of the images thus obtained, see Fig. IV-4, is comparable to that obtained in our Jamin-Lebedev interferometer.

X-Ray Microradiography (D. Stupin, R. Day, R. Whitman, M. Winkler). We have continued our development of photometric techniques (first used by KMS-Fusion) to analyze microradiographs and have defined our assessment of the resolution attainable with our TV-vidicon image-analysis system.⁸ The microballoon images are formed as

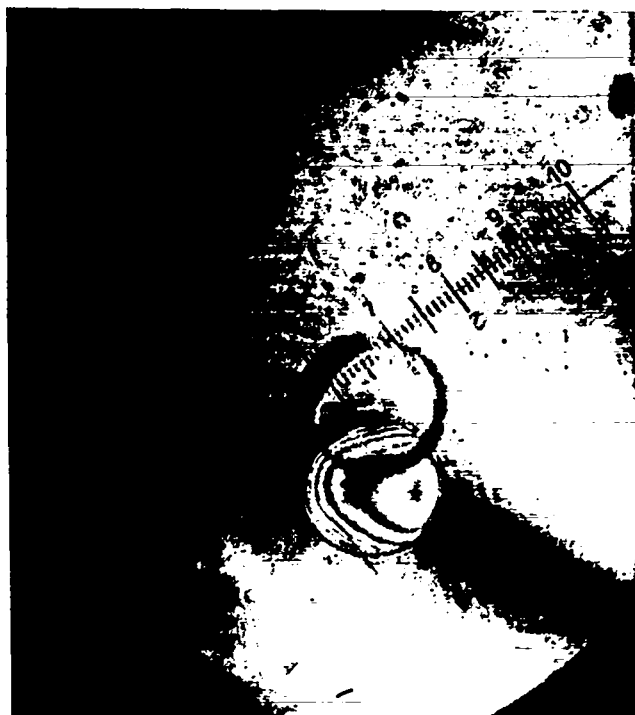


Fig. IV-4.
Interferogram of a GMB obtained on the shearing-plate interferometer.

contact microradiographs on Kodak HRP plate using either a nearly monochromatic Henke tube⁴ or a low-voltage tungsten Bremsstrahlung source⁵ as an x-ray source.

We calculated the image contrast per unit thickness of glass (dD/dX , in units of optical density D per μm of glass) to be expected for thin and for thick glass as a function of x-ray energy and obtained the results shown in Fig. IV-5. For thin glass (Fig. IV-5a), corresponding to the central region of our GMBs, maximum contrast change per unit thickness change is obtained at an x-ray energy of ~ 1 keV and the radiation should be nearly monochromatic. For the thick glass near the edge of the microballoons (Fig. IV-5b), optimum energy is 3 to 4 keV and the limits on monochromaticity are less severe.

We have written a simulation code to model the generation and analysis of microballoon radiographs and used it to calculate and plot radiographs to be expected for various geometries.⁶ We assumed a scanning x-y microdensitometer with a $2\text{-}\mu\text{m}$ -square window and a step size of $1\ \mu\text{m}$ would correspond to

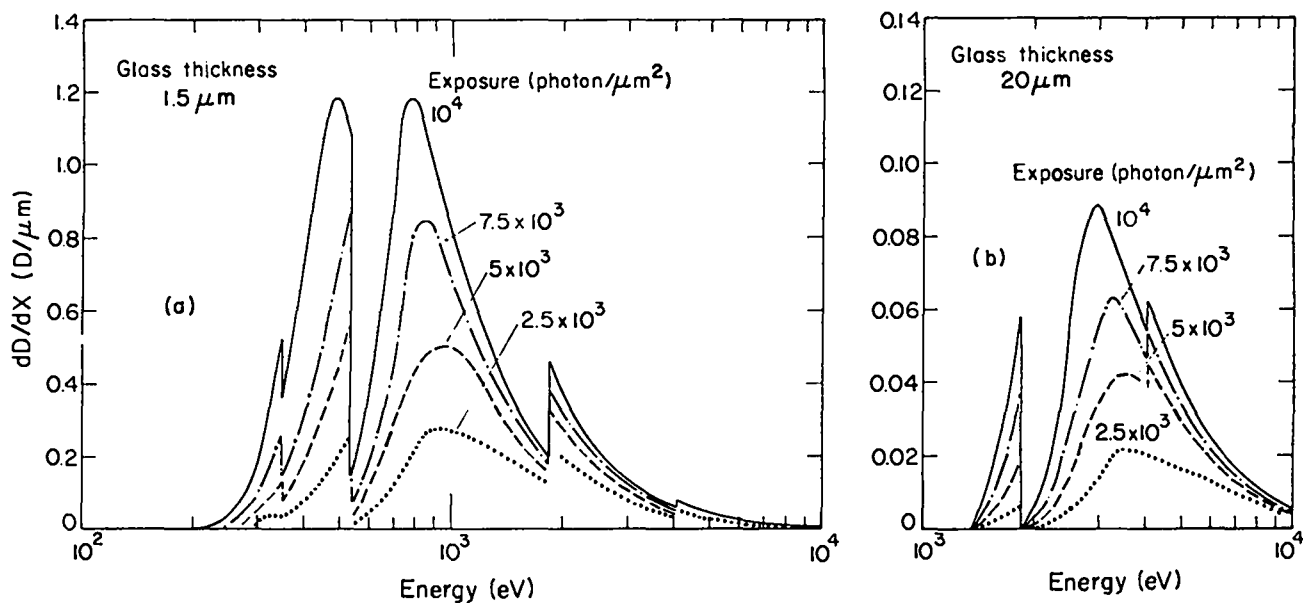


Fig. IV-5.

Optical density contrast per micrometer of glass thickness for microballoons as a function of x-ray energy for (a) thin glass and (b) thick glass.

one of the analyzers that we use—Photometric Data Systems Model 1050. Typical results are shown as solid lines in Fig. IV-6, for microballoons whose inner and outer surfaces are spherical but not concentric. The data points are obtained from values for an actual GMB radiographed with monoenergetic 930-eV x rays. These data agree very well with those predicted on the basis of parameters obtained for this GMB by optical interferometry. The wall thicknesses calculated by the two techniques also agree to within $\pm 250 \text{ \AA}$ (the accuracy of the interferometric technique).

We have used this code to predict the sensitivity of our radiographic technique to various types of defects. For nonconcentricity-type defects, using monochromatic 930-eV radiation, we estimate a sensitivity of $\sim 250 \text{ \AA}$, whereas with a Bremsstrahlung source at 4 keV peak (3.3 keV assumed mean energy), the sensitivity is about $\pm 500 \text{ \AA}$.

We can determine if one or both surfaces of a GMB are nonspherical by measuring the wall thickness as viewed through the center of the GMB in different orientations. For monochromatic 930-eV radiation the sensitivity for such wall-thickness measurements should be $\pm 350 \text{ \AA}$.

A similar analysis for small-scale nonuniformities viewed near the center of the GMB image yields a sensitivity, S , in glass of:

$$S = 5.1 \times 10^8 (A)^{-1/2}$$

where A is the area of the asymmetry in micrometers squared.

In a related effort, we have been trying to determine the resolution of our Interpretation Systems Inc. (ISI) vidicon-type image-analysis system in analyzing radiographic images of microballoons obtained with monochromatic x rays of optimal energy. A series of GMBs was examined by Jamin-Lebedev interferometry and was also radiographed and analyzed with our ISI system. These GMBs were glued to a duplex polystyrene/nitrocellulose plastic film transparent to both visible light and 930-eV radiation. The GMBs could thus be examined in exactly the same orientation by both techniques.

Representative pairs of photographs are shown in Fig. IV-7, with the ISI output presented as pseudocolor isodensity plots. The agreement between the two techniques is striking. The centers of the interference fringes and the isodensity contours

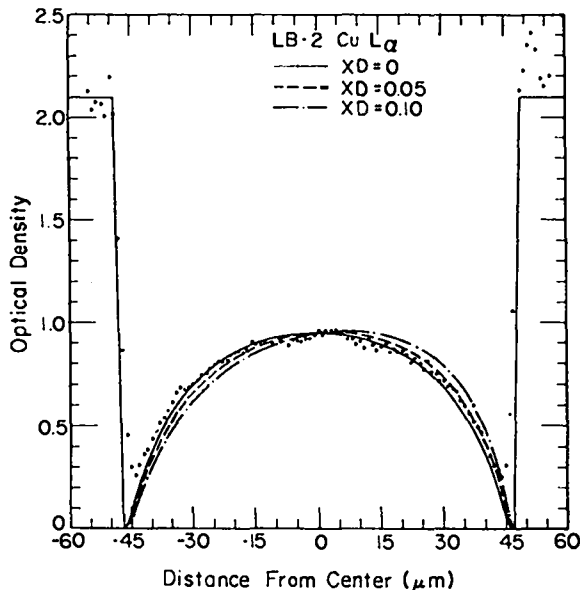


Fig. IV-6.

Optical density cross section for a radiograph of a GMB (96- μm diam by 0.68- μm wall) taken with monochromatic 930-eV x rays. Solid curves are computer simulations for various values of inner- and outer-shell nonconcentricity (XD = displacement of the centers of the two spheres in micrometers).

occur at similar locations on the microballoon image; additionally, the detailed shape of the interference fringe is generally replicated by the isodensity contours. We conclude that both techniques have comparable sensitivity, that is, of at least 250 \AA .

We have also been using the ISI system to assess the quality of Solacel metal microballoons from their radiographs. Typical results (pseudocolor isodensity plots) for two Solacels having average wall thicknesses of $\sim 1 \mu\text{m}$ and wall-thickness variations of ± 5 and $\pm 15\%$ are shown in Fig. IV-8a and 8b, respectively. These radiographs were obtained with our bremsstrahlung source at an end-point energy of 3 keV, which should be near optimum. From the obvious noncentricity of the isodensity contours in the image of the 5%-nonuniform Solacel, we conclude that the sensitivity of the technique in this case is better than $\pm 500 \text{\AA}$.

The analyses of our radiographic technique, in general, and of its sensitivity in combination with

the ISI readout system in particular, are continuing. It now appears that this combination, which can be used to characterize and measure opaque microballoons, has a sensitivity approaching that of the optical interferometer technique used with GMBs.

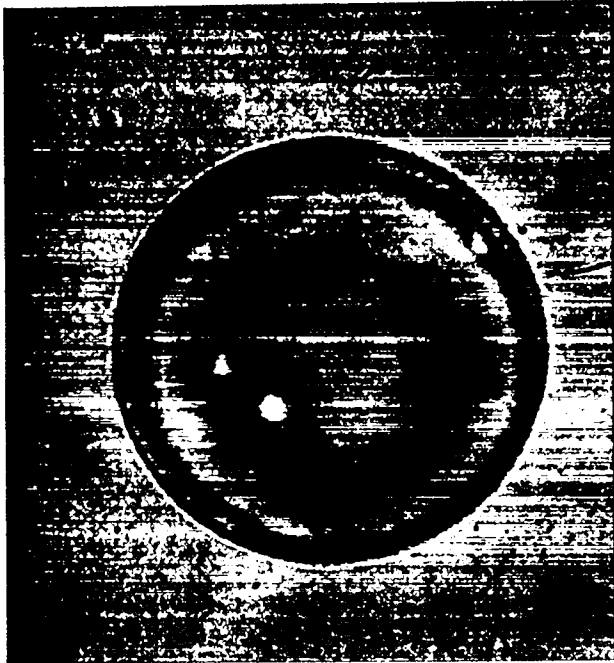
Microballoon Properties

General. Many of our present targets use uncoated individual microballoons as the primary laser-target structure. Thus, we are engaged in a continuing study of specific microballoon properties such as strength and permeation rate for various gases at elevated, room, and cryogenic temperatures.

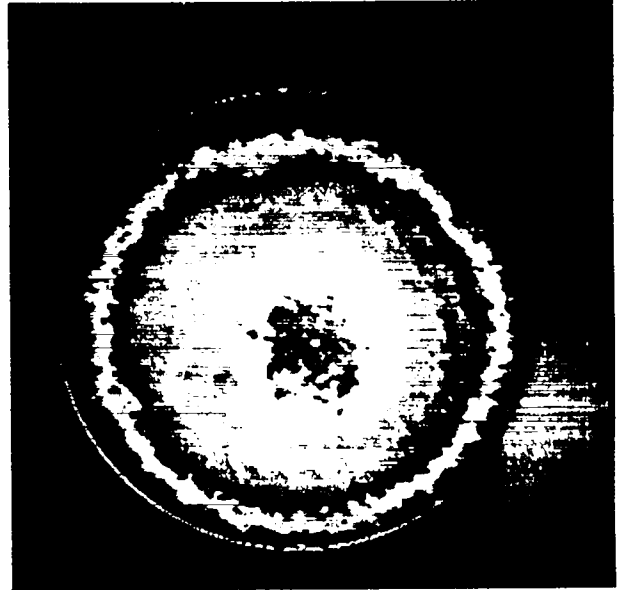
Permeation Measurements (H. R. Maltrud, E. Redemann). We have measured permeation rates to determine both the removal of residual gases from the GMBs and their fuel-gas leakage rates at room temperature and below.

Residual-Gas Removal. Theoretical calculations indicated that target performance could be enhanced if fuel-gas pressures in the GMBs were low (for example, 1 atm total). However, the gases entrapped during the process of blowing the GMBs caused some concern because of the higher relative concentration of these low fuel-gas pressures. We were, therefore, interested in developing techniques to remove these residual gases.

The GMBs of interest were Type BXX8 specimens obtained from 3M Company. Our previous studies⁷ had determined that the primary residual gases in these microballoons are SO_2 , oxygen, and a small amount of nitrogen. In addition, we found that heat treatment of these GMBs in a hydrogen-gas-fluidized bed at 623 K for 24 h was effective in removing most of the SO_2 and oxygen. However, in our current work we used previously characterized and measured GMBs for which this heat treatment was very inconvenient. Therefore, we were prompted to evaluate the effectiveness of our standard fuel-gas filling cycle (that is, 20 to 24 h at 675 K in a static DT environment consistent with the desired fill pressure) for removal of the GMB residual gases. These results are summarized in Table IV-II. The GMBs as filled with 1 atm of DT



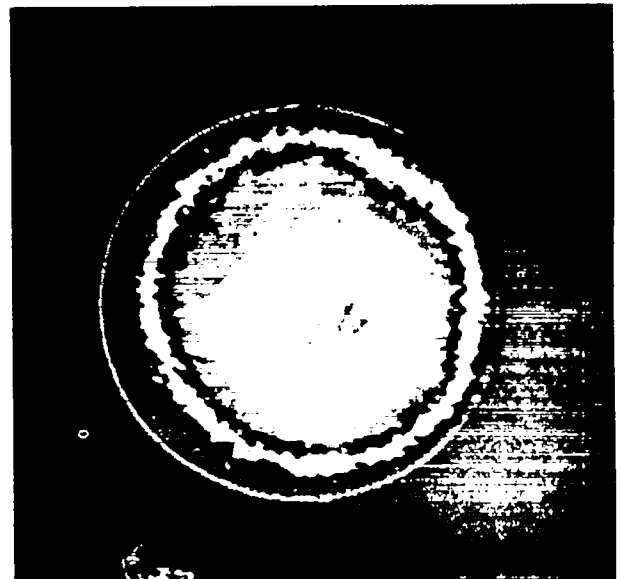
(a)



(b)

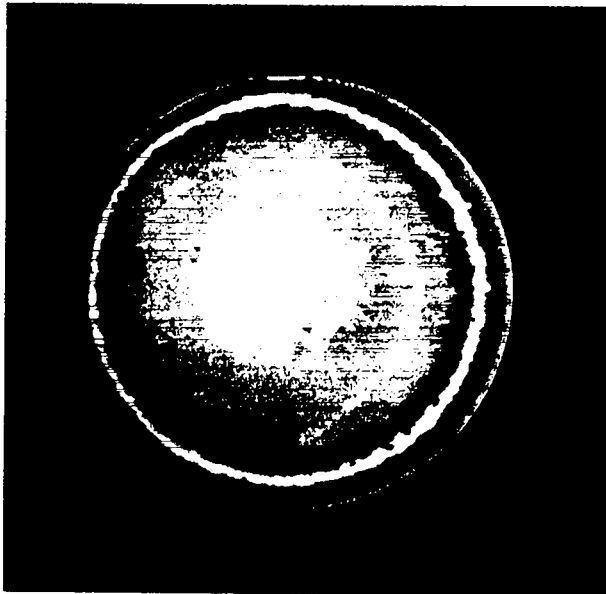


(c)

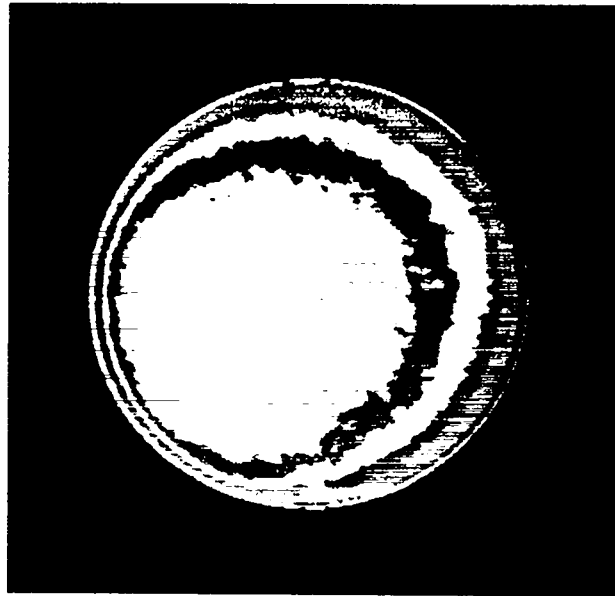


(d)

Fig. IV-7.
Comparison of interferograms (a and c) of a GMB with pseudocolor isodensity plots (b and d) obtained from the radiographs of the same GMB. Adjacent pairs are for the same microballoon.



(a)



(b)

Fig. IV-8.

Pseudocolor isodensity plots obtained from radiographs of Solacel metal microballoons having estimated wall-thickness nonuniformities of (a) $\pm 5\%$ and (b) $\pm 15\%$.

TABLE IV-II
RESIDUAL GASES IN 3M GLASS
MICROBALLOONS

Gas Type	Residual-Gas Pressure (torr)	
	In As-Received GMBs	In DT-Filled GMBs ^a
SO ₂	~65	≤0.1
O ₂	≤33	≤3
N ₂	≤3	≤3

^aSoaked in ~2 atm DT for 20 to 24 h at 673 K.

fuel contained a maximum of ~2 wt% of nitrogen impurity, not considered enough to be a problem.

One surprising aspect of these measurements is the gas pressure measured in the as-received GMBs: ~100 torr total. Considering softening temperatures of 775 to 875 K for the glass and an internal pressure somewhat higher than 1 atm at the final stages of the microballoon blowing process we expected that

the pressure of the residual gases was at least 250 torr. A condensable gas such as water vapor might provide a significant fraction of the blowing-gas pressure when the GMBs are hot, but 3M assured us that they do not intentionally add any such blowing agent.³

Fuel-Gas Leakage from GMBs (R. Fries, H. R. Maltrud, E. H. Farnum). Several years ago we measured the DT loss rate from several types of 3M-produced GMBs preselected for their high quality.⁹ Fuel-retention half-lives of 1 to 2 yr were indicated. Because the average chemical composition of the various types of 3M GMBs are similar, we assumed that these half-life data would apply to most 3M microballoons.

However, late in 1976 workers at the University of Rochester (UOR) observed¹⁰ relatively short room-temperature fuel-gas-retention half-lives for some 3M-type B18A GMBs we had filled with DT. Our subsequent remeasurement on two types of 3M GMBs (B18As and BXX8s) confirmed the Rochester observations.

Data for 14 type B18A GMBs (~60- μ m diameter by ~0.7- μ m wall) obtained at UOR indicated half-lives for room-temperature gas loss ranging from 8

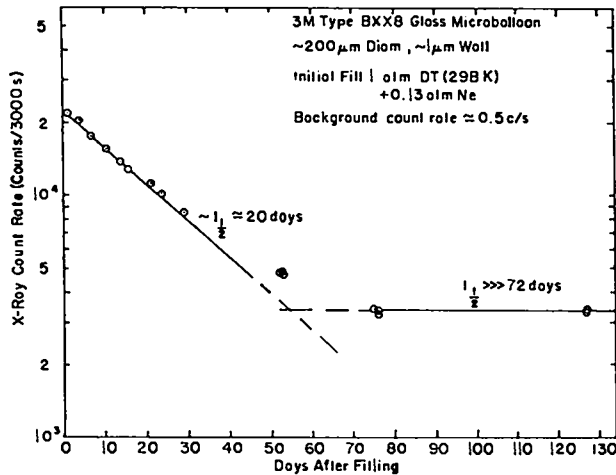


Fig. IV-9.

Gas content of a GMB (as measured by our x-ray counting technique) as a function of time after filling.

days to ~ 2 yr, with an average of ~ 50 days.¹⁰ Our measurements on 11 similar GMBs filled at the same time as the UOR GMBs, gave half-lives ranging from 54 to 385 days, with an average of 125 days; our measurements on larger type BXX8 GMBs (~ 200 - μm diameter by ~ 1 - μm wall) gave half-lives ranging from 21 to 231 days, with an average of 80 days.

We are considering two causes for the observed range of gas loss rates. Some of the GMBs could possess submicroscopic defects (for example, pores and cracks) that provide leakage paths for the contained high-pressure gas; or their chemical composition may vary enough to result in widely varying permeation rates. These possibilities would affect differently the gas loss rate at reduced storage temperature. If a composition variation is responsible, then moderate reductions in storage temperature should reduce the gas loss rate significantly. However, if leakage paths are the cause, the effect will be much smaller. Preliminary data indicate that gas loss is essentially stopped at 76 K (that is, no detectable loss in 7.5 months).

A typical gas loss rate curve for one BXX8 GMB is shown in Fig. IV-9. These data were obtained with our x-ray counting technique for nondestructive fuel assay.⁹ The initial fill consisted of 1 atm DT plus 0.13 atm neon. Two different loss processes with

significantly different rate constants are indicated: an initial fast process with a half-life of ~ 21 days followed by a much slower process with a half-life $\gg 72$ days. Percentage of initial count remaining at the break in the curves is $\sim 16\%$. This result was compared with gas-counting measurements in which we punctured the wall of a GMB to allow the gas to escape, measuring the x-ray count rate before and after puncturing to determine how much of the initial count rate is contributed by the DT dissolved in the walls of the GMB. These measurements indicate that the contribution from gas dissolved in the walls is $\sim 4\%$ for similar BXX8 GMBs with 1 atm DT fill. Additional measurements are in progress to improve our understanding of these results.

Microballoon Fabrication and Quality Upgrading (S. Dunn, Bjorksten Research Laboratory, Inc., Madison, Wisconsin)

We are supporting work at Bjorksten Research Laboratory to develop techniques for levitating and spinning microballoons in a reduced-pressure, elevated-temperature environment. Such a capability might lead to improved surface finish and/or strength by a fire-polishing-type treatment. Additionally, we might be able to expand the microballoons to larger diameters and thinner walls and, perhaps, improve their wall-thickness uniformity. Finally, if the microballoon can be spun randomly, rapidly changing the position of the heavy spot of the microballoon with respect to the axis of rotation, it might be possible to improve wall-thickness uniformity by centrifugal forces. (This rotational behavior has been observed for ping-pong balls levitated on an air stream, but has not yet been seen for microballoons.)

Our initial goal was the development of reliable microballoon levitation and spinning techniques, regardless of pressure and temperature. A rotameter-type device was evaluated first, but the GMBs were attracted to the tube wall and stuck to it. A small gas jet in the center of a large tube was tried next, but it was almost impossible to introduce and levitate a microballoon in this system. Finally, an array of stainless steel tubes known as a

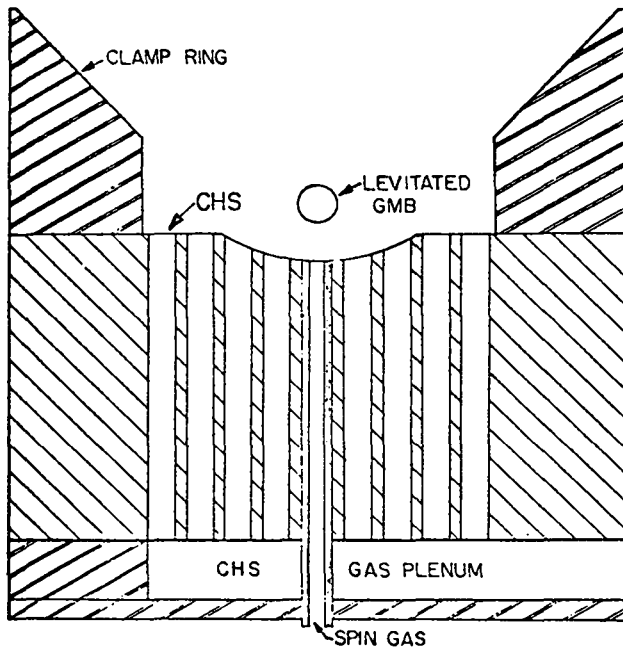


Fig. IV-10.

CHS device used to levitate and spin microballoons.

Collimated Hole Structure* provided stable levitation of one or many GMBs which could be inserted easily.

The best arrangement to date is shown in Fig. IV-10; it uses a CHS of 130- μm -i.d. tubes in a closely packed hexagonal array on 190- μm center-to-center spacing. A dimple, machined into the upper surface of the CHS, forms a potential-energy well in which a microballoon will locate stably. In addition, a single tube with a separately controllable gas flow is inserted into the bore at the center of the dimple to allow shear forces to be set up to spin the microballoons. With this arrangement we attained spin rates as high as 22 rps, but we have not yet observed the complex motion thought to be necessary if centrifugal forces are to smooth out wall-thickness non-uniformities.

We will next incorporate the CHS assembly into an apparatus to allow reduced-pressure, elevated-temperature operation.

*CHS is available in a range of sizes from Wintec Division, Brunswick Corp., Los Angeles, California.

PUSHER SHELL DEPOSITION AND CHARACTERIZATION (R. J. Fries, D. F. Catlett)

General

We have continued our development of methods to deposit uniform layers of high-Z metals onto various types of mandrels for use as pusher shells. In our laser fusion targets, pusher shells are primarily employed to provide inertial momentum during compression (to allow the attainment of higher fuel densities before the pellet disintegrates) and to shield the fuel from the laser-produced plasma (to minimize preheating of the fuel). High-strength pusher shells are desirable to allow the use of high fuel pressures (that is, high densities). Also, pusher shells should have useful DT permeation rates. As described previously, we are developing electroless and electroplating techniques for depositing a wide range of metals and alloys onto microsphere substrates,¹¹ and we are perfecting chemical vapor deposition (CVD) methods for the application of several metals and alloys.¹² In addition, we are developing physical vapor deposition (PVD) and sputtering processes to offer us the widest possible choice of metals and alloys for use in coating target microspheres. Emphasis during this report period was on CVD and sputtering.

CVD (W. McCreary, D. Carroll)

The CVD process involves the chemical or thermal reduction of a metal-containing compound at the surface of a substrate. The method has been useful for coating microsphere substrates in a gas-fluidized-bed coating apparatus, which mixes the substrates well and allows us to apply useful metal coatings to these otherwise difficult-to-handle particles.

We needed a thin, high-Z coating on ~ 100 preselected GMBs and evaluated the possibility of depositing tungsten from WF_6 . Before a protective tungsten film could be formed, the bare GMBs were eroded to an unacceptable degree by the HF formed from the hydrogen reduction of the WF_6 . A 2- μm precoat of Mo_2C eliminated this problem.



Fig. IV-11.

Metallographic section of a beryllium-copper microsphere coated with aluminum by sputtering.

Work was continued on the development of techniques to coat a few preselected target mandrels with CVD nickel from $\text{Ni}(\text{CO})_4$ while mixed with a bed of carrier particles, separating the coated mandrels from the carriers after the run. Although we have been able previously to coat $\sim 200\text{-}\mu\text{m}$ -diam GMBs, our current efforts to coat $\sim 120\text{-}\mu\text{m}$ -diam GMBs have not been very successful. We are evaluating microballoons of other sizes and materials for use as carriers.

Sputtering (A. Lowe)

Our development of a sputtering technique to coat microspheres with a uniform layer of metals and/or oxides was continued, further exploring the use of combined electromechanical and plasma agitation of the microsphere substrates. We established that short, alternating coating and cooling cycles enabled us to maintain good bouncing motion of the microspheres and to obtain $1.5\text{-}\mu\text{m}$ -thick aluminum coatings on beryllium-copper microspheres, uniform to at least $0.2\ \mu\text{m}$ (the resolution limit of the measurement technique used). A photomicrograph of a typical metallographic section is shown in Fig. IV-11, illustrating the good uniformity and adherence obtained. We have also sputtered $\sim 1\text{-}\mu\text{m}$ -thick coatings of nickel onto $100\text{-}\mu\text{m}$ -

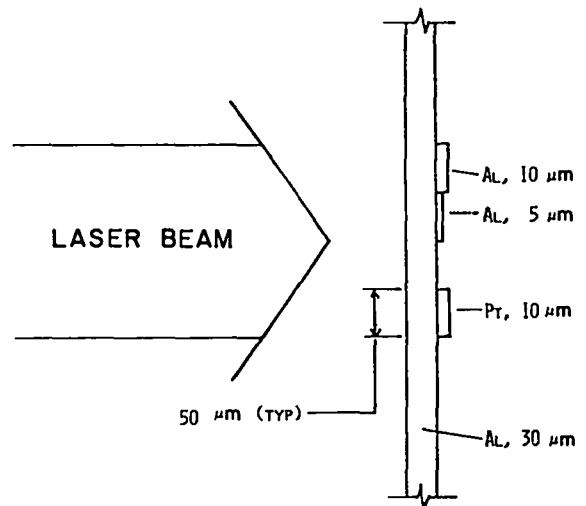


Fig. IV-12.

Metal-film target used for equation-of-state measurements.

diam GMBs and $\sim 1\text{-}\mu\text{m}$ -thick coatings of MgO onto 0.5-mm -diam beryllium-copper microspheres, with good adherence in both cases; we are now characterizing thickness uniformity of both these coatings.

METAL FILMS (A. Lowe, C. Hosford)

A wide range of metal films, both freestanding and on substrates, is needed as targets and in diagnostic devices. One type of metal-film target prepared for some equation-of-state measurements (one of several military applications experiments for which we provide targets) is shown in Fig. IV-12. These are made by vapor deposition through an appropriate mask, using a multiple-hearth electron-beam evaporator that allows deposition of up to four different materials without having to break the vacuum.

Significant additional effort was devoted to making special (Ross-type) x-ray filters from specific thicknesses of platinum, gold, neodymium, iridium, tungsten, and osmium, each deposited onto $770\text{-}\mu\text{m}$ -diam beryllium disks. These filters will enable spatial energy distribution of imploding targets to be determined with our x-ray pinhole camera images.

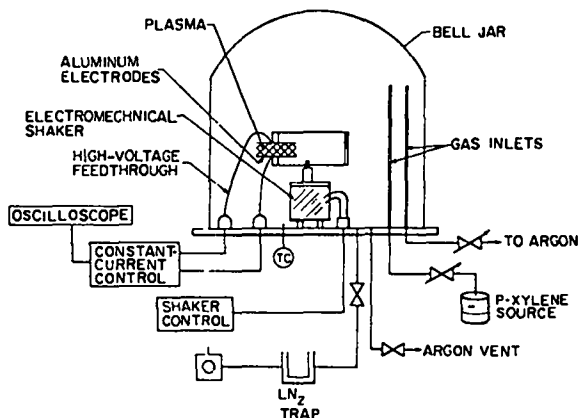


Fig. IV-13.

Glow-discharge-polymerization system used to apply plastic coatings.

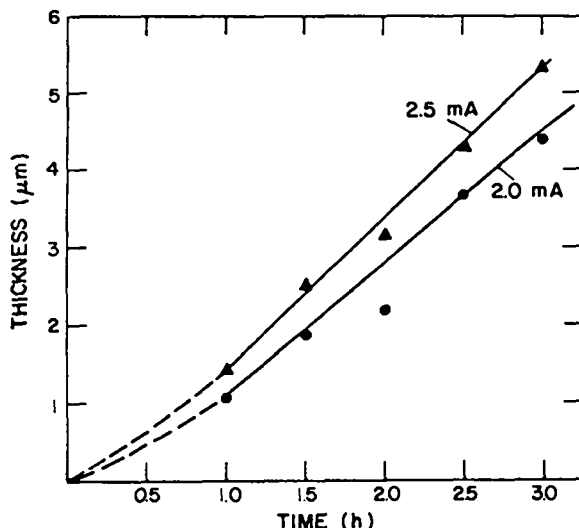


Fig. IV-14.

Polymerized p-xylene coating thickness as a function of time for several plasma currents.

PLASTIC SHELL DEPOSITION (A. Lowe)

Many of our multilayered laser fusion targets use an outer shell of low-density, low-Z material as an absorber/ablator layer. This layer absorbs energy from the incident laser, is heated, vaporized, and streams away from the pusher shell causing the pusher shell to implode via the rocket reaction forces. For designs that do not depend on the strength of this absorber/ablator to contain the fuel-gas pressure, we generally use plastic. We are also frequently requested to provide freestanding cylindrical and spherical shells of plastic as targets for special diagnostic measurements. These shells are generally fabricated by coating appropriate mandrels with plastic, and then dissolving the mandrels in acid.

We have extended our capabilities in, and our understanding of, the glow-discharge-polymerization technique we use for the deposition of plastic.¹³ In a series of experiments we coated beryllium-copper microspheres with p-xylene in the apparatus shown in Fig. IV-13 to explore polymer deposition rates and film properties as a function of process variables. The deposition rate was nearly constant with time (or thickness) to at least 3 h, as shown in Fig. IV-14. In addition, higher plasma currents increased the coating rate somewhat more rapidly than linearly, as shown in Fig. IV-15.

We had previously determined that large-aspect-ratio shells were strengthened if deposited from a 25% argon:75% p-xylene mixture rather than in

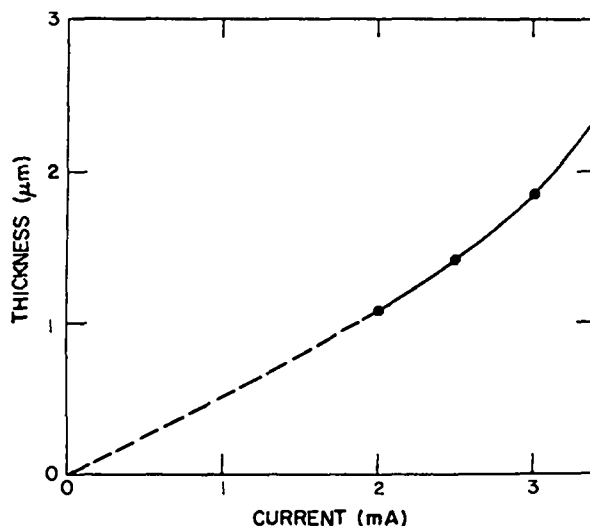


Fig. IV-15.

Polymerized p-xylene coating thickness as a function of plasma current for a coating time of 1 h.

pure p-xylene.¹² We extended that study to higher argon concentrations, judging the film strength by the fraction of hemispherical shells recovered from the acid solution used to dissolve the mandrel, as tabulated in Table IV-III. These data suggest that

TABLE IV-III
PERCENTAGE OF HEMISPHERICAL SHELLS RECOVERED
FOR DIFFERENT COATING GAS MIXTURES

<u>Gas Mixture</u>	<u>Amount Recovered (%)^a</u>	<u>Thickness (μm)</u>	<u>Deposition Rate ($\text{\AA}/\text{m}$)^b</u>
Pure p-xylene	0	3.0	334
25% Ar:75% p-xylene	100	2.2	243
50% Ar:50% p-xylene	95	1.6	178
75% Ar:25% p-xylene	90	1.5	167
25% Ar:75% p-xylene	100	2.0	---
25% Ar:75% p-xylene	80	1.0	---
25% Ar:75% p-xylene	40	~0.5	---

^aPercentage of hemishells recovered after each step.

^bAt 2.0 mA electrode current.

argon concentrations above 25% have minimal effect on strength, but increasingly deleterious effects on coating rates, at least for shells of 1.5- to 2- μm thickness. Higher argon concentrations might be advantageous for much thinner shells.

Other studies¹⁴ have demonstrated that polymer films prepared by GDP generally contain many free radicals and reactive sites, and that these gradually react with oxygen and water if the films are left in air. We view oxygen as an undesirable contaminant of our films and were thus prompted to use infrared (ir) spectroscopy to examine our films and the effects of treatments designed to minimize oxygen and/or water pickup. An effective technique to strip thick films from the electrodes is to soak the coated electrode in water, which evidently causes the film to swell, degrading the bond to the electrode. An ir spectrum of such a film is plotted as Curve B in Fig. IV-16, and the characteristic bands for -OH ($\sim 3400\text{ cm}^{-1}$) and -C=O ($\sim 1700\text{ cm}^{-1}$) are clearly evident. Spectrum A in Fig. IV-16 is an ir scan of a similar electrode coating that had been heat-treated immediately after deposition (for 1 h in vacuum at 375 K), after which the film was again removed in water. In this case, the -OH and -C=O bands are significantly reduced and perhaps even entirely absent. This provides good evidence that the heat

treatment decreases the free-radical/active-site concentration, thus minimizing the opportunity for subsequent reaction of the film with water or atmospheric oxygen.

One target we are fabricating requires a very thick plastic coating—from 10 to $> 25\ \mu\text{m}$, depending on the other details of the target design. Because of this requirement, we have determined that usable coatings of GDP p-xylene as thick as 10 μm can be applied to microsphere substrates. The brittleness of these films increases with coating thickness, and flaking becomes a problem for thicknesses larger than 10 μm .

Because of this limited thickness range for GDP p-xylene, we evaluated the possibility of obtaining thicker plastic coatings with Parylene (a product of Union Carbide Co.). Previously, we had experienced serious difficulties in coating microballoons with Parylene because of interparticle and particle-to-support plate agglomeration;¹⁵ evidently as-deposited Parylene is rather sticky. For our current application, we succeeded in mounting microspheres on support stalks and holding these individual assemblies stationary during the coating process. Under these conditions, the Parylene technique was usable, giving high-quality coatings as thick as 25 μm .

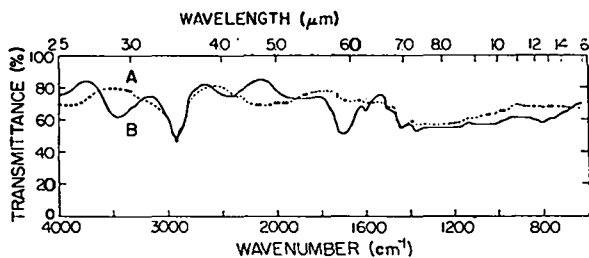


Fig. IV-16.

Infrared spectra of polymerized p-xylene films prepared by our glow-discharge-polymerization process. Film A was vacuum heat treated prior to exposure to water and Film B was not.

PLASTIC FILMS (B. S. Cranfill)

We use plastic films both as targets, per se, and as components in more complex designs. The requirements have ranged from nitrocellulose films as thin as 10 nm to polyethylene films as thick as 3 mm; additionally, we are sometimes asked to provide deuterated polyethylene for some special-purpose targets. In response to these varied requests, we have developed several different techniques to fabricate films of plastic, which we extend and/or modify as necessary.

We have produced a series of very thin nitrocellulose films by dipping glass slides in appropriate plastic solutions to obtain a thin coating on the slide from which the solvent then evaporates, leaving a plastic film that can be floated off onto water. Specifically, films with thicknesses ranging from ~10 to 75 nm were needed for CO₂ laser absorption/transmission studies. The thickness of these films was measured with a 10-pass holographic interferometer in 632.8-nm laser light, to an accuracy of ± 2.5 nm. The measured and desired film thicknesses, compared in Fig. IV-17, for specimens thinner than 60 nm, were within 10 nm of the desired thickness.

Our ability to fabricate large, thick films of deuterated polyethylene was improved by extending our mold technique described previously.¹² We made a mold by milling a recess in an aluminum block, the recess having the same areal size as the desired target and a depth 10 times the desired film thickness. In one specific case, a film of 4.5 cm by 10

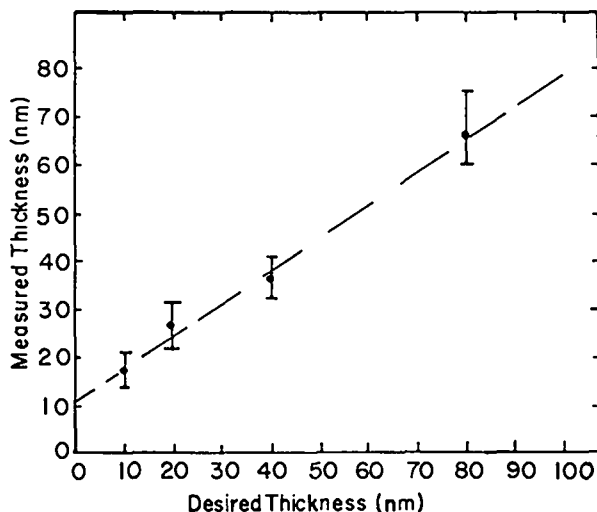


Fig. IV-17.

Measured nitrocellulose film thickness as a function of desired thickness.

cm by ~250- μ m thick was to be prepared for some nuclear scattering experiments. We milled a recess of this size to a depth of 2.5 mm into the aluminum block and filled it with a hot, 10 wt% solution of deuterated polyethylene in xylene. Best results were obtained when the aluminum was heated independently to maximize the solvent loss rate without boiling (which causes bubbles in the film). However, even this technique did not completely prevent powdery, rough-surfaced films; therefore, after all the solvent had evaporated, we increased the temperature of the aluminum block to allow the polyethylene to flow out and to form a smooth film.

Originally, we prepared deuterated polyethylene films from solutions made up with normal protonated solvents, assuming that hydrogen/deuterium (H/D) exchange between the deuterated polyethylene and the protonated solvent would be slow at our modest temperatures (~400 K). However, this was a gross underestimation; chemical analyses indicated that in films made from one of our solutions that had been used to make many films (and therefore had been heated to ~400 K many times) the deuterium content had decreased from ~97 to ~36 at.%. As a result, we are now using deuterated xylene to prepare our solutions. More detailed measurements of the H/D exchange rate are in progress.

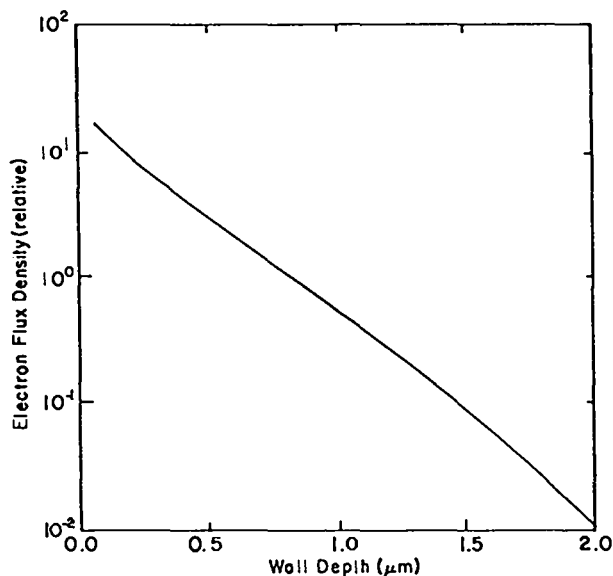


Fig. IV-18.

Relative electron flux density at various depths in a GMB wall, considering only electrons originating in the DT gas contained within the GMB.

NONDESTRUCTIVE FUEL-GAS ASSAY (M. M. Mueller)

We have developed several techniques to non-destructively assay the fuel-gas content of laser targets, including x-ray photon counting⁹ and optical photon counting.¹² In both cases, we must know the flux distribution of beta particles within and through the walls of the target for various possible microballoon materials and geometries. We have recently extended our earlier calculations¹⁸ and are now able to accurately account for the angle at which the electrons impinge on the target walls. (However, we still do not account for electron backscatter at the interfaces.)

We mainly calculate the total electron flux for a given depth in the wall due to beta particles emission within the sphere of fuel gas, accounting for attenuation in both the gas and the solid. For glass walls, the results are expected to be reasonably accurate despite the neglect of boundary backscattering; however, this neglect may cause serious errors at higher atomic numbers (for example, $Z \geq 25$).

Figure IV-18 shows the relative beta particle flux density as a function of depth in a 2- μm -thick glass wall in a microballoon of 100- μm i.d. at a fill pressure of 30 atm DT. Note that the flux declines exponentially over much of the wall thickness, the roll-off past 1.2 μm being insignificant for most purposes because of the low flux density. Obversely, however, the steeper-than-exponential decline at depths less than 0.5 μm is quite significant. Other results, not shown, produce similar curves over a wide range of parameters. For example, absorption within the emitting gas has an important, although not dramatic, effect; at a pressure of 200 atm DT, the flux fall-off curve is similar to, but the slope is $\sim 25\%$ steeper than, that shown in Fig. IV-17.

The transmission of electrons past a given wall layer is linearly related to the indefinite integral of the particle flux density, thus somewhat reducing departures from a pure exponential curve. Also, the slope of the transmission curve is slightly less than that of the flux density curve. Nevertheless, the general shape of the transmission curve is similar to the flux density curve. Thus, relatively small uncertainties in experimental parameters (such as wall thickness) or in calculational methods can produce large uncertainties in the predicted beta-particle transmission, particularly at wall thicknesses exceeding $\sim 1 \mu\text{m}$. If desired, we can also calculate the flux of beta-particle kinetic energy through the wall.

Because an appreciable fraction of the tritium may reside in the glass walls of microballoons, the contribution from this source to the wall fluxes needs to be assessed. The result of calculating the particle flux density for a 2- μm -thick wall containing a uniform distribution of tritium is shown in Fig. IV-19, in which the flux density that would obtain within an infinite medium of the same tritium density is assigned the value 2. The calculation takes the complicated path lengths within a spherical shell into full account. The symmetry of the result for a 100- μm -i.d., 2- μm -thick glass wall is caused by the high aspect ratio and by the range of most of the tritium betas being less than the wall thickness; other conditions result in somewhat different shapes.

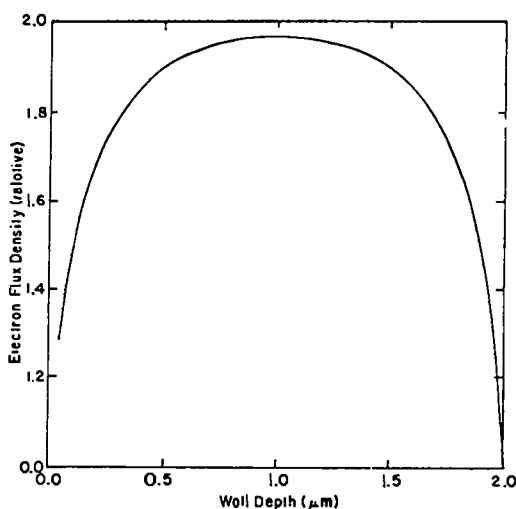


Fig. IV-19.

Relative electron flux density at various depths in a GMB wall, considering only electrons originating from DT dissolved in the glass wall. (Uniform concentration assumed.)

CRYOGENIC TARGETS (R. J. Fries)

General

Laser fusion targets fueled with cryogenic liquid or solid DT offer the advantage of high initial fuel density without the disadvantage of diluent atoms that are present in room-temperature solids having a high hydrogen density such as, for example, lithium in Li(D,T) or carbon in (-CDT). Calculations indicate that the yields from targets fueled with liquid- or solid-density DT can be considerably higher than those from targets of the same design, but fueled with high-pressure DT gas. As a result, we are actively pursuing the development of cryogenic targets despite the significant experimental complications encountered in the fabrication of such targets and in their use in laser-target interaction experiments. We are also engaged in a modest program of basic properties measurements for the cryogenic deuterium-tritium system such as compressibility and thermal expansion coefficient.

The geometry of cryogenic targets receiving the most emphasis is a uniform, hollow shell of solid or liquid DT condensed onto the inside surface of a glass or metal microballoon container that serves as

the pusher shell. We are concentrating our efforts on GMBs, simultaneously developing the techniques (a) to condense the DT into a uniformly thick layer on the inside surface of the glass and (b) to measure the thickness uniformity of the DT shell. Two general approaches are being examined. In one case, we deliberately impose a temperature gradient either by blowing a jet of cold helium onto the top of the target or by removing heat from the target via a cooled, high-conductivity support stalk, in an attempt to counteract the effect of gravitational forces; in the other, we surround the target with an isothermal environment and try to rapidly freeze the DT uniformly onto the surface.

Fast Isothermal Freezing (FIF) Technique (J. R. Miller)

We continued our development of the FIF technique (previously described in detail)¹⁷ in which we rapidly condense and freeze the DT fuel gas in a GMB to form a uniformly thick layer of solid DT on the inside surface of the GMB. We first use a cw He:Ne laser beam to vaporize the DT contained in a GMB that is supported by a thin glass stalk in an ~4 K copper cell filled with low-pressure helium gas that serves as a heat-exchange fluid. When we shutter the laser beam, the helium gas rapidly cools the GMB, and the DT condenses and freezes, forming a uniformly thick layer of solid DT. We have extended our thickness-uniformity measurements of solid DT shells produced by the FIF technique by making interferometric observations along a second axis (the heating-laser axis). Because two normal interferometric views of a spherical object provide a complete description of the optical path lengths through the object, we now have measured the thickness uniformity of the entire cryogenic shell. The results are consistent with those reported previously—cryogenic shells are reproducibly formed by the FIF method with a thickness nonuniformity over the entire DT layer of no more than 20% where nonuniformity is defined as the ratio of the film thickness variation to average shell thickness. The resolution of our interferometric analysis currently prevents assignment of a smaller value to the layer nonuniformity.

Temperature-Gradient Technique (E. Grilly)

We have previously obtained liquid DT films with good thickness uniformity via the temperature-gradient technique,¹⁸ generating the gradient by blowing cold helium onto the top of the target microsphere. We recently evaluated the use of a high-conductivity support stalk (gold or copper) to remove heat from a target that is otherwise surrounded by room-temperature walls. This second approach, first used at KMS-Fusion,¹⁹ should be both easier to control and easier to install in the laser-target chamber than the helium jet technique. We have examined targets glued to fibers of gold or copper, using diameters of 12 and 17 μm , respectively. In all cases these metal stalks were carefully ground to provide a flat end that was then attached to a DT-filled GMB with a small amount of epoxy glue. The other ends of the fibers were glued to a larger copper wire that was, in turn, soldered to a cryostat tip whose temperature could be controlled from ~ 4 K upward.

Results with 17- μm -diam copper fibers in two orientations are typical of the range of behavior observed. Two GMBs, both of $\sim 94\text{-}\mu\text{m}$ diameter and $\sim 0.7\text{-}\mu\text{m}$ wall thickness, were filled at the same time with DT to give 187 atm at 300 K. With these targets, first liquid should appear at ~ 38 K and the uniform liquid layer thickness should be ~ 2 μm .

In one orientation, the fibers were about vertical. Target A was below its fiber and Target B was above its fiber; this pair of targets should show the effect of gravity directly. The targets are shown in Figs. IV-20 to -22, in order of increasing thermocouple temperature T_{tc} , beginning with the fuel as a frozen spheroid at ~ 16 K. Figure IV-20 shows melting in both targets, as might be expected. In Figs. IV-21 and -22, Target A continues with no surprises, but it was disappointing to find lack of condensate at the bottom of the shell (which indicates the radiation heating could not be overcome). In viewing these pictures, one must block out imperfections such as dirt or excess cement (seen on the Target A shell at the left of the fiber). Surprisingly, Target B condensate at 17.76 K (Fig. IV-21) forms a misty state before becoming a spread-out, approximately uniform layer, which persists between 18 and 25 K. At higher temperatures, the layer thins, not quite symmetrically, until only gas is present, as illustrated in Fig. IV-22. All the states were stable at a given tem-

perature, were reversible, and were reproduced on different days. Of course, the fairly uniform layer of condensate in Target B in the 18 to 25 K range is the desirable form for a laser fusion target, and its insensitivity to temperature is a convenience. However, its formation is puzzling if only gravity and thermal gradients are considered. The appearance of the intermediate misty state might provide a clue. Also, close observation of the solid and liquid when heated or cooled near the freezing temperature indicates the possible shifting of layers. Because the system has three components (D_2 , DT, and T_2), one might expect some thermal separation in the condensed phases.

For an approximate reversal of target positions, the copper wire loop was rotated so that there was a back-front reversal as well as an inversion, with the fibers left $\sim 30^\circ$ off the vertical so that Target A was above and Target B below their respective fibers. As the targets were warmed from frozen spheroid to spread-out layer, the condensate behavior corresponded to the target position (above or below the conducting fiber, Figs. IV-23 and -24). This reorientation caused near-reversal of condensate behavior in Targets A and B. In particular, the diffuse state in Target B illustrated in Fig. IV-24, resembles the misty state in Target B at 17.76 K (Fig. IV-21).

The results of this experiment are much different from those obtained by Henderson et al.¹⁹ They observed that the condensed DT film was thinnest nearest the shell-fiber contact point, regardless of the orientation. This occurred even with the contact at the shell bottom, in which case the thermal gradient should reinforce gravity in producing a thicker film at the bottom. It is difficult to explain the differences between the results of these two experiments. Future tests will be made with thin fibers of various materials to minimize mass.

Cryogenic Target Support Systems (J. R. Miller, E. H. Farnum, R. D. Day)

Our current plan for loading targets (both room-temperature and cryogenic) into the EBS target chamber calls for one-at-a-time insertion rather than for utilization of a multiple-position target wheel. In our approach, the target will be positioned accurately on a kinematic mounting fixture in the

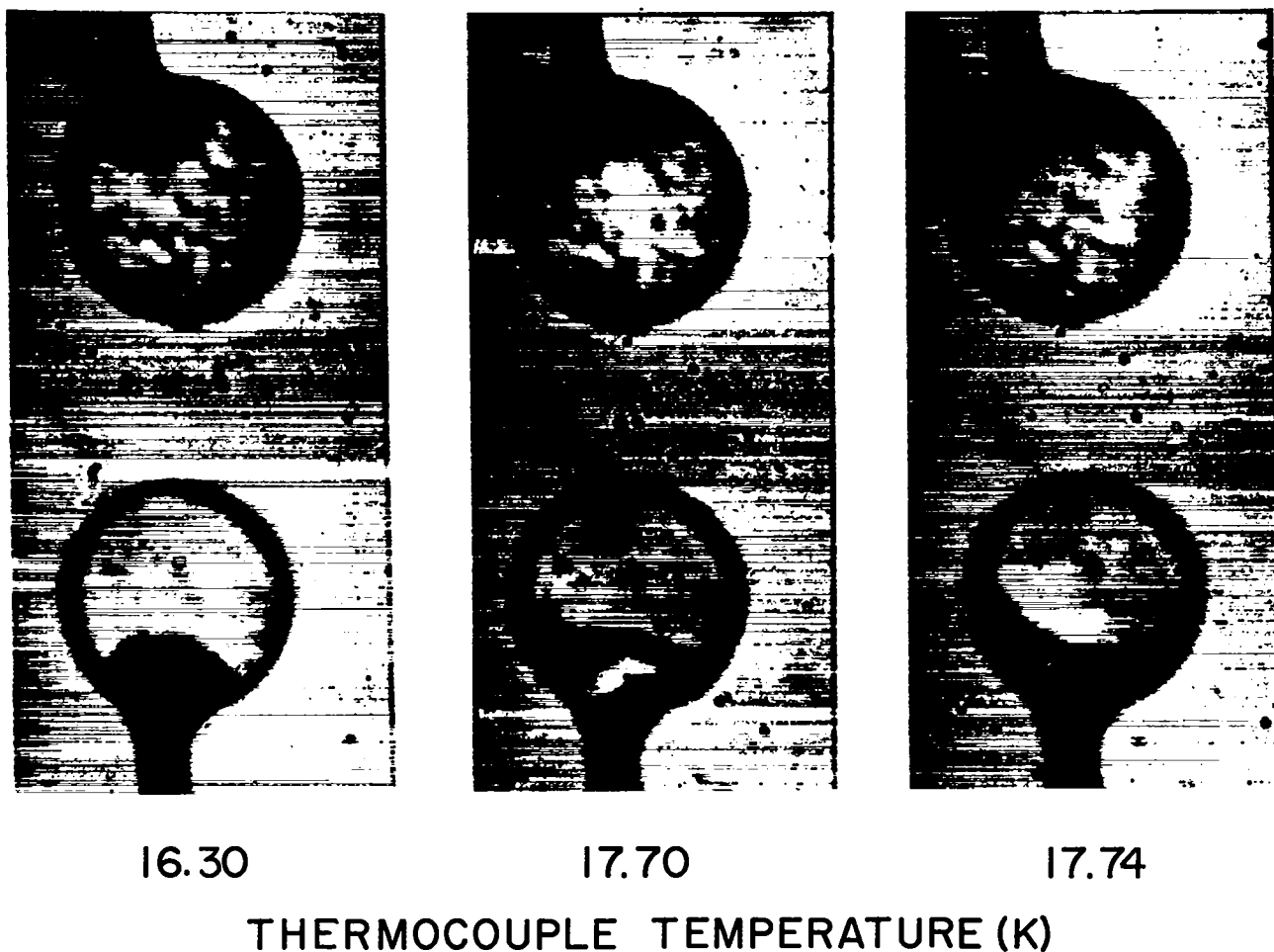


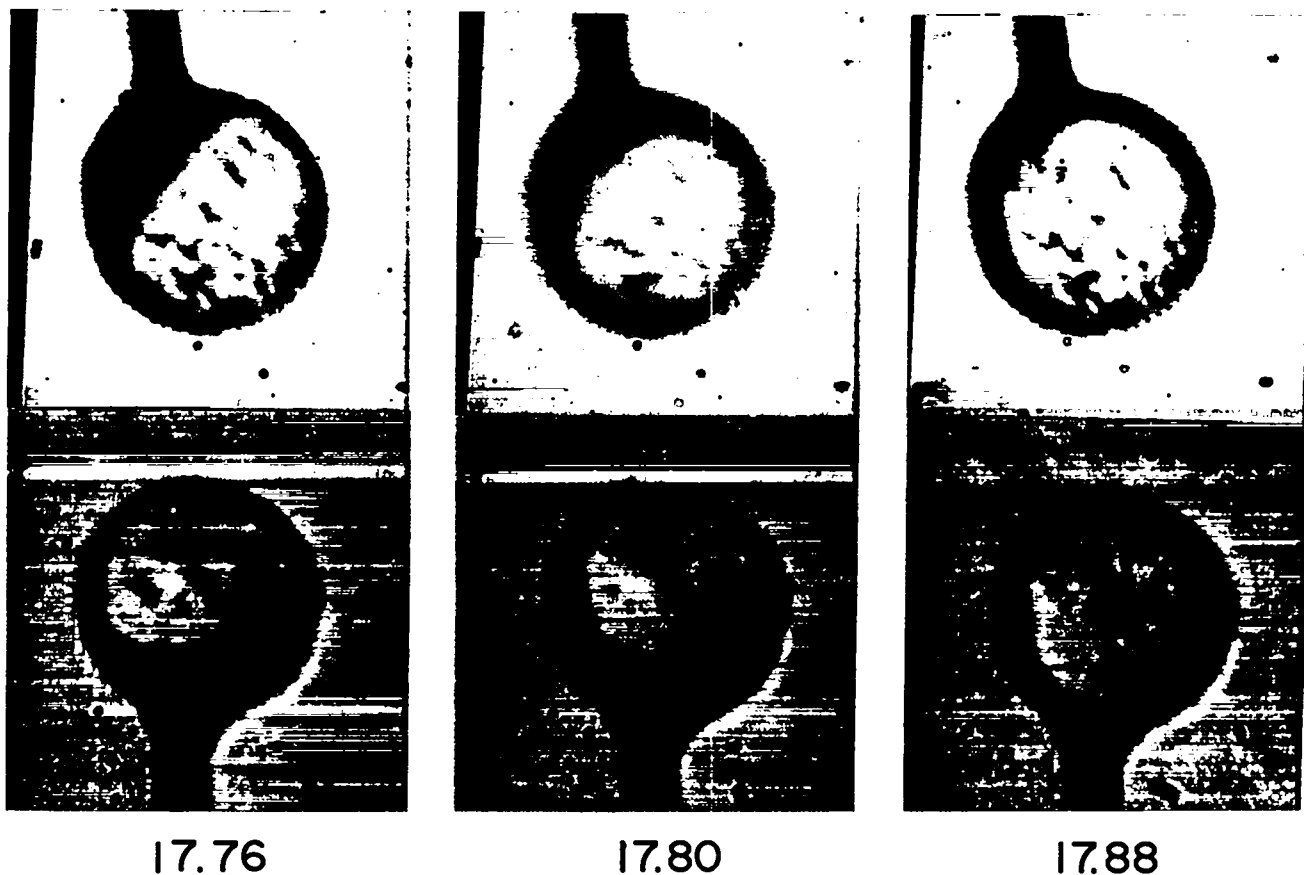
Fig. IV-20.

Photomicrographs of cryogenic targets with vertical fibers at thermocouple temperatures of 16.30 to 17.74 K. Target A is at top and Target B is below.

laboratory, to be transported through a vacuum lock into the target chamber. There, a mating fitting for the fixture will position the target in the desired location. Because this scheme relies on maintaining an accurate relative position between target and fixture, and because cryogenic targets will be produced directly in the target chamber, the suitability of this procedure for use with cryogenic targets depends on accurate repositioning of the target and support fiber from one cooldown to the next.

We have developed a new apparatus, shown in Fig. IV-25, to test the contraction and bending reproducibility of target supports. The support fiber

is mounted inside a copper cell with the target located near a reference pointer. The cell, filled with gaseous helium to a pressure of a few torr, is attached to the tailpiece of a continuous transfer refrigerator. The experimental procedure involves lowering the cell temperature to ~5 K, measuring the position of the target relative to the reference pointer on two axes, warming to room temperature, and then again cooling to 5 K for a second relative-position measurement. Fibers of various materials and treatments are being tested for suitability in the planned, single-target loading scheme for cryogenic targets.



THERMOCOUPLE TEMPERATURE (K)

Fig. IV-21.

Photomicrographs of cryogenic targets with vertical fibers at thermocouple temperatures of 17.76 to 17.88 K. Target A is at top and Target B is below.

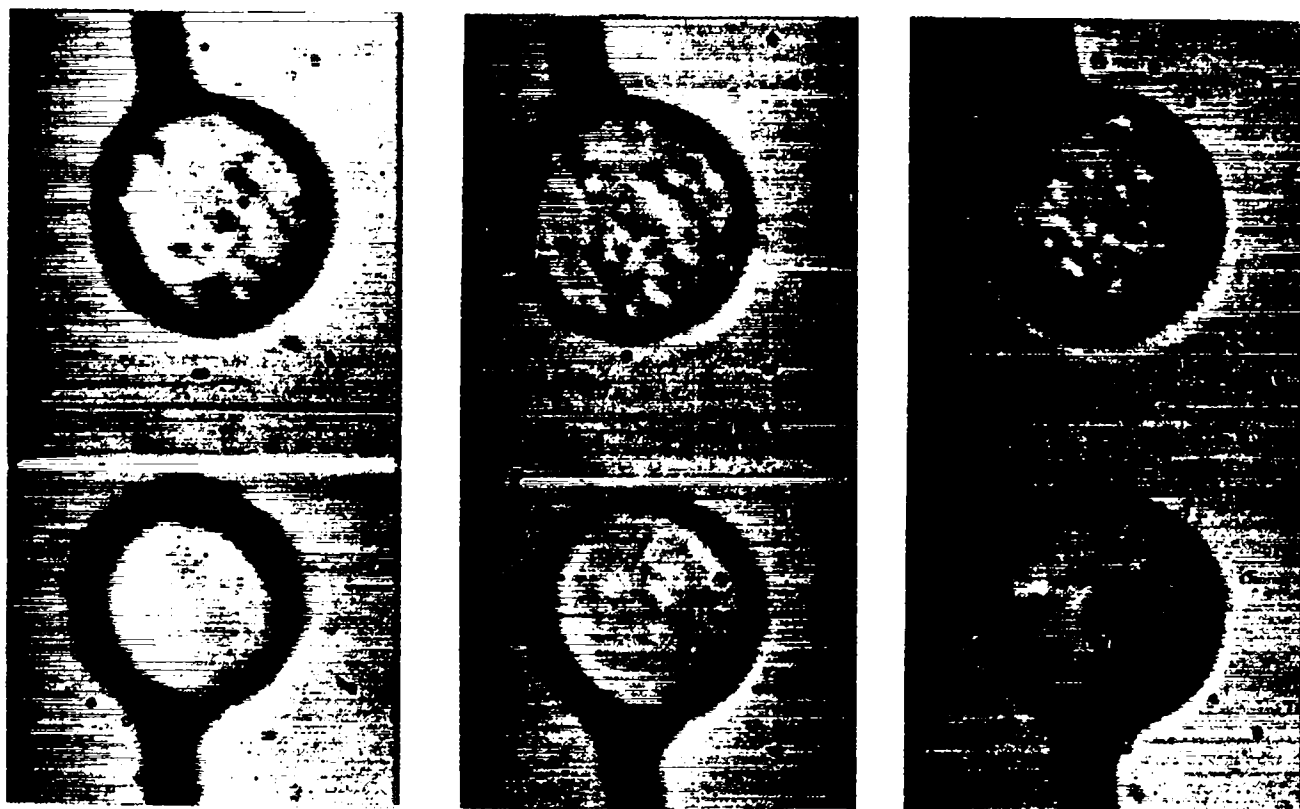
Property Measurements of Cryogenic DT (L. Schwalbe)

We have continued our measurements of the properties of liquid and solid H-D-T systems. Extensive measurements were made for the normal deuterium liquid-phase isothermal compressibility K and for the thermal expansion coefficient β . As a representative compressibility isotherm, the one corresponding to a temperature T of 20.000 K varied from $\sim 9.3 \times 10^{-4} \text{ atm}^{-1}$ at zero pressure to $6.55 \times 10^{-1} \text{ atm}^{-1}$ at the melting pressure (51.74 atm). Thermal expansivity isobars measured at intervals of $\sim 13.7 \text{ atm}$ have been nearly completed. For instance, the isobar corresponding to a pressure P of

14.6 atm varied quite uniformly from $\sim 13.7 \times 10^{-8} \text{ K}^{-1}$ 21.000 K to a value of $12.1 \times 10^{-8} \text{ K}^{-1}$ at the melting temperature (19.075 K).

Typical deviations of the individual expansivity and compressibility measurements from their respective smooth curve were seen to be less than 1%. These data have, moreover, been shown to be mutually consistent with respect to their temperature and pressure dependences according to the well-known thermodynamic identity,

$$\left(\frac{\partial \beta}{\partial P}\right)_T = -\left(\frac{\partial K}{\partial T}\right)_P.$$



20.0

30.0

46

THERMOCOUPLE TEMPERATURE (K)

Fig. IV-22.

Photomicrographs of cryogenic targets with vertical fibers at thermocouple temperatures of 20.0 to 46 K. Target A is at top and Target B is below.

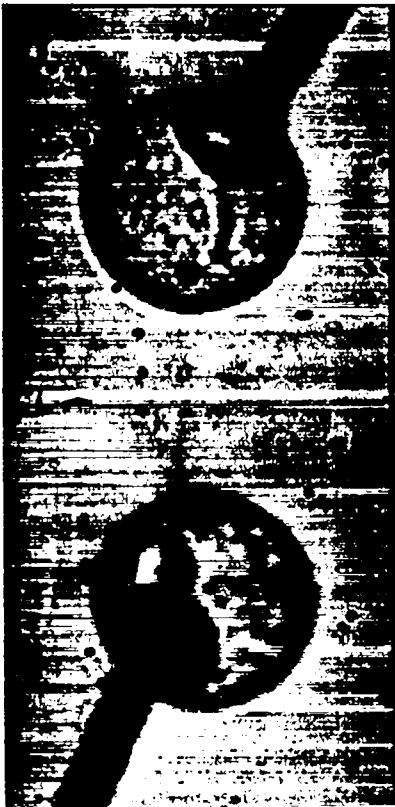
For temperatures and pressures in the ranges 19 to 21 K and 3 to 55 atm, respectively, these derivatives were found to be $\sim 6 \times 10^{-5} \text{ atm}^{-1} \text{ K}^{-1}$.

Although sufficient compressibility data are now available so that the behavior of this parameter along the melting line is reasonably well determined (that is, to ~ 1 or 2%, see Fig. IV-26), some additional work is still necessary before a similar thermal-expansion curve can be drawn.

In addition, the accessible pressure range (0 to ~ 70 atm) has been broadly covered for melting pressure, volume change on melting, and solid compressibility measurements. Solid compressibilities were roughly 20% of the corresponding liquid values.

We have also measured the volume changes on melting for normal deuterium. This quantity decreases from an extrapolated triple-point ($T = 18.73$ K) value of 11.8% to $\sim 10.8\%$ at $T = 20.4$ K. Precise liquid-density values along the melting curve were also determined and the two sets of data were combined to find corresponding solid densities. Plots of these data are shown in Figs. IV-26 through -28.

Finally, additional melting-pressure measurements were made so that accurate melting enthalpies and entropies could be derived from the volume in the determination of solid isobaric thermal expansivities and isothermal compressibilities.



16.20



17.90

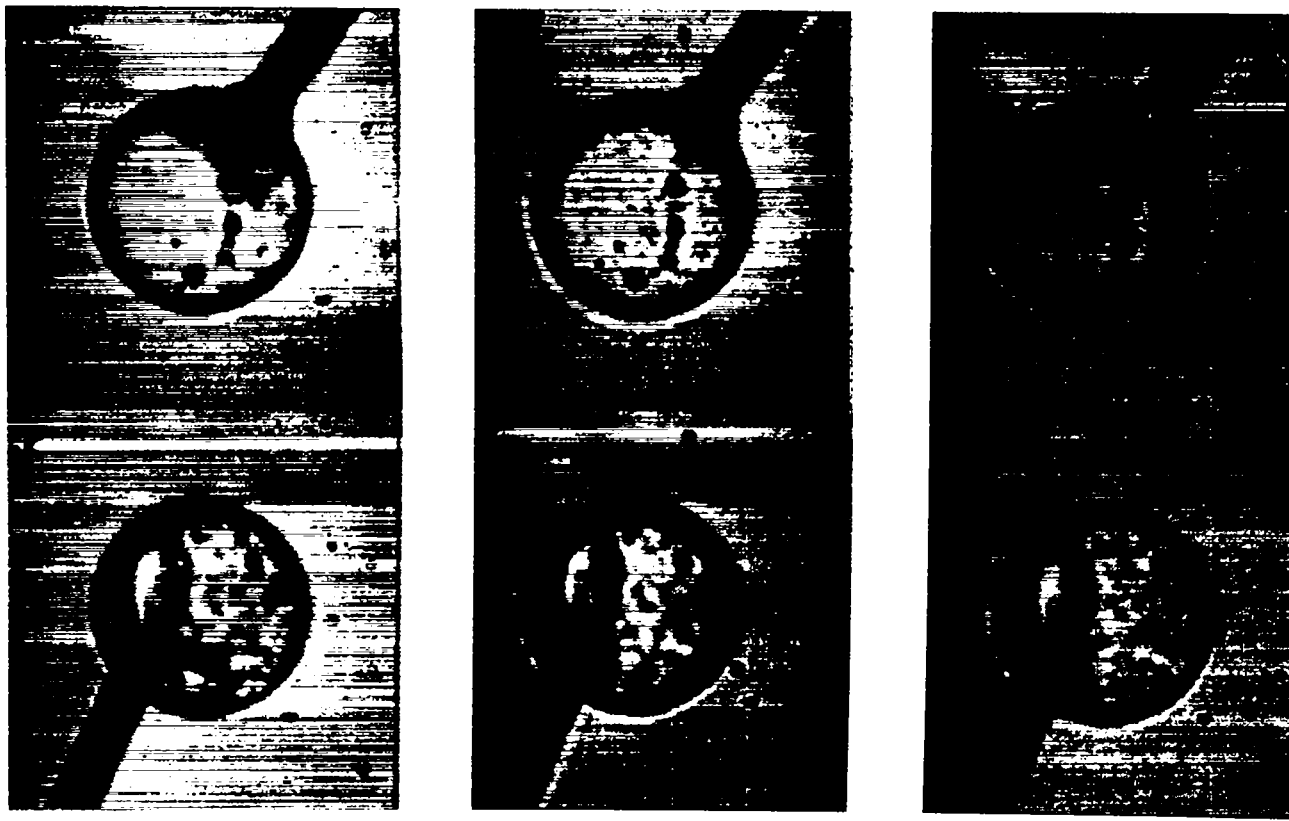


18.00

THERMOCOUPLE TEMPERATURE (K)

Fig. IV-23.

Photomicrographs of inverted cryogenic targets with nonvertical fibers at thermocouple temperatures of 16.20 to 18.00 K. Target B is at top and Target A is below.



18.04

18.10

53

THERMOCOUPLE TEMPERATURE (K)

Fig. IV-24.

Photomicrographs of inverted cryogenic targets with nonvertical fibers at thermocouple temperatures of 18.04 to 53 K. Target B is at top and Target A is below.

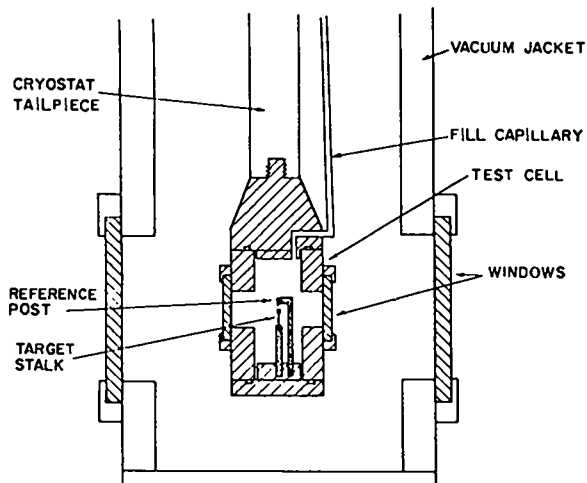


Fig. IV-25.

Apparatus for evaluating reproducibility of thermal contraction of targets upon cooling from 298 K to 4 K when using various mounting systems.

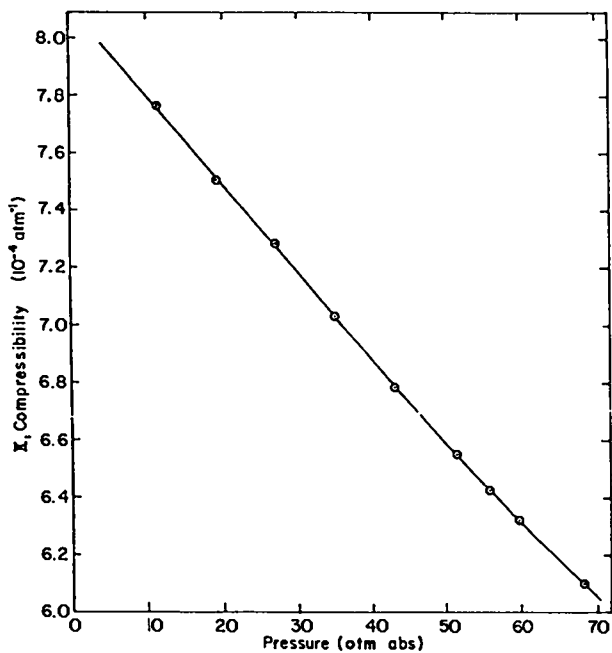


Fig. IV-26.

Compressibility of liquid normal deuterium along the melting curve.

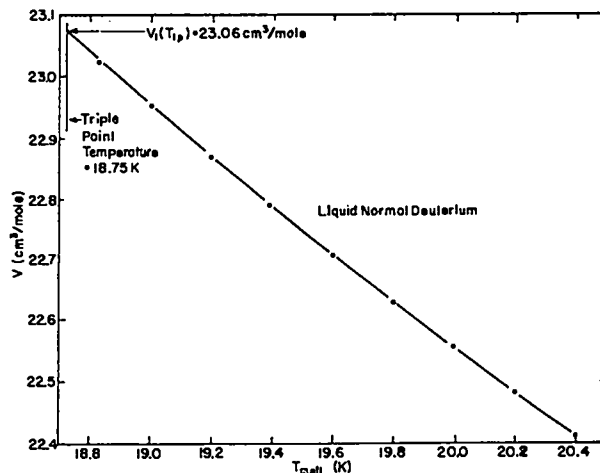


Fig. IV-27.

Specific volume of liquid normal deuterium along the melting curve.

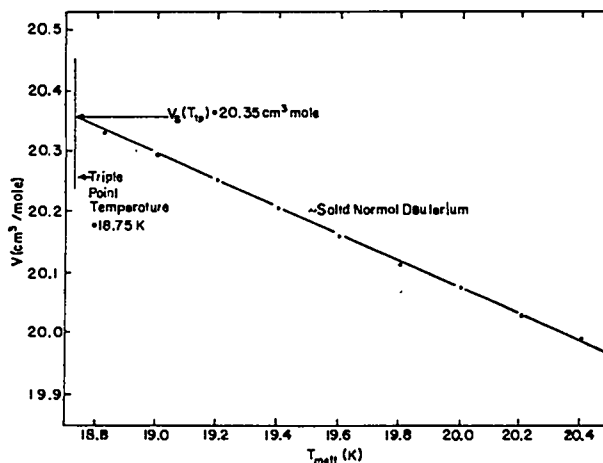


Fig. IV-28.

Specific volume of solid normal deuterium along the melting curve.

REFERENCES

1. R. J. Fries and E. H. Farnum, Los Alamos Scientific Laboratory report LA-5703-SR Rev. (November 1974).
2. W. B. Kunkel, *J. App. Phys.* **21**, 820 (1950).
3. E. Stark and F. Skoberne, Los Alamos Scientific Laboratory report LA-6616-PR (May 1977), Sec. IV.
4. R. H. Day and E. J. T. Burns, *Adv. X-Ray Anal.* **19**, 597 (1975).
5. M. A. Winkler, Los Alamos Scientific Laboratory internal report (June 1977).
6. R. H. Day, T. L. Elsberry, R. P. Kruger, D. M. Stupin, and R. L. Whitman, Los Alamos Scientific Laboratory internal report (June 1977).
7. R. J. Fries and E. H. Farnum, Los Alamos Scientific Laboratory report LA-5703-SR Rev. (November 1974) p. 6.
8. Peter Howell, 3M Company, St. Paul, Minnesota, private communication (March 1977).
9. R. J. Fries and E. H. Farnum, *Nucl. Instrum. Methods* **126**, 285 (1975).
10. G. Halpern, Exxon Research and Engineering Co., Linden, New Jersey, private communication (January 1977).
11. A. Mayer and D. S. Catlett, Los Alamos Scientific Laboratory reports LA-6583 and LA-6584 (April 1977).
12. E. Stark and F. Skoberne, Los Alamos Scientific Laboratory report LA-6834-PR (October 1977) Sec. IV.
13. A. T. Lowe and R. J. Fries, Los Alamos Scientific Laboratory internal report (July 1977).
14. See, for example, M. R. Havens, M. E. Biolsi and K. G. Mayhan, *J. Vac. Sci. Technol.* **13**, 575 (1976) and H. Yasuda in *Plasma Chemistry of Polymers*, M. Shen, Ed. (Marcel Dekker, New York, 1976).
15. R. J. Fries and E. H. Farnum, Los Alamos Scientific Laboratory report LA-5703-SR Rev. (November 1974) p. 8.
16. M. M. Mueller, Los Alamos Scientific Laboratory internal report.
17. E. Stark and F. Skoberne, Los Alamos Scientific Laboratory report LA-6616-PR (May 1977), Sec. IV, pp. 60-63.
18. E. Stark and F. Skoberne, Los Alamos Scientific Laboratory report LA-6510-PR (November 1976) Sec. IV, pp. 98-100.
19. T. M. Henderson, D. E. Solomon, R. B. Jacobs, G. H. Wuttke, D. L. Musindki, and R. J. Simms, "Cryogenic Microshell Pellets and Other Advanced Targets for Laser Fusion," paper presented at 4th Workshop on Laser Interaction and Related Plasma Phenomena, RPI, Troy, New York (November 8-12, 1976).

V. TARGET DIAGNOSTICS

The tiny volume and brief duration involved in the laser fusion process create needs for new diagnostic techniques having spatial and temporal resolutions in the submicrometer and 1- to 100-ps regime, respectively. These needs are being met with a vigorous program of diagnostics in such areas as laser calorimetry, charged particle and neutron detection, x-ray spectrometry, and subnanosecond streak-camera development.

INTRODUCTION

We are striving continuously to improve our ability to examine the fine details of laser-induced plasmas and to record with greater precision the phenomena associated with laser-target interactions. To do this, we need diagnostic instruments that record data faster and with greater resolution than presently possible; they should be simple and rugged and must function with a reproducibility that minimizes shot-to-shot variations and uncertainties.

These requirements impose demands that can be met only by continually advancing the state of the art through, for example, modifications and improvement of conventional techniques and equipment; enhancement of capabilities through invention and new development; and exploration of new concepts and theories. This varied approach to improving our diagnostic capabilities is discussed in the following paragraphs.

Major emphasis was placed on optical determination of density profiles in quasiplanar plasmas and on x-ray diode development. Work on laser pulse shaping is reported in Sec. I.

DIAGNOSTICS

A New Optical Diagnostic Method for Determining Profiles in Quasiplanar Plasmas (M. M. Mueller)

The computer code previously developed¹ to perform ray tracing through gradient-index media and

to calculate simulated interferograms from spherical plasmas was used to study various plasma density profiles.² Particular emphasis was given to profiles containing a narrow region of steep slope as a simulation of the profile to be expected with very intense irradiation. These studies showed that the strong refraction resulting from even modestly steep density gradients in dense laser-generated plasma severely limits the usefulness of visible-light interferometry as a diagnostic probe of steep profiles. Even for wavelengths as short as 0.25 μm , interferometry is limited to probing plasma electron densities less than $10^{21}/\text{cm}^3$ under most conditions of moderately steepened gradients. In many cases of extended plasmas with steep gradients, the limiting density is less than $10^{20}/\text{cm}^3$. Because the top of the steepened portion may be as high as $10^{21}/\text{cm}^3$, even in CO_2 laser-generated plasmas, this limitation may be important in interpreting our experimental interferograms even when uv probes are used.

This limitation is mainly caused by the fact that interferometers are usually limited to acceptance half-angles of 15° or less, whereas refraction at all but shallow radial depths in the plasma results in much larger angular deflections. Thus, we need a diagnostic tool that accepts large angles of deflection if larger radial depths are to be probed. Reflectance data as a function of impact parameter would seem to serve the purpose in principle; however, primarily because of the complexities stemming from spherical geometry, no practical way of generally inverting the data to obtain the plasma profile has yet been developed for cases of reasonably large plasma curvature.

Therefore, we turned our attention to a diagnostic method based on measured absorptance of probe beams as a function of angle of incidence on planar or quasiplanar plasmas, in the hope that practical unfolding methods could be developed in the simpler geometry. In the era of low laser power this approach would have been of academic interest only, because plasma planarity over dimensions of many wavelengths was difficult to achieve. Now, however, the advent of laser beams in the terawatt regime makes plasma quasiplanarity attainable in two different approaches: as the central portion of a fairly large focal spot on a flat target, or as an extended spherical plasma with a steep profile. In the latter case, one might have, for example, a plasma of 200- μm radius, while steepening might limit the penetration into plasma of even a short-wavelength probe beam to as little as 10 μm . Thus, in the terawatt regime, plasmas of effectively small curvature may be more the rule than the exception.

Thus, we need a code that will perform ray tracing in plasmas of small and smoothly varying curvatures. The basic problem is due to the nearly 180° turn the rays may make in a small region of path where the refractive index is very small and strongly varying. This puts a severe strain on any algorithm; a new code had to be developed which could handle very steep density gradients and sharp turns and would compute the light absorption along each ray path. For concreteness and simplicity, only inverse bremsstrahlung absorption (at a low effective electron temperature) has been used so far. Also, the present code cannot include wave effects such as resonance absorption. The case is thus valid only for s-polarization, or for p-polarization at fairly large angles of incidence.

For a given plasma profile density function and a specified microscopic absorption function, the code is then used to calculate the macroscopic probe-beam absorption as a function of the angle of incidence with probe-beam frequency as a parameter. The resulting reflectances are then used as simulated input data for a sequence of unfolding operations designed to reconstruct the profile.

While a general unfolding method has not yet been developed, success has been achieved for cases in which the electron density profile can be fitted by adjustable parameters in one of the following

shapes: exponential, arbitrary power, or segmented-linear with an arbitrary number of layers. For the last shape (of greatest interest because of its adaptability), the unfolding procedure is now only roughly approximate under certain conditions—primarily when a layer of gentle slope follows a layer of very steep slope. However, for most cases of interest, the reconstruction is fairly accurate (that is, with slope accuracy of 10% or better). For the exponential and arbitrary power profiles, in comparison, the reconstructions using noise-free simulated data are usually better, that is, accurate within few per cent, if the data are chosen to cover angle-space effectively and if the probe frequency is chosen properly for the given profile and the specified absorption model. Obviously, the finer the profile structure the greater the number of data points needed; however, for many purposes, data at only four or five angles would be quite useful. While the present reconstruction scheme employs reflectance data at only one frequency, accuracy over a wide range would be greatly enhanced if more than one probe frequency were used, particularly if covering extreme ranges of electron density; for example, 10^{18} to $10^{22}/\text{cm}^3$, were desired in one experiment.

Inherent in this diagnostic method is the fact that only the product of scale length and absorption coefficient of the plasma can be determined—not these factors separately. Thus, if independent evidence leads to a specification of one factor, the other can be computed. Because scale length at some instant of the plasma expansion could be measured by other means, this implies that the microscopic plasma absorption could be determined by using absorptances of short-pulse probe beams synchronized to that instant.

As mentioned previously, the plasmas encountered experimentally will probably have small, non-zero curvatures, whereas the unfolding scheme has so far been developed only for planar plasmas. To ascertain whether the scheme is useful for plasmas of small curvature, numerous simulation runs have been carried out, but the results cannot be summarized easily. However, as might be expected, there is a tradeoff between allowable plasma curvature ratio and acceptable accuracy of profile reconstruction. With probe beams of a single, adequately short wavelength, a curvature ratio (here

defined as the depth of the probe critical density divided by the radius of curvature of the plasma (at its outer boundary) of about 1/40 is roughly the upper limit for fairly accurate reconstruction. However, when more than one probe frequency is employed, this limit can be raised at least twofold. There is also the favorable prospect of developing an iterative scheme, which will greatly increase the acceptable curvature ratio limit, but this has not yet been done. In brief, the prospects appear reasonably favorable for using this diagnostic method on an extended spherical plasma with a steepened profile. In practice, the largest uncertainty in the reconstruction will probably be caused by departures of the actual profile from any of the three canonical forms; however, curvature, unless it is independently measured (for example, by angular displacements of reflected beams), will also contribute greatly to the uncertainty.

One of the profile functions that can be reconstructed almost exactly, using noise-free data from a planar plasma, is shown in Fig. V-1. This is the arbitrary-power form: $N_e = N_{ch} \cdot (z/z_0)^P$, with P chosen to be 7.0, N_e is the electron density, N_{ch} is

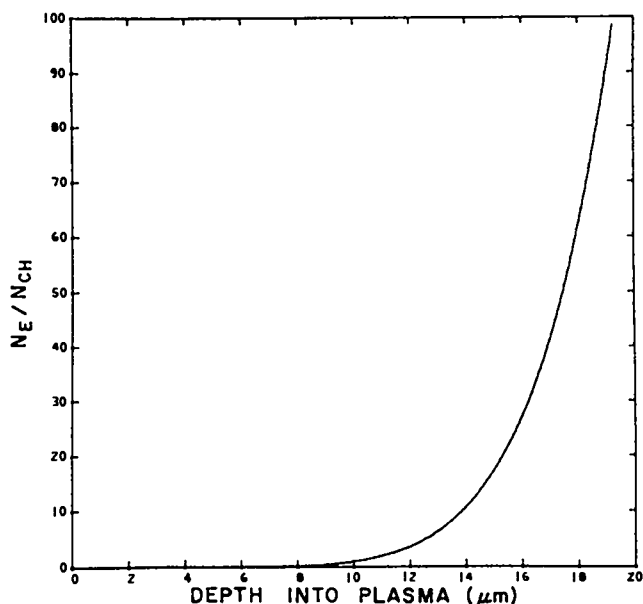


Fig. V-1.

Arbitrary-power plasma profile for $P = 7$; N_e/N_{ch} is the electron density relative to the critical density for the heating laser.

the critical density for the heating frequency, z_0 is the plasma scale length, and z is the depth beneath the outer boundary. Note that this is a rather steep, but smooth, density profile, falling to half-value in less than $2 \mu\text{m}$ from the probe-light critical surface. The curvature ratio for the heating frequency is taken as 0.03, whereas that for the probe frequency (here taken to be 10 times the heating frequency) turns out to be 0.058. Fig. V-2 displays 11 ray paths over a range of angles incident on a common point on the plasma boundary. The dotted line is merely a straight line for reference to a planar plasma. Note that, because of the steepness of the profile, the turning points at even large angles are never displaced far from the critical surface, in marked contrast to a case having moderate profile declination. For this plasma profile, the scale factor $z_0 = 10 \mu\text{m}$ and, for a CO_2 laser-heated plasma, the probe wavelength would be $1.06 \mu\text{m}$. The maximum depth of penetration is $19.3 \mu\text{m}$, at an electron density of $1 \times 10^{21}/\text{cm}^3$.

The effect of plasma curvature is clearly illustrated by Fig. V-3, which plots the logarithm of

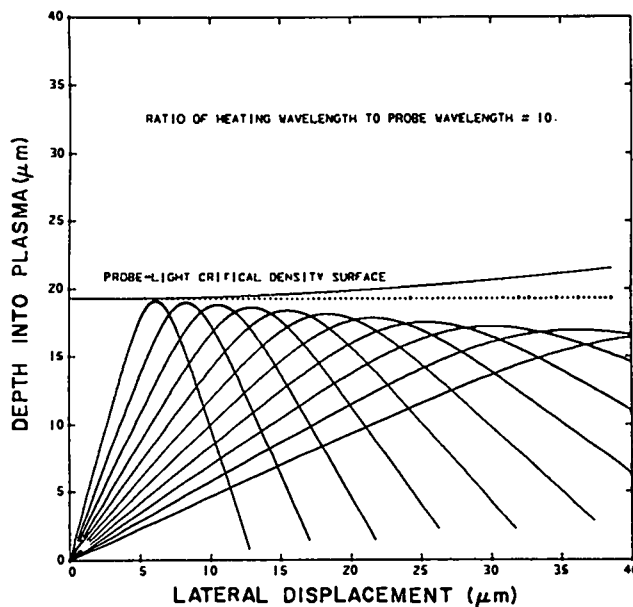


Fig. V-2.

Ray paths in a plasma having the density profile given in Fig. V-1 for a frequency 10 times the heating frequency and for a curvature ratio of 0.058. The 11 paths shown range in angle of incidence from 15 to 65° .

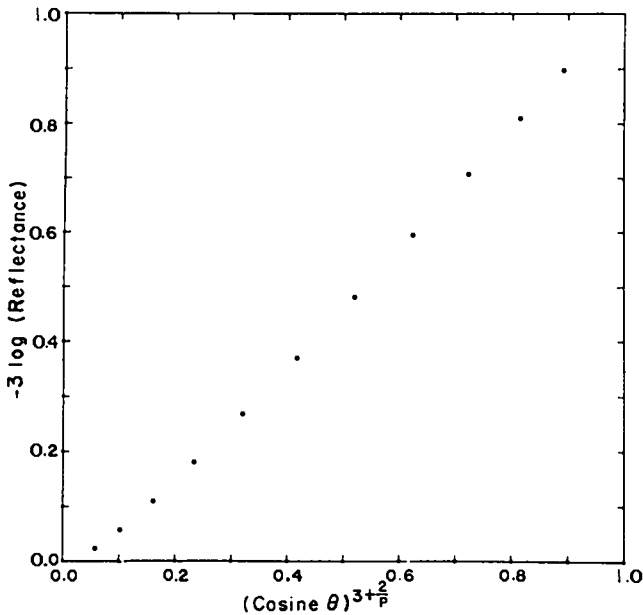


Fig. V-3.

Semilogarithmic plot of reflectances of the ray paths shown in Fig. V-2 for inverse bremsstrahlung absorption vs a function ($P = 7$) of the angle of incidence θ . Plasma curvature causes the nonlinearity at large θ .

the reflectance "data" (calculated by using an inverse-bremsstrahlung model of plasma absorption under the conditions of Figs. V-1 and 2) vs $(\cos\theta)^{3+2/P}$, where θ is the angle of incidence of the probe beam on the plasma; θ varies from 15 to 65°, inclusively. If the curvature were zero, the points would lie on a straight line through the origin. The departure from linearity occurs from angles larger than ~45°. Therefore, whenever curvature is suspected, large angles should be avoided, but resonance absorption may interfere with the unfolding unless s-polarization is used.

While the absorption is integrated along all of the ray path through the plasma, most of the total absorption occurs near the turning point. Therefore, this method is most sensitive at densities above about one-tenth the probe critical density, and becomes ineffective below ~0.03 N_{cp} . To cover a range factor of 50 or higher, at least two probe frequencies are required. For steepened CO₂-heated plasmas, the most useful probe wavelength should be ~1 μm .

X-Ray Diode Development (R. H. Day, D. B. vanHulsteyn, P. Lee)

General. We have designed, built, and calibrated x-ray diodes (XRD) to study the time dependence of soft x rays produced in laser fusion plasma. Two different versions of XRDs have been built: a four-channel system and a single-channel system, both with aluminum cathodes, as shown in Fig. V-4.

Four-Channel System. The following absorbers were used:

Channel No.	Absorber	Response
1	1 mm Al	Zero
2	0.5 μm Al	80 eV and 1 keV
3	272 ng/cm ² Kimfoil plus 0.1 μm Al	270 keV
4	bare cathode	0.01 - 1.0 keV

The transmissivity of these detectors as a function of energy leads to a shaped response, which has been measured and is incorporated into the data presented in Fig. V-5. A potential of 600 V was applied between the cathode and anode of each diode by a battery. A blocking capacitor, located 10 cm from the XRD, provided charge during its operation.

Single-Channel System. This XRD also contained an aluminum cathode and a wire-mesh

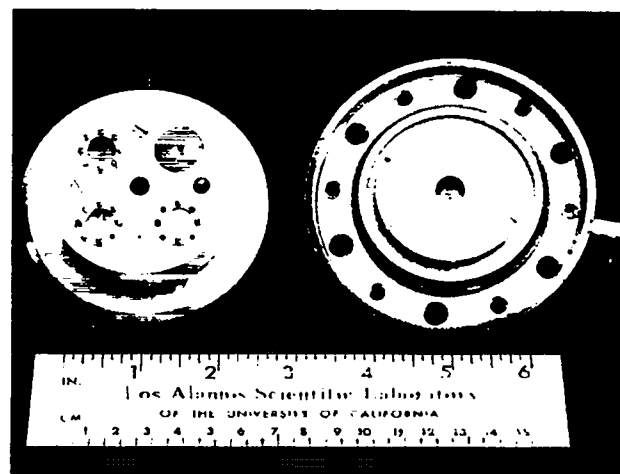


Fig. V-4.

Single-channel x-ray diodes with capacitor built radially around the cathode.

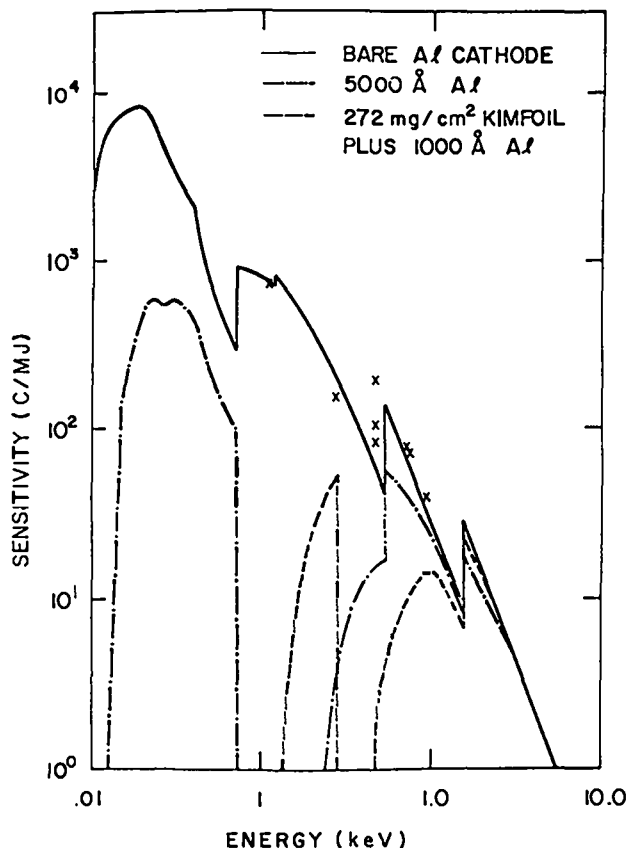


Fig. V-5.

Calibration results for aluminum x-ray diodes.

anode, but the capacitor was built radially around the cathode and was moved closer to the anode. A biasing potential of 600 V was applied for most of the calibration shots.

The time response of the XRDs was determined from the x rays produced by 3-J, 40-ps (FWHM) neodymium:glass laser pulses interacting with plane CH₂ and aluminum targets. A 5-GHz oscilloscope, with a risetime of 75 ps and a writing speed of up to 0.5 ns/cm displayed the XRD time response. Figure V-6a shows the risetime of the four-channel XRD to be 250 ps, whereas Fig. V-6b shows the risetime of the single-channel XRD to be 140 ps. In both cases, the sweep rate was 1 ns/div. Note that the soft x-ray emissions, due to the slow bound-bound recombinations, last ~1 ns.

We found the risetime of the XRD to vary approximately as $V^{-1/2}$, where V is the biasing voltage, because electron transit time from cathode to anode is the limiting effect. Shorter risetimes can be ob-

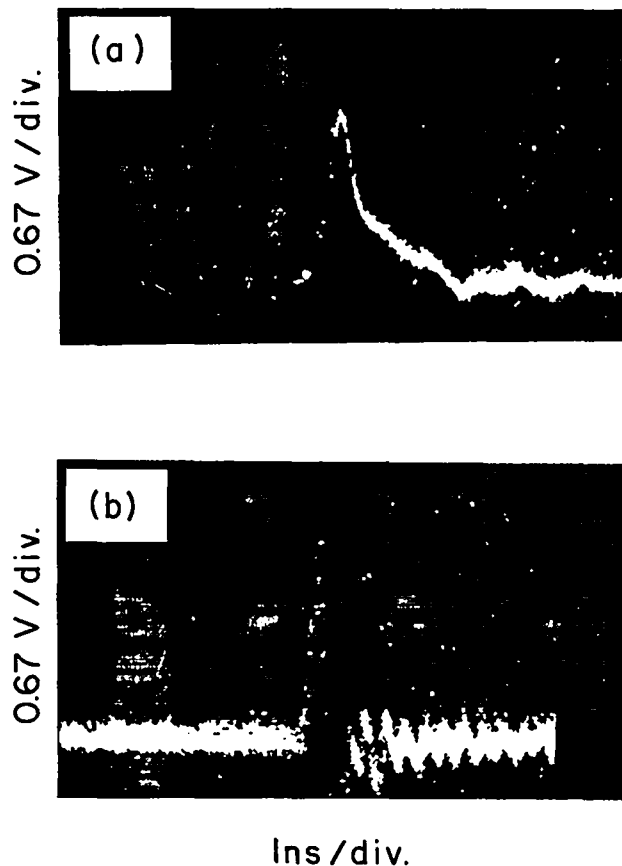


Fig. V-6.

Time response of x-ray diode obtained with 30-ps, 3-J neodymium:glass laser pulse on aluminum target: (a) four-channel response with a risetime of 250 ps, (b) single-channel response with a risetime of 140 ps.

tained with the capacitor built uniformly around the cathode and with a decreased cathode-anode separation. These diodes will allow us to obtain a detailed, time-dependent, soft x-ray emission characteristic for CO₂ laser-produced plasmas whose duration is 1.5 ns.

Pyroelectric Vidicon Cameras (D. Kohler, P. Weiss)

We have begun to evaluate pyroelectric vidicon (PEV) tubes and cameras in imaging the light from CO₂ lasers. In tests of three camera-tube combinations, the PEV tubes had a linear dynamic range

close to 1000. Most cameras display too much preamplifier noise to take advantage of that range and clip the video signal to fit the small useful range of TV monitors. A properly designed custom camera with appropriate readout should provide quantitative information about energy distributions in laser beams and focal spots. We recently received an improved camera which, however, still leaves room for improvement. The camera has been used to observe the focal spot on the SBS, as described below.

A better camera has been ordered and should be received soon. In addition to the standard video display of the signal, which is severely clipped, this camera will have a full-range output designed to match the 1000:1 dynamic range of the PEV tube. The preamplifier input noise will be ~ 0.5 nA in a 5-MHz bandwidth, which is significantly less than in most cameras. The camera will produce synchronizing signals so that the tube signal on selected horizontal TV lines can be displayed on an oscilloscope.

Ten-Micrometer Microscope

An infrared microscope assembly has been installed on the SBS to examine the focal spot and assist in target alignment. The assembly consists of germanium relay lenses that image the focal spot and/or a target on the face of a PEV tube at a magnification of $\sim 20X$. A target may be back-lit with the broad beam from a small, pulsed, auxiliary CO_2 laser as well as with the focused beam from the main laser oscillator.

An indication of the resolution of the system is shown in Fig. V-7. The lower image shows the view through an optical microscope of a bifilar crosshair. The wire separation is $125 \mu m$ center to center. An image of these crosshairs in $10.6\text{-}\mu m$ light is shown in the top image. The resolution appears to be of the order of $20 \mu m$. The distortion of the image is the result of nonlinear sweep ramps in the TV monitor and is not camera-related.

The microscope was used to examine the shape of the focal spots in the SBS as the location and orientation of the focusing mirror were adjusted.

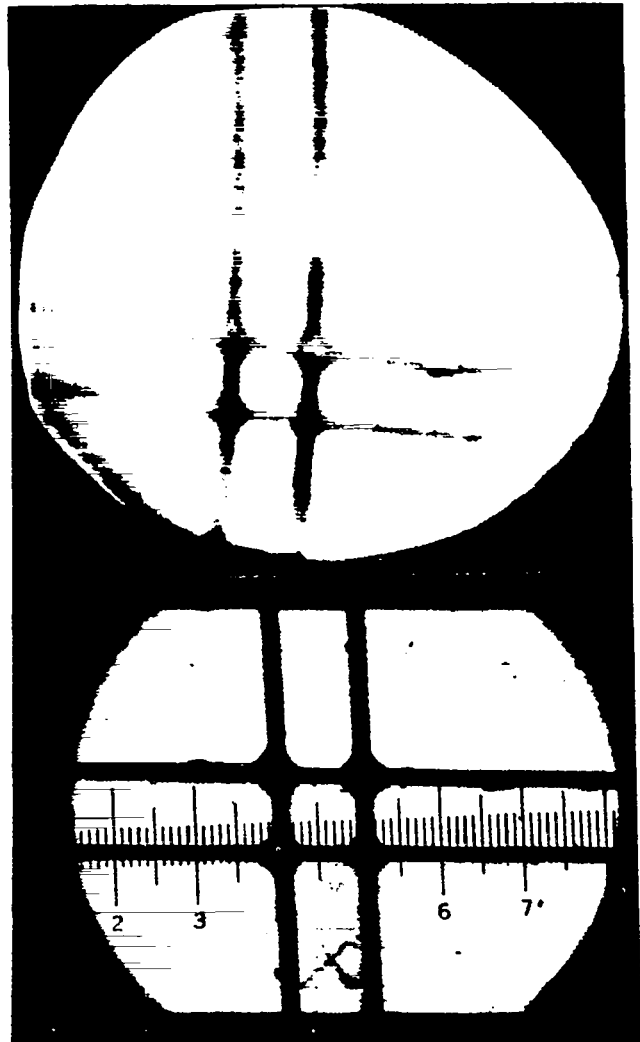


Fig. V-7.

Bifilar crosshairs as seen through a visible-light microscope (lower photo) and through our $10\text{-}\mu m$ microscope. The wires have a diameter of $25 \mu m$ and are spaced $125 \mu m$ apart, center to center.

Photographs of the spots are shown in Fig. V-8. The central position in the array of photos was the starting position. The shapes of the spots compare well with ray-trace calculations and indicate an azimuthal error in the original position of the focusing mirror.

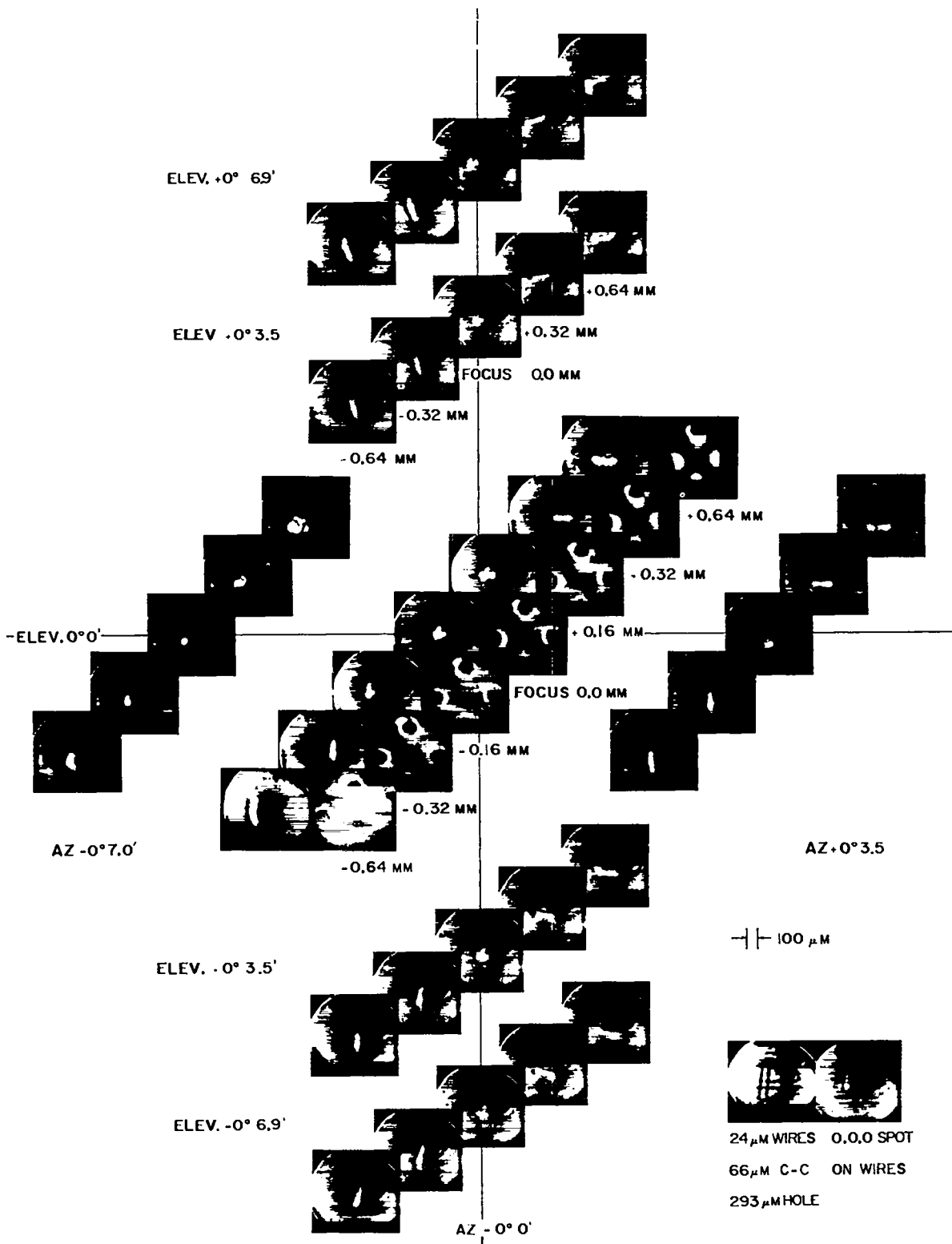


Fig. V-8.

Array of images of the micrometer focus for various focus, azimuth, and elevation adjustments of the focusing mirror.

Comparison of Mask Test and 10- μ m Microscope (D. Kohler, I. Liberman, J. Manning)

We compared two means of focusing and aligning the CO₂ beam for the SBS: the 10- μ m microscope and an autocollimating mask test (developed by EG&G, Inc.). Both employ PEV detection of the 10.6- μ m light. The mask, having 5-cm-diam holes, was placed \sim 5 m from the focusing mirror, and a 1.3-cm-diam ball was placed at the target position. Some photographs of the 10- μ m light retroreflected onto the mask are shown beside the central pictures in Fig. V-8.

Optimum focusing required detailed knowledge of the beam's spatial profile. In our tests using the SBS oscillator pulse, we obtained optimum focus with the microscope system by minimizing both astigmatism and focal-spot diameter. A check with the mask test revealed that the nonuniform intensity distribution in the oscillator pulse caused the visual appearance of a defocused beam. This systematic error is highly reproducible, indicating that the signature of the mask test may be used for alignment. Alternatively, the use of an apodizing filter to correct the beam profile is being investigated. Our tests are of comparable sensitivity to pointing errors and defocusing, and both tests are convenient to use with a video storage and display system.

Aberrations and depth of field were also studied. Aberrations could lead to erroneous estimates of best focus with either system. Annular and disk masks were placed on the CO₂ beam to check for spherical aberration, and none was observed with the microscope. The microscope diagnostic was also used to reduce astigmatism and coma. Thus, the focusing off-axis paraboloid mirror could be aligned to within 1.0 mrad of optimal focus. Many photographs were taken of the misaligned conditions, using both microscope and mask tests to provide a catalog of signatures for future alignment tasks. Depth of field, as measured by both techniques, is $\pm 150 \mu\text{m}$.

We also used the microscope to estimate the intensity distribution in the focal spot. The test was performed with only a nanosecond oscillator pulse. The measurements are being analyzed, but the core of the focal spot appears to be less than 100 μm in diameter.

REFERENCES

1. E. Stark and F. Skoberne, Los Alamos Scientific report LA-6510-PR (November 1976) p. 102.
2. E. Stark and F. Skoberne, Los Alamos Scientific report LA-6616-PR (May 1977).

VI. APPLICATIONS OF LASER FUSION—FEASIBILITY AND SYSTEMS STUDIES

Our feasibility and systems studies are being performed to analyze the technical feasibility and economic aspects of various commercial and military applications of lasers and laser fusion. The direct production of electricity in electric generating stations is of major concern. The general objectives of these studies are: the conceptualization and preliminary engineering assessment of laser fusion reactors and other generating-station subsystems; the development of computer models of generating-station subsystems for economic and technology tradeoff and comparison studies; and the identification of problems requiring long-term development efforts. Emphasis in military applications studies is placed on relatively near-term weapons-effects simulation sources and facilities.

SYSTEMS ANALYSIS COMPUTER PROGRAMS

Program CAPITAL and Improvement of the Functions of Program TROFAN for Estimating Electric Power Production Costs for Laser Fusion Power Plants (J. H. Pendergrass)

Upgrading of Program TROFAN. TROFAN¹ is a computer program for estimating electric power production costs of laser fusion generating stations, which was developed here over the past few years. TROFAN was designed to perform certain design scaling calculations; compute energy and mass balances; and estimate relative capital, operating, and maintenance costs to facilitate tradeoff studies. Many computations carried out by TROFAN are based on simplified or preliminary physical models and economic theories, consistent with the early state of development of conceptual plant designs, and with simple economic and physical-property data bases.

Recent advances in our knowledge of these areas and a preference for absolute rather than relative projections of power production costs have resulted in efforts to upgrade the capabilities of TROFAN. It has been recognized that all aspects of estimation of power production costs embodied in TROFAN re-

quire significant improvement, but because the required effort would be large, this task will be performed in stages using the best data available and doing the upgrading as resources permit.

Program CAPITAL. The capital cost estimating procedure of TROFAN was to be improved first, motivated by the desire to have a generalized capability for estimating capital costs for advanced-technology facilities of all types. The result was the stand-alone FORTRAN code CAPITAL, which was designed to interface with programs performing other functions of TROFAN in an improved manner, and to be merged with TROFAN as an initial step in improving power-production cost estimates. CAPITAL provides sufficient flexibility to encompass the entire range of capital-cost-estimate stages from the preliminary to the final Title III estimate, with data requirements commensurate with the level of estimates being performed.

Detailed Characteristics of CAPITAL

Account Structures. The framework of CAPITAL is the account structure. Each account in the account structure contains an item or items isolated or grouped for some logical reason.

To estimate the capital cost for a particular facility, the user must first set up an appropriate account structure by specifying the list of reference accounts. The user can associate with each account a description of the items covered by the account. The user must then designate a subset of the entire list of reference accounts as the set of base accounts, for each of which cost data are to be supplied.

The user must also designate one or more subsets of the reference account list as summary account lists for which computed cost data are to be output. The base-level account list can be so specified. By specifying summary accounts which are not themselves base-level accounts one can obtain summations of cost data over all contained base-level accounts.

Construction Schedule. The user can either define a construction schedule in terms of an arbitrary number of construction periods of arbitrary duration or assign a common length to an arbitrary number of construction periods.

Cost Data Input Options. Considerable care has been taken to eliminate unnecessary data input requirements when only simple cost models are justified, by providing the user with options regarding required detail of data input for each type of economic parameter. In a number of instances, default values, which represent reasonable average or typical values for various parameters, have been provided.

Cost Categories. The costs to be associated with the items covered by each base-level account are divided into categories of factory equipment, spares, site materials, engineering and design, inspection and testing, craft labor, transportation and equipment, subcontract or package deal, use tax, overhead, and profit.

Cash Flow and Interest Expense Summaries. CAPITAL can also provide a summary of the total capital expenditures for each construction period, the cumulative total capital expenditures through each construction period, the total interest expense incurred during each construction period, the cumulative total interest expense through each con-

struction period, the cash flow, total interest expense incurred plus total capital expenditure during each construction period, and the cumulative cash flow through each construction period.

Merger of Programs CAPITAL and TROFAN. Programs CAPITAL and TROFAN have been merged in the following sense. TROFAN is used to compute energy and mass balances, to size plant components, and to generate purchase costs of laser fusion power-plant components, but TROFAN also generates a base-cost data file for input to CAPITAL. With proper additional input for, e.g., the cost of construction money, for a construction schedule, for sales taxes, overhead, and profit, CAPITAL computes the final capital cost of a power plant at the end of construction, including interest during construction. The merged TROFAN-CAPITAL no longer computes a cost of production of electric power. That function is performed much more accurately by the program VENTURE, which is described in the following section.

Future Work. The principal aims for the future with regard to improvement of the functions previously performed by TROFAN in estimating laser fusion power-production costs include: (1) development of more accurate physical models for laser fusion power-plant components to permit more accurate calculation of, for example, mass and energy balances, plant performance, and sizing of components; and (2) development of more accurate data bases for capital costing, construction scheduling, operation and maintenance; and improvement in estimation techniques for operating expenses, maintenance costs, and plant reliability.

Program VENTURE (J. H. Pendergrass)

Introduction. A FORTRAN program called VENTURE has been written to perform venture-worth analyses and to compute lifetime-discounted average or levelized costs of production for a projected enterprise. Although the terminology of VENTURE is that of the electric power industry, it can be used generally for economic analysis of any proposed venture. At present, VENTURE is a

stand-alone program, with no capability for computing items such as operating costs, maintenance costs, capital costs, unit operating characteristics, or working capital requirements. However, VENTURE is designed to interface readily with sub-routines or programs used to compute values of these parameters. Parameter studies, sensitivity analyses, and examinations of effects of changes in economic conditions, among others, are facilitated by the flexibility provided in VENTURE.

Structure of Utility Ventures. VENTURE is aimed at performing economic analyses of electric generating plants with sufficient flexibility to allow treatment of multiple units with different operating characteristics and histories and with multiple depreciable and nondepreciable capital investments. This allows, for example, consideration of energy parks or entire utility organizations, of environmental- and/or public-safety-related retrofitting of equipment and facilities mandated by regulatory bodies, of capital investments to improve unit operational performance, and of the evolution of an electric generating station over a long period of time.

The user can specify an arbitrary number of non-depreciable capital investments, each beginning in an arbitrary venture year and disposed of in an arbitrary venture year. Similarly, an arbitrary number of depreciable capital investments made in arbitrary venture years with arbitrary estimated venture years of salvage for income-tax depreciation purposes can be specified.

The number of operating units at an electric generating station or stations, the venture years in which each begins normal operations and is decommissioned, and year-by-year operating characteristics, that is, nominal electric power output, overall plant thermal conversion efficiency, and plant or availability factors can be specified arbitrarily.

Venture Worth and Levelized Power Cost. The discounted annual venture profit or loss for a particular year is defined as the summation of the discounted income cash flows minus the summation of the discounted outlays for that year. Incomes considered by VENTURE include revenue from sales of

electric power, tax credits for investments, and income or losses due to error in estimation of salvage values and capital gains from sale of nondepreciable investments.

Outlays considered include operating costs, maintenance costs, capital recovery, decommissioning costs, return on capital investments, federal, state, and local income taxes paid on credits earned, and property, sales, and franchise taxes.

The venture worth for a particular undertaking is defined as the summation over all venture years of the discounted annual venture profits and/or losses for that venture. The venture worth represents the profit or loss relative to the cost of doing business for the venture, with return on invested capital included, discounted to take into account the time value of money, plus monetary inflation if present. The levelized cost of power production is defined as the constant sales price for which the venture worth is zero and, therefore, represents the cost of doing business for the venture on a unit power basis.

VENTURE is intended to apply to publicly owned utilities and especially to utility companies of sufficient size and profitability so that immediate advantage can be taken of all tax credits in any venture year. The cost of money to the venture can be computed as an arbitrary mix of debt and equity at arbitrary rates and rates of return.

All cash flows, annual revenue from sale of electric power, and income taxes can, at user option, be discounted to an arbitrary year in one of several different ways in accordance with the type of cash flow. Interest rates and rates of return on stock are in terms of yearly values compounded annually.

The capital required for decommissioning of each unit is accumulated through equal annual sinking-fund deposits for each unit, beginning in the first year of normal operation of that unit and ending in the last year of normal operation, that is, the year before decommissioning, of that unit. Expenditures for decommissioning are subtracted from taxable income during the venture years in which expenditures for decommissioning are actually made.

If errors are made in establishing the salvage value of a depreciable capital investment, then the depreciation allowed for income-tax purposes will be too small or too large, resulting in either an operating income or loss during the actual year of

salvage. The error is computed as the difference between user-supplied actual and estimated salvage values for each depreciable capital investment.

The return on invested capital for a particular venture year is computed by multiplying the sum of (1) the nondepreciated depreciable capital in force during that year, (2) the nondepreciable capital in force during that year, and (3) the working capital for that year by the cost of money to the venture during that year.

Capital recovery for depreciable capital investments is performed by means of equal annual sinking-fund deposits for each such investment beginning in the year the depreciable capital investment is made and ending in the year before the estimated venture year in which the investment is salvaged. The capital to be recovered consists of the difference between the original value of the investment and the estimated salvage value. At user option, the capital to be recovered can be increased by an amount sufficient to allow for recovery of purchasing power at the time of salvage equivalent to the investment when originally made.

At the option of the user VENTURE will compute for each depreciable capital investment for each year during which the depreciable capital investment is in force a depreciation allowance for income-tax purposes using either the straight-line method or the sum-of-the-years'-digits method.

The actual electric power production during a particular venture year is computed as the sum of the products of nominal electric power production rate and the plant or availability factor for all units operating during that year.

The gross receipts from sales of electric power during each venture year are computed as the product of the actual annual power production from all units operating during that year and a user-supplied sales price of electric power.

The amounts of state and local gross receipts or sales taxes collected by the utility organization are computed by multiplying total sales of the electric power by user-supplied state and local tax rates.

Property taxes levied against the sum of the total depreciated value, assuming straight-line depreciation between user-supplied investment years and actual salvage years, of all depreciable capital investment, all nondepreciable capital investments, and/or of the working capital in force during a ven-

ture year can be computed at both state and local levels.

Franchise taxes or taxes assessed for the privilege of doing business can be computed at both state and local levels.

VENTURE can compute income tax liabilities at the federal, state, and local levels. The taxable income for any venture year for each of the three levels before subtraction of income tax assessed at the other two levels is taken to be the same.

State and local income taxes paid during a given year are always subtracted from the federal taxable income for that year. At user option federal and/or state income taxes can be subtracted from the local taxable income, and/or federal and/or local income taxes can be subtracted from the state taxable income. The user can also specify delay in payment of a portion of the income tax liability incurred in a venture year until the following year.

Investment tax credits, which are based on qualifying portions of depreciable investments, can be computed at the federal, state, and local levels. The investment tax credits, which are subtracted directly from income tax liabilities rather than from taxable incomes, are applied in the venture year in which they are earned.

Concluding Remarks. VENTURE is believed to be an accurate and flexible code for estimating economic performances of future electric power-plant ventures. To avoid the necessity for providing detailed economic data where not available or justified, various data input options are provided.

The intention is eventually to merge VENTURE with the recently completed merged form of TROFAN and CAPITAL and to write improved subroutines for estimation of operating costs, maintenance costs, working capital, and plant availability factors, to permit more accurate estimation of laser fusion power-plant economics.

REACTOR CONCEPT STUDIES

MHD Deceleration in Magnetically Protected Reactor Concept (I. O. Bohachevsky)

Introduction. Calculations carried out as part of continuing fusion reactor systems analyses^{2,3}

revealed that the energy sinks intended to collect the energy of the pellet debris in the magnetically protected reactor cavity may suffer excessive sputtering erosion, which could result in excessive economic penalties. At the same time, numerical modeling of fuel-pellet debris expansion with the LIFE code^{2,4} showed that the background magnetic field (1 to 2 kG) used to protect the cylindrical portion of the reactor cavity wall may be used effectively to channel the plasma debris into a narrow axial duct. It appears natural to impose across such a duct a transverse magnetic field of sufficient strength to extract a substantial fraction of kinetic energy from the particles and thus to decelerate them. The extracted kinetic energy may be converted into electric power to energize the magnet and thus to make the protection device self-sufficient in energy. A possible arrangement is shown schematically in Fig. VI-1.

In our subsequent discussion we will present estimates of the kinetic energy flow out of the cavity and of the electric field developed, and will provide a description of a magnet that will convert 20% of the plasma kinetic energy into electric power without consuming more than this amount in the process. Preliminary results appear reasonable.

Power and Potential Difference. We assume that the pellet mass, repetition rate, and background gas density in the reactor cavity are such that the mass flow rate out of the cavity, m , is 10 g/s. LIFE code calculations indicate that a debris velocity v of 10^6 cm/s may be representative.

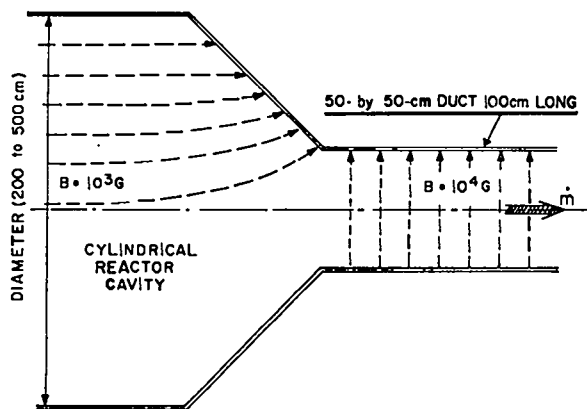


Fig. VI-1.
Schematic of MHD decelerator.

Therefore, the kinetic energy flux out of the cavity, that is, the power P , is given by:

$$P = 1/2 m \cdot v^2 = 5 \times 10^{12} \text{ erg/s} .$$

If we assume that 20% of this amount can be converted into electric power, that is, that the MHD generator will be 20% efficient, the electric power available will be:

$$P_e = 10^{12} \text{ erg/s} = 10^6 \text{ W} .$$

A conductor moving in the direction perpendicular to the magnetic field develops an electric field E given by:

$$E = v \cdot B(\text{emu}) ,$$

where B is the strength of the magnetic field in gauss. Therefore, the potential difference developed across a duct of width d is

$$V = v \cdot B \cdot d \times 10^{-8} \text{ V} .$$

For $v = 10^6$ cm/s, $B = 10^4$ G, and $d = 50$ cm, the potential difference is 5×10^6 V. The Larmor radius of, for example, a tungsten ion (unit charge) moving at 10^6 cm/s in the field of 10^4 is 1.90 cm; this is much smaller than the duct size, and the particles will therefore be thermalized in the proposed MHD decelerator.

Magnet Description. The number of ampere-turns, At , required to generate a magnetic field of B gauss in an air gap d cm wide is given by:⁵

$$At = 0.7958 B \cdot d .$$

For $B = 10^4$ G and $d = 50$ cm, $At = 3.979 \times 10^6$.

A U-shaped iron magnetic core with a 50-cm-wide air gap may require a flux length of 300 cm. From Ref. 5 (Sec. 2-55, p. 2-17), 6 At/cm are required to generate the flux of 10^4 G in iron. Hence, the number of ampere-turns required for the flux through the core is $6 \times 300 = 1.8 \times 10^6$ At, which is small compared to the number required to provide that flux through the air gap.

Assuming a current I of 100 A, the number of turns required N is $At/I = 4 \times 10^6/100 = 4 \times 10^4$.

For a 100-cm-long magnet the length of wire required per turn may be 250 cm. Hence, the total length of wire L will be 250 N or $L = 250 \times 4 \times 10^8 = 10^9$ cm.

Using 20% of the potential difference developed across the 50-cm-wide channel, the voltage available to drive the current I is 10^8 V. Hence, the electric power required is:

$$P = V \cdot I = 10^8 \times 10^2 = 10^6 \text{ W} .$$

This value equals 20% of the kinetic energy flux out of the cavity which, by assumption, can be made available as electricity.

The wire resistance compatible with the values of current and voltage thus far determined is:

$$R = P/I^2 = 10^6/10^4 = 10\Omega .$$

The cross-sectional area of the wire A is determined from:

$$A = \frac{\rho \cdot L}{R} ,$$

where ρ is the volume resistivity in ohm-centimeter. For copper and its alloys at room temperature $\rho = 1.75 \times 10^{-6}\Omega$ cm. Therefore, the cross-sectional area of the wire must be at least

$$A = \frac{1.75 \times 10^{-6} \times 10^6}{10} = 0.175 \text{ cm}^2 .$$

and its radius r is therefore 0.236 cm, which is reasonable. Assuming that 0.5-cm-diam wire is used for the windings, the length required to accommodate 4×10^8 turns is 2×10^9 cm. Thus, a U-shaped core with an arc length of 400 cm will need five layers of windings to accommodate 4×10^8 turns.

The estimates that resulted from this preliminary analysis indicate that the concept is feasible and merits further evaluation. Twenty percent of the debris energy would be extracted to provide power for the deceleration apparatus. If the efficiency of the MHD generator is greater than 20%, the excess electric power would be available for other use, for example, for pumping power for the lasers. After passing through the MHD duct, the debris will be a thermalized gas from which the remaining energy could be extracted by thermal conduction.

Scaling of Cavity Wall Loads and Stresses (I. O. Bohachevsky)

Introduction. Inertial-confinement fusion reactors are in a conceptual design stage. At this stage it is desirable to have estimates of loads and stresses resulting from reactor operation in the form of explicit expressions that provide scaling information about the dependence of these qualities on relevant parameters such as fuel-pellet mass, energy yield, pulse duration, and/or blanket and shell thickness. Such information in an explicit form is also useful and convenient in systems studies and mathematical modeling of inertial-confinement fusion applications.

The purpose of the study described in this section is threefold:

1. to derive analytic expressions for different loads applied to reactor cavity walls by fuel-pellet microexplosions;
2. to derive explicit expressions relating induced stresses to wall thicknesses; and
3. to identify problems that require additional investigation before satisfactory expressions for the reactor wall loads and stresses can be obtained.

Reactor Vessel Model. Inertial-confinement fusion reactors require a reaction chamber to contain pellet microexplosions and to withstand the external pressure developed in the surrounding lithium blanket because of neutron energy deposition. The need for a lithium blanket requires at least two concentric structural shells; the lithium pressure exerts an external load on the interior shell and an internal one on the exterior shell. An ideal containment vessel that offers most opportunities to obtain explicit results is the sphere. Therefore, it was used in our analysis to obtain least thicknesses of structural shells that would withstand the stresses developed during cyclic reaction operation.

Our reactor vessel model consists of two concentric spherical shells separated by a layer of liquid, as shown in Fig. VI-2. In general, shell thicknesses are small relative to shell radii and blanket thicknesses; however, specific assumptions or approximations are stated when needed. It suffices to consider one shell to derive most of the results; two shells with liquid between them are required only to obtain loading due to blanket thermal expansion and wave reflections.

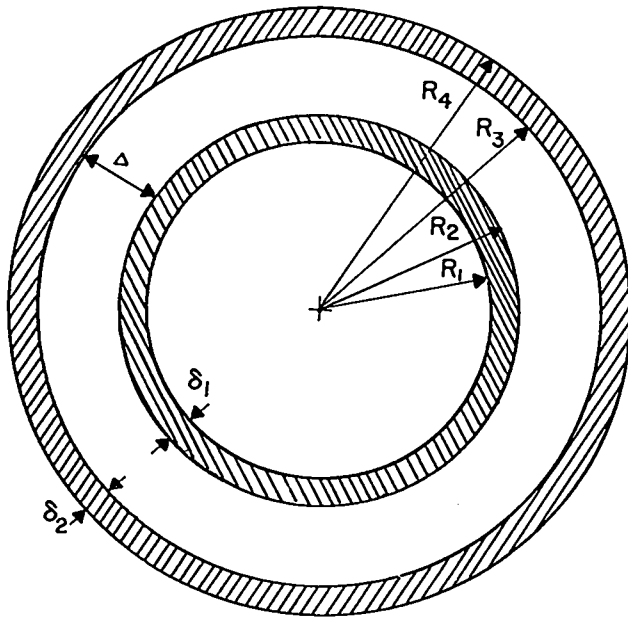


Fig. VI-2.

Schematic of laser fusion reactor vessel.

Structural Shell Loads. Fuel-pellet microexplosion and blanket thermal expansion generate internal and external mechanical loads on the structural shell; spatial and temporal temperature gradients inside the shell generate thermal loads. Scalings of these loads will now be described.

Mechanical loads are the forces from the conversion of fuel-pellet-debris kinetic energy into pressure, blast-wave reflection, and ablation-evaporation recoil. The pressure on the cavity wall exerted by the pellet debris is proportional to the square root of the product of pellet mass and yield, inversely proportional to the time spread of debris arrival, and decreases as the square of the cavity radius. The blast-wave pressure on the wall is directly proportional to the yield, inversely proportional to the cube of the cavity radius, and is independent of the background density. The pressure developed due to wall ablation-evaporation recoil is directly proportional to the energy yield and inversely proportional to the square of the cavity radius, the pulse duration, and the square root of the heat of evaporation. The external pressure exerted on the shell by the blanket due to its thermal expansion is directly proportional to the product of yield and a blanket material constant and inversely proportional to the blanket volume. The blanket material

constant is the ratio of two products: adiabatic bulk modulus and volume coefficient of thermal expansion in the numerator, and heat capacity and density in the denominator.

Thermal loads arise because of the incompatibility of thermal expansions and contractions of the different parts of the shell. They are statically induced by steady-state temperature gradients and dynamically induced when local energy deposition rates exceed those at which heat can be conducted away. Expressions for these loads have been derived and parameter ranges have been determined in which simplifying approximations are admissible.

Stresses. Explicit expressions have been derived that relate static, buckling, and dynamic stresses induced by the above loads to the structural shell thicknesses. These relations contain the parameters that specify the fuel-pellet and reactor-cavity combination and thus describe the scaling of either stress or shell thickness with any parameter. Complete descriptions of the analysis and the results are contained in Ref. 6. Here we summarize the conclusions and present the scaling laws.

In general, the loading-pulse durations for the inertial-confinement fusion reactors are small relative to the natural periods of the structural shells and therefore can be approximated with δ -functions. With this approximation the following conclusions have been obtained.

- The wall-membrane stress calculated with the inclusion of acceleration effects is, in general, almost 10 times smaller than the corresponding value determined for the static conditions, that is, with the implicit assumption that the pressure at the wall remains acting indefinitely after its application;
- The maximum stress developed in the presence of a massive liquid blanket is approximately 10 times smaller than the value that would obtain for an isolated shell;
- The maximum stress value is attained, generally, before the pressure wave generated in the liquid blanket and reflected from the outer shell reaches the inner shell; and
- The shell stress relaxation time, in general, is much longer than the wave transit time in the blanket; therefore, wave reflections between the two structural shells will have a significant effect on the stress history.

Scalings of the reactor wall stresses are summarized in Table VI-I where, along each parameter, is entered its exponent in the expression for static and maximum dynamic membrane stress induced by four loading mechanisms: debris impact, blast-wave reflection, evaporation recoil, and blanket thermal expansion. Dynamic stress in Table VI-I refers to an isolated ringing shell; the expressions for dynamic stress in a shell coupled to a liquid blanket are too complex to admit such a convenient and comprehensive summary representation.

Concluding Remarks. The results described in this section have been useful in:

- Obtaining rapid estimates of loads and stresses expected in the walls of (micro) explosion containment vessels,
- Providing direct information on the variations of these loads and stresses with different parameters that characterize the pellet-vessel combination,
- Revealing areas and topics that require further investigation to facilitate effective analyses of laser fusion applications.

These areas and topics are:

- Firm and accurate estimates of the loading-pulse durations,
- Nonlinear wave motion in the blanket between the two shells with the coupling to the elastic response of the shells and investigation of the possibility of resonance conditions,
- Elastic stress wave motion in the structural shells,
- Extension of the results to designs containing more than two structural shells and one blanket region.

Investigations of these problems are being pursued and the results will be reported as they become available.

LASER STUDIES (I. O. Bohachevsky)

Compressor Power Requirements for Gas Lasers

Model. To calculate the ideal compressor power required to circulate a lasing gas, let us consider the model shown in Fig. VI-3. It is a closed duct in which the lasing medium circulates in a steady state. Under this condition the mechanical work w

added to maintain the circulation, equals the heat generated by friction losses Q , which is removed from the system.

Analysis. Assuming that the heat Q is removed reversibly at constant pressure, the work per unit mass w added to the fluid by the compressor is:

$$w = c_p (T_c - T_o) \quad , \quad (1)$$

where c_p is the heat capacity at constant pressure, and T_o and T_c are temperatures at the entrance and exit of the compressor, respectively.

In reversible compression of an ideal gas the temperature and pressure are related by:

$$\frac{T_c}{T_o} = \left(\frac{p_c}{p_o} \right)^{\frac{\gamma-1}{\gamma}} = \lambda^{\frac{\gamma-1}{\gamma}} \quad , \quad (2)$$

where γ is the ratio of specific heats and $p_c/p_o = \lambda$ is the pressure ratio across the compressor; in steady state, λ is also the pressure-ratio loss due to friction.

Combining Eqs. (1) and (2) we obtain:

$$w = c_p T_o (\lambda^{\frac{\gamma-1}{\gamma}} - 1) \quad . \quad (3)$$

Therefore, the compressor power required to maintain the flow, CP, is:

$$CP = m c_p T_o (\lambda^{\frac{\gamma-1}{\gamma}} - 1) \quad , \quad (4)$$

where m is mass flow rate. It is convenient to introduce the flow loss parameter η_F :

$$\eta_F = (\lambda^{\frac{\gamma-1}{\gamma}} - 1) \quad , \quad (5)$$

which is the amount of energy that must be supplied to a unit mass of the flowing medium each time it makes one circuit around the system. In terms of η_F and the ideal gas expression for the enthalpy $c_p T$:

$$CP = m \frac{\gamma}{\gamma-1} \frac{p_o}{\rho} \eta_F \quad (6)$$

where ρ is the density.

TABLE VI-I
SCALING OF REACTOR VESSEL WALL STRESSES

Parameter	Loading Mechanisms							
	Debris Impact		Blast-Wave Reflection		Evaporation Recoil		Blanket Expansion	
	Stat	Dyn	Stat	Dyn	Stat	Dyn	Stat	Dyn
M	0.5	0.5	---	---	---	---	---	---
Y	0.5	0.5	1	1	1	1	1	1
f	0.5	0.5	1	1	---	---	(1-f-x)	(1-f-x)
x	---	---	---	---	1	1	(1-f-x)	(1-f-x)
R _i	-1	-2	-2	-3	-1	-2	-1	-2
δ _i	-1	-1	-1	-1	-1	-1	-1	-1
ρ _s	---	0.5	---	0.5	---	0.5	---	0.5
H	---	---	---	---	-0.5	0.5	---	---
E	---	0.5	---	0.5	---	0.5	---	0.5
1-ν	---	0.5	---	0.5	---	0.5	---	0.5
Δ	---	---	---	---	---	---	-1	-1
ρ _r	---	---	---	---	---	---	-1	-1
C _{pr}	---	---	---	---	---	---	-1	-1
b	---	---	---	---	---	---	1	1
β	---	---	---	---	---	---	1	1
τ	-1	---	---	---	-1	---	---	1
η	---	---	---	---	---	1	---	---

Nomenclature

M: fuel-pellet mass
Y: fuel-pellet energy yield
f: fraction of yield in debris kinetic energy
x: fraction of yield in radiation
R_i: mean radius of interior shell
δ_i: shell thickness
ρ_s: shell material density
H: heat of evaporation
E: Young's modulus of elasticity
ν: Poisson's ratio
Δ: liquid-blanket thickness
ρ_r: blanket material density
C_{pr}: sound speed in the blanket medium
b: volume coefficient of thermal expansion
β: adiabatic bulk modulus
τ: loading-pulse duration
η: ratio of average velocity to maximum velocity of evaporated or ablated material.

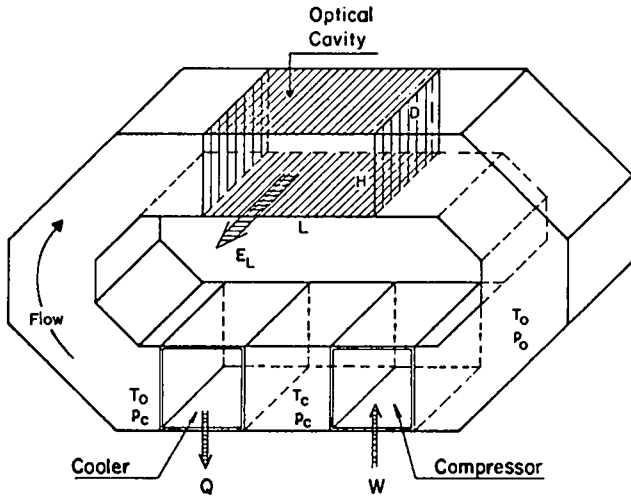


Fig. VI-3.

Schematic of a gas laser with circulating medium.

The mass flow rate m is:

$$m = DHu\rho \quad (7)$$

where D and H are the depth and height of the active volume (i.e., optical cavity, see Fig. VI-3) and u is the flow velocity given by

$$u = LFf \quad (8)$$

where L is the length (in the flow direction) of the active region, F is the laser-pulse repetition frequency, and f is the flush factor that indicates the fraction of volume of the active region that must be replaced after each pulse. For chemical lasers, f must be greater than unity because the reactants are used up in the production of inversion; however, for electrically pumped lasers $f > 1$ is not a necessity and its value will depend on the flow uniformity achieved in the design and on the beam quality requirements.

Combining Eqs. (6), (7), and (8) we obtain the final expression for the compressor power required:

$$CP = \frac{\gamma}{\gamma - 1} p_o V f F \eta_F \quad (9)$$

where V is the volume of the active cavity.

To estimate the effect of the compressor power requirements on the overall laser efficiency it is con-

venient to formulate an expression for the ratio of compressor power to electrical pumping power required to produce the population inversion. The latter pumping power PP is given by:

$$PP = V F e_i \quad (10)$$

where e_i is the electrical energy input per unit volume required to produce the inversion (e_i depends on the operating pressure p_o).

Combining Eqs. (9) and (10) yields the following expression for the ratio $\kappa = CP/PP$:

$$\kappa = \frac{\gamma}{\gamma - 1} \frac{p_o}{e_i} f \eta_F \quad (11)$$

which shows that κ is independent of both the volume V and the laser pulse frequency F .

The overall laser efficiency is defined as

$$\eta_o = \frac{P_L}{PP + CP} \quad (12)$$

where P_L is the laser power output. It is convenient to rewrite Eq. (12) as:

$$\eta_o = \frac{\eta_L}{1 + \kappa} \quad (13)$$

where $\eta_L = P_L/PP$ is the conventional laser efficiency. Equation (13) may be used either directly or in the form:

$$\frac{\eta_o}{\eta_L} = \frac{1}{1 + \kappa} \quad (14)$$

which expresses the reduction in laser efficiency caused by the compressor power requirements.

Results. The variation of the flow loss η_F with the compressor pressure ratio has been calculated for three representative values of γ and is plotted in Fig. VI-4. The result shows that for many applications the assumption of a linear dependence of the flow loss on pressure ratio may be justified.

Equation (11) shows that the ratio of compressor power to electric pumping power κ is directly proportional to the flow loss η_F , with the proportionality constant depending on the lasing medium

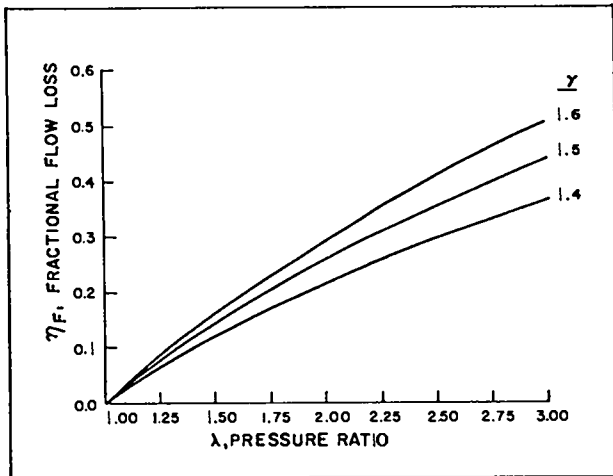


Fig. VI-4.

Variation of flow loss with pressure ratio.

and on laser operating conditions. Therefore, in analyses which do not require high accuracy it may be assumed that κ is directly proportional to the flow loss η_F and the proportionality constant determined from the specifications of the particular laser system.

The relative efficiency η_o/η_L given by Eq. (14) is plotted in Fig. VI-5 as a function of pressure ratio λ for $p_o = 2.36$ atm, $e_l = 160$ J/l and $f = 1.5$. These conditions are representative of new-generation CO₂ lasers (for example, Antares) in which inversion is produced in a 0:1:4::He:N₂:CO₂ mixture with a current of 6 A/cm² at 18 kV/cm. The value of 1.5 for the flush factor f makes the results shown in Fig. VI-5 conservative. In a recent investigation of low-pressure-loss laser cavities, Feinberg and collaborators⁷ determined that it may be possible to keep flow losses below 8 psi which, for the conditions of Fig. VI-5, corresponds to $\lambda = 1.23$ and to a 30% reduction in laser efficiency caused by the compressor power requirements. The same authors suggested, however, that it may be possible to operate an electrically pumped laser system with a flush factor as low as $f = 0.3$. If this is true, the required compressor power would reduce the laser efficiency by only 8%.

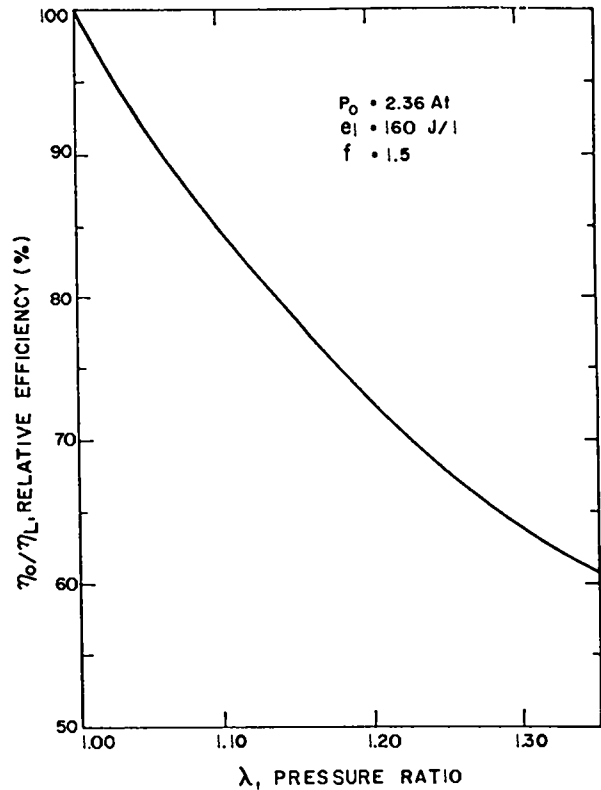


Fig. VI-5.

Reduction in laser efficiency as a function of pressure ratio.

PRELIMINARY ASSESSMENT OF ENVIRONMENTAL EFFECTS OF LASER FUSION ELECTRIC GENERATING STATIONS (J. J. Devaney, L. A. Booth, J. H. Pendergrass, T. G. Frank)

Introduction

A preliminary assessment of the environmental effects of conceptual laser fusion generating stations has been made and compared with magnetic-confinement fusion, fission, fossil-fired, and/or solar-energy sources where appropriate. To be conservative a conceptual generating station based on the wetted-wall reactor concept⁸ was chosen for analysis because of higher inventories of radioactive materials than those of generating stations based on

other reactor concepts.⁹ Values of all parameters were based on a typical 1000-MWe plant, unless otherwise noted.

Hazards and Environmental Impacts

Possible environmental impacts and hazards to mankind from laser fusion generating stations can occur from:

- Nuclear excursions,
- Loss of coolant,
- Tritium releases,
- Chemical fires and accompanying releases,
- Releases of induced radioactivity other than tritium,
- Radioactive waste disposal,
- Lasers,
- External intrusions and normal disasters,
- Land use,
- Resource and transportation use,
- Thermal pollution, and
- Air and water pollution.

Nuclear Excursions. Because fusion pellets are extremely small and require high symmetry of implosion, and because the burnup in normal operation is high, significant nuclear excursions of fusion pellets are effectively impossible, and even if they occurred, could yield at most only ~50% more energy, neutrons, and consequent radioactivity per pellet than its design output. Simultaneous ignitions of several pellets is inconceivable. Perturbations of the reaction system are overwhelmingly more likely to destroy all pellet nuclear reaction possibilities than to lead to excess radioactivity or to a blast beyond normal design limits.

Loss of Coolant. There is no possible reactor fuel meltdown in the sense of fission-reactor core meltdown. Loss of coolant is multiply detected, and independently and redundantly causes shutdown of laser oscillator, laser power, and pellet insertion. The only problems associated with energy removal would be due to decay of induced radioactivity in structural and other materials. We have calculated the induced radioactivity and afterheat of the structural materials and the contaminants in the lithium

coolant.^{10,11} The maximum energy release due to radioactive decay in the coolant occurs after 3.7 yr of continuous operation, and is only 1.2×10^{-6} of the normal reactor heat production. The afterheat after 1 yr of operation due to radioactive decay of a niobium reactor structure is ~0.16% of the normal operational heat production. The projected maximum temperature rise from afterheat is only a few hundred Kelvin so that emergency cooling is not required and a significant loss of coolant accident is impossible.

Tritium Releases. The total plant inventory of tritium is 5 to 10 times less than that of an equal-power Tokamak reactor. The tritium inventory in our reference power plant during steady-state operation is given in Table VI-II, based on a tritium concentration of 1.47 ppm in the lithium coolant.

The systems in Table VI-II comprise two broad categories, tritium dissolved in lithium in coolant loops (386 g) and reserve fuel stored separately (2.02 kg). Even the slow release of *all* the tritium in the reserve-fuel storage facility would lead to average doses at the plant boundary of $\sim 8 \times 10^{-6}$ rem, a negligible exposure. Total release of the production subtotal in 8 h would result in average doses of 1.5×10^{-6} rem. If the tritium release is associated with fire or other buoyant gases, that is, occurs rapidly, the above doses would be reduced by factors of a thousand. Thus, gaseous tritium releases of even total portions of the plant tritium inventory would not

TABLE VI-II
PLANT TRITIUM INVENTORY

System	Inventory (g)
Reactors	351
Piping	8
Separator	12
Steam generators	16
Production Subtotal	386
One-Day Fuel Reserve, 2.02 kg	

result in a significant biological burden in the environment. Such total releases are also extremely unlikely.

Even though tritium is one of the least noxious radionuclides with body burdens of up to 1 mCi permissible, the rapid exchange of hydrogen in compounds and of water in the atmosphere and the biosphere make control of T_2O and other tritium compounds necessary. Fire, especially of the lithium blanket and consequent formation of tritium compounds, can lead to hazardous tritium release, but such release is a negligible hazard compared to the associated lithium release.

For a worst-case credible accident one assumes that both the lithium blanket containment of a reactor and the fire-suppressant blanket would fail, with a consequent fire leading to the escape of one-third the lithium plus tritium combustion products into the traps; because these traps have a conservative removal efficiency of 99%, the total release of tritium would be 0.04 g in the form of $LiOT$ (or $T_2 + Li_2O$ if hot).

The maximum dose at plant boundary (100 m) would then be 0.7 rem if the release was at ground level and also cool. For hot-fire release, the value is 7×10^{-4} rem at plant boundary, and for a 100-m stack, the dose is reduced an additional factor of 100. However, long before one receives the maximum permissible tritium dose one has already received a toxic chemical dose from the lithium. The lethal chemical dose from lithium is $200 \mu\text{g}/\text{m}^3$ for a 1-h exposure,¹² at which time the associated tritium dose will be only 9×10^{-3} rem. The biological hazard potentials of the tritium in a Tokamak and in a laser fusion generating station are given as a function of time after plant shutdown in Fig. VI-6.*

Chemical Fires and Releases. The largest chemical inventory in a first-generation laser fusion reactor is the 600 000 kg of lithium (see Table VI-III). This inventory is about one-half that of an equal-power Tokamak. Although lithium fires are the most hazardous credible hypothetical accident, sabotage or accidental lithium fires are unlikely; if they occur, they are unlikely to be large; even if

*The biological hazard potential is a dilution factor, that is, the ratio of the induced radioactivity per unit power to the maximum permissible concentration for uncontrolled areas.

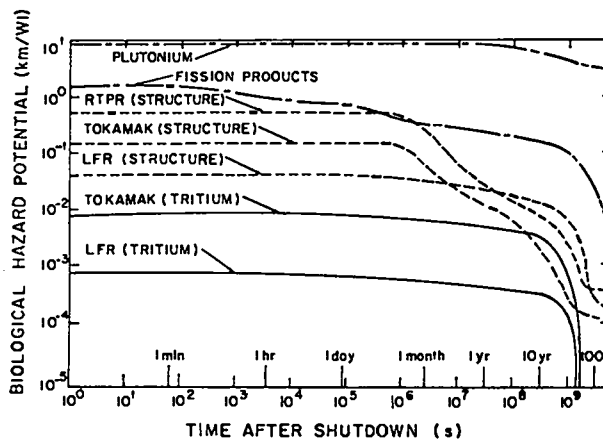


Fig. VI-6.

Decay of biological hazard potential for various reactors.

TABLE VI-III

LITHIUM MASS IN 1000-MWe,
30-CAVITY WETTED-WALL,
HIGH-TEMPERATURE STEAM-CYCLE,
LFR PLANT

	Lithium Masses (10 ³ kg)
Reactors	548
Piping	12
Separator	18
Steam generator	24
Total	602

large, they are likely to be automatically extinguished. The technology of handling molten alkali metals safely is well developed, and although lithium fires are the maximum credible accident, the probability of large destructive fires is believed to be extremely low. Ninety per cent of the lithium is contained in microexplosion-proof reactor vessels with 2.2-cm-thick outer walls, located within steel-lined reinforced concrete chambers of ~600 times the reactor volume and equipped with rare-gas or puffed (so as to float) mineral fire-blanket

sprinklers. Moreover, lithium has a high thermal conductivity, high specific heat, and high boiling point (1620 K). Also, for tritium leakage protection, all piping will likely be double-walled. Thus, the lithium system is remarkably sabotage- and fire-proof.

With the same consecutive failures as detailed under tritium release, one can be exposed to lethal chemical doses (that is, to $\geq 200 \mu\text{g}/\text{m}^3$ LiOH for 1 h) at the plant boundary from any of Li, Li₂O, or LiOH species, all of which form caustic LiOH on flesh.

Note that no one would complacently remain in lithium smoke, because the smoke is highly irritating and the eyes will smart at very low levels. Therefore, smoke irritation will drive persons away from the smoke plume, unless incapacitated, and the 1 h needed for lethal exposure at $200 \mu\text{g}/\text{m}^3$ will be unlikely to be attained.

Significant quantities of insulating oil, about a million gallons, may be required for the electrical pulse-forming networks for electrical pumping of the lasers. If flammable, this oil inventory contains 1.5×10^8 MJ of stored chemical energy, which is large enough to warrant careful fire avoidance, but small compared to industrial quantities in, for example, regular petroleum storage or refining.

Induced Radioactivities (Other than Tritium).

Induced radioactivities of structure, coolant, and pellet materials are to some degree at the option of the designer because some flexibility exists in the choice of materials and of their impurities. For simplicity, the cavity structure was assumed exclusively niobium. The comparative biological hazard potentials or required dilution factors to prevent detectable effects are given in Fig. VI-6 for different reactors having equal thermal powers. The laser fusion reactor structure has roughly ten times less induced radioactivity than magnetically confined fusion reactors. The structure activity is just over 1% that of the fission products in a fission reactor, and its induced radioactivity is less than 1% that of the plutonium in a liquid-metal fast breeder reactor (LMFBR). For a laser fusion power with an intense cavity-wall irradiation of $6.4 \text{ MW}/\text{m}^2$ of neutron energy flux, the total plant niobium activity after five years of operation, 17 minutes to 12 days after shutdown is $\sim 1500 \text{ MCi}$ for a plant of 27% overall efficiency.

We expect little entrainment or oxidation of niobium in a lithium fire. Conservatively, we expect at most 0.1% niobium escaping the chamber in the lithium. The escaping niobium activity is thus $\sim 90 \text{ Ci}$, primarily ^{92m}Nb (99% 0.934 MeV γ). This activity is one-fourth the activity of tritium in the lithium, which, in turn, is negligible compared to the chemical toxicity of lithium.

Argon activation in air (if present) surrounding the reactor proper can be as high as 2000 Ci (⁴¹Ar) for slow air exchange (10 h) and 1% neutron leakage, but this activity drops 100-fold in 8 h. Of course, argon, as a rare gas, has an extremely small biological effect. Similarly, ¹⁴C activity released from ¹⁴N (n,p)¹⁴C through traps is on the order of 1.0 mCi.

Pellets containing low-Z materials such as beryllium lead to relatively minor activities, although each element must be investigated individually. Heavy metals in pellets (with exceptions such as lead) can produce very considerable activities because they are compressed close to the 14-MeV neutron source at the time of emission, and have appreciable 14-MeV neutron cross sections. The amount of induced activity is typically less than that of structural materials and is expected to be deposited or plated on metal substrates on the cavity walls and in exhaust plenums.

We studied the activation of 12 lithium impurities. With rather dirty (~ 7000 -ppm atomic) lithium, releases could be as high as 545 Ci for our maximum credible catastrophic fire release. For high-purity (10-ppm atomic) lithium the corresponding maximum release is 0.039 Ci. These radioactive toxicities are small compared to the chemical toxicity of the lithium itself.

Radioactive Waste Disposal. Neutron-activated structure, pellet debris, and lithium-coolant impurities must be disposed of properly. Because all the materials are to some degree at the option of the designer, capture cross sections, radioactive intensities and half-lives, and metallurgical, biological, and chemical properties are controllable to a considerable degree. A weighing of benefits vs drawbacks is a matter for systems studies. In general, with careful choice of primary materials plus good control of impurities, it appears possible to control

radioactive hazards to negligible levels in times much less than geologic, perhaps in times close to an additional plant lifetime.

Lasers. The lasing medium (if other than CO₂) may be poisonous (for example, mercury or HF), but is likely to be hazardous only for plant personnel. The quantities of lasing material required would amount to only a few tens of kilograms (pilot-plant scale by chemical industry standards). The handling technology of such materials in such amounts is well developed by decades of industrial experience.

Any strong shocks, vibration, or dirt intrusion into the lasers or the beam transport system can cause shutdown, but is not likely to cause a hazard to humans beyond local overheating, a hazard only to plant personnel.

External Intrusion, Natural Disasters. Because the reactors are built to withstand microexplosions and are enclosed within steel and reinforced concrete to contain lithium leaks or fires and to reduce radioactive releases, catastrophic broachings of sensitive structures from external events are extremely unlikely. In LWR plants, turbine failure leading to serious strike damage is less than 3×10^{-10} per reactor-year. Large aircraft strikes even within five miles of an airport occur $\sim 10^{-6}$ /yr. Associated aircraft crash fires are not significant compared to strike consequences. The structures are secure against tornados and all but the most severe earthquakes. Indeed, laser fusion reactor design is expected to be more substantial than other critical structures such as bridges, dams, or fossil-fueled power plants. Because first-generation plants will contain $\sim 600\,000$ kg of lithium, the plant should not be located where large long-duration floods or tsunamis are a possibility. Because the consequences of sabotage are less severe than for fission plants or at national laboratories, security procedures deemed necessary for these installations should be adequate for fusion plants.

Land Use. Laser fusion generating stations will occupy about 25 to 100 acres. By comparison, magnetic-confinement and fission-reactor (except spent fuel storage) installations need about the same area, fossil plants a somewhat larger area

because of the need for fuel storage, and solar plants at least 2000 acres for solar collectors (at maximum insolation of 700 cal/cm²/day).

Resource and Transportation. The daily operating need of laser fusion generation is ~ 1 kg deuterium and 4.5 kg lithium, a negligible transportation burden. Isotope separation is at an absolute minimum because the mass ratio of deuterium to protium in hydrogen is maximum.⁹ Lithium ore contains typically 1 to 2% lithium and requires no separation. Neither lithium nor deuterium is radioactive. In comparison fission plants require radioactive fuel that is difficult to separate, and fossil plants require enormous masses of fuel causing significant to dominant effects on transportation and resources. Structural-metal demands of the various fusion reactors are about equal and are 20% higher than, say, for LMFBR.

Thermal Pollution. Heat-rejection requirements for laser fusion plants are likely to be slightly higher than for fossil or fissile plants because of (probable) lower overall efficiencies (recirculating power requirements are high). However, it is likely that most future electric generating stations, regardless of thermal-energy source type, will be required to use some type of cooling tower rather than to reject heat directly to fresh-water streams. The water makeup requirement for fossil-plant cooling towers is ~ 2.9 million gallons per day.

Air and Water Pollution. The air and water pollution from fusion plants is expected to be negligible. In contrast, the air pollution even from a modern coal-fired plant ranges from massive to catastrophic, being capable of polluting in excess of 100 000 square miles. The consequent effects on health, economics, and even weather are extreme and have not yet been fully realized.

Conclusions

Inadequate design of laser fusion power plants could lead to hazardous accidental radioactive release, but, in general, the chemical hazard of large-scale lithium fires is the dominant hazard.

The likelihood of such fires is, however, exceedingly small. Because of the extreme difficulty of disruptive access to significant radioactivities, sabotage is unlikely to release activities that are significantly worse than the instigatory event itself. Plants can be designed with little or no need for radioactive waste disposal beyond isolation for a few decades. There is no possibility of a nuclear explosion, nor of core melting, nor of a loss-of-coolant accident.

Effects of land use and thermal pollution are about the same as for other plants (except solar plants, which require much more land). Effects on resources and transportation are generally much less. Potential chemical hazards are comparable to those of LMFBRs and somewhat less than for magnetic-confinement reactors. Potential radioactive hazards are much lower than those of fission reactors and are slightly less than those of magnetic confinement reactors. Electric, magnetic, and steam hazards are comparable to those of fossil-fueled plants.

The largest source of radioactivity is activated reactor structural material; however, because these materials are high-melting-point metals, immobile, and not subject to significant dispersal, radiation protection of the public will be straightforward and not a primary concern. Protection from tritium hazards and induced radioactivity of pellet debris will require engineered safeguards, and conservative assumptions of accident releases indicate minimal doses to uncontrolled areas. The maximum credible accident is deemed a lithium fire which could result in lethal doses of lithium compounds by caustic chemical burning of flesh. In such an accident the lithium poisoning is far more hazardous than the concomitant hazard of radioactive materials.

REFERENCES

1. E. A. Kern, F. T. Finch, and J. F. Hafer, "TROFAN, A Computerized Parametric Model for Laser Fusion Electric Generating Station Analysis," presented at the CUBE Symposium, Albuquerque, New Mexico (October 26-28, 1976).
2. I. O. Bohachevsky and J. F. Hafer, Los Alamos Scientific Laboratory report LA-6633-MS (December 1976).
3. I. O. Bohachevsky and J. F. Hafer, Los Alamos Scientific Laboratory report LA-6991-MS (November 1977).
4. J. C. Goldstein, I. O. Bohachevsky, and D. O. Dickman, "Ion Motion in Laser Fusion Reactor Studies," Bull. Am. Phys. Soc. Paper 9P7, Series 11, 21, 1186 (October 1976).
5. *Standard Handbook for Electrical Engineers*, 3rd edition, Sec. 2-56, p. 2-18.
6. I. O. Bohachevsky, "Scaling of Reactor Cavity Wall Loads and Stresses," Los Alamos Scientific Laboratory report LA-7014-MS (November 1977).
7. R. M. Feinberg, R. S. Lowder, and O. L. Zappa, "Low Pressure Loss Cavity for Repetitively Pulsed Electric Discharge Lasers," Air Force Weapons Laboratory report AFWL-TR-75-99 (October 1975).
8. J. Williams, T. Merson, F. Finch, F. Schilling, and T. Frank, "A Conceptual Laser Controlled Thermonuclear Reactor Power Plant," Proc. 1st Topical Meeting on Tech. of Controlled Nuclear Fusion, ANS, San Diego, California (April 1974).
9. D. A. Freiwald, T. G. Frank, E. A. Kern, and L. A. Booth, "Laser Fusion Generating Stations Based on the Magnetically Protected Reactor Cavity," presented at ANS 1975 Winter Meeting, San Francisco, California (November 1975).
10. T. Frank, D. Dudziak, and E. Heck, "Some Neutronics Aspects of Laser Fusion Reactors," Trans. Am. Nucl. Soc., San Diego, California (April 1974).
11. T. G. Frank, D. J. Dudziak, and E. L. Heck, "Laser Fusion Reactor Induced Radioactivity and Afterheat," Trans. Am. Nucl. Soc., San Diego, California (April 1974).
12. H. Schulte, private communication (December 1976).

VII. RESOURCES, FACILITIES, AND OPERATIONAL SAFETY

The design of HEGLF Facilities continued. Safety policies and procedures continued to be applied successfully to minimize the hazards of operating high-energy lasers.

MANPOWER DISTRIBUTION

The distribution of employees assigned to the various categories of the DOE-supported Laser-Fusion Research Program is shown in Table VII-I.

FACILITIES

High-Energy Gas Laser Facility (HEGLF)

The Title II design for Package I, including the laser building, mechanical building, office building, warehouse, and some site and utilities work has been completed and sent out for bids.

The Title II design for Package II, that is, the target building and the remaining site and utilities work, has been completed and reviewed internally.

In the interest of continuity, we have presented details in HEGLF design and construction in Sec. I.

TABLE VII-I
APPROXIMATE STAFFING LEVEL
OF LASER PROGRAM
June 30, 1977

Program	Direct Employees (Actual)
CO ₂ Laser System Development	147
Pellet Design and Fabrication	43
Laser-Target Experiments	49
Diagnostics Development	23
Systems Studies and Applications	10
Total	272

New Laboratories

General. Two laboratories are to be constructed with GPP funds: an Optics Evaluation Laboratory and a High-Voltage Development Laboratory.

An intermediate review of the Title II design was held in June 1977. The present cost estimates are \$370 000 for the Optical Evaluation Laboratory and \$200 000 for the High-Voltage Development Laboratory. Award of the construction contract is scheduled for September 1977.

High-Voltage Development Laboratory. The purpose of the High-Voltage Development Laboratory is to develop hardware for Antares and other laser projects, to develop technology and data for all laser groups, and to maintain and repair existing equipment.

The following hardware developments are planned for Antares: prototypes for energy storage units; high-voltage bushings; electron-beam guns; high-voltage trigger generators; front-end power; and plasma curtain isolators.

Further uses of the laboratory in support of Antares will be the life-testing of cables, capacitors, electrodes, bushings, and other high-voltage components.

Hardware to be developed for other laser projects will include electron-beam guns, pulse generators, special spark-gap switches, and bushings. The services offered to all the laser groups will include the generation of dielectric strength data for pulsed high voltages, of design procedures, and of equipment configurations; the development of power and switching repetition-rate capabilities, the performance of component life tests, and the development of safety devices.

Maintenance and repair of existing equipment will include components of the 100-kJ, 300-kV

pulser in the SBS; components of the 100-kJ, 600-kV pulse-forming networks in the EBS; and the various beam generators, pulse generators, and other components being developed.

Optics Evaluation Laboratory. This laboratory will evaluate all incoming optical components for the various laser facilities, either in operation or planned, and will maintain the optical components used in our laser research and development programs. Optical components will be evaluated to determine compliance with specifications, to determine beam quality, and to estimate focal-spot sizes and their effect on optical error budgets. The facility will also provide the space and equipment for the maintenance of optical components, including cleaning and refinishing.

OPERATIONAL SAFETY

Historically, our laser fusion research activities have never produced biological damage to any em-

ployee from laser radiation. This record continues. Neither were any lost-time accidents reported. A special Laser Electrical Safety Committee was formed, and inspection of electrical facilities has been initiated. The development of laser protective prescription eyewear from Schott Optical Glass Co. color filter glass has been continued to include essentially all wavelengths in the visible portion of the spectrum, selecting for each specific wavelength attenuated, the maximum luminous transmission practically permissible.

MISCELLANEOUS

In January 1977, a documentary motion picture was started on the Laser Fusion Program at LASL. A preliminary print was completed. The final version will show a fully animated description of a laser fusion generating station.

pulser in the SBS; components of the 100-kJ, 600-kV pulse-forming networks in the EBS; and the various beam generators, pulse generators, and other components being developed.

Optics Evaluation Laboratory. This laboratory will evaluate all incoming optical components for the various laser facilities, either in operation or planned, and will maintain the optical components used in our laser research and development programs. Optical components will be evaluated to determine compliance with specifications, to determine beam quality, and to estimate focal-spot sizes and their effect on optical error budgets. The facility will also provide the space and equipment for the maintenance of optical components, including cleaning and refinishing.

OPERATIONAL SAFETY

Historically, our laser fusion research activities have never produced biological damage to any em-

ployee from laser radiation. This record continues. Neither were any lost-time accidents reported. A special Laser Electrical Safety Committee was formed, and inspection of electrical facilities has been initiated. The development of laser protective prescription eyewear from Schott Optical Glass Co. color filter glass has been continued to include essentially all wavelengths in the visible portion of the spectrum, selecting for each specific wavelength attenuated, the maximum luminous transmission practically permissible.

MISCELLANEOUS

In January 1977, a documentary motion picture was started on the Laser Fusion Program at LASL. A preliminary print was completed. The final version will show a fully animated description of a laser fusion generating station.

VIII. PATENTS, PRESENTATIONS, AND PUBLICATIONS

PATENTS ISSUED

There was no patent activity in the laser fusion area during this reporting period.

PRESENTATIONS

The following presentations were made at the IEEE/OSA Conference on Laser Engineering and Applications, Washington, DC (June 1-3, 1977):

R. L. Carlson, M. D. Montgomery, J. S. Ladish, and C. M. Lockhart, "Simultaneous Multiline Saturation of Gallium Doped Germanium SF₆ on the 10.6 μm Band."

K. D. Ware, B. J. Feldman, and G. T. Schappert, "Isolation of 10.6 μm Retropulse by Self-Induced Breakdown in CO₂ Gas and with an Air Spark Channel."

M. D. Montgomery, R. L. Carlson, J. S. Ladish, and G. T. Schappert, "Application of a Rate Equation Model in the Design of High Power, Short Pulse, Multiline, CO₂ Laser Systems."

J. S. Ladish, R. L. Carlson, E. L. Jolly, and M. D. Montgomery, "Multiline Energy Extraction Measurement in the LASL Eight-Beam Laser Fusion Facility."

S. Singer, "Parasitic Oscillation in High Gain Multipass CO₂ Laser Amplifier Systems."

G. Lawrence, (Optical Sciences Center, University of Arizona) I. Liberman, Westinghouse, and V. K. Viswanathan, "Numerical Modeling of the Los Alamos Scientific Laboratory CO₂ Laser Fusion System."

J. V. Parker, J. P. Carpenter, J. J. Hayden, M. J. Nutter, and S. Singer, "A Two-Beam CO₂ Laser System for Laser Induced Fusion Experiments."

E. L. Zimmermann and T. A. Carroll, "A Dual Beam CO₂ Laser-Amplifier."

J. S. Ladish, R. L. Carlson, E. L. Jolly, M. D. Montgomery, and E. L. Zimmermann, "Multiline Energy Extraction Measurement in the LASL Eight-Beam Laser System (EBS)."

D. V. Giovanielli, D. B. Henderson, G. H. McCall, and R. B. Perkins, "Laser Fusion Target Interactions Studies at 10.6 μm."

C. R. Phipps, S. J. Thomas, J. Ladish, S. J. Czuchlewski, and J. F. Figueira, "Saturation Behavior of P-Type Germanium Over the CO₂ Laser Spectrum."

S. J. Czuchlewski, B. J. Feldman, R. A. Fisher, E. McLellan, and A. V. Nowak, "Attenuation and Reshaping of Intense Subnanosecond CO₂ Laser Pulses in SF₆ and in Hot CO₂."

S. J. Thomas and C. R. Phipps, Jr., "A Simple Multifrequency, Time-Smoothed CO₂ Oscillator."

E. J. McLellan and J. S. Lunsford, "A Single-Sweep 5-GHz Oscilloscope-Detector Combination for CO₂ Laser Pulse Measurements."

The following presentations were made at the University of Michigan, Ann Arbor, Michigan (May 16, 1977).

J. M. Kindel, "Laser Plasma Interaction at CO₂ Wavelength."

J. M. Kindel, "Review of Nonlinear Laser Plasma Interactions."

The following presentations were made at the 1977 IEEE International Conference on Plasma Science, Troy, New York (May 23-25, 1977):

K. B. Mitchell, "Laser Produced Plasmas."

D. V. Giovanielli, D. B. Henderson, G. H. McCall, and R. B. Perkins, "Laser Fusion Target Interactions Studies at 10.6 μm ."

D. W. Forslund, J. M. Kindel, K. Lee, and E. L. Lindman, Jr., "Stability at High Laser Intensity."

W. P. Gula, "Hydride Targets for Relativistic Electron Beams."

B. B. Godfrey, R. J. Faehl, W. R. Shanahan, and L. E. Thode, "Computer Simulation of the Localized Pinch Model of Collective Ion Acceleration."

S. J. Gitomer, B. S. Newberger, and R. L. Morse, "Hydrodynamic Stability of Laser-Driven Ablative Implosions."

S. J. Gitomer, D. B. Henderson, and R. N. Remund, "Re-Examination of Strongly Flux-Limited Thermal Conduction."

J. L. Shohet, D. B. VanHulsteyn, S. J. Gitomer, and J. F. Kephart, "Anisotropy of Intensity and Polarization of Free-Free X-Ray Bremsstrahlung from Flat Targets."

K. Lee and E. L. Lindman, Jr., "Heat Flux Across Plasma Diode."

W. R. Shanahan, "Relativistic Corrections to the Ponderomotive Force and Their Effect on Profile Modifications."

L. E. Thode, "Preliminary Investigation of Anomalous Relativistic Electron Beam Deposition into Dense (10^{17} to $10^{20}/\text{cm}^3$) Plasma."

The following presentations were made at the 7th Annual Symposium on the Anomalous Absorption of Intense High Frequency Waves, University of Michigan, Ann Arbor, Michigan (May 18-20, 1977):

V. M. Cottles and D. V. Giovanielli, "The Absorption of 1-ns CO_2 Laser Pulses by Plane Targets."

D. V. Giovanielli, D. B. Henderson, G. H. McCall, and R. B. Perkins, "Laser Fusion Target Interactions Studies at 10.6 μm ."

R. J. Faehl and N. F. Roderick, "Intensity Dependence of Inverse Bremsstrahlung Absorption in an Inhomogeneous Standing Wave."

D. W. Forslund, J. M. Kindel, K. Lee, and E. L. Lindman, Jr., "Plasma Stability in the Presence of Extreme Profile Modification."

J. M. Kindel, C. W. Cranfill, D. W. Forslund, S. J. Gitomer, D. B. Henderson, K. Lee, and E. L. Lindman, Jr., "Theoretical Calculations of a High Intensity CO_2 Laser Interacting with Fusion Plasmas."

E. L. Lindman, Jr., "Relativistic Corrections to the Ponderomotive Force and Their Effect on Profile Modification."

The following presentations were made at the 1977 IEEE Microcomputer Conference, Oklahoma City, Oklahoma (April 6-8, 1977):

M. E. Thuot, "A Microcomputer-Based Area Control System."

B. G. Strait, M. E. Thuot, and J. P. Hong, "Distributed Microcomputer Control System for a High Energy Gas Laser Facility."

B. G. Strait and M. E. Thuot, "A Microprocessor Controller for Stepping Motors."

The following presentations were made at the 1977 IEEE Power Engineering Society Winter Meeting, New York (January 31-February 4, 1977):

T. G. Frank and L. A. Booth, "Commercial Applications of Inertial Confinement Fusion."

L. A. Booth and R. A. Krakowski, "Fusion Electric Generating Station Systems."

The following presentations were made at the Third International Congress on Waves and Instabilities in Plasmas, Palaiseau, France (June 27-July 1, 1977):

E. L. Lindman, Jr., "Absorption and Transport in Laser Plasmas."

E. L. Lindman, Jr., "Two-Electron Temperature Isothermal Rarefaction Waves in Laser-Produced Plasmas."

V. M. Cottles and D. V. Giovanielli, "The Absorption of 1-ns CO₂ Laser Pulses by Plane Targets."

The following presentations were made at the 13th Annual Symposium of the New Mexico Chapter of the American Vacuum Society, Albuquerque, New Mexico (April 19-21, 1977):

A. T. Lowe, C. Hosford, R. J. Fries, "Thin Film Technology Applications in Laser Fusion Target Fabrication."

D. E. Bannerman, "Large Vacuum Systems."

In addition, the following presentations were made at various institutions:

T. F. Stratton, "CO₂ Lasers for Fusion Research at LASL," Optical Sciences Center, University of Arizona, Tucson, Arizona (April 4, 1977).

P. Wolfe, (Westinghouse) "The Laser Fusion Program at LASL," Westinghouse Colloquium, Pittsburgh, Pennsylvania (May 31, 1977).

J. J. Devaney, "Power, Politics, and Pollution," lecture delivered under the auspices of the Assistant Director for Energy, Los Alamos, New Mexico (April 13, 1977).

J. J. Devaney, "Laser Fusion," lecture delivered to the Pacific Northwest Association for College Physics, Energy Tutorial for Physicists, Seattle University, Seattle, Washington (April 15, 1977).

T. G. Frank and L. A. Booth, "Inertial Confinement Fusion Reactor and Generating Station Concepts," ANS 1977 Annual Meeting, New York, New York (June 12-17, 1977).

D. O. Dickman, "The Big E: Energy, Education, and Efficiency Through Computer Graphics," National COMTEC Meeting, Houston, Texas (February 22-25, 1977).

R. A. Kopp, "Theory of Solar Wind Expansion," Joint Symposium on Solar Interplanetary Physics, Tucson, Arizona (January 12-15, 1977).

D. V. Giovanielli, D. B. Henderson, G. H. McCall, R. B. Perkins, "Laser Fusion Target Interactions Studies at 10.6 μ m," University of California, Irvine, California (May 24, 1977); University of Rochester, Rochester, New York (June 3, 1977).

R. L. Carman and C. K. Rhodes, "Multiple-Photon Absorption as a Mechanism for Funneling Broadband Optical Energy into Narrow-Band States," International Conference on Multiple Photon Processes, Rochester, New York (June 6-9, 1977).

R. P. Godwin, "Experiments in Richtung Laser Fusion," Colloquium, Bonn University, Bonn, W. Germany (January 14, 1977); Seminar, Technical University Munich, Garching, W. Germany (March 31, 1977); Colloquium, University of Munich, Munich, W. Germany (May 24, 1977); Colloquium, Kiel University, Kiel, W. Germany (June 21, 1977); DESY Seminar, DESY, Hamburg, W. Germany (June 24, 1977).

R. P. Godwin, "Diffuse Reflexionsverluste bei Laseraufheizung fester Targets," Plasma Physics Division Meeting, German Physical Society, Essen, W. Germany (March 31, 1977).

R. P. Godwin, "Wavelength Scaling and Energy Transport in Laser-Produced Plasma Experiments," Colloquium, University of Bern, Bern, Switzerland (May 12, 1977).

PUBLICATIONS

B. L. Kortegaard, "A 40 db Regulator—With One Chip Plus a Triac," *Electronic Design Magazine* (May 24, 1977).

K. D. Ware, "Limitations to the Choice of Lumped Elements in a High-Frequency Integration," *Plasma Focus—Ion Acceleration by Collective Fields* (Newsletter).

J. J. Devaney, L. A. Booth, J. H. Pendergrass, and T. G. Frank, "Preliminary Assessment of Potential Accidents of Laser Fusion Electric Generating Stations," *ANS Trans.* 26 (June 1977) p. 31.

G. H. McCall, "Design of X-Ray Microscopes for Laser Fusion Applications," in *Advances in Precision Machining of Optics*, T. T. Saito, Ed., Proc. Seminar, San Diego, California, T. T. Saito, Ed., S.P.I.E., (1976) 11-23.

R. Bezzerides, D. F. Dubois, D. W. Forslund, J. M. Kindel, K. Lee, and E. L. Lindman, "Recent Developments in Understanding the Physics of Laser Produced Plasmas," Proc. Symp. on Plasma Physics and Controlled Nuclear Fusion Research, Berchtesgaden, FRG, October 6-13, 1976.

E. Stark, "Laser Fusion Program at LASL," Los Alamos Scientific Laboratory report LA-6510-PR (November 1976).

R. P. Godwin, "X-Ray Diagnostics in the Laser Initiated Fusion Program," Proc. 24th Annual Conf. Applications of X-Ray Analysis, Denver, Colorado (1976) 533-569.

R. C. Sze and P. B. Scott, "Laser Action in Krypton Fluoride and Molecular Nitrogen in a Fast Pin Laser," *J. Appl. Phys.* 47, 5492-5493 (1976).

T. G. Frank and L. A. Booth, "Engineering Aspects of Laser Fusion Reactors," in *Advanced Nuclear Energy Systems*, Proc. ASME-ANS Int. Conf., Pittsburgh, Pennsylvania (1976) 544-544.

S. J. Gitomer, R. L. Morse, and B. S. Newberger, "Laser Driven Ablative Implosions," *Phys. Fluids* 20, 234-238 (1977).

K. B. Riepe and J. Jansen, "Pulsed Power Systems for the LASL High Energy Gas Laser Facility," Proc. IEEE Int. Pulsed Power Conf., Lubbock, Texas, November 9-11, 1976

S. J. Czuchlewski, B. J. Feldman, and A. V. Nowak, "Observation of Coherent Resonance Fluorescence in Hot Carbon Dioxide," Winter APS Meeting, Stanford, California, December 1976.

A. Mayer and D. S. Catlett, "Electroless or Autocatalytic Coating of Microparticles for Laser Fusion Targets," Los Alamos Scientific Laboratory report LA-6583 (1977).

L. A. Booth and T. G. Frank, "Technology Assessment of Laser Fusion Power Production," Proc. ANS Topical Meeting on Technology of Controlled Nuclear Fusion, Richland, Washington, September 21-23, 1976.

A. Mayer and D. S. Catlett, "Electrolytic Coating of Microparticles for Laser Fusion Targets," Los Alamos Scientific Laboratory report LA-6584 (1977).

R. L. Carman, A. G. Engelhardt, and N. Clabo, "Multiwave Picosecond Laser Interferometry of Carbon Dioxide," Proc. Fourth Workshop on Laser Interaction and Related Plasma Phenomena, Troy, New York, November 8-12, 1977.

E. R. Grilly, "Condensation of Hydrogen Isotopes," *Rev. Sci. Instrum.* 48, 148-151 (1977).

- S. Singer, "Optics in Terawatt Carbon Dioxide Lasers," Electro-Optics Laser Conf. and Exposition, New York City, September 14-16, 1976.
- T. H. Tan, G. H. McCall, A. H. Williams, and D. V. Giovanielli, "Measurement of High Energy Charged Particles from Laser Produced Plasmas," Proc. Fourth Workshop on Laser Interaction and Related Plasma Phenomena, Troy, New York, November 8-12, 1977.
- L. A. Booth and T. G. Frank, "Commercial Applications of Inertial Confinement Fusion," Los Alamos Scientific Laboratory report LA-6838-MS (1977).
- M. A. Stroschio, "Suprathermal Electrons in a Laser-Heated Plasma—A Theoretical Temperature Relationship," Opt. Commun. 21 267-271 (1977).
- T. G. Frank and L. A. Booth, "Laser Fusion Reactor Materials Problems Resulting from Fusion Micro Explosion," J. Nucl. Mater. 63 31-36 (1976).
- C. W. Cranfill, "One Dimensional Computer Simulations of the Implosion of Simple Shell Targets with the Los Alamos Two-Beam Carbon Dioxide Laser," Los Alamos Scientific Laboratory report LA-6827-MS (1977).
- B. J. Feldman and S. J. Gitomer, "Annular Lens Soft Aperture for High Power Laser Systems-- Authors Reply to Comments," Appl. Opt. 16, 1484 (1977).
- T. G. Frank and L. A. Booth, "Inertial Confinement Fusion Reactor and Generating Station Concepts," Trans. Am. Nucl. Soc. 26, 8-9 (1977).
- J. J. Devaney, L. A. Booth, and J. H. Pendergrass, "Preliminary Assessment of Potential Accidents of Laser Fusion Electric Generating Stations," Trans. Am. Nucl. Soc. 26, 31-32 (1977).
- B. S. Newberger and W. S. Hall, "Computer-Generated Interferograms to Characterize Microballoons," Los Alamos Scientific Laboratory report LA-6864-MS (1977).
- J. S. Pearlman and R. F. Benjamin, "Sub-KeV X Ray Imaging Using a Low Cost Ellipsoidal Lens," Appl. Opt. 16, 94-96 (1977).
- P. B. Weiss, "Attenuation of 10.6 Micrometer Beams by Electrically Initiated Laser Driven Plasmas," Appl. Phys. Lett. 30, 261-263 (1977).
- E. L. Lindman and M. A. Stroschio, "On the Relativistic Corrections to the Ponderomotive Force," Nucl. Fusion 17, 619-622 (1977).
- E. Stark and F. Skoberne, "Laser Fusion Program at LASL," Los Alamos Scientific Laboratory report LA-6616-PR (May 1977).
- R. J. Fries, "Selection, Characterization and Coating of Laser Fusion Targets," Proc. Fifth Annual Conf. Int. Nucl. Target Development Society, Los Alamos, New Mexico (1976) 1-31; Los Alamos Scientific Laboratory report LA-6850-C (1977).
- B. S. Cranfill, "Preparation of Ultrathin Polyethylene Foils by Film Casting," Proc. Fifth Annual Conf. Intern. Nucl. Target Development Society, Los Alamos, New Mexico (1976) 130-137; Los Alamos Scientific Laboratory report LA-6850-C (1977).
- D. B. Henderson and M. A. Stroschio, "Energy Deposition in Laser-Heated Plasmas," Phys. Rev. Lett. 37, 1244-1246 (1976).
- D. W. Forslund, J. M. Kindel, and K. Lee, "Theory of Hot Electron Spectra at High Laser Intensity," Phys. Rev. Lett. 39, 284-285 (1977).
- K. B. Riepe, "High-Voltage Microsecond Pulse-Forming Network," Rev. Sci. Instrum. 48, 1028-1030 (1977).
- B. J. Feldman, R. A. Fisher, and E. J. McLellan, "Transient Versus Steady-State Molecular Absorption—Application to Carbon Dioxide Laser Pulse," Appl. Phys. Lett. 31, 189-191 (1977).

R. L. Carman, "Advanced Laser Technology for Laser-Induced Fusion Applications," Proc. Fourth Workshop on Laser Interaction and Related Plasma Phenomena, Troy, New York, November 8-12, 1977.

W. L. Thompson, "Neutron-Photon-Electron Shielding Study for a Laser Fusion Facility," Proc. Conf. on Reactor Shielding, Knoxville, Tennessee, April 18-22, 1977.